Single-molecule and biochemical characterization of the human myosin isoforms IIb, VI and IXa

DISSERTATION

an der Fakultät für Biologie

zur Erlangung des Doktorgrades der Naturwissenschaften

Ludwig-Maximilians-Universität München

vorgelegt von

Markus Kröss

aus Südtirol

München, 23. September 2021

Diese Dissertation wurde angefertigt
unter der Leitung von Prof. Dr. Claudia Veigel
am Institut für zelluläre Physiologie
der Ludwig-Maximilians-Universität München

Erstgutachterin: Prof. Dr. Kirsten Jung
Zweitgutachter: Prof. Dr. Thorben Cordes

Tag der Abgabe: 23. September 2021
Tag der mündlichen Prüfung: 25. Februar 2022

Abstract

Myosins are actin-dependent molecular motors which convert chemical energy from ATP hydrolysis into mechanical work. They form a large superfamily but all of them share a common domain structure consisting of three parts: a head, neck and tail region. The catalytic head region is evolutionary conserved and includes a nucleotide-binding site together with an actin-binding site. The head is followed by the neck domain, which binds additional accessory proteins (light chains, e.g. calmodulin) and acts as a lever arm. Finally, the tail region is the most variable domain and regulates cellular functions and dynamics of the motor.

The myosin superfamily interacts with actin filaments to generate a variety of cellular functions including muscle contraction, exo- and endocytosis, cytokinesis and even signal transduction. Twelve different myosin classes have evolved in humans to adapt to their specific cellular function. In this work I selected isoforms from three myosin classes to investigate their biochemical and single-molecule properties. The isoforms IIb, VI and IXa are structurally, biochemically and kinetically tailored to their specific cellular tasks and not much is known about their regulation (e.g. calcium, phosphorylation) to adapt to changing cellular environments or external stimuli. The aim of the study is to elucidate the molecular roles of the myosin isoforms IIb, VI and IXa and how their structural and regulatory characteristic lead to their specific cellular functions. Besides diverse biochemical methods and functional *in vitro* assays an optical tweezers transducer was used to study the single-molecule behaviour of the different myosin isoforms. These optical tweezers experiments are able to resolve the nanometre displacements and piconewton forces generated by single motor molecules and allow insights into the basic molecular mechanism of the chemo-mechanical energy transduction cycle.

Myosin IXa is a intriguing molecular motor and is localized in acto-myosin networks at cell-cell adhesions. Recent studies identified myosin IXa as a key requirement for collective cell migration, which is an important mechanism during epithelial morphogenesis, tissue regeneration and cancer metastasis. On a structural level, myosin IXa contains several

unique features: The tail domain links this motor to signalling functions as it contains a Rho-GTPase activating domain (RhoGAP) which can alter the dynamics of the actin cytoskeleton. Additionally, the head domain comprises a unique, ∼200 aa insertion in the loop 2 region involved in actin binding. This work clearly demonstrates that this insertion allows myosin IXa to bundle actin filaments into actomyosin networks. Quantitative TIRF microscopy revealed that myosin IXa assembles actin into bundles of up to seven or even more filaments. A collaboration project using transmission electron microscopy combined with single particle image processing showed that the bundles consisted of a highly ordered 2D actomyosin network, with three distinct conformations. The novelty found in this work is that the bundles were also present at micromolar ATP concentrations and bundle dissociation occurred in a stepwise manner, suggesting a dynamic assembly and disassembly of the actomyosin networks in a cellular context. Furthermore, the presence of a calmodulin-binding site in the unique loop 2 insertion indicates that the motor and bundling activity of myosin IXa is regulated by calcium/calmodulin, which was also in the focus of this work.
At the cellular level, the actin lattices might introduce specific tracks for other myosin motors and represent platforms, which allows specific RhoGAP activity from the tail of myosin IXa to be focused to distinct intracellular locations.

In contrast to myosin IXa, the non-muscle myosin isoform IIb (NMIIb) is ubiquitously expressed and has key functions in fundamental cellular processes such as cytokinesis, cell migration and control of cell morphology. This double-headed myosin contains a coiled-coil motif in the tail domain, enabling it to form large filaments. In this work I compared the single-molecule properties of single and double-headed human NMIIb to gain insights into the cooperative nature of the myosin heads. The results indicate that the single myosin heads act in an independent, non-cooperative manner. Furthermore, I show that single and double headed NMIIb produces two types of power strokes: A ∼5 nm working stroke known also from other myosin II isoforms, and unusual close-to-zero attachment events. The results suggest that the latter events might represent transient, weak binding states of myosin to actin. These weak binding interactions could have important cellular relevance to bind and tether the NMIIb myosin filament to actin without the consumption of further ATP, especially as this NMII isoform is known to be involved in tension maintenance and structural anchoring.

Myosin VI is the only known member of the myosin superfamily moving towards the minus end of actin filaments. This molecular motor is involved in diverse cellular func-

tions such as vesicle transport, endocytosis and intracellular membrane trafficking. In this work I investigate the role of myosin head phosphorylation on the mechanical functions of myosin VI. *In vitro* motility assays from a collaboration partner at the University of Cambridge (UK) have shown that phosphorylation of serine at position 267 had a huge impact on the actin gliding velocity. Using an optical tweezers transducer, I show that the differences observed in the ensemble assay can be explained by tuning the ADP release and ATP binding rate in the actomyosin cycle without a change in the power stroke size. This dramatic effects on the *in vitro* properties of myosin VI might have pronounced cellular consequences on myosin VI activity in membrane dynamics and cytoskeletal organisation.

Zusammenfassung

Myosine sind aktinabhängige molekulare Motoren, die chemische Energie aus der Hydrolyse von ATP in mechanische Arbeit umwandeln. Sie bilden eine große Superfamilie mit einer gemeinsamen Domänenstruktur, die aus drei Teilen besteht: einer Kopf-, Hals- und Schwanzregion. Die katalytische Kopfregion ist evolutionär konserviert und umfasst eine Nukleotid- zusammen mit einer Aktinbindungsstelle. Dem Kopf folgt die Halsdomäne, die zusätzliche akzessorische Proteine (leichte Ketten, z.B. Calmodulin) bindet und als Hebelarm fungiert. Die Schwanzregion ist die variabelste Domäne und bestimmt die zellulären Funktionen und reguliert die Dynamik des Motors.

Die Myosin-Superfamilie interagiert mit Aktinfilamenten und spielt eine wichtige Rolle bei einer Vielzahl von Zellfunktionen, wie z.B. Muskelkontraktion, Exo- und Endozytose, Zytokinese und sogar Signaltransduktion. Zwölf verschiedene Myosinklassen haben sich beim Menschen entwickelt, um die unterschiedlichen zellulären Funktionen zu erfüllen. In dieser Arbeit habe ich Isoformen aus drei Myosinklassen ausgewählt, um ihre biochemischen und Einzelmoleküleigenschaften zu untersuchen. Die Isoformen IIb, VI und IXa sind strukturell, biochemisch und kinetisch auf ihre spezifischen zellulären Aufgaben angepasst. Über ihre Regulation, z. B. durch Calcium oder Phosphorylierung, zur Anpassung an sich ändernde zelluläre Umgebungen oder externe Stimuli ist kaum etwas bekannt. Ziel dieser Studie ist es, die molekularen Rollen der Myosin-Isoformen IIb, VI und IXa aufzuklären und zu ermitteln, wie ihre strukturellen und regulatorischen Eigenschaften zu ihren spezifischen Zellfunktionen führen. Neben verschiedenen biochemischen Methoden und funktionellen *in vitro* Assays wurde eine optische Falle verwendet, um das Einzelmolekülverhalten der verschiedenen Myosin-Isoformen zu untersuchen. Diese Einzelmolekülexperimente sind in der Lage, die von einzelnen Motormolekülen erzeugten Nanometerruderschläge und Piconewton-Kräfte aufzulösen, um Einblicke in den grundlegenden molekularen Mechanismus des chemomechanischen Energieübertragungszyklus zu ermöglichen.

Myosin IXa ist ein einzigartiger molekularer Motor, der sich in Actomyosin-Netzwerken an Zell-Zell-Adhäsionen befindet. Neueste Studien identifizierten Myosin IXa als Schlüsselvoraussetzung für die kollektive Zellmigration, die ein wichtiger Mechanismus bei der epithelialen Morphogenese, Geweberegeneration und Krebsmetastasierung ist. Auf struktureller Ebene enthält Myosin IXa mehrere einzigartige Merkmale: Die Schwanzdomäne verbindet diesen Motor mit Signalfunktionen, da sie eine Rho-GTPase-aktivierende Domäne (RhoGAP) enthält, die eine wichtige Rolle bei der Regulierung des Umbaus des Aktin-Zytoskeletts spielt. Zusätzlich umfasst die Kopfdomäne eine spezielle Insertion von ∼200 Aminosäuren in der Loop 2-Region, die an der Aktinbindung beteiligt ist. Die vorliegende Arbeit zeigt deutlich, dass diese Insertion es Myosin IXa ermöglicht, Aktinfilamente in Actomyosin-Netzwerke zu bündeln. Mittels quantitativer TIRF-Mikroskopie stellte sich heraus, dass Myosin IXa Aktin zu Bündel von bis zu sieben oder sogar mehr Filamenten zusammensetzt. Ein Kollaborationsprojekt unter Verwendung von Transmissionselektronenmikroskopie in Kombination mit Einzelmolekülbildverarbeitung ergab, dass die Bündel aus einem hochgeordneten 2D-Actomyosin-Netzwerk mit drei unterschiedlichen Myosinkonformationen bestanden. Die Neuheit in dieser Arbeit ist, dass die Bündel auch bei mikromolaren ATP-Konzentrationen vorhanden waren und die Bündeldissoziation schrittweise erfolgte, was auf einen dynamischen Auf- und Abbau der Actomyosin-Netzwerke im zellulären Kontext hindeutet. Darüber hinaus weist das Vorhandensein einer Calmodulin-Bindungsstelle in der einzigartigen Insertion von Loop 2 darauf hin, dass die Motor- und Bündelungsaktivität von Myosin IXa durch Calcium/Calmodulin reguliert wird, was ebenfalls ein Untersuchungsgegenstand dieser Arbeit war.
Auf zellulärer Ebene könnten die Myosin IXa-induzierten Aktinnetzwerke spezifische Schienen für andere Myosinmotoren bilden und Plattformen darstellen, um die RhoGAP-Aktivität auf bestimmte intrazelluläre Stellen zu fokussieren.

Im Gegensatz zu Myosin IXa wird die Nicht-Muskel-Myosin-Isoform IIb (NMIIb) ubiquitär exprimiert und hat Schlüsselfunktionen bei grundlegenden zellulären Prozessen, wie Zytokinese, Zellmigration und Kontrolle der Zellmorphologie. Dieses doppelköpfige Myosin enthält ein Coiled-Coil-Motiv in der Schwanzdomäne, das es ihm ermöglicht große Filamente zu bilden. In dieser Arbeit habe ich die Einzelmoleküleigenschaften von ein- und zweiköpfigem humanem NMIIb verglichen, um Einblicke in die kooperative Natur der Myosinköpfe zu erhalten. Die Ergebnisse zeigen deutlich, dass die einzelnen Myosinköpfe unabhängig und nicht kooperativ wirken. Darüber hinaus weisen die Ergebnisse darauf hin, dass ein- und zweiköpfiges NMIIb zwei Arten von Interaktionen mit Aktin erzeugt: einen Ruderschlag von ∼5 nm, der auch von anderen Myosin II-Isoformen bekannt ist,

sowie ungewöhnliche Bindungsereignisse, die nicht zu einem Ruderschlag führen. Die Ergebnisse legen nahe, dass die letzteren Ereignisse vorübergehende, schwache Bindungs-Zustände von Myosin an Aktin darstellen könnten. Diese schwachen Bindungswechselwirkungen könnten eine wichtige zelluläre Relevanz bei Bindung des NMIIb-Myosin-Filaments an Aktin ohne den Verbrauch von ATP haben. Dies ist insofern von Bedeutung, da diese NMII-Isoform an der Aufrechterhaltung von Spannung an Aktinfilamenten über einen längeren Zeitraum und der strukturellen Verankerung beteiligt ist.

Myosin VI ist das einzige bekannte Mitglied der Myosin-Superfamilie, das sich in Richtung des Minus-Endes der Aktinfilamente bewegt. Dieser molekulare Motor ist an verschiedenen zellulären Funktionen wie Vesikeltransport, Endozytose und intrazellulärem Membranaustausch beteiligt. In dieser Arbeit untersuche ich die Rolle der Myosinkopfphosphorylierung für die mechanischen Funktionen von Myosin VI. *In-vitro*-Motilitätsexperimente eines Kooperationspartners an der Universität von Cambridge (UK) haben gezeigt, dass die Phosphorylierung von Serin an Position 267 einen großen Einfluss auf die Gleitgeschwindigkeit des Aktins hatte. Mit einer optischen Falle zeige ich, dass die beobachteten Unterschiede darauf zurückgeführt werden können, dass die ADP-Freisetzungsrate und die ATP-Bindungsrate im Actomyosin-Zyklus verändert wird, ohne dass es zu einer Änderung der Ruderschlaggröße kommt. Diese dramatischen Auswirkungen auf die *in vitro*-Eigenschaften von Myosin VI könnten ausgeprägte zelluläre Konsequenzen für die Myosin VI-Aktivität in der Membrandynamik und der Organisation des Zytoskeletts haben.

Contents

Abbreviations

4QD	4-quadrant diodes/detector
aa	amino acids
AB	assay buffer
AB+	assay buffer including ATP
ACEX	actin extraction buffer
AOD	acousto-optic deflector
APS	ammonium persulfate
ATP	adenosine triphosphate
bp	base pair
BSA	bovine serum albumin
CCD	charged coupled device
DNA	deoxyribonucleic acid
DTT	1,4-dithiothreitol
EGTA	ethylene glycol-bis(β -aminoethyl ether)-N,N,N',N'-tetraacetic acid
ELC	essential light chain
F actin	filamentous actin
FPGA	field programmable gate array
G actin	globular actin
HMM	heavy meromyosin

HNMIIb	human non-muscle myosin IIb
IR	infrared
krpm	thousands of rotations per minute
LED	light emitting diode
LMM	light meromyosin
MD	motor domain
MOPS	3-(N-morpholino)propanesulfonic acid
NA	numerical aperture
NEM	N-ethylmaleimide
PBS	phosphate-buffered saline
PCR	polymerase chain reaction
RLC	regulatory light chain
SDS-PAGE	sodium dodecyl sulphate polyacrylamide gel electrophoresis
SDS	sodium dodecyl sulphate
TEM	transmission electron microscopy
TEMED	N,N,N',N'-tetramethylethylenediamine
TIRF	total internal reflection fluorescence microscopy
TRIS	tris(hydroxymethyl)-aminomethane
UV	ultraviolet
v/v	volume per volume
w/v	weigth per volume
WT	wild type

List of Figures

List of Tables

1 Introduction

1.1 Molecular motors

Molecular motors, also called molecular machines, are proteins that convert chemical energy into mechanical forces and motion. Most molecular motors use the energy of ATP or the electrochemical potential of protons across the cell membrane as an energy source. Well-studied examples of ATP-driven motors include myosin, kinesins and dynein, which are responsible for diverse cytoskeletal activities. ATP synthase, V-ATPase and the bacterial flagellar motor are examples of molecular motors driven by the proton-motive force. Interestingly, also the RNA polymerase and the ribosome can be counted as molecular machines as they move along nucleic acid tracks to read and write genetic information (Iino et al., 2020).

The cytoskeletal motor proteins that move along tracks composed of actin filaments are known as myosin, whereas kinesin and dynein move along microtubule tracks. They have specialized also regarding their directionality on their specific track. Most kinesin motors move towards the plus end of microtubules, whereas dynein shows a minus end directed movement on the microtubules. Impressively, all known myosin isoforms, with the exception of myosin VI, perform a plus end directed movement on actin filaments (Buss and Kendrick-Jones, 2008).
Dynein and kinesin are highly processive motors and can walk on microtubules up to a few micrometers (Taylor and Borisy, 2000). Therefore, they are best suited for long distance movement of cargo, while the myosin superfamily can anchor organelles to actin filaments and enable movement over short distances along the actin cytoskeleton (Peckham, 2011). Apart from cargo transport, the myosin superfamily with over 30 classes performs a multitude of cellular functions, ranging from exo- and endocytosis, actin reorganisation, tension generation during cytokinesis to signal transduction (Batters and Veigel, 2016). Kinesins and myosins are structurally very similar and have related force-

producing mechanisms. Dynein is structurally more complex, containing several subunits and has a different power stroke mechanism compared to kinesins or myosin (Mallik and Gross, 2004).

Why does a eukaryotic cell possess so many different cytoskeleton-associated molecular motors? Eukaryotic cells are much bigger in size than prokaryotic cells, with almost 10.000 times the volume of the latter ones (Milo and Phillips, 2016). Along with this huge size difference, eukaryotic cells are much more complex and they are organised in compartments in order to perform their specific functions more efficiently. This compartmentalization requires an efficient regulation of the cytoskeletal architecture including transport of cargo along specific tracks, because diffusion would be too slow over long distances. All cytoskeletal motors couple ATP hydrolysis to the binding and dissociation from actin or microtubules. Structurally diverse isoforms have evolved to adapt to their specific function within the cell to ensure correct spatiotemporal localization of cell compartments.

A detailed molecular understanding of the structural and biochemical features that allows each myosin isoform to perform their specialized cellular functions, gives rise to a better understanding of pathologies caused by myosin dysfunctions. It is becoming more and more clear that myosins are associated with severe diseases including cardiomyopathies, neurological defects, cancer, blindness, and deafness (Coluccio, 2020).

In a broader context, the design of synthetic or artificial molecular machines is of particular interest in the field of nanotechnology to develop new materials, sensors and energy storage systems. The 2016 Nobel Prize in Chemistry has been awarded "for the design and synthesis of molecular machines" to Sauvage, Stoddart and Feringa. They have developed molecules that can perform specific movements when they are supplied with energy (e.g. alkene-based light-driven molecular motors; van Leeuwen et al. (2017)). Although this field is still in the early stage in terms of performance, synthetic molecular motors have great potential to perform new functions beyond the capabilities of biological motors (Iino et al., 2020).

1.2 Actin-based cytoskeleton and cellular motility

The actin-based cytoskeleton, consisting of actin filaments and actin-binding partners is responsible for very different forms of cellular motility. In its most basic form directional movement is mediated by the polymerization of actin. Spatially controlled it is responsible for a multitude of cellular processes by which cells change shape based on environmental signals, move through narrow spaces, extend protrusions like lamellipodia and filopodia, or enclose particles in phagocytic cups (Pantaloni et al., 2001).

In the 1980s it was shown that the lamellipodium of fibroblasts contains a dense meshwork of actin filaments with uniform polarity. The plus ends are pointing towards the plasma membrane whereas minus ends of the filaments are depolymerizing at the rear. The continuous actin treadmilling provides an effective mechanism for protrusion of cytoplasm in the lamellipodium (Wang, 1985). A similar situation exists in the 'comet tail' of the bacterial pathogen *Listeria monocytogenes*, which invades macrophages and other mammalian cells. *Listeria* are internalized by host cells and incorporated into phagolysosomes. The bacteria then escape from the phagolysosome and enter the cytoplasm by nucleating host cell actin filament polymerization from its surface. These filaments rearrange to form an actin tail with which the bacterium moves (Dabiri et al., 1990). Several other pathogens, including *Shigella*, *Trypansoma* and *Vaccinia virus* have a similar intracellular lifestyle. Interestingly, it was shown that the rate of actin polymerization equaled the rate of Listeria movement in the cytoplasm (up to 0.4 µm/s; Theriot et al. (1992)). Furthermore, *in vitro Listeria* movement was observed in cell-free extracts, which formed the basis for fully reconstituting actin-based movement from a minimal set of purified components (Theriot et al., 1994).

1.2.1 Different types of actin networks

Actin polymerisation, depolymerisation, branching and many other processes are controlled by a very large number of different actin-binding proteins. This allows the organisation of different types of actin networks: branched and crosslinked networks, parallel bundles, and anti-parallel contractile structures (see Fig. 1.1). The cell cortex, a thin layer of crosslinked actin, is located underneath the plasma membrane, which is important for cell shape maintenance and changes. At the forefront of the cell, branched and crosslinked networks form a two-dimensional sheet and shape the lamellipodium. Actin polymerization directly at the cell membrane pushes the membrane and allows cell movement. The finger-like structures of filopodia are composed of parallel actin bundles and

are important for directional response of the cell. Additionally, the cytoplasm contains a three-dimensional mesh of crosslinked filaments containing stress fibres with anti-parallel contractile actin bundles, which couples the cell cytoskeleton to the extracellular matrix via focal adhesions. Contractile bundles contain myosin and allows contraction of the cell and tension at focal adhesion sites. These sites are connected to the extracellular matrix and allow to transmit biochemical and mechanical signals between the intracellular actin network and the extracellular substrate (Blanchoin et al., 2014).

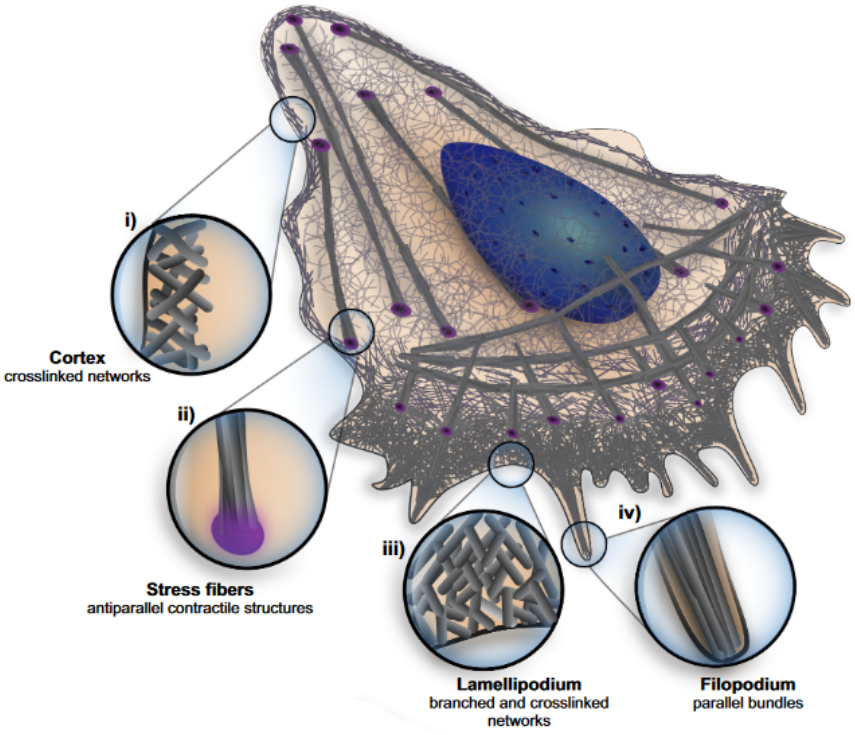

Fig. 1.1: Schematic representation of different types of actin networks. i) cell cortex with crosslinked actin; ii) stress fibers with anti-parallel contractile actin bundles; iii) lamellipodia containing branched and crosslinked actin networks and iv) filopodia with parallel actin bundles (Blanchoin et al., 2014).

An important player in the branched actin network consists of a complex of seven proteins: the Arp2/3 complex. The complex contains two actin-related proteins (Arp2 and Arp3) that form a dimer similar to an actin dimer. The Arp2/3 complex leads to the nucleation of actin filaments as 70° branches on the sides of more matured filaments (Robinson, 2001). The interaction with capping proteins (e.g. gelsolin), which block growth at filament plus ends, limits branch elongation (Pantaloni et al., 2001). Disassembly of actin structures involves ADF/cofilin. This protein binds to actin filaments and leads to debranching and fragmentation of actin networks.

In parallel actin bundles the filaments are oriented with their plus end in the same direction, mostly in direction to the cell membrane. The filaments are kept in vicinity by cross-linking proteins including α-actinin, fimbrin, and fascin. In contrast, antiparallel actin assemblies with myosin-induced contractions are very important for cytokinesis and for stress fiber function during the formation of cell-cell and cell-matrix adhesions. The antiparallel actin arrangement is stabilized by α-actinin and fimbrin but its not directly dependent on these proteins as cross-linking limits the possibility of myosin-induced contraction (Blanchoin et al., 2014).

1.2.2 Cytoskeleton-based pathologies

Understanding the architecture and dynamics of the cytoskeleton can contribute to a molecular understanding of diseases of the cytoskeleton ranging from microbial or virus infections to deafness and immune system pathologies. As already mentioned above, the study of how bacteria and viruses move in infected cells, put forth the understanding of actin-based motility (Blanchoin et al., 2014).
Altered ADF/cofilin regulation is associated with Alzheimer's disease and ischemic kidney disease. Furthermore, also atherosclerosis is connected to cytoskeleton-based pathologies. Constriction of arteries occurs in places with arterial branches and curvatures where cells are stretched under tension by blood flow. It is suggested that this mechanical tension in the actin cytoskeleton triggers signaling pathways that lead to cell death (Davies, 2009). Another example that has become very prominent in recent years is cancer metastasis and invasion. Invasion is a step during metastasis when tumour cells disrupt extracellular matrix barriers and invade surrounding tissues. Tumour cells use their lamellipodia and filopodia, but also new specialized structures (invadopodia) to escape from the extracellular matrix (Kumar and Weaver, 2009; Mierke, 2013; Blanchoin et al., 2014).

1.3 Myosin superfamily

Myosins are molecular motors that convert chemical energy into mechanical work. They comprise a large superfamily of proteins that share a common motor domain which binds to actin, hydrolyses ATP and produces movement (Sellers, 2000). Myosins are typically assembled of three subdomains, namely an N-terminal motor domain, the neck or lever arm domain and the C-terminal tail domain (see Fig. 1.2).
The motor domain interacts with actin, binds ATP and is highly conserved within the myosin superfamily with the exception of several surface loops. The neck domain binds light chains of the calmodulin superfamily. They bind to a helical sequence called the

IQ motif with a consensus sequence of IQxxxRGxxxR (Cheney and Mooseker, 1992). Myosins can have up to six IQ motifs in the neck region. The lever arm domain plays a key role in transducing and amplifying the small conformational changes generated by ATP hydrolysis in the motor domain into nanometre displacements at the end of the lever arm. The tail domain binds and position the motor domain to its cellular target and determines its functional characteristics (e.g. the tail contains SH3, GAP, FERM or PH domains). Furthermore, the tails of many myosins have coiled-coil-forming sequences that allow dimerisation or even the formation of large arrays (thick filaments) like in muscles (Sellers, 2000; Batters and Veigel, 2016). In a coiled-coil structural motif several α-helices are assembled together like the strands of a rope.

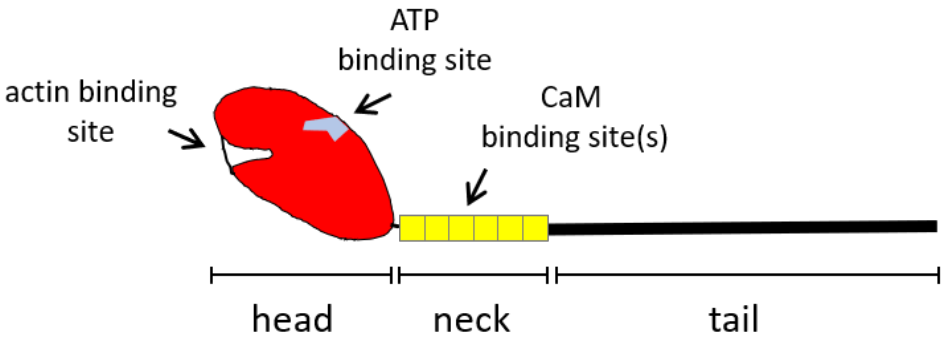

Fig. 1.2: Schematic depiction of the common myosin structure. They comprise a head or motor domain, a neck domain with a variable number of calmodulin (CaM) binding IQ motifs, and a tail domain, which specifies the myosin function. Some myosins contain coiled-coil sequences in the tail, allowing them to form dimers or large oligomers.

Myosins are evolutionarily conserved and found in nearly all eukaryotic cells. Traditionally, the classification of myosins is based on the conserved motor domain sequence. A genomic analysis of 2269 myosin sequences from 328 eukaryotic species arranged myosins into 35 classes (Fig. 1.3; Odronitz and Kollmar (2007)). It is striking that the myosin classes I and II (the latter termed 'Mhc' in Fig. 1.3) comprise the biggest group. In the human genome there are a total of 39 myosin genes which are encoding myosin heavy chains from 12 different classes (Berg et al., 2001).

After discovering skeletal muscle myosin (see next section) two myosins from class I and II were purified from *Acanthamoeba castellani* in the 1970s (Pollard and Korn, 1973a,b). They observed in the EM that myosin II from the amoeba was structurally similar to muscle myosin and it formed filaments at physiological ionic strength (Pollard et al., 1978). Therefore, those myosins were assigned to myosin class II and referred to as conventional myosins (Sellers, 2000). Conventional myosin II isoforms have been discovered in smooth and cardiac muscles as well as non-muscle cells (Berg et al., 2001). All other myosin classes are termed unconventional myosins. After identification of class I and II myosins all subsequent classes were numbered in roman numerals in chronological order of the discovery of the founding member of the class (Sellers, 2000).

The historically based differentiation into conventional and unconvential myosins suggests that the latter ones have less important cellular functions. The significance of unconventional myosins is emphasized by the fact that they make up four out of five myosin genes in *Saccharomyces cerevisiae* and approx. 70 % of the myosin genes in humans. Additionally, studies show that typical non-muscle cells express only one or two conventional myosin genes but more than ten unconventional myosins (Bement et al., 1994; Berg et al., 2001).

The wide distribution of myosins in eukaryotic organisms and the large number of isoforms suggest that they can fulfill very different cellular functions and that they are important for the maintenance of life. Besides muscle contraction, conventional myosins were shown to be involved in the narrowing of the cytokinetic groove during cell division and in the arrangement of stress fibres (Glotzer, 2005; Hotulainen and Lappalainen, 2006). Unconventional myosins have been implicated in vesicle transport, intracellular membrane trafficking, exo- and endocytosis, signal transduction and actin reorganisation (Thompson and Langford, 2002; Batters and Veigel, 2016).

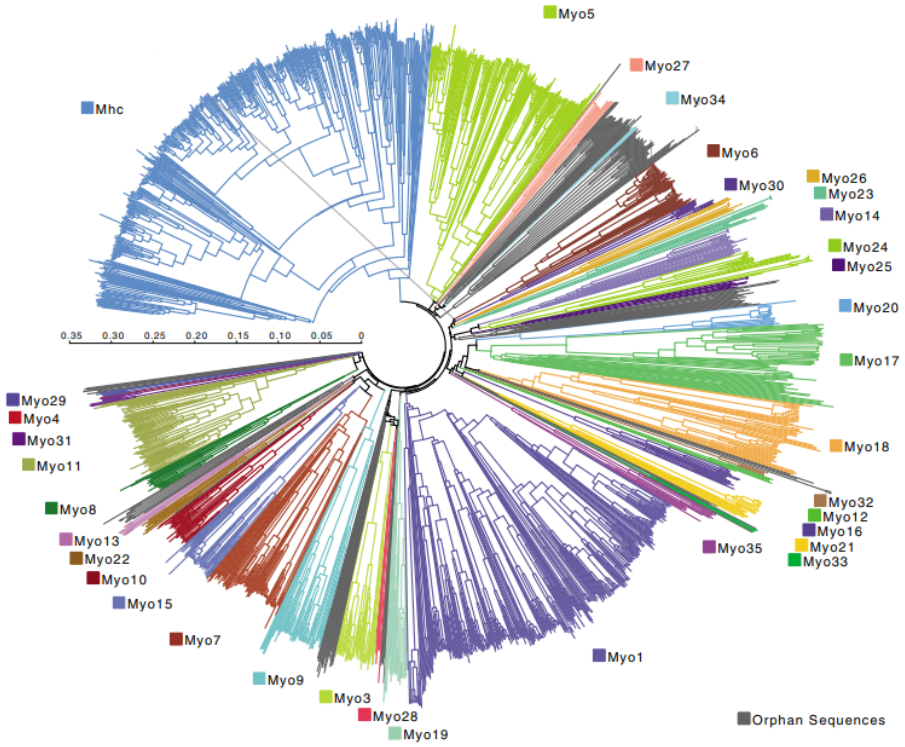

Fig. 1.3: Phylogenetic tree of the myosin superfamily. The tree was constructed from the multiple sequence alignment of ∼2000 myosin motor domains and yielded 35 myosin classes. The scale bar corresponds to the number of amino acids in a sequence. Figure modified from Odronitz and Kollmar (2007).

1.4 Discovery of myosin and first insights into actomyosin interaction

The German physiologist W. Kühne extracted in 1864 a protein at high salt from muscle and termed it 'myosin' (Kühne, 1864). The protein formed threads under low salt conditions e.g. water. Lyubimova and Engelhardt (1939) showed in 1939 that those extracts exhibit an ATPase activity. The idea that myosin was an ATPase was controversial at that time, because enzymes were thought to be small globular proteins, which apparently does not apply to the thread forming myosin. The importance of this study was supported by the earlier discovery that ATP was likely to be the source of energy for muscle contraction.

In an improved extraction protocol Banga and Szent-Györgyi (1942) observed that short-time exposure of muscle to high salt concentrations extracted a low viscosity protein, whereas overnight exposure solubilized a high viscosity protein. The viscosity of the latter fraction was decreased by adding ATP while the viscosity of the first fraction remained

unaffected. Szent-Györgyi discovered that the threads prepared from the high viscosity fraction shortened on addition of ATP (see Fig. 1.4). In his autobiography, Szent-Györgyi (1963) describes that 'to see them (the threads) contract for the first time, was perhaps the most thrilling moment of my life.'

Fig. 1.4: Contraction of muscle threads on ATP addition. Shown are the same thread A before and B after addition of boiled muscle juice (an ATP source). Figure taken from Szent-Györgyi (2004).

Straub joined Szent-Györgyi during world war II and it became clear that the difference between the low and high viscosity fractions was due to the presence of a different protein they called 'actin'. Combination of actin with myosin was responsible for the high viscosity (and therefore called 'actomyosin') and addition of ATP resulted in contractility. The final evidence that the actomyosin interaction observed in extracts in the presence of ATP is the fundamental mechanism for muscle contraction was obtained with glycerol-extracted psoas muscle fibres. This preparation consists of a chemically skinned muscle fiber bundle that is permeable to ions. When MgATP was added, the fibers began to contract and created tension that was comparable to that of living muscle. The demonstration that contraction can be generated *in vitro* by two proteins, actin and myosin, initiated the modern phase of muscle biochemistry (Szent-Györgyi, 2004).

1.5 Structure of striated muscle

From a histological perspective, both skeletal and heart muscles are classified as striated because the force-producing elements are ordered in a particular regularity. This regularity can be seen clearly through a microscope with contrast intensification or by using specific stains (see Fig. 1.5 (a)). In contrast, no such order is visible in smooth muscles (Huxley, 2000).

Skeletal muscles are mainly composed of the proteins actin and myosin, which are the building blocks of the thin and thick filaments. These filaments are organised in small functional units called sarcomeres (Fig. 1.5 (b)). Thousand consecutively ranked sarcomeres build the so-called myofibrils, long cylindrical protein strands that constitute the majority of a muscle cell (muscle fibre). The sum of the shortening of many sarcomeres

leads to a visible shortening of the entire muscle fibre (up to 30 % of the fibre length; Lodish et al. (2008)).

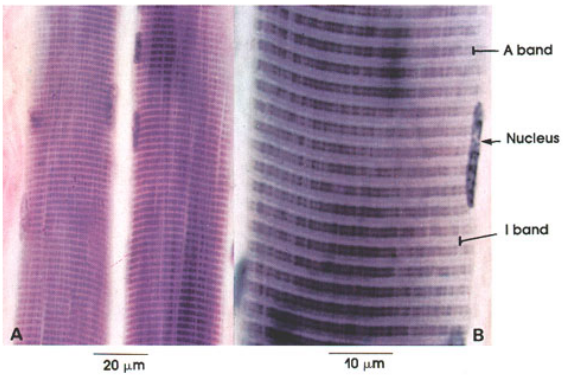

(a)

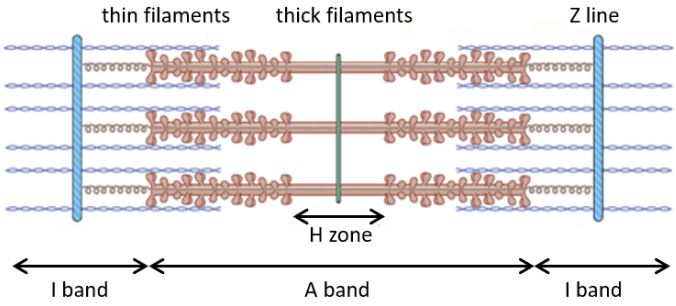

(b)

Fig. 1.5: Structure of striated muscle. (a) Phosphotungstic acid hematoxylin stain is used to demonstrate the striations in skeletal muscle. At low magnification (A) only the two major cross striations are visible. The dark band is the A band, whereas the light band is termed I band. Only at higher magnifications (B) details are apparent: The light-staining in the center of the A band is called the H zone. The thin, dark line in the middle of the I band is known as the Z line. The repeating structural element between two Z lines is termed sarcomere (Costanzo, 2017). (b) Schematic structure of a sarcomere. Figure modified from Bergmann et al. (2020).

Electron micrographs of muscle fibres provided insights into the structure of the sarcomere and their building blocks (Huxley, 1957b). Each sarcomere is about 2 -3 µm long and extends between two Z-lines. Actin forms 1 µm long thin filaments between the Z-line and the H-zone, whereas myosin builds 1.6 µm long thick filaments in the A-band. The H-zone is found in the center of the sarcomere, where there is no overlap between the thick and the thin filaments. The I-band is the part of the thin filament in direct vicinity to the Z-line without overlapping thick filaments (Szent-Györgyi, 2004).

1.6 Muscle myosin II

Enzymatic digestion of isolated thick filaments gave insights into the function of different myosin domains, and their mechanical properties. In the 1950s it was discovered that the ATPase activity of myosin was solubilized by a short digestion with trypsin. The digestion resulted in the formation of two well-defined parts that made it possible to separate them by using differential centrifugation in the presence of actin. The slow component was called light meromyosin (LMM), whereas the faster sedimenting part was termed heavy meromyosin (HMM). On the basis of further experiments it became clear that LMM is responsible for filament formation, while HMM carries the sites responsible for ATPase activity and the actin-interacting sites.

Exposure of HMM to trypsin for an extended time or digestion with papain resulted in further digestion products, called subfragment 1 and 2 (S1 and S2). The S1 bound to actin and was an active ATPase. It became evident that HMM is a two-headed molecule linked to LMM via S2 (see Fig. 1.6 (a)). LMM together with S2 forms the rod portion of the molecule, which mostly forms a coiled-coil helix (Szent-Györgyi, 2004).

A single muscle myosin II molecule (520 kDa) is a hexamer made up of two heavy chains and two pairs of bound light chains. Two light chains bind to the neck region (the transition between the head and the rod-like part) of each heavy chain. The light chains are also called regulatory and essential light chains. They mechanically stabilize the neck region of the myosin molecule. The regulatory light chain can bind Ca^{2+} and has phosphorylation sites, both of which regulate the contractile apparatus (Lodish et al., 2008). The light chains have important functions in the regulation of contraction in molluscan muscles and light chain-phosphorylation is required for smooth muscle activity (Galler, 2008).

In skeletal muscle about 200 to 400 myosin II tails self-associate to form the thick filaments backbone from which the myosin heads protrude at regular angles (see Fig. 1.6). Each thick filament interacts with six thin filaments grouped around it. The central region of the filament does not contain myosin heads (bare zone) and consists of oligomerised myosin rods. Globular myosin heads are protruding from the filament and project towards the thin filament, forming the so-called ‘cross-bridges‘ (Szent-Györgyi, 2004).

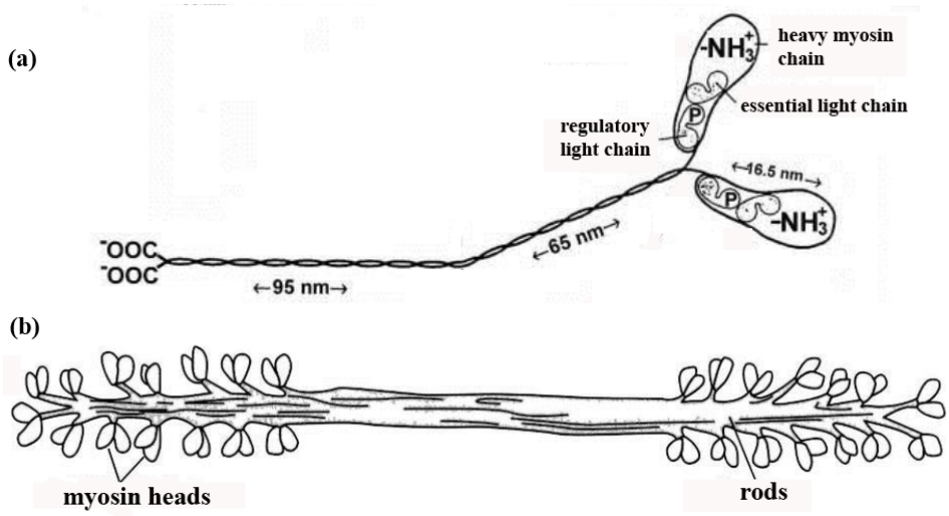

Fig. 1.6: Myosin molecules (a) are the building blocks of thick filaments (b). The globular N-terminal head with the regulatory and essential light chains is named S1 (subfragment 1). The S1 can bind actin, hydrolyses ATP and functions as a 'minimal' crossbridge. Two S1 molecules are linked by a short region of the rod and form a heavy meromyosin (HMM) molecule. The isolated section of the rod in HMM is termed S2. The remaining part of the rod region is named light meromyosin (LMM), which contains domains leading to filament formation under physiological conditions (Szent-Györgyi, 2004). Figures have been modified based on (a) Aidley and Ashley (1998) and (b) Lodish et al. (2000).

1.7 Sliding filament hypothesis

The sliding filament theory was based on the observations of length uniformity of the A band and the shortening of the I band during a contraction. As mentioned by A.F. Huxley, this observation was made using interference microscopy on intact frog muscle fibres (Huxley and Niedergerke, 1954). A very similar observation was made by H.E. Huxley on glycerol-extracted myofibrils using phase contract microscopy (Huxley and Hanson, 1954). During muscle contraction, the thin filaments slide telescope-like into the thick filaments (see Fig. 1.7). This sliding leads to a shortening of the sarcomere, while the length of the filaments remain the same (Szent-Györgyi, 2004).

To give the sliding filament theory a molecular explanation the (swinging) cross-bridge hypothesis became the common view in the 1970s. According to this hypothesis myosin cross-bridges bind to the actin filament in an initial conformation and then undergo a change of state that moves the actin filament past the myosin filament. This fundamental event, driven by ATP hydrolysis, leads to a rowing-like stroke, also known as the 'power stroke' (Holmes and Geeves, 2000).

The cross-bridges were first visualized in electron microscopy studies by H.E. Huxley

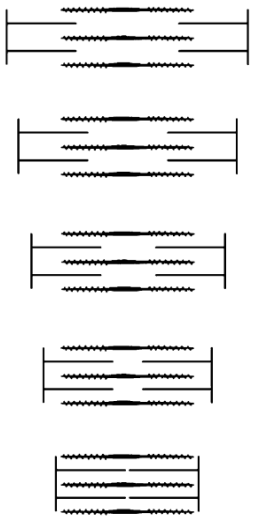

Fig. 1.7: A schematic illustration to explain the sliding filament theory. Thick and thin filaments slide past each other in the presence of ATP. The top sarcomere is relaxed while the bottom sarcomere is contracted. Both filament types remain at a constant length during contraction. Filament sliding explains the uniformity of the A-band and the changes of the I-band and the H-zone (Szent-Györgyi, 2004).

(Huxley, 1957b). A quantitative cross-bridge theory of muscle contraction with coupled ATP hydrolysis was proposed by A.F. Huxley (Huxley, 1957a) which was based on mechanical experiments on single muscle fibres.

1.8 The swinging lever-arm hypothesis

The cross-bridge hypothesis provided good insights into the entire muscle-contraction cycle but lacked the molecular details of the effective movement of the cross-bridge. This missing aspect was clarified by the determination of crystal structures of myosin and actin and the 'swinging lever-arm hypothesis' was developed. In this hypothesis, the largest part of the cross-bridge binds to actin with a fairly fixed geometry and only the neck region changes its orientation relative to actin. It has been suggested that the small conformational movements in the active center of the motor are amplified into large swinging motions of the neck region. Because of this amplification effect, the neck region is also termed 'lever arm' (Holmes, 1997).

Cryo-electron microscopy directly visualized the conformational change in the neck region by means of decorated actin with myosin S1 in the presence and absence of ADP. This experiment was first performed with skeletal muscle S1 but no differences in the position of the lever arm could be observed. However, experiments with brush border myosin

I (BBMI) S1 and smooth muscle myosin S1 revealed that the neck domain changes its angle relative to actin after ADP release. Image analysis indicated that the end of the lever arm of smooth muscle S1 and BBMI swings by ∼3.5 nm and ∼7.2 nm, respectively. The discrepancy between the two motors was accounted to a different number of light chains bound to their neck domain (two for smooth muscle myosin and three for BBMI, Jontes et al. (1995); Whittaker et al. (1995)).
This electron microscopy data indicated an ADP-induced structural change in actomyosin. Because neither ATP hydrolysis nor phosphate release was involved, the observed movement must be accounted by the affinity of myosin for the ADP molecule. Furthermore, the results demonstrated that at least part of the myosin power stroke is a transition between so-called strongly attached states. This makes sense because myosin could only produce high force if it were already attached tightly to the actin filament (Jontes et al., 1995; Whittaker et al., 1995).
In fluorescence polarisation experiments it was approved that an angular change in the position of the lever arm took place in a contracting muscle. By fluorescently labeling the regulatory light chains in single skeletal muscle fibres, tilting of the neck regions of myosin heads was detected (Irving et al., 1995).

A direct prediction of the swinging lever-arm hypothesis is that the size of the displacement produced by each stroke is proportional to the length of the neck domain. Therefore, the myosin velocity should be proportional to the amplitude of the lever rotation, and consequently to the lever arm length. By using molecular biology tools and recombinant protein expression, the *in vitro* motility assay (see chapter 2.4.1) was used to demonstrate that the sliding speed of myosin depends linearly on the neck domain length (see Fig. 1.8). The lever arm of *Dictyostelium* myosin II was gradually truncated by a single light chain-binding site at a time or was lengthened by one additional motif (Uyeda et al., 1996). The y-intercept corresponded to the position of the fulcrum point in the motor domain, which serves as a pivot point through which the swing of the lever arm occurs (a SH1-SH2 helix). This region is known to undergo rearrangement during the crossbridge cycle.

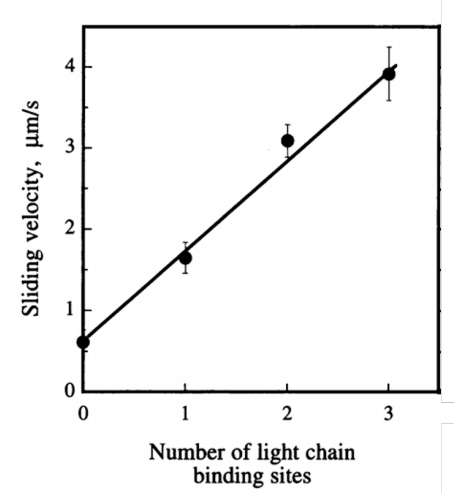

Fig. 1.8: The actin gliding velocity of myosin as a function of the number of light chain binding domains. *Dictyostelium* myosin II having 0, 1, 2 (wild type) or 3 light-chain binding sites in the neck domain moved actin filaments in the *in vitro* motility assay proportional to the length of the lever arm. Figure adapted from Uyeda et al. (1996).

In more recent studies using single-molecule techniques it was shown that the power stroke size is directly proportional to the lever arm length (Warshaw et al., 2000; Ruff et al., 2001). The single-molecule displacement and force data indicate that the neck acts as a rigid lever arm. Furthermore, they concluded that the fulcrum for rotation is located approx. 3 nm inside the C-terminus of the motor domain.

The power stroke size of a myosin molecule depends on the length and the angle of lever arm rotation (Ruff et al., 2001). Single-molecule studies with myosin Id reported a lever arm rotation of 90° (Köhler et al., 2003), in comparison *Dictyostelium* myosin II pivots only by 30° (Ruff et al., 2001). Spectroscopic studies on proteins in solution are very helpful in estimating the lever arm swing angle. A rotation of 70° of the neck region of *Dictyostelium* myosin II was measured by means of fluorescence energy resonance transfer (FRET) (Suzuki et al., 1998; Shih et al., 2000).

1.9 The myosin ATPase cycle

The general mechanism of the actomyosin ATPase cycle is conserved in the myosin superfamily. Most biochemical studies on this pathway have been carried out in solution with purified actin and myosin subfragment S1 and HMM. This solution kinetics studies do not completely describe the biochemical events in muscle fibres, since stress can influence the kinetics (Fenn effect; Fenn (1923)). On the other hand experiments within whole muscle fibres are limited because diffusion in the fibre is slow and limits most observations. Nevertheless, major discoveries have been made on skinned muscle fibre preparations using caged nucleotides (Goldman et al., 1982) and fluorescently labelled phosphate binding proteins to study the phosphate release (Ferenczi et al., 1995).

1.9.1 The Lymn-Taylor cycle

The basis of the current view on the biochemical cycle was provided by solution kinetics measurements of Lymn and Taylor in the 1970s performed with rabbit muscle HMM (Lymn and Taylor, 1971). They combined their biochemical measurements with the models of A.F. Huxley and H.E. Huxley (Huxley, 1957a,b) and came up with the Lymn-Taylor cycle, which explains how enzymatic events are coupled to mechanical work. Their kinetic cycle consists of four steps (see Fig. 1.9): i) fast dissociation of the actomyosin complex after ATP binding, ii) hydrolysis of ATP to ADP.Pi, iii) binding of the myosin-ADP.Pi complex to actin, iv) product release from actomyosin.
For rabbit myosin II S1 this reaction takes place in the absence of actin at a rate of <0.1 s^{-1}, although ATP binds rapidly to myosin and is hydrolysed to ADP and phosphate at >100 s^{-1}. Slow release of the products limits the overall turnover to 0.1 s^{-1} (Geeves, 1991). The fast hydrolysis of ATP to ADP.Pi is also known as 'Pi burst' (Tokiwa and Tonomura, 1965). The addition of F-actin increases the ATPase rate by a factor of 100 (Trentham et al., 1976; Webb and Corrie, 2001).
The Lymn-Taylor cycle has a couple of limitations: Firstly, the Pi burst seemed to be faster than the maximum actin activated ATPase. In this pathway, the rate-limiting step is the release of products once myosin has bound to actin. This argumentation implies that at the maximum ATPase rate almost all the myosin is actin-bound. Myosin II, however, is a low duty ratio motor and spends only a short time attached to actin during the crossbridge cycle. Secondly, Lymn and Taylor did not take into account the reversibility of the pathway steps. They also hypothesized that M.ATP had a lower affinity than M.ADP.Pi for actin, although later studies have revealed that these two states have very similar 'weak' affinities for actin (Stein et al., 1979).

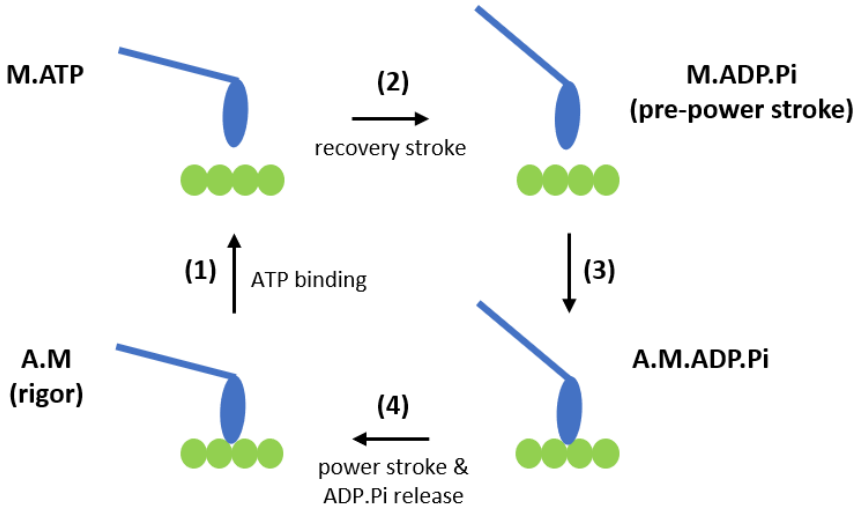

Fig. 1.9: The kinetic pathway of Lymn and Taylor demonstrates the coupling of the myosin ATPase cycle with mechanical events. (1) The rigor actomyosin complex (A.M) dissociates following ATP binding (M.ATP). Binding of ATP and dissociation of actin is indicated as a single step, since actin dissociation occurs very quickly after substrate binding. (2) Myosin hydrolyses ATP to ADP.Pi (M.ADP.Pi) with a subsequent movement of the lever arm (recovery stroke). (3) The pre-power stroke state (M.ADP.Pi) binds to actin (A.M.ADP.Pi) and myosin undergoes a power stroke accompanied with product release (4) resulting in formation of the initial actomyosin complex. M - myosin, A.M - actomyosin. Figure modified from Lymn and Taylor (1971).

1.9.2 The 3G model

The Lymn and Taylor cycle suggests a direct coupling between discrete kinetic and mechanical steps of myosin on actin. Alternatively, an indirect coupling model (3G model) was proposed by Geeves et al. (1984) on the basis of a classification of actomyosin interactions into weak and strongly bound states which was first described by Eisenberg and Greene (1980). Solution kinetics studies with pyrene labelled actin have shown that myosin S1 can bind to actin in a weak or strong way. The studies revealed that weak actin binding is in fast equilibrium with the detached states and is preferred when ATP or ADP.Pi are bound to myosin. In contrast, strongly bound S1 is favoured by an ADP or rigor conformation. It is therefore believed that the weak to strong transition is associated with phosphate release. Whether a certain myosin nucleotide complex is referred to as a weak or strong actin-binding state depends on the actual value of the equilibrium constant of the reaction step (Geeves, 1991).

In the 3G model it was suggested that myosin-nucleotide (M.N) complexes bind actin (A)

via two major binding events:

$$A + M.N \overset{K_0}{\rightleftharpoons} A \sim M.N \overset{K_1}{\rightleftharpoons} A - M.N \overset{K_2}{\rightleftharpoons} A.M.N$$

where A $\sim$ M.N represents the collision complex, A - M.N the A state and A.M.N the R state (Geeves and Conibeart, 1995).
This model suggests that force generation happens due to changes in the affinities between myosin and actin in a nucleotide-dependent manner. After actin binding, myosin first forms a weak collision complex with the filament (weakly bound attached- or A-state), which is followed by an isomerisation to a strong-binding complex (strongly bound Rigor-like or R-state). This change in the affinities between the two steps need not lead to a major structural change of myosin S1, and can only feature small changes in the actomyosin complex. This differs to the direct coupling model of Lymn and Tylor that implies that force generation is the direct result of the conformational change in the myosin.
In the 3G model each myosin nucleotide complex could dock onto actin following the same pathway, but the nature of the bound nucleotide had a major influence on the equilibrium constant of the A to R transition. Only formation of the R state leads to fast product release and acceleration of the S1 ATPase. The isomerisation of the A to the R state involves a structural change that results in the actin being bound more tightly and the nucleotide being bound more weakly. The A to R transition is coupled to the force-generating event in muscle contraction (Geeves and Conibeart, 1995).
The most common scheme of the actomyosin ATPase cycle is shown in Fig. 1.10.

1.10 Myosin crystal structure

Rayment and his group were the first to solve the X-ray crystallographic structure of a myosin in the 1990s, namely the chicken skeletal myosin S1 fragment (Rayment et al., 1993b). The proteolytic fragment S1 includes the first 843 residues of the heavy chain along with the two light chains. It represents the morphological cross-bridge and carries the entire enzymatic activity of myosin (Geeves and Holmes, 1999).
Previous knowledge of the organisation of the S1 was derived from enzymatic studies. Limited digestion of vertebrate skeletal S1 with trypsin indicated that the head consisted of three main regions: a 25 kDa N-terminal nucleotide binding region, a central 50 kDa segment and a 20 kDa C-terminal segment. The last two segments were shown to bind to actin. The digestion occurred at flexible loops connecting the three major regions (termed loop 1 and loop 2; Rayment et al. (1993b); Sweeney and Houdusse (2010)).
The striking feature of the structure of Rayment et al. was the presence of a large cleft

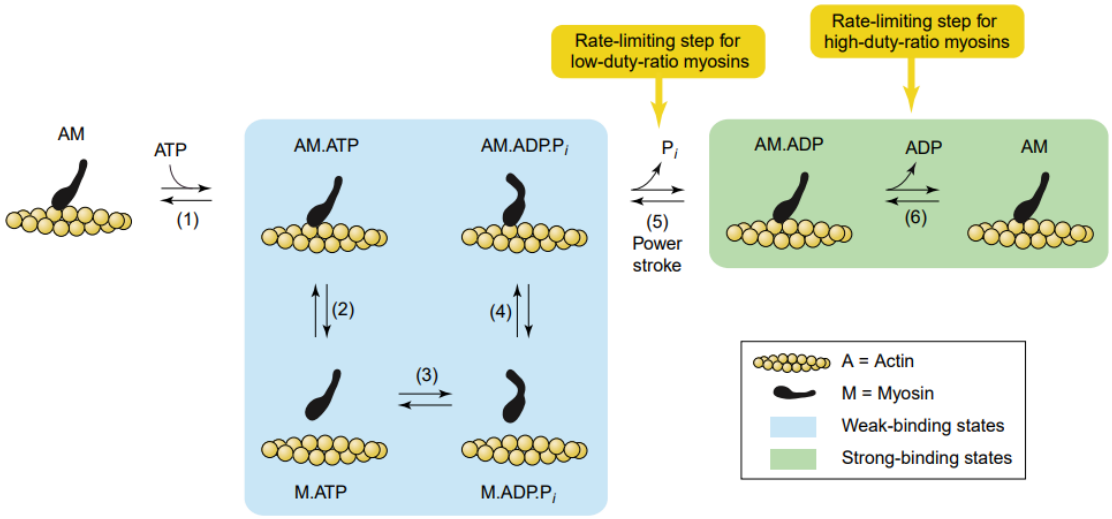

Fig. 1.10: The myosin ATPase cycle with focus on weak and strong actin binding states. Note the highlighting of the rate limiting steps for low and high duty ratio motors. The actin-detached M and M.ADP states are excluded for clarity and to illustrate that these states are not populated during enzymatic cycling in the presence of saturating actin and ATP (De La Cruz and Ostap, 2004).

(so-called 50 kDa cleft) in the middle of the head, extending from the nucleotide binding site to the actin interface (see Fig. 1.11). This prominent cleft separates the upper and lower 50 kDa subdomains (both together correspond to the proteolytic 50 kDa segment mentioned above). Rayment et al. (1993b) proposed that the 50 kDa cleft closes when myosin loses its hydrolysis products when strongly bound to actin. This is supported by cryo-electron microscopy studies which indirectly showed that movement of the upper 50 kDa region can close the cleft. Parts of the lower 50 kDa region are meanwhile stabilized by strong interactions with actin (Volkmann et al., 2000). The nucleotide binding pocket is 4 - 6 nm away from the actin binding site. Opening and closing of the cleft may provide the physical link between the ATP- and actin-binding sites. Actin binding is thought to favour the closed-cleft form (Holmes, 1997).

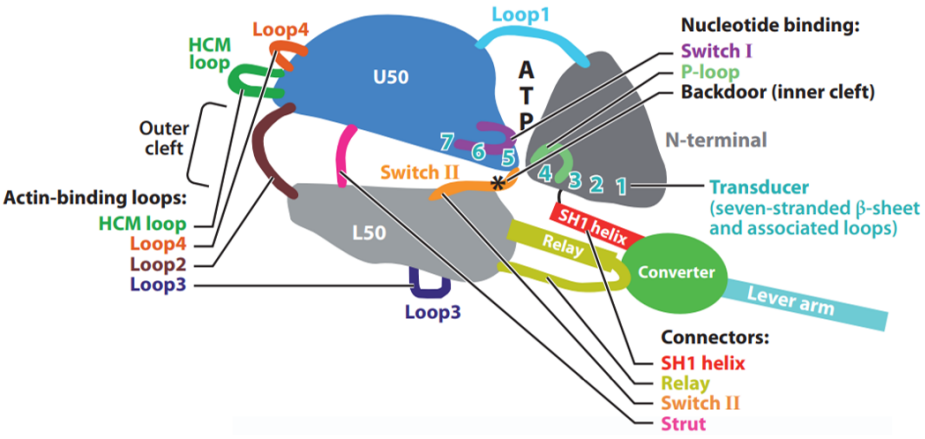

(a)

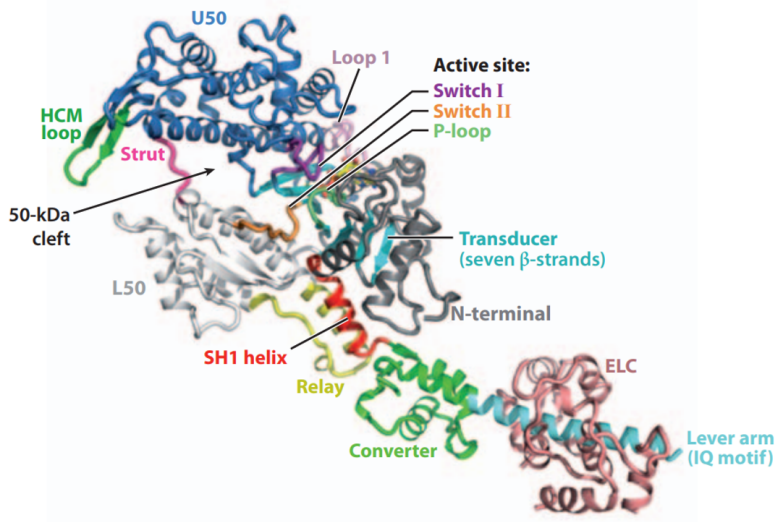

(b)

Fig. 1.11: A schematic (a) and a ribbon diagram (b) of myosin V motor domain shows important elements. Note the big cleft between the upper (U50) and lower (L50) 50 kDa domain. The actin-binding region and the nucleotide-binding site of myosin are on opposite sides of the seven-stranded β-sheet. The converter domain acts as the pedestal for the C-terminal light chain-binding domain and plays a very important role in communication between the motor domain and the light chain-binding domain (Sweeney and Houdusse, 2010).

The globular myosin head consists of α-helices surrounding a seven-stranded central β-sheet which consists mainly of the N-terminal and upper 50 kDa fragments. It is localised near the nucleotide-binding site containing the P-loop and switch 1. The central β-sheet has an important function in closing the cleft during the power stroke on actin and therefore has been termed the transducer region. Reorganisations within the motor domain are transferred to the lever arm by rotation of the most mobile part of the head, the so-called

converter, which is coupled to the rest of the motor domain by two highly deformable parts (relay and SH1 helix).
The actin-binding site contains parts of both upper and lower 50 kDa subdomains, including positively charged actin-binding loops and helix-loop-helix regions. Loop 2 contains conserved lysines and seems to contribute to the major interactions necessary for formation of the initial weak interactions between myosin and actin (Geeves and Holmes, 1999). See section 1.14 for detailed informations about loop 2.

Although the chicken S1 structure from Rayment et al. (1993b) was crystallized with a sulphate ion in the nucleotide-binding pocket, it is believed that it represents the end of the power stroke, with no bound nucleotide (rigor state, Holmes (1997)). Although S1 was not bound to actin, this structure was believed to correspond to the post-power stroke (or rigor state), because the lever arm was at an angle of 45° to the actin filament axis (Houdusse et al., 2000).

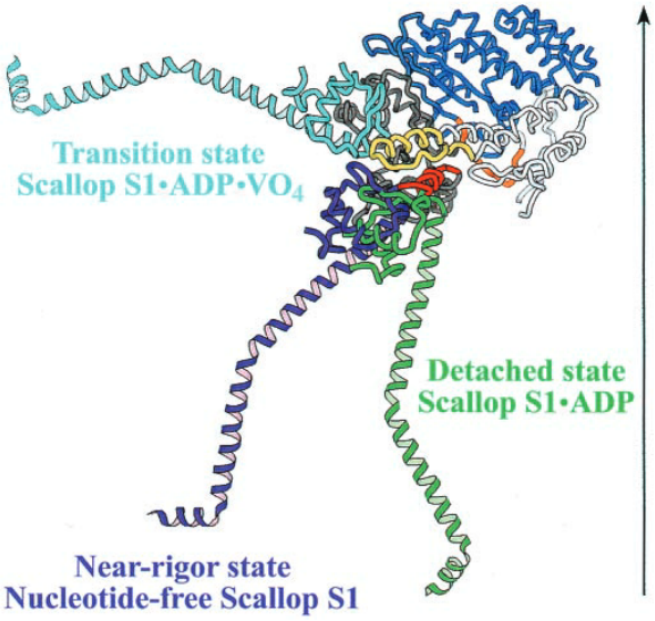

Fig. 1.12: The nucleotide-free scallop S1 structures in near-rigor, transition and detached states. The structures are oriented so that the lower 50 kDa subdomains are superimposed. An arrow shows the approximate direction of the actin filament axis relative to the 50 kDa subdomain (Houdusse et al., 2000).

1.10.1 Open and closed conformation of the active site

Crystallographic studies with truncated *Dictyostelium* myosin fragments containing ATP analogues showed differences in the catalytic site between the pre and post power stroke conformations and are called the 'open' and 'closed' states (see Fig. 1.13). Myosins with ADP.Vanadate, an analogue to the transition state showed large differences in the structure compared to chicken S1 structure without nucleotide ('open' state). In the ADP.Vanadate structure the γ-phosphate–binding pocket closes, which causes a partial closing of the 50K upper/lower-domain cleft. The actin-binding domain and the 50K upper domain rotate a few degrees toward each other so that the nucleotide-binding pocket gets closed, which correspond to a movement of about 0.5 nm. This structure is referred as 'closed' state (Geeves and Holmes, 1999).

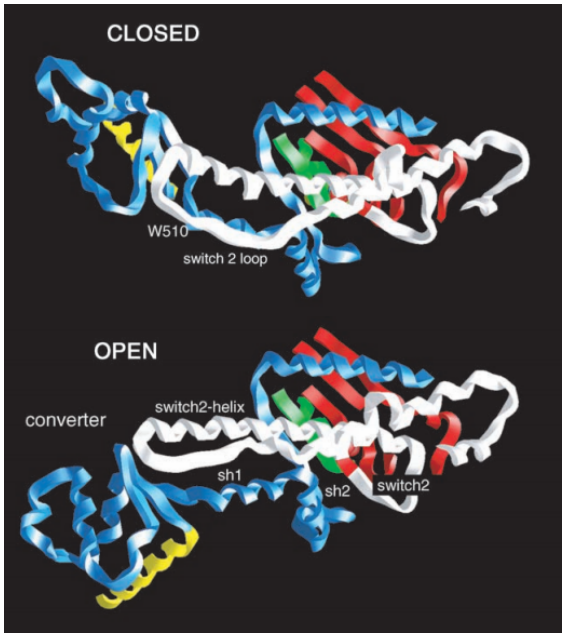

Fig. 1.13: The 'open' and 'closed' conformation of the active site. It shows the large changes in the orientation of the converter domain (left) that results from the inward movement of the switch 2 element (right; Geeves and Holmes (1999)).

The structural organisation of the active site of myosin is conserved across a large number of enzymes that bind nucleotides including G-proteins and kinesins. They have been shown to contain a short, highly conserved polypeptide, the phosphate binding loop (P-loop). The consensus sequence for this motif (Gly-x-x-x-x-Gly-Lys-Thr/Ser) is often used as a fingerprint to identify new members of this group (Smith and Rayment, 1996a).

Smith and Rayment (1996b) pointed out that the active site of 'closed' myosin is very

similar to that of Ras p21 and other G proteins. They observed that the differences between the 'open' and 'closed' state near the active site are located almost exclusively in the conformation of the linker region (Sk465-470; 'Sk' referring to the chicken skeletal myosin head sequence), which joins the 50K upper and lower domains. This region is structurally very similar to the switch 2 region in Ras p21, which moves in an nucleotide dependent way. In the chicken crystal structure ('open' state) the switch 2 region is not part of the nucleotide-binding pocket. The hydrogen bond between the amide of SkG466 and the γ-phosphate of ATP can only be formed in the 'closed' form. Additionally, the γ-phosphate is also coordinated by a Mg^{2+} ion, the P-loop lysine and S181. The amino acids SkR236 and E468 form a salt bridge, which brings the latter side chain close enough so that ATP hydrolysis can occur (Yount et al., 1992; Geeves and Holmes, 1999).

The γ-phosphate interaction is important for stabilizing the closed form both before and after cleavage. Opening the switch 2 region destroys the γ-phosphate–binding pocket and facilitates phosphate release. An interesting aspect of this opening is the idea that the γ-phosphate leaves via the 50 kDa cleft rather than back out the active site pocket, the so-called 'back-door' mechanism (Yount et al., 1995).
The movement of switch 2 in the 'closed' state has also more wide-reaching effects, specifically the rotation of the converter domain by about 60°. Holmes (1997) used the coordinates of the chicken S1 structure to recreate the missing lever arm and suggested that the lever arm's new orientation was the start of the power stroke. The end of the lever arm moved about 11 nm along the actin helix axis between 'open' and 'closed'. This was exactly the expected size of the working stroke. Interestingly, this large change is amplified from a small (0.5 nm) shift in the active site (Holmes and Geeves, 2000).
The idea of the moving lever arm was considered sceptical in Rayments original publication, as they believed that the lack of the light chains could cause artefacts to the C-terminal conformation. This concern was cleared in the crystallographic study of Dominguez et al. (1998), where the structure of smooth muscle S1 including the essential light chain was solved. This study allowed a detailed investigation of the conformational changes between the 'open' and 'closed' states (Geeves and Holmes, 1999).

1.11 Actin structure

Actin is one of the most abundant proteins in all eukaryotes with a cytoplasmic concentration of about 100 µM (Kiuchi et al., 2011). Straub (1942) originally isolated the actin monomer (G-actin) from muscle and showed that raising the salt concentration leads to

the formation of F-actin polymers.
Actin is present in cells in a dynamic equilibrium between globular, monomeric G-actin and fibrous, polymerised F-actin. The structure of G-actin (42 kDa) was crystallised as a complex with DNase I (Kabsch et al., 1990). As shown in Fig. 1.14 (a) a single G-actin molecule consists of two domains each consisting of a 5 stranded β- sheets and associated α-helices. Because of their position within the actin filament, the two main domains of actin are also referred to as outer and inner domains (Dominguez and Holmes, 2011). The nucleotide ATP or ADP is bound together with Mg^{2+} between the two domains. The outer and inner domains can be divided into two subdomains, namely an actin-actin interaction domain and the second forms the top of the nucleotide-binding pocket.

At physiological salt concentrations the globular protein polymerizes itself into polar, helical filaments with a 36 nm pitch, which consists of 13 monomers. As the rotation per monomer is 166°, the actin helix morphologically appears as two right-handed helices which twine slowly round each other (Holmes et al., 1990). The rates of attachment and detachment of actin monomers to F-actin polymers are different at both ends, resulting in a process termed as treadmilling with a slow and fast growing end. This reaction is coupled to an irreversible hydrolysis of the bound ATP to ADP (Pantaloni et al., 2001). The filaments have a polarity because of an asymmetry in the monomers. The end, where the ATP binding site is exposed, is called the minus (slow growing) end, while the other side is called plus (fast growing) end.

Actin is one of the highest conserved proteins. The amino acid sequence of human actin is 87 % identical to that of yeast actin. This is very likely related to the large number of actin-binding proteins. More than 50 proteins have been identified that specifically bind to actin (Geeves and Holmes, 2005).

The F-actin structure was inferred first from X-ray fiber diagrams where the crystal structure of G-actin was fitted (Holmes et al., 1990) and more recent with cryo-electron microscopy (see Fig. 1.14 (b); Fujii et al. (2010)). Further structural details of F-actin could be inferred from electron microscopy studies using F-actin decorated with myosin S1 fragments (Moore et al., 1970). The myosin heads bind in a polar, very characteristic ‘arrowhead’-way to actin, resulting in ‘pointed’ and ‘barbed’ ends, corresponding to the minus and plus end, respectively.

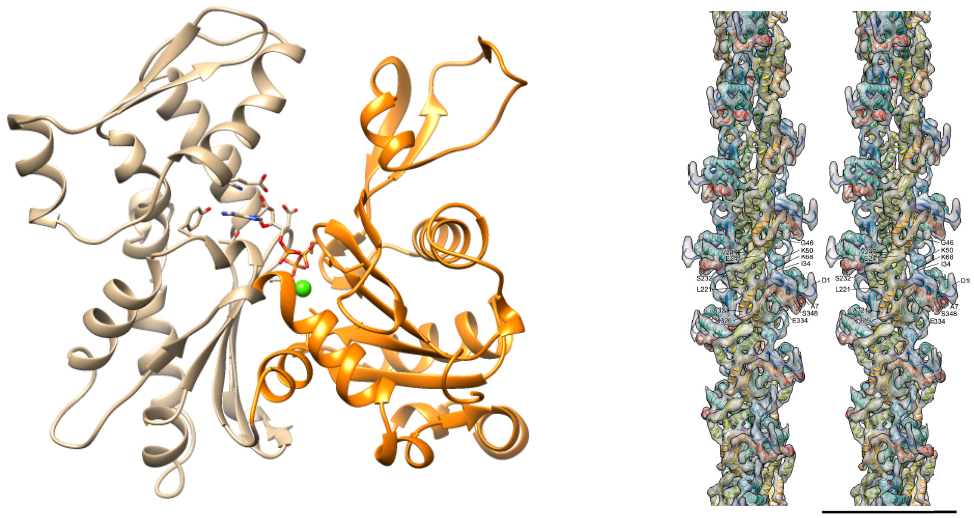

(a) (b)

Fig. 1.14: The structure of globular (G) and filamentous (F) actin. (a) The crystal structure of G-actin with bound ATP. The two main domains are coloured in grey and orange. Note the big cleft that forms the nucleotide binding pocket. ATP is coordinated by Ca^{2+} (green sphere). The structure was adjusted from the DNase I-actin complex structure (Kabsch et al., 1990) and made with UCSF chimera (PDB: 1atn). (b) Three-dimensional density map of F-actin with a fitted atomic model. Approx. 15 subunits of actin are shown. Scale bar is 10 nm (Fujii et al., 2010).

1.12 Actomyosin interaction

Although X-ray crystallography has solved many important issues of the power stroke, many aspects of the actomyosin interaction are not yet completely clear, for example how actin binding to myosin weakens the affinity for nucleotide. To understand this mechanism, atomic models of the actomyosin complex were constructed by fitting the structures of the myosin motor domain and F-actin into 3D-cryoelectron microscope reconstructions of 'decorated actin' (Rayment et al., 1993a; Holmes et al., 2003; Geeves et al., 2005). In decorated actin, myosin binds to actin in a 1:1 ratio in the absence of nucleotide.
Initial fitting attempts by Rayment et al. (1993a) indicated that the cleft between the upper and lower 50K domains could close when the rigor state is formed. In further studies a potential hinge point around switch 1 at the myosin nucleotide site has been identified that allows the upper 50K domain to rotate towards the lower 50K domain (Holmes et al., 2003; Conibear et al., 2003). In a series of solution experiments Conibear et al. (2003) showed using excimer fluorescence that nucleotide binding favours the 'open cleft' state and actin binding promotes the 'closed cleft' state. Together with structural studies these results indicated that movement of switch 1 to the closed state causes the myosin cleft to

open and the actin-binding site to be weakened.

1.13 Calmodulin

Calmodulin (CaM) is a ubiquitous, highly conserved, calcium binding protein that binds to and regulates a number of diverse target proteins including myosins. The 17 kDa protein (148 aa) plays important roles in calcium signalling and regulates various intracellular processes such as cell motility, proliferation, growth, and apoptosis (Park et al., 2008; Tidow and Nissen, 2013).

The crystal structure revealed that calmodulin consist of two small globular domains separated by a flexible linker (see Fig. 1.15). Each domain binds two calcium ions through a helix-loop-helix (EF hand) conformation, similar to other intracellular calcium -binding proteins (Babu et al., 1985). Calcium binding to each globular domain alters interhelical angles in the EF-hand motifs, which causes a change from a 'closed' to an 'open' conformation. This conformational change leads to the exposure of hydrophobic sites and allows calcium-CaM to bind to a large number of target proteins such as myosins, kinases, voltage-gated calcium channels and ATPases (Park et al., 2008).

Calmodulin can also bind in its apo form (without bound calcium) to target sites, the so-called IQ motifs. Subsequent calcium binding can alter the affinity of the CaM-target bond, which generates a very versatile system linking calcium concentration to the regulation of CaM target proteins (Tidow and Nissen, 2013).

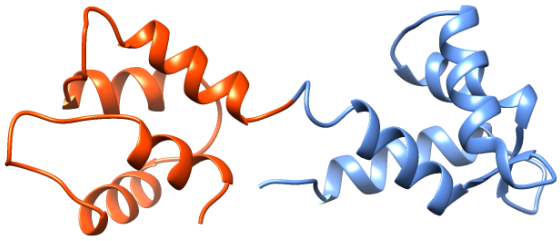

Fig. 1.15: Crystal structure of calcium-free calmodulin (CaM) from *Xenopus laevis*. The two globular domains (orange and blue) are connected by a flexible linker. The CaM sequence is highly conserved in eukaryotes, having 100 % protein sequence identity between calmodulin from *Xenopus*, termed CaMX, and human calmodulin. The figure was made with UCSF chimera (PDB: 1cfd; Kuboniwa et al. (1995)).

1.14 Loop 2

Loop 2 bridges the cleft between the upper and lower 50 kDa domain and together with loop 1 they are susceptible to proteolysis as described in section 1.10 (Rayment et al., 1993b; Sweeney and Houdusse, 2010). In older literature, loop 2 is also referred to as the loop at the junction of the 50 kDa and 20 kDa domain. Together with other structural parts of the upper and lower 50 kDa catalytic domain, loop 2 is involved in actin binding (Saczko-Brack et al., 2016).
The length of loop 2 varies in different myosin isoforms, with myosin V and IX having the longest one (see chapter 3.1.7). In general, loop 2 is rich in lysine and glycine residues and the C-terminus is marked by a conserved threonine. The N-terminus of loop 2 contains an invariant phenylalanine. Loop 2 is usually not visible in crystal structures of myosin S1, with the exception of *Dictyostelium* myosin II, where the loop 2 is very short and ordered (Lorenz and Holmes, 2010).

Studies in the 1990s with chimeric *Dictyostelium* myosin II containing loop 2 from different isoforms showed that the actin-activated ATPase activity was correlated with the donor loop (Uyeda et al., 1994). Similar experiments also showed that loop 2 variants had different affinities for actin both in the presence and in the absence of nucleotides (Murphy and Spudich, 1999). Additionally, Yengo and Sweeney (2004) showed with myosin V that changes in loop 2 affected the actin-binding kinetics and that loop 2 had a relatively high affinity in the weak binding states. There are various other studies which showed that variability in the length and number of charged residues in loop 2 can modify myosin's

affinity for actin and also its enzymatic activity (Rovner, 1998; Furch et al., 1998; Knetsch et al., 1999; Joel et al., 2001, 2003).
In a recent work Lorenz and Holmes (2010) showed using molecular dynamics simulations that loop 2 is involved in establishing the association between the myosin head and actin (see Fig. 1.16).

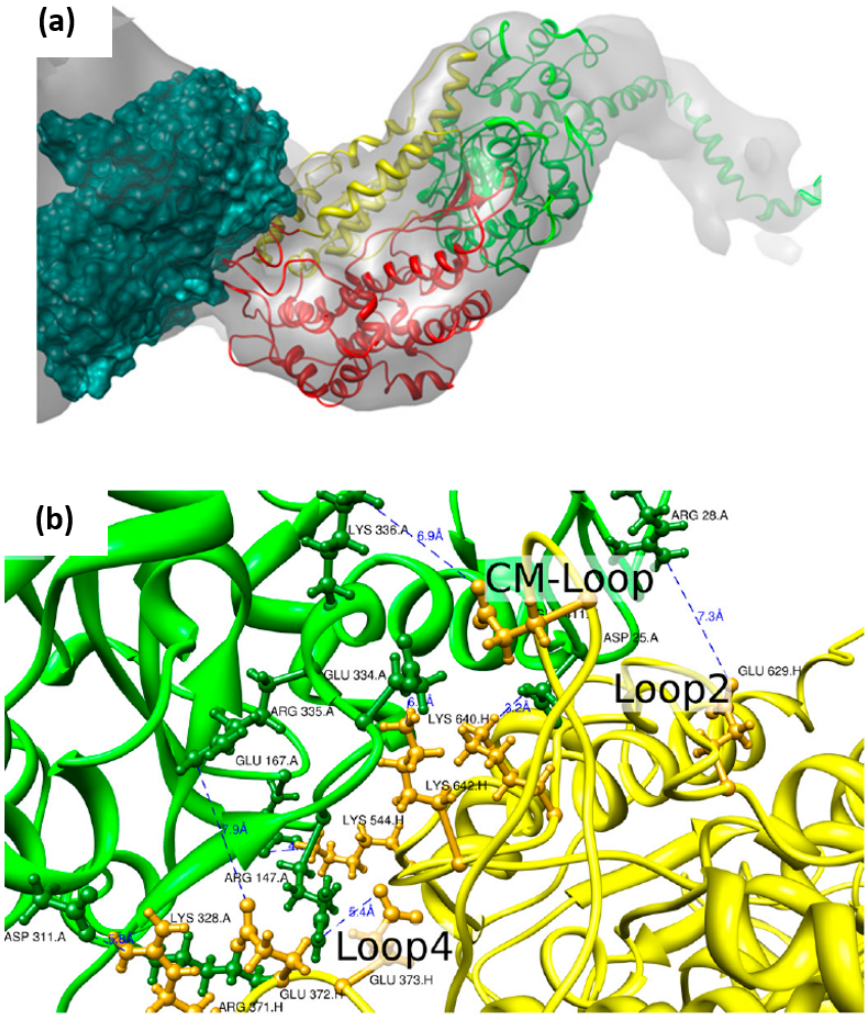

Fig. 1.16: A molecular dynamics study showing the main interactions sites of loop 2 with actin. (a) Overview of the acto myosin complex embedded in a cryo-electron microscopy map. Actin is shown as surface representation in dark green and the head of myosin V (S1) is shown as ribbon. (b) Electrostatic interactions between S1 and actin showing that the main interactions partners are coming from loop 2, loop 4 and the cardiomyopathy loop (CM-loop). Individual amino acids are labelled and show residue type, residue number, and protein (A for actin, H for S1). Possible hydrogen bonds between S1 and actin are not shown (Lorenz and Holmes, 2010).

1.15 Duty ratio and processivity

Myosin molecules go through a characteristic cyclic interaction with actin. During each cycle the motor domain spends time attached to the filament, τ_{on}, during which it makes its working stroke and time detached from the filament, τ_{off}, during which it makes its recovery stroke. Mechanical force generation, work, and directed movement on actin are possible only during times when the myosin is strongly bound to actin. The duty ratio (r) can be defined as the fraction of time that each head spends in its attached phase (see Fig. 1.17 (a); Howard (1997)):

$$r = \frac{\tau_{\text{on}}}{\tau_{\text{on}} + \tau_{\text{off}}} = \frac{\tau_{\text{on}}}{\tau_{\text{total}}}$$

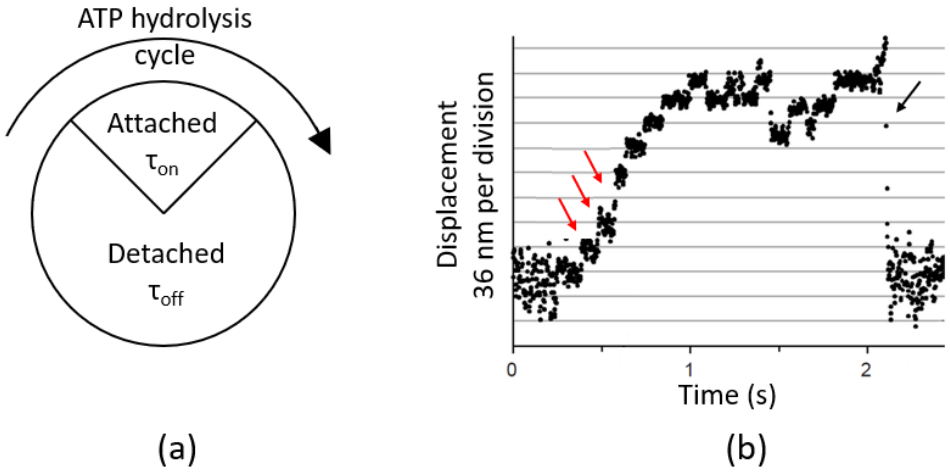

Fig. 1.17: Duty ratio and processivity. (a) During one ATP hydrolysis cycle each myosin head spends time τ_{on} attached to actin and time τ_{off} detached from actin (Howard, 1997). (b) Optical tweezers data showing processive steps of myosin V. After a single encounter with actin, myosin V takes several successive steps (red arrows) before detaching (black arrow). The high processivity can be explained by a 'gating mechanism' where both heads get coordinated by internal strain (Veigel et al., 2002).

Myosin II is an example of a low duty ratio motor and spends a large amount of its time detached from actin. The interaction time with actin is very short and consists of a single working stroke per single binding event with the filament. To sustain continuous sliding in the sarcomeres of muscles, myosin II molecules need to be organised in a large filamentous structure. The kinetic cycles of the heads are not synchronized, which means that all heads are in different phases of the ATPase cycle at a given point in time (Uyeda et al., 1990; Howard, 2001).

Like the duty ratio, processivity is a intrinsic property of a molecular motor. Processive motors bind an actin filament and take successive steps before detaching (Higuchi and Endow, 2002). Processive movement was first demonstrated for single molecules of kinesin moving in 8 nm steps along the microtubule, corresponding to the distance between tubulin dimers in a protofilament (Svoboda et al., 1993).
Processivity and duty ratio are closely connected. To achieve processivity, a two-headed myosin such as myosin V or VI, each of the two myosin heads must have a high duty ratio. A two-headed myosin walking along an actin filament cannot unbind both heads from the actin at the same time, or it diffuses away before it attaches to the next contact site on the filament. Each head must be strongly bound to actin in ∼50 % of the time, which requires a duty ratio of more than 0.5 (Howard, 2001).
Veigel et al. (2002) showed for the first time that processivity of a two-headed myosin can be enhanced via internal strain within the lever arms while both heads are bound to actin. This so-called 'gating' mechanism of myosin V makes the chemical cycles of the two heads cooperative and increases their processivity (see Fig. 1.17 (b)).

1.16 The mechanism of processivity of dimeric molecular motors

Processive dimeric molecular motors, like kinesin 1, myosin V and myosin VI, undergo multiple catalytic cycles before they detach from their specific cytoskeletal tracks (Mehta et al., 1999; Rock et al., 2001; Veigel et al., 2002; Toprak et al., 2009). This allows those molecular motors to move for hundreds or thousands of nanometres, which is important to transport organelles and other cargoes inside cells (Hammer and Sellers, 2012). Such movements requires a motor with mechanochemical properties different from those of myosin II, which has a low duty ratio and works in large filaments to drive high-speed motility during muscle contraction.

The best-known model for processive motility is the hand-over-hand model (see Fig. 1.18). In that model, both heads are initially bound to an actin filament, one in front (leading head) of the other (trailing head). The trailing head hydrolyses ATP, creates the power stroke and passes the leading head. After the strong binding of the new leading head to actin, the (new) trailing head binds ATP. This head than unbinds from the filament and searches for the next binding position. The motor undergoes numerous such cycles, which results in a directional movement on the filament (Mehta et al., 1999; Veigel et al., 2002; Yildiz and Selvin, 2005).

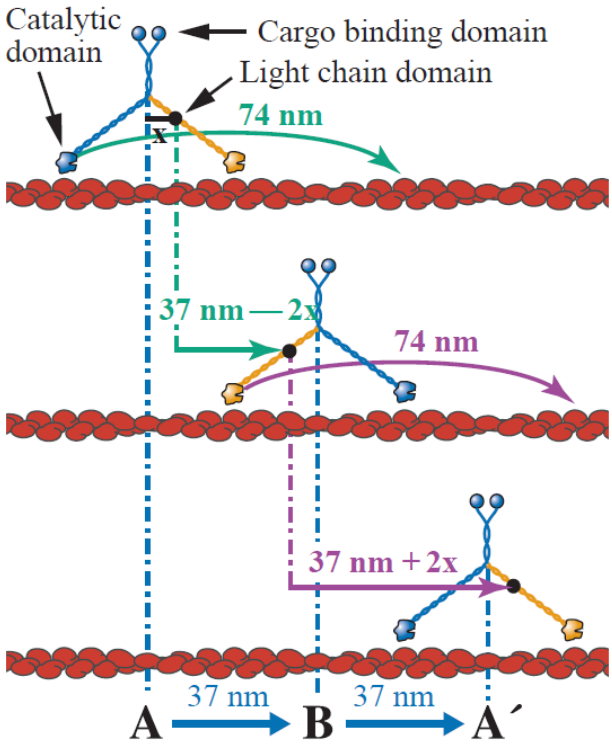

Fig. 1.18: Hand-over-hand model of myosin V motility. Myosin V motor proteins were labelled with fluorescent light chains. With the technique of FIONA Yildiz et al. (2003) were able to localise the position of a single dye within approx. 1 nm in the x-y plane. In the hand-over-hand model myosin V takes several steps, with the centre of mass moving ∼37nm (blue dashed lines). The trailing head moves 74 nm forward, while the leading head does not move. The stalk moves 37 nm, which means that the dye takes alternating 37 ± 2x steps. x is the average distance of the dye from the stalk (because different light chains can be labelled in the leading and trailing heads; Yildiz et al. (2003)).

Single-molecule optical trapping experiments had a huge impact in elucidating the hand-over-hand movement of myosin V. The dimer myosin V has a long light chain binding domain, containing six calmodulin-binding sites. Mehta et al. (1999) showed that myosin V takes large, 36 nm steps in a processive manner. Interestingly, this value matches the helical pseudorepeat of actin (36 nm) and allows this myosin to move along actin filaments in a linear motion. If myosin V would take smaller steps, it would have to turn around the actin filament. Studies of Veigel et al. (2002) showed the strain-based gating mechanism of myosin V. Later, nanometre-resolution fluorescent studies (FIONA) confirmed the 37 nm-steps consistent with the hand-over-hand movement (Yildiz et al., 2003). The processive movement of myosin V was also visualised using electron microscopy (Walker et al., 2000) and recently with high-speed atomic force microscopy (see Fig. 1.19, Kodera et al. (2010)).

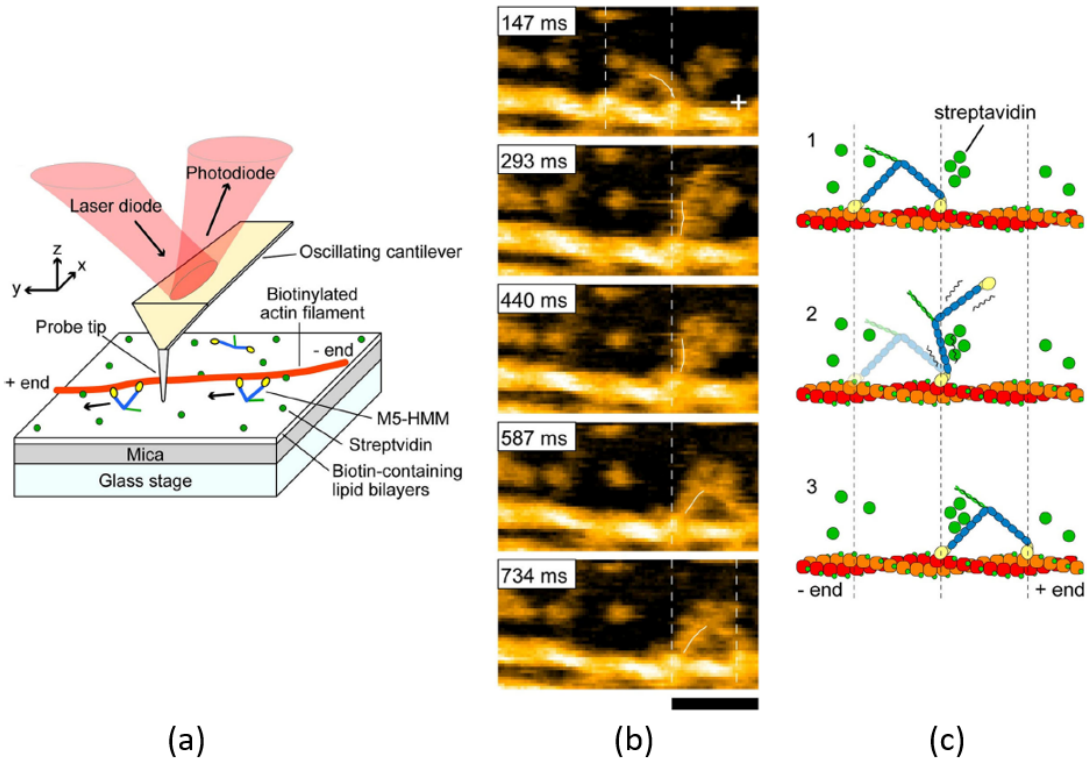

Fig. 1.19: High-speed atomic force microscopy (HS-AFM) directly visualises walking of myosin V on actin filaments. (a) Schematic visualisation of the assay system. (b) Consecutive HS-AFM images showing the stepping behaviour of myosin V in the presence of ATP. The swinging lever-arm is marked with a thin white line. The vertical dashed line represents the centres of mass of the motor domain. Scale bar is 50 nm. (c) Schematic explanation of the images shown in (b). Figures taken from Kodera and Ando (2014).

It is important to distinguish between step size and power (or working) stroke as these two terms often lead to confusion. Step size is the distance between two heads of a processive motor when bound to an actin filament. On the other hand, power stroke size is the distance of lever arm movement during the hydrolysis of an ATP. For a single myosin, the step size does not correspond to the power stroke size. Veigel et al. (2002) measured the power stroke size of a single head of myosin V (25 nm). They suggested that the 36 nm steps of the double-headed myosin (Mehta et al., 1999) are a combination of the power stroke (25 nm) of the attached head and a biased, thermally driven diffusive movement (11 nm) of the free head to the nearest binding position on actin. Similarly, the power stroke size of monomeric myosin VI was determined to 18 nm (Lister et al., 2004), whereas Rock et al. (2001) observed a step size of 30 nm for the dimeric molecule. A diffusive movement of 12 nm of the free head would be enough to reach the next binding position on actin (Veigel et al., 2002).

1.17 Biomedical significance of myosins

Myosins play an important role in nearly every cell type in the human body. The human genome contains nearly 40 different myosin genes which can be grouped into 12 classes (see Fig. 1.20). Myosin mutations are linked to serious pathologies like cardiomyopathies, blindness, hearing loss and many other diseases (Redowicz, 2002; Coluccio, 2020). Many myosin isoforms are also over- (or under-) expressed in cancer cells and play important functions during tumourigenesis and tumour progression (Courson and Cheney, 2015; Li and Yang, 2016; Peckham, 2016).
Around 30 % of patients with familial hypertrophic cardiomyopathy have mutations in the genes that code for the β-cardiac myosin heavy chain or both light chains. To date, over fifty mutations have been detected within these genes, most of which are located in the myosin head. The mutations lead to a destabilization of sarcomeres and a reduction in myosin ATPase activity. Clinically, the myopathy is heterogeneous and characterized by an increased left ventricular mass. This leads to heart failure, stroke and sometimes to a sudden death at young age (Redowicz, 2002; Tajsharghi and Oldfors, 2013).

Several myosin classes are associated with deafness (myosin I, IIa, IIIa, VI, VIIa and XV). Deafness is the most common type of a genetic sensory disorder in humans. More than 100 genes participate in the hearing process, illustrating the complex structure of the inner ear. Myosin I is found at the tips of stereocilia of the hair cells which transform mechanical stimuli into electrical signals. Studies showed that the myosin If isoform is a candidate gene for nonsyndromic deafness (Cyr et al., 2002; Redowicz, 2002).
Similarly, also non-muscle myosin IIa has been found to be involved in the hearing process. Several studies found connections between mutations within the myosin IIa gene and May-Hegglin anomaly, Sebastian, Fechtner, Epstein and Alport-like syndromes. Those syndromes are characterized by autosomal dominant alterations in platelets, i.e. macrothrombocytopenia, nephritis, cataracts and deafness (Heath et al., 2001).
Indications that myosin VI is involved in the hearing process originated from studies on Snell's waltzer mice which showed a deafness phenotype and symptoms like hyperactivity, head-tossing and circling. Histology of hair cells of mutant mice revealed the absence of stereocilia and degradation of the cells about six weeks after birth (Avraham et al., 1995). It is thought that the absence of functional myosin VI leads to a dysfunction of intracellular vesicle transport and thus to the destruction of stereocilia (Coluccio, 2020).

It was found that mutations within the genes coding for myosin III and VIIa are re-

sponsible for blindness. Originally, myosin III of *Drosophila* was isolated as a visual mutation with an electrophysiological phenotype (Montell and Rubin, 1988). The myosin contains a 34 kDa kinase domain in the tail which is approximately 50 % identical to the human serine/threonine kinases of the p21-activated kinase (PAK) family. Expression of myosin III is restricted exclusively to photoreceptor cells and it plays important roles in phototransduction (Dosé and Burnside, 2000).

Besides sensory disorders, mutations in myosin genes have been also found involved in other diseases. The Bardet–Biedl syndrome is a heterogeneous autosomal recessive disorder characterized by mental retardation, short stature, obesity, syndactyly and/or polydactyly, retinitis pigmentosa, and hypogenitalism. Human myosin IXa on chromosome 15 has been identified as a target gene for this syndrome (Gorman et al., 1999).
In recent studies myosin IXa was found to be associated with neuromuscular diseases (O'Connor et al., 2016) and to be required for the collective migration of human epithelial cells, which is important during epithelial morphogenesis, tissue regeneration and cancer metastasis (Omelchenko, 2012). See section 1.18.3 for further informations about myosin IXa-associated disorders.

Although myosin XIV and XXI are not found in humans, they also have biomedical implications for humans. Myosin XIV is found in the parasites *Plasmodium falciparum* (malaria parasite) and *Toxoplasma gondii* which cause severe diseases in immunocompromised humans and congenital disease in infants (Johnson et al., 2007). Myosin XXI is the only myosin isoform expressed in the protozoan parasite *Leishmania donovani*. This flagellated pathogen causes leishmaniasis which affects over 12 million people worldwide. A detailed understanding of the function of this parasite myosins could lead to the generation of specific drugs that inhibit their function and at the same time have few side effects on the hosts (Batters et al., 2012, 2014).
Recently, new myosin classes have been identified in intracellular parasites of the phylum Apicomplexa (myosin XXII, XXIII, XXIV) which emphasizes the importance of myosins in those pathogens (Coluccio, 2020).
In recent years, various highly specific myosin inhibitors have been identified with high potential for the development of pharmacological agents for the treatment of human diseases. The small molecule effectors target the motor domains of myosin classes I, II, V, and VI and can either inhibit or activate the function of the specific isoform (Manstein and Preller, 2020).

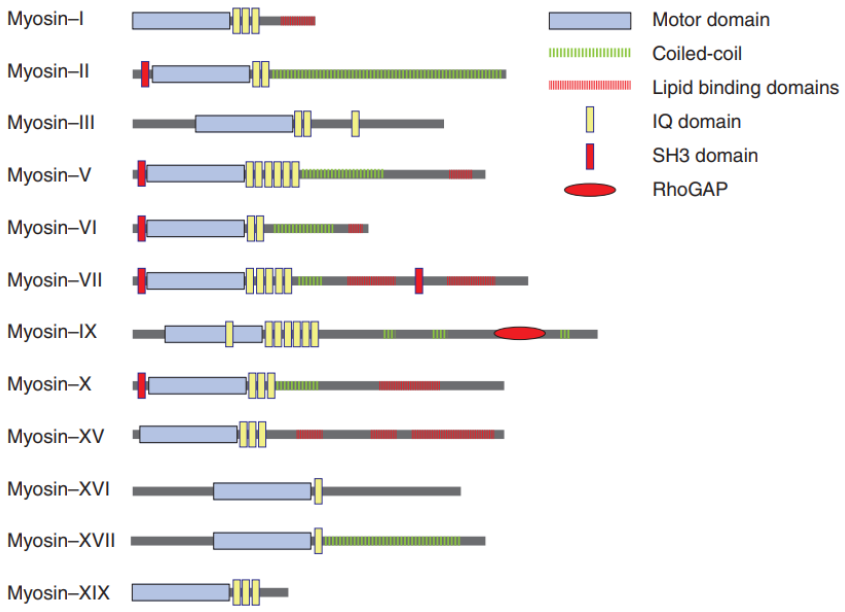

Fig. 1.20: Domain structure of the 12 myosin classes found in humans. Myosin mutations are linked to serious pathologies like cardiomyopathies, blindness, hearing loss and many other diseases (Batters and Veigel, 2016).

1.18 Class IX myosins

Class IX myosins from rat and human were identified in searches for novel unconventional myosins (Bement et al., 1994; Reinhard et al., 1995). Human myosin IXa represents the orthologue of rat myr 7 (seventh unconventional myosin from rat), whereas human myosin IXb is the orthologue of rat myr 5 (Baehler et al., 1997; Chieregatti et al., 1998). From an evolutionary perspective class IX myosins developed in metazoan after the fungi had split off. Invertebrates have only one myosin class IX gene with the exception of *Drosophila*, which have lost their myosin IX. Most vertebrates contain two genes and the two class IX myosins in mammals exist in different splice variants (Odronitz and Kollmar, 2007; Liao et al., 2010).

Expression analysis showed that human myosin IXa is expressed during development and in many adult tissues, most abundantly in brain and testis. In the brain, myosin IXa is found in all regions, particularly in the hippocampus, cortex, and cerebellum, during both development and in adulthood (Chieregatti et al., 1998; Gorman et al., 1999). In contrast, human myosin IXb is predominantly expressed in various cells of the immune system (Wirth et al., 1996). Mouse studies revealed that myosin IXb has important functions in controlling cell shape and migratory activity of macrophages, and thus contributes to innate immune responses (Hanley et al., 2010).

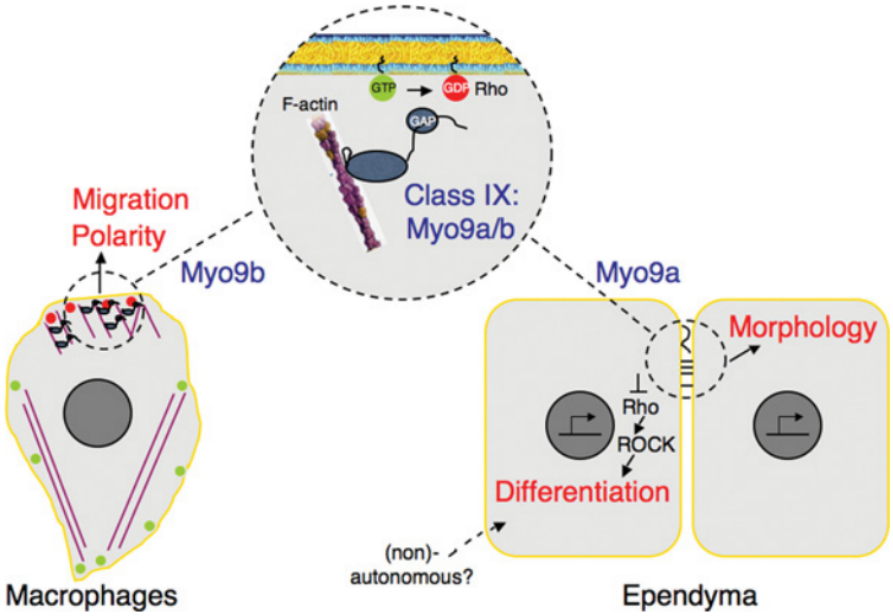

Fig. 1.21: Schematic representation of the cellular functions of the two mammalian class IX myosins. Myosin IXa was found to be localised to cell-cell adhesions in epithelial cells and regulates their morphology and differentiation. The differentiation is controlled through Rho and ROCK signalling. Myosin IXb is mainly expressed in various cells of the immune system including macrophages. It was shown that myosin IXb controls cell polarity and cell migration of macrophages. It is speculated that processive movement of the motor protein along actin filaments towards the cell front carrying as cargo the Rho-GAP domain could lead to local inactivation of Rho. Figure taken from Bähler et al. (2011).

1.18.1 Structure of myosin IXa

On a structural level class IX myosins have several unique features. Within the myosin head they contain a very large insertion of 100-200 amino acids (human IXa: 207 aa, human IXb: 145 aa) into loop 2. Conventional class II myosins have at this position a short sequence of variable length that is not conserved (Bähler, 2000). Loop 2 bridges the gap between the upper and lower 50 kDa domains and is involved in actin binding along with other elements of the upper and lower 50 kDa catalytic domain (Geeves and Holmes, 2005; Lorenz and Holmes, 2010; Saczko-Brack et al., 2016). This loop is well positioned to modify motor properties as exchange of flexible loops between different members of class II myosins was shown to affect the ATPase rates and the mechanochemical coupling (see section 1.14; Uyeda et al. (1994); Rovner et al. (1995)).
Additionally, class IX myosins exhibit a further extension N-terminal to the myosin head. This 100-150 aa extension structurally forms a Ras-binding fold, but lacks conserved positive surface charges which are important for Ras binding and hence its function is unknown (Kalhammer et al., 1997).
The third striking feature is the presence of a Rho-GTPase–activating protein (Rho-GAP) domain in the tail, which deactivates the GTPase Rho (Hanley et al., 2010). The presence of such a domain with signalling activities makes class IX myosin to so-called 'motorized signalling molecules' which link signal transduction to the actin cytoskeleton. Besides class III myosins, which contain a protein kinase domain that plays important roles in phototransduction, no other myosin class is known with signalling functions (Bähler, 2000; Hanley et al., 2020).

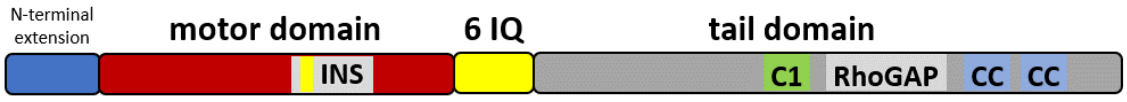

Fig. 1.22: Human myosin IXa consists of 2548 aa and has several unique structural features. The N-terminal extension with a Ras-binding fold is followed by the motor domain with the characteristic loop 2 insert (∼200 aa). The neck region is composed of 6 unevenly spaced IQ motifs and the tail domain includes the RhoGAP domain. Additionally, the tail contains two short segmented coiled-coil regions (CC) and an atypical C1 domain. The C1 domain is characterized by six cysteines and two histidine residues that coordinate two zinc ions. The function of the C1 domain is not known (Bähler et al., 2011). Note that there are in total seven supposed calmodulin-binding sites: one in the loop 2 insert and six in the neck region. In rat myr7 four alternatively spliced regions have been identified, two in the head domain and two in the tail domain (Chieregatti et al., 1998). The myosin IXa heavy chain has a molecular weight of 293 kDa.

1.18.2 The Rho-GAP domain in myosin IX

The Rho subfamily has various members, including Rho A-G, Rac and Cdc42. They cycle between a GTP-bound and a GDP-bound form, and hydrolyse GTP. The level of active, GTP-bound protein is regulated by different factors, involving GTPase-activating proteins (GAPs). Rho GTPases are thought to act like molecular switches and play important roles in regulating the remodelling of the actin cytoskeleton such as formation of actin filament bundles (stress fibres) and focal adhesions, which attach cells to the extracellular matrix (Ridley, 1996; Hall, 1998; Bähler, 2000). It was shown that the RhoGAP domain of rat myr7 (ortholog of human myosin IXa) inactivates *in vitro* Rho A, B and C. The overexpression of myr7 in cells causes morphological alterations characteristic for Rho A inactivation (Chieregatti et al., 1998). Furthermore, also immunoprecipitated human myosin IXb exhibited RhoGAP activity (Post et al., 1998).
Overexpression of myr7 in HeLa cells (and therefore increasing the amount of negative regulator of Rho) leads to a loss of stress fibres and of focal contacts, which induces the cells to adopt a 'neuronal' morphology including a rounding up and the formation of protrusions (Chieregatti et al., 1998; Bähler, 2000).

1.18.3 Myosin IXa and pathologies

In recent studies human myosin IXa was found in an siRNA-based screen to be required for the collective migration of human epithelial cells. Collective cell migration is a key process during epithelial morphogenesis, tissue regeneration and cancer metastasis. Depletion of myosin IXa resulted in an altered organisation of the actin cytoskeleton and tension-dependent disordering of cell-cell adhesions. This resulted in an inability of the cells to form new adhesions and subsequent random migration (Omelchenko and Hall, 2012; Omelchenko, 2012).
In line with disrupted cell-cell junctions, myosin IXa knockout in mice results in severe hydrocephalus. Hydrocephalus is a condition in which an accumulation of cerebrospinal fluid occurs within the brain (1–3 per 1000 live births). The ventricular system in the brain is lined by a single-layered, multiciliated epithelium. Studies showed that those epithelial cells from mice lacking myosin IXa were irregularly shaped and displayed reduced maturation. The cells had a reduced capability to mature to multiciliated cells, which could explain an irregular flow of the cerebrospinal fluid in brain ventricles, resulting in hydrocephalus (Abouhamed et al., 2009). The removal of myosin IXa might lead to increased Rho signalling and it is hypothesized that this in turn leads to an overactivation of ROCK (Rho kinase), an effector of Rho signalling. Interestingly, hydrocephalus for-

mation could be significantly reduced by the inhibition of ROCK. These results suggest that myosin IXa could regulate specifically Rho signalling at cell-cell contacts (Bähler et al., 2011; Hanley et al., 2020). Recently, also a human fetus with hydrocephalus and no observed movements (akinesia) was found to carry a homozygous nonsense mutation in myosin IXa (Maddirevula et al., 2019).
Furthermore, a current study identified a myosin IXa loss-of-function mutation in a family with focal segmental glomerular sclerosis (FSGS), a renal disease which can lead to kidney failure (Li et al., 2021).

Myosin IXa was found to be the first unconventional myosin motor protein associated with a neuromuscular disorder. Whole-exom sequencing of patients with congenital myasthenic syndrome (CMS) revealed mutations in the myosin IXa gene (O'Connor et al., 2016). CMS represents a group of rare hereditary diseases that are defined by impaired function of the neuromuscular junction (NMJ). The syndrome is characterized by fatigable muscle weakness and often affects facial muscles. In a recent CRISPR/Cas9-mediated approach in zebrafish it was shown that NMJ defects were related with the RhoA/ROCK pathway of myosin IXa (see Fig. 1.23). Additionally, treatment of zebrafish with ROCK inhibitors provided improvements to the morphology of NMJs (O'Connor et al., 2019). Myosin IXa depleted NSC-34 cells (mouse motor neuron-derived cells) show a decrease in secretion of key proteins for NMJ formation and maintenance, including agrin, which could be a new therapeutic target for the treatment of CMS patients (O'Connor et al., 2018). These results emphasize the role of myosin IXa in motor axon functionality.

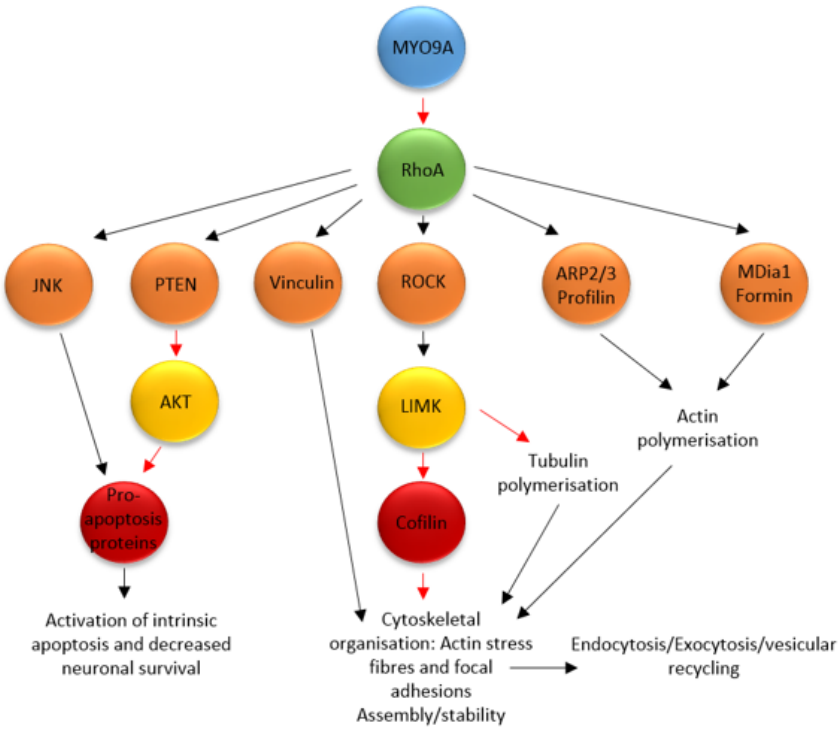

(a)

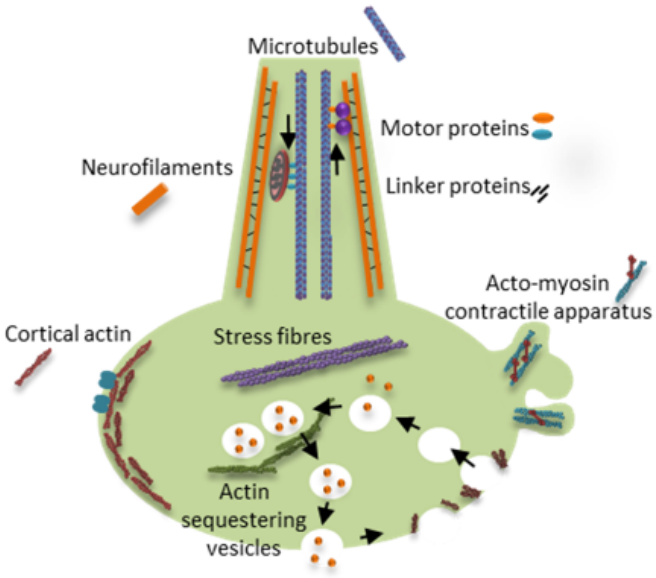

(b)

Fig. 1.23: The connection of myosin IXa with the Rho A signalling pathway and a schematic representation of nerve cell cytoskeleton. (a) Myosin IXa is a negative regulator of Rho A, which influences various downstream pathways, e.g. controlling cytoskeletal dynamics or apoptosis. Red arrows = negative regulation, black arrows = positive regulation. (b) Cartoon of nerve cell cytoskeleton. Microtubules are important for long distance axonal transport, whereas actin networks are responsible for diverse functions such as shape regulation, signalling, stress fibres and vesicle sequestration. Myosin IXa is thought to be involved in several pre-synaptic processes involving the neuronal cytoskeleton (O'Connor et al., 2018).

1.18.4 *In vitro* studies on myosin IX

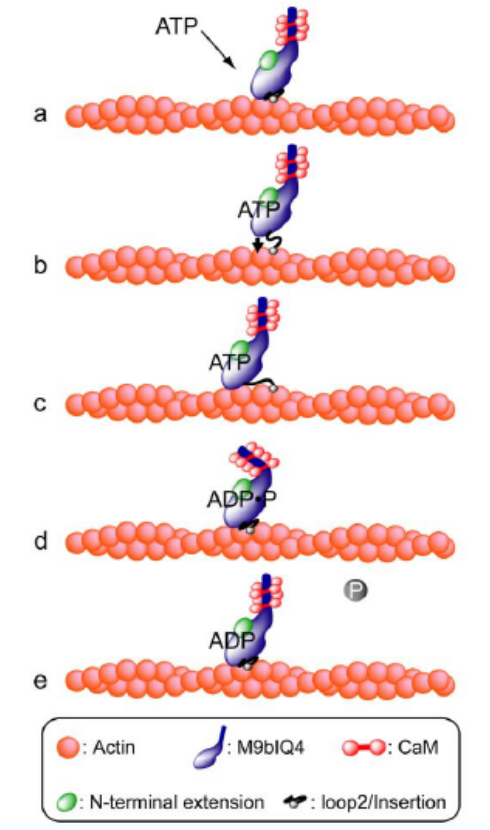

Fig. 1.24: Inchworm-like model for processive movement of single-headed myosin IX. (a) In the presence of ATP the binding between the myosin IX head and actin forms a weak binding state. (b) The head just partially dissociates from actin, because of the presence of the unique loop 2 insert, which tethers the head to actin. (c) The myosin head searches for the next binding location on the actin filament and (d) ATP hydrolysis occurs. (e) After hydrolysis, the myosin head binds in a strong actin binding form, phosphate is released and the power stroke occurs. This model requires a coupling of the loop 2 insertion with the motor domain, in order to allow the head to search for the next binding position on actin (Kambara and Ikebe, 2006).

The majority of *in vitro* studies on myosin IX are coming from biochemical studies of recombinant myosin IX from *C. elegans* (Liao et al., 2010; Elfrink et al., 2014), and native and recombinant human and rat myosin IXb constructs (Post et al., 1998; Inoue et al., 2002; Nalavadi et al., 2005; Nishikawa et al., 2006; Struchholz et al., 2009). Various publications proposed that myosin IX is a single headed processive motor (Inoue et al., 2002; Post et al., 2002; Liao et al., 2010; Elfrink et al., 2014). Interestingly, the processivity of a single-headed motor cannot be described by a hand-over-hand model as shown for myosin V or VI (see section 1.16). However, it has been suggested that the loop 2

insertion in the head domain, unique for class IX members, acts as an electrostatic tether that allows single-headed processive movement like an inchworm (see Fig. 1.24, Kambara and Ikebe (2006); Nishikawa et al. (2006)). This hypothesis is supported by experiments with isolated loop 2 fragments, where the basic loop 2 peptide bound stoichiometrically and with high affinity to F-actin (Struchholz et al., 2009).
With the exception of our laboratory, *in vitro* studies with the myosin IXa isoform are still missing, mainly because of difficulties in obtaining a active recombinant protein and low tissue expression levels of myosin IXa.

1.19 Non-muscle myosins

Higher animals express a variety of different myosin II motors. While some of this myosin II isoforms are specific to skeletal, cardiac, or smooth muscle, some isoforms have a ubiquitous tissue distribution and are therefore called non-muscle (or cytoplasmic) myosin II isoforms (Kovács et al., 2003; Billington et al., 2013). In humans there have been identified three different non-muscle (NM) myosin II isoforms termed NMIIa, NMIIb, and NMIIc (Berg et al., 2001). They are widely distributed throughout the entire organism, while a few cells contain a single isoform, but most cells contain more than one isoform. Cells of the immune system (platelets, lymphocytes, neutrophil granulocytes) and brush border cells lining the intestinal walls are selectively enriched with NMIIa (Maupin et al., 1994; Kovács et al., 2003), whereas neuronal tissue contains high amounts of NMIIb (Rochlin et al., 1995).
These three isoforms play a role in many fundamental cellular and developmental processes such as cytokinesis, cell migration, cell adhesion and control of cell morphology. Recent studies have shown that they are also involved in viral infection and autophagy (Heissler and Manstein, 2013). The term 'non-muscle myosin' leads often to misunderstandings, as these myosin II isoforms are also present in all muscle cells, however in significantly smaller quantities compared to muscle myosin II (Conti et al., 2008).

On a structural level each NM heavy chain (230 kDa) forms a dimer and binds two pairs of light chains (see Fig. 1.25), one commonly referred to as the regulatory light chain (RLC) and the other as the essential light chain (ELC). Both light chains structurally stabilize the lever arm, whereas the RLC plays an important function in regulating the enzymatic activity of the myosin in a phosphorylation-dependent manner (Heissler and Manstein, 2013). The C-terminal tail domain contains an α-helical coiled-coil motif, which leads to homodimerisation of two NM heavy chains and the formation of a rod-like

structure. A short nonhelical tail region (NHT) terminates the heavy chain. The NMII homodimers connect to minifilamentous bipolar structures with an approximately length of 300 nm, comprising about 30 molecules. For comparison, thick filaments of skeletal muscle are up to 30-fold bigger (Billington et al., 2013; Heissler and Manstein, 2013).

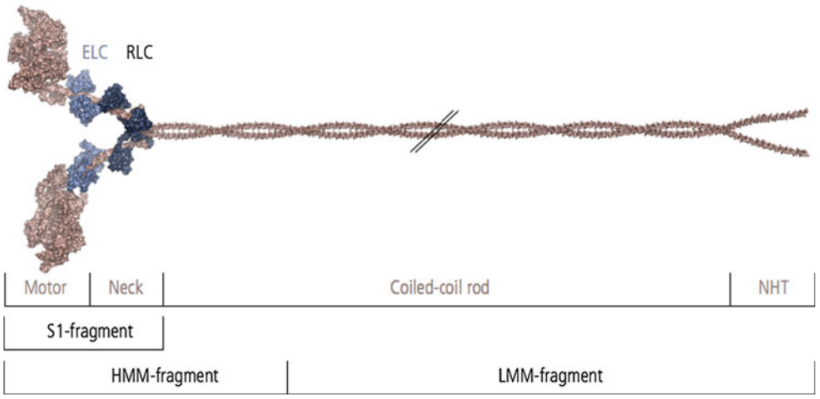

Fig. 1.25: Domain structure of the non-muscle II isoform. The heavy chain of NMII comprises a motor, a neck, and a tail domain which contains a coiled-coiled motif and ends in a nonhelical tailpiece (NHT). The neck domain of each heavy chain binds two pairs of light chains, the essential (ELC) and regulatory light chain (RLC; Heissler and Manstein (2013)).

The ATPase activity and the filament assembly of each of the NMII isoforms are controlled by phosphorylation of the RLC by myosin light chain kinase (MLCK; Melli et al. (2018)). *In vitro* studies suggested that non-phosphorylated NMII forms a compact molecule through a head-to-tail interaction. This leads to an assembly-incompetent (10S) form that cannot bind to other dimers. Only after RLC phosphorylation by MLCK the compact 10S structure unfolds and turns into an assembly-competent form (6S; Vicente-Manzanares et al. (2009)).

Analysis of kinetic parameters revealed subtle differences between the NMII isoforms. All NMII isoforms show a slow ATPase and low coupling between the nucleotide and actin binding sites. Compared to the three NMII isoforms, NMIIa has the highest rate of ATP hydrolysis and it translocates actin filaments in the *in vitro* motility assay more rapidly (∼300 nm/s) than NMIIb and IIc (90-100 nm/s). The duty ratio also shows an isoform dependence: NMIIa has a low duty ratio similar to smooth and skeletal muscle myosins, whereas NMIIb and NMIIc have slightly higher duty ratios (Heissler and Manstein, 2013).

This study focuses on the myosin IIb isoform, the most commonly expressed NMII isoform in the central nervous system. In addition, NMIIb is strongly expressed in the heart muscle (Rochlin et al., 1995). Kinetic analysis showed that NMIIb has an exceptionally

high affinity for ADP compared to other myosins and the ADP release is slowed down by load. These results indicate that NMIIb is well adapted to exert tension on actin filaments for longer periods of time and with less energy consumption than NMIIa. Indeed, NMIIb has been implicated for smooth muscle function, especially in the prolonged force maintenance phase (tonic contraction). Under resisting loads, long attachment intervals on actin will enable tension maintenance and structural anchoring with a very low energy consumption (Kovacs et al., 2007; Vicente-Manzanares et al., 2009).

1.19.1 The role of NMII in cytokinesis and cell migration

Together with non-muscle myosin IIa, the IIb isoform is a component of the contractile ring formed during cell division. The so-called cytokinesis starts after beginning of sister chromatid separation during the anaphase, in which a contractile ring is positioned and narrowed, leading to abscission of two daughter cells. The importance of NMIIb in these events is highlighted by the fact that NMIIb deletion in mice leads to defects in myocyte cytokinesis.
The contractile ring that is formed during cytokinesis consists of different NMII isoforms, actin and associated regulatory and scaffolding proteins. Interestingly, the ability of NMII to move actin filaments does not appear to be required for constriction of the cleavage furrow. Rather, NMII is important in creating tension and resisting expansion of the contractile ring by binding and cross-linking actin filaments (Ma et al., 2007; Heissler and Manstein, 2013).

Directed cell migration is an essential process in multicellular organisms and is associated with cellular functions such as wound and tissue repair, angiogenesis, immunity, normal and malignant motility. NMII isoforms are important regulators of these processes and they are involved in the dynamic remodelling of the actin cytoskeleton and in interactions between the cell and its surrounding (e.g. focal adhesions). Actin is organised in special cellular protrusions (lamellipodia) which drives cell migration. Fibroblasts from NMIIb-deleted mice show unstable and disorganised protrusions, but migrate faster and with reduced persistence. This suggests that NMIIb coordinates protrusive activities and stabilizes cell polarity (Lo et al., 2004; Heissler and Manstein, 2013).

During cancer metastasis, tumour cells change from an immobile epithelial-like to an amoeboid-like migration state. Reports on MDA-MB-231 breast cancer cells indicated that inhibition of either NMII or MLCK was accompanied with a decreased rate of migra-

tion. Additionally, they showed that the non-muscle myosin IIb isoform has an important function in the mechanics of lamellar protrusive events (Betapudi et al., 2006).

1.19.2 NMII isoforms and pathologies

Due to the importance of of NMII isoforms in diverse cellular functions, it is not surprising that they are involved in numerous disorders. Almost 40 heterozygous mutations in the MYH9 gene, encoding NMIIa, have been reported to cause disease. The most common phenotype has been linked to dysfunctions of the blood platelets (macrothrombocytopenia), which play a key role in blood clotting and clot retraction. Additionally, affected patients suffered from deafness, progressive nephritis, and presenile cataracts (Pecci et al., 2008; Coluccio, 2020). Patient platelets had a abnormal cytoskeletal composition and failed to form and to reorganise cytoskeletal structures. *In vitro* studies with recombinant expressed variants showed that they had a decreased ATPase activity and could not move actin filaments. These results revealed that the motor function of NMIIa has an important role in platelets (Hu et al., 2002).

Mice with deleted NMII genes die during embryogenesis and NMIIb depleted mice show cardiac and brain defects (hydrocephalus). Loss of NMIIb causes malfunctions of cell–cell adhesion of neuroepithelial cells that surround the spinal canal (Ma et al., 2007; Vicente-Manzanares et al., 2009).
Finally, there have been found five mutations in MYH14, the gene which encodes NMIIc. Those mutations found in the myosin head and tail domain result in deafness, which demonstrates the crucial role of the myosin superfamily in auditive functions (Donaudy et al., 2004).

1.20 Myosin VI

Unlike all other members of the myosin superfamily, myosin VI has the unique ability to move toward the minus end of actin filaments (Wells et al., 1999). Class VI myosins were initially discovered in *Drosophila* and were subsequently found to be expressed ubiquitously in species from *C. elegans* to humans (Buss et al., 2004).
Similar to other myosins, myosin VI is composed of a N-terminal motor domain, that hydrolyses ATP and binds F-actin. The neck following the head domain contains two calmodulin binding sites and the tail comprises a coiled-coil region as well as a globular carboxy-terminal region (see Fig. 1.26). A unique, approx. 50 amino acids insert between the motor domain and IQ motif is predicted to be the ‘reverse gear’ that enables myosin

VI to move backwards. Cryo-electron microscopy showed that the myosin VI lever arm points toward the minus end of the actin filament. It was suggested that the unique insert is involved in modifying the converter to reposition the lever arm (Wells et al., 1999; Sweeney and Houdusse, 2010). Stabilized by a calmodulin the 'reverse gear' moves in the opposite direction to all other studied myosins and thus allows minus end directed movement (Bahloul et al., 2004).

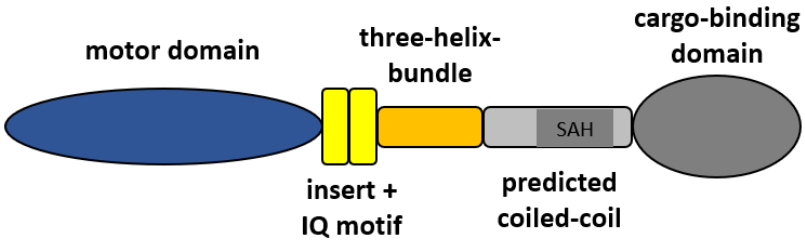

Fig. 1.26: Cartoon illustrating the domain organisation of the 1253 aa long human myosin VI. The motor domain is followed by a unique insert (∼50 aa), which binds calmodulin. A second calmodulin binding site (IQ motif) is located N-terminally to the insert. A three-helix-bundle is continuing the structure. The tail domain comprises a predicted coiled-coil region, including a single α-helix (SAH) and a globular cargo binding domain. Figure modified from Buss et al. (2004).

Interestingly, despite the very short lever arm myosin VI produces a large working stroke of 18 nm in single-molecule optical trapping experiments with a monomeric full-length construct (Lister et al., 2004). Based on a simple lever-arm mechanism myosin VI takes much larger steps than expected, compared e.g. to the 5 nm power stroke of skeletal muscle myosin which also contains two IQ motifs in the neck region (Veigel et al., 1998). It was proposed that the magnitude of a myosin's power stroke depends not only on lever arm length, but also on its orientation with respect to the actin filament (Lister et al., 2004). Alternatively, Rock et al. (2001) suggested a different mechanism to explain the large step size of 30-36 nm, they measured with a (enforced) dimeric myosin VI construct. They speculated that the large step size was the result of the combination of a small power stroke in the 'lead' head together with a large conformational change, that permits the free 'trailing' head to reach the next accessible binding side on actin. The large conformational change is thought to be caused by unfolding of the ∼50 aa insert between the converter domain and light-chain binding domain together with neighbouring structures (Buss et al., 2004).

1.20.1 Is myosin VI a monomer or dimer?

There is a debate in the literature, whether myosin VI acts as a monomer or dimer *in vivo*. Given myosin VI's diverse functions in the cell, it is possible that it switches between both conditions depending on the cell's demands. Initial sequence analysis of the tail domain revealed that it forms a double-helical coiled coiled, and therefore myosin VI was thought to be a dimer (Buss et al., 2004). Therefore, many *in vitro* experiments have been carried out with dimer constructs where dimerisation was achieved by a C-terminal leucine zipper (Rock et al., 2001) or a part of the myosin II rod domain (Nishikawa et al., 2002). These dimeric constructs moved processively along actin filaments in single-molecule experiments with a large step size of 30-36 nm. In contrast, Lister et al. (2004) showed by hydrodynamic and electron microscopy studies that myosin VI can exist as a stable monomer, which produced non-processive movements in optical trapping experiments. They performed a more detailed bioinformatical analysis of the tail domain and observed that the helical region is interrupted two times by prolines, which could fold into loops and therefore prevent dimerisation.
To date there is no final proof in which form (monomer or dimer) myosin VI is present in the cell. However, certain functions as tethering vesicles to actin filaments, maintaining membrane tension or clustering transmembrane receptors would require a non-processive monomer. On the other hand, transport of vesicles along actin filaments to different cellular compartments can only be performed by a processive dimer. It is hypothesized that dimerisation could be induced by regulation mechanisms (e.g. phosphorylation), binding to lipid membranes or by binding partners (Buss et al., 2004). In fact, studies revealed that binding to optineurin and Dab2 can cause dimerisation (Phichith et al., 2009; Yu et al., 2009; Magistrati and Polo, 2021).

1.20.2 Cellular functions of myosin VI

As myosin VI is the only known member of the myosin superfamily which moves towards the minus end of actin filaments, it must have unique cellular functions and properties. Even if the polarity of actin filaments in cells is not fully understood, it is thought that actin filaments have their plus end near the plasma membrane and the minus end toward the surface of cellular organelles such as the Golgi complex or the phagosome (Cramer, 1999; Defacque et al., 2000). Therefore, a minus-end-directed motor would move away from the plasma membrane into the interior of the cell (Buss and Kendrick-Jones, 2008).

Myosin VI is ubiquitously expressed in higher, multicellular eukaryotic organisms. It

is involved in the formation of stereocilia in cells of the auditory system, in endocytosis, in membrane ruffling and in the maintenance of Golgi complex morphology and secretion. Intracellularly, myosin VI is located in membrane ruffles, at the Golgi complex and in clathrin-coated and -uncoated vesicles (Buss et al., 2004). Additionally, myosin VI has been implicated in spermatogenesis in *C. elegans* and *Drosophila* (Tumbarello et al., 2013; Zakrzewski et al., 2021). As myosin VI is also involved in cell migration, it is discussed as an early marker of cancer development and metastasis, because it was found to be upregulated in ovarian and prostata cancer (Yoshida et al., 2004; Dunn et al., 2006; Li and Yang, 2016). The detailed molecular mechanism how this molecular motor might promote cancer cell migration is still unknown.

1.20.3 The role of myosin VI in endocytosis

Endocytosis is a basic process involved in the uptake of macromolecules such as proteins, various nutrients and cell surface receptors. A well-known mechanism is the clathrin-mediated endocytosis, used to internalize surface receptors. One splice variant of myosin VI containing a large insert in the tail domain has been localised to clathrin-coated pits and vesicles in the cortical actin network under the plasma membrane and in microvilli. Those studies lead to the identification of Dab2 (disabled 2) as a myosin VI-binding partner and suggested that myosin VI is involved in a very early step in endocytosis (Morris et al., 2002). Dab2 was found to colocalise with the low-density lipoprotein receptor (LDLR) family and associates myosin VI with cell surface receptors (Morris and Cooper, 2001). Given that myosin VI was localised to microvilli and is known that this structures contain highly ordered actin filaments with the plus ends at the tips and the minus ends at the base, myosin VI could transport receptor complexes from the tip of a microvillus to the base for accumulating in a clathrin-coated pit (see Fig. 1.27). Additionally, myosin VI could transport clathrin-coated vesicles through the cortical network away from the plasma membrane towards the cell interior (Buss and Kendrick-Jones, 2008).

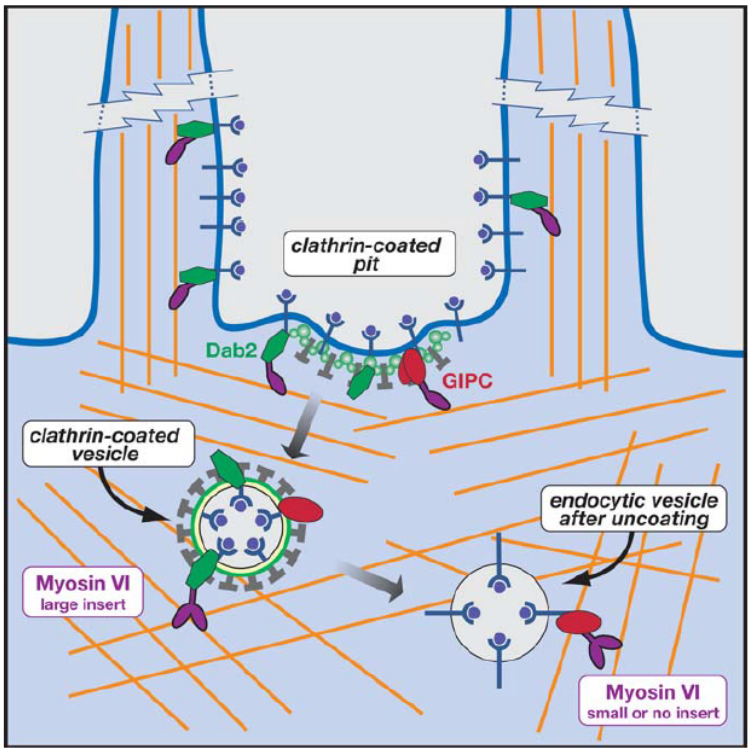

Fig. 1.27: Schematic model of the functions of myosin VI during early and late stages of endocytosis. The myosin VI isoform with a large tail-insert is expressed in polarised epithelial cells with apical microvilli. During the initial steps of endocytosis, myosin VI is involved in transporting receptors down the microvillus to create a clathrin-coated pit. Myosin VI binding partners such as Dab2 and GIPC (GAIP-interacting protein C-terminus) were colocalized with clathrin-coated vesicles. In later stages of endocytosis, it is assumed that the myosin VI isoform without the large insert transports uncoated vesicles through the dense cortical actin network in direction to the later endocytic compartment (Buss et al., 2004).

Aschenbrenner et al. (2003) found that the splice variant of myosin VI with a small or no insert was found on uncoated endocytic vesicles prior to fusion with the early endocytic compartment, suggesting that myosin VI is also involved in later stages of endocytosis. Myosin VI could be also involved in vesicle formation either by dragging the membrane with the clathrin-coated pit into the cell or by pressing actin filaments into the vesicle neck which leads to vesicle scission (Buss et al., 2001).

1.21 Optical trapping

The idea that light can exert optical force arose already in the seventeenth century by the German astronomer Johannes Kepler, which he used to explain the observation that a tail of a comet always points away from the sun (Kepler, 1619). The concept of radiation pressure was theoretically described by James Clerk Maxwell in 1862, stating that electromagnetic radiation has a momentum and therefore exerts a pressure upon any surface that it is exposed (Maxwell, 1862). It was not until the 1970s until the effect of radiation pressure could be described experimentally by Arthur Ashkin of AT&T (Bell) Laboratories, mostly because the effect is quite moderate. Very bright light corresponding to milliwatts of power produce a radiation pressure of a few piconewtons. Ashkin used lasers as an intense, collimated source of light and showed that micron-sized particles freely suspended in water could be accelerated and even trapped (Ashkin, 1970). Over the next years, Ashkin and colleagues experimented with different optical systems that could capture small objects, atoms and molecules. In 1986, Ashkin and others developed a single-beam optical trap (Ashkin et al., 1986). Since then, the technique is called 'optical trapping' or 'optical tweezers' (Svoboda and Block, 1994).

In general, an optical trap is created by focusing a laser beam with an objective of high numerical aperture (NA). A dielectric particle close to the focus will encounter a force because of the transfer of momentum from the scattering of incident photons. The resulting optical force can be divided into two components: A scattering force which acts in the direction of light propagation and a gradient force, which acts in the direction of the spatial light gradient. For the most common situations, the scattering force dominates, and particles get 'pushed' away from the laser source (see Fig. 1.28 (a)). The situation differs near the focus of a laser, where the three-dimensional intensity gradient creates an axial force which balances the scattering force. Off-axis rays mostly contribute to the gradient force, while the central rays are primarily responsible for the scattering force. As the bead moves in the focused beam, the mismatch of optical forces pushes it back into the equilibrium position (see Fig. 1.28 (b)). This results in a stable trapping of the particle (Neuman and Block, 2004).

After the development of the single-beam optical trap, Ashkin and collaborators explored the use of optical tweezers in biology. The first organisms to be experimented were *E. coli* and Tobacco Mosaic Virus (Ashkin et al., 1987; Ashkin and Dziedzic, 1987). It became possible to hold *E. coli* bacteria and yeast cells for hours in isolation and even observe cell

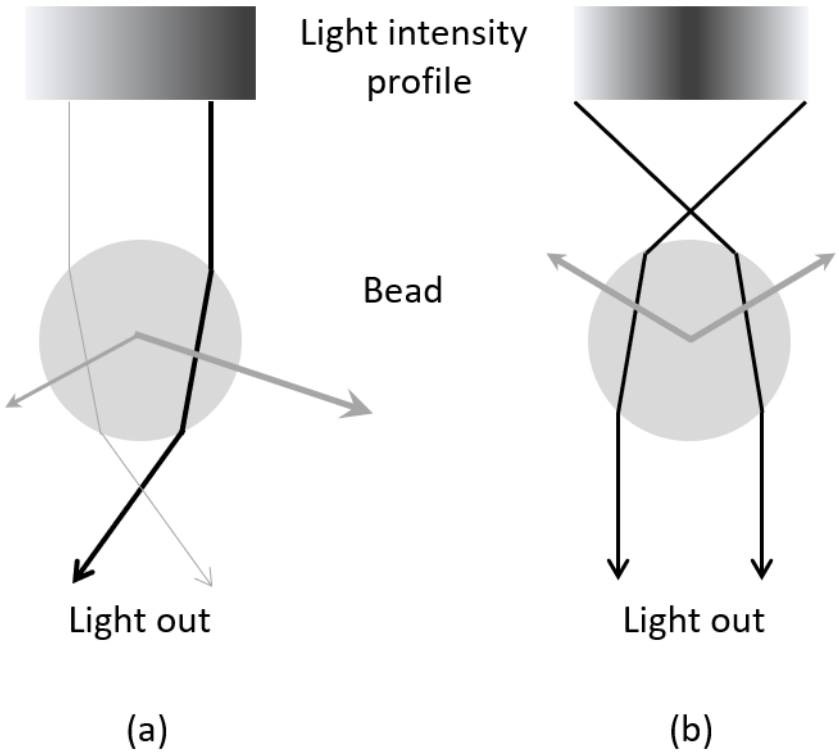

Fig. 1.28: Ray optics description of the forces acting on micron-sized particles. (a) A transparent bead is illuminated by a parallel light beam with a linear intensity gradient. Two example light beams of distinct intensities (indicated by lines of different thickness) are depicted. The refraction of the rays by the bead alters the momentum of the photons. Conservation of momentum leads to a change of the momentum in equal but opposite direction, which results in forces shown with grey arrows. (b) The light must be focused to create a radial intensity gradient in order to form a stable trap. The change in momentum leads to a net force towards the focus, which results in trapping of the particle. Figure modified from Neuman and Block (2004).

division within the trap, which showed that its possible to manipulate cells under damage free conditions. Remarkably, manipulation was also possible on organelles within plant cells and protozoa, without damaging the cell wall (Ashkin, 1997). For his pioneering work Ashkin was awarded with the Nobel Prize in Physics 2018 "for the optical tweezers and their application to biological systems" together with G. Mourou and D. Strickland (Essiambre, 2021).

1.21.1 Optical trapping of molecular motors

In the last 25 years work by other groups showed that single molecules can be studied with optical tweezers. In those experiments the molecule of interest was attached to a bead or other object that could be controlled with optical tweezers. The advantage of this method is that proteins or DNA are too small to be trapped directly. Additionally, the constant size of beads allows the system to be calibrated easily. It was possible to measure the force on single actin filaments moving on a myosin-coated surface by attaching a latex bead to the actin filament and measuring its movement in a single-beam optical trap (Simmons et al., 1993). Furthermore, similar geometries were used to measure single-molecule events by kinesin molecules (Block et al., 1990).

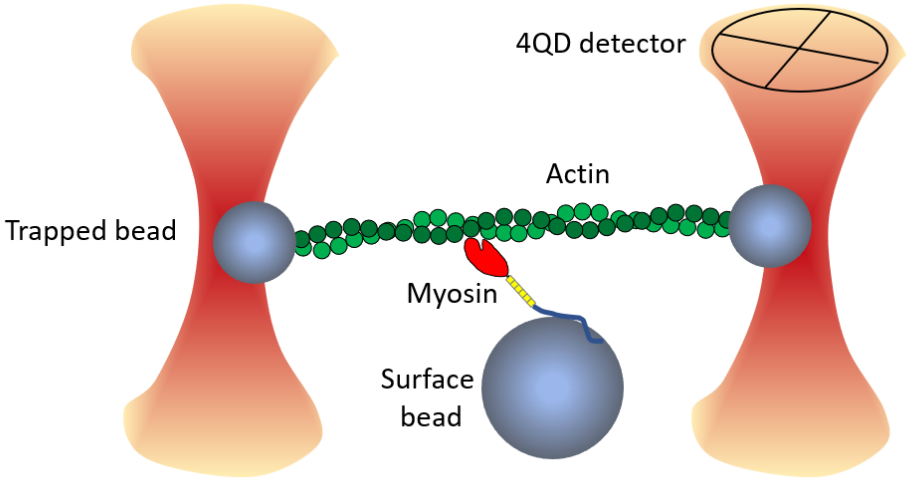

Fig. 1.29: The three bead geometry devised by Finer et al. (1994).

Studying single-molecule events of myosin motors was quite challenging at that time because of the large fraction of time in the ATPase cycle that myosin spends detached from actin (compared to other molecular motors as kinesins). Therefore, Finer et al. (1994) developed the so-called three bead assay, where they added a second optical trap to hold and manipulate an actin filament through beads attached on both ends (so-called bead-actin-bead dumbbell; see Fig. 1.29). This geometry prevented the filament from diffusing away from a surface bead coated with myosin. By attaching myosin molecules on a 'third' bead above the cover glass surface prevented interactions of the beads or the actin filament with the surface. With this assay geometry it was possible to measure for the first-time single-molecule binding events of myosin acting on actin. Additional, Finer et al. introduced the four-quadrant photodiode detectors (4QDs) to record the bead position

in the trap. 4QDs are extremely sensitive to motion in two dimensions and therefore well suited to make nanometre-precision measurements (see chapter 2.5.5).

To prevent damage of biological samples by light absorption, most trapping lasers work in the near infrared. Its counterproductive to go too far into the infrared range, as water starts to absorb strongly beyond 2 µm. Therefore, the neodymium-doped yttrium aluminium garnet (Nd:YAG) laser that emits light at a wavelength of 1064 nm is a good compromise and was used in this study. Additionally, this laser has a good beam pointing stability and a high output power (Svoboda and Block, 1994).
In chapter 2.5 I describe the building of an optical trapping setup from individual components.

1.21.2 Single-molecule mechanics of myosins

Using the three-bead assay and technical improvements from the study of Finer et al. (1994) allowed to explore the field of single-molecule mechanics (see Fig. 1.30). Molloy et al. (1995) measured the power stroke and work done by a single muscle myosin subfragment 1 (S1) head and showed that a single head behaves as an independent generator of force and motion. A few years later, Veigel et al. (1999) determined the stiffness of rabbit skeletal myosin using a sinusoidal oscillation applied to one bead in the bead-actin-bead dumbbell. Additionally, single-molecule measurements were extended to study different myosin isoforms, such as myosin I (Veigel et al., 1999), myosin V (Mehta et al., 1999) or myosin VI (Lister et al., 2004). The transition to 'unconventional' myosin motors allowed researcher to observe a two-step working stroke (Veigel et al., 1999), previously not observed with skeletal muscle myosin.
Sophisticated technical improvements by Veigel et al. made it possible to apply load to single myosins during crossbridge formation, allowing to observe a strain sensing mechanism within different myosin isoforms. The load dependence of the ADP release in smooth muscle myosin provided a molecular explanation of the Fenn effect (Fenn, 1923; Veigel et al., 2003), whereas the load dependence of myosin V introduced the mechanism of 'head-gating' to ensure and increase processivity (Veigel et al., 2002, 2005).

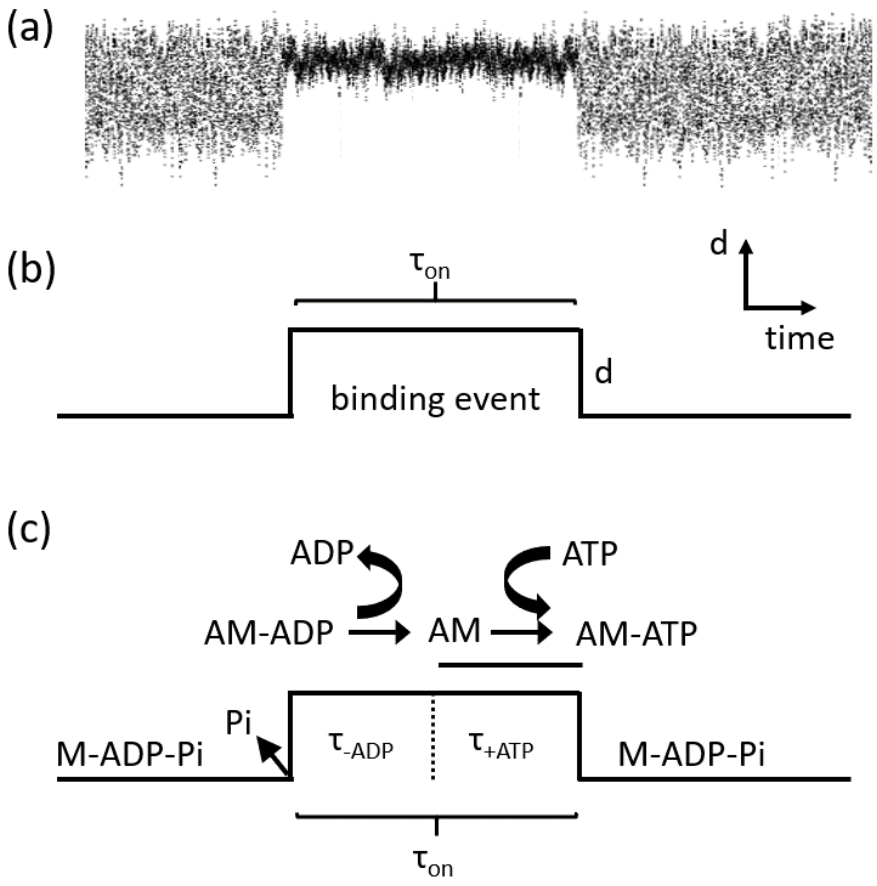

Fig. 1.30: Single-molecule mechanical measurements of myosin motors. (a) Raw data trace of a single myosin interaction in the three-bead assay. The time series shows the displacement of one dumbbell bead cast on the 4QD detector. A single myosin interaction is clearly visible in the middle of the record. (b) Schematic representation of the binding event indicating the displacement amplitude (d) and the characteristic τ_{on}. (c) Illustration of the coupling of mechanical events with the biochemical ATPase cycle. AM represent a state where myosin is strongly bound to actin, whereas M represents a detached or weakly bound state. The τ_{on} can be further subdivided into ADP release and ATP binding. Phosphate (Pi) release occurs very fast directly after the beginning of the binding event.

1.22 Research aims and objectives

The superfamily of myosin motors interact with actin filaments to generate a variety of cellular motile functions including muscle contraction, exo- and endocytosis, cytokinesis and even signal transduction. Different myosin isoforms have evolved to adapt to their specific functions. In this work I investigate the biochemical and single-molecule properties of the human myosin isoforms IIb, VI and IXa. Those isoforms are structurally, biochemically and kinetically tailored to their specific cellular tasks and not much known is about their regulation (calcium, phosphorylation) to adapt to changing cellular environments or external stimuli. The aim of the study is to elucidate the molecular roles of the myosin isoforms IIb, VI and IXa and how their structural characteristic lead to their specific cellular functions. Diverse biochemical methods, *in vitro* assays and an optical tweezers transducer are used in this study. In chapter 2.5 I describe the building of an optical trapping setup from individual components.

Section 3.1 focuses on myosin IXa, which is localised in actomyosin networks at cell-cell adhesions. This molecular motor contains a unique, ∼200 aa insertion in the loop 2 region of the head domain, which allows this motor to bundle actin filaments into highly ordered actomyosin networks. The properties and functions of this large loop 2 insertion and other domains will be studied with different *in vitro* assays and an optical tweezers transducer. Additionally, I show how the motor activity and bundling capability is regulated by calcium/calmodulin, which can bind to the unique loop 2 insertion in myosin IXa.

In section 3.2 the non-muscle isoform IIb (NMIIb) is introduced, which plays an important function in fundamental cellular processes such as cytokinesis and cell migration. Using single-molecule experiments I show that NMIIb produces two types of power strokes and that this behaviour does not depend if the motor is single or double headed. Furthermore, I investigate the dependence of the two power stroke types on lifetime and stiffness.

In the last section (3.3) I investigate the role of myosin head phosphorylation on the mechanical functions of myosin VI. This molecular motor has the unique ability to move towards the minus end of actin filaments and is involved in diverse cellular functions such as vesicle transport, endocytosis and intracellular membrane trafficking. *In vitro* motility assays of the Buss lab (University of Cambridge, UK) have shown that phosphorylation of serine at position 267 had a huge impact on the velocity of actin filaments in actin gliding assays. Using an optical tweezers transducer I show that the differences observed

in the ensemble assay can be explained by tuning the ADP release and ATP binding rates in the actomyosin cycle.

2 Methods

2.1 Molecular biology methods

2.1.1 DNA amplification, restriction, ligation and transformation into *E. coli* DH5α

Polymerase chain reactions (PCR) were carried out using the Mastercycler Personal (Eppendorf) or T3 Thermocycler (Biometra). 50 µl reactions were performed with Phusion™Hot Start II High Fidelity DNA-Polymerase (#F549L, ThermoScientific) according to manufacturer's protocols. To facilitate optimal primer annealing a touchdown program was used:

1. Initial denaturation 98°C 45 s
2. 8 cycles, annealing temperature decline 1°C per cycle: denaturation 98°C 15 s, annealing 68°C 30 s, extension 72°C 60 s/1kbp
3. 28 cycles: denaturation 98°C 15 s, annealing 60°C 30 s, extension 72°C 60 s/1kbp
4. Final extension 72°C 5 min

PCR products were analysed by DNA electrophoresis. DNA purification was performed using the Pure Link™ Quick Gel Extraction & PCR Purification Combo Kit (#K220001, Thermo Scientific) following manufacturer's instructions. DNA digestion was carried out using the appropriate restriction enzymes (NewEngland BioLabs). In a general protocol, 40 µl reactions included 1x NEBuffer, BSA (optional), 20 µl purified DNA, 1.5 µl of each enzyme and this mix was incubated for 3-4 h on a shaker with 400 rpm at 37°C. The entire sample volume was combined with SYBR Green (Thermo Scientific) together with 1x loading dye and digested products were inspected by DNA electrophoresis. The separated constructs were cut out of the agarose gel and purified with the Pure Link™ Quick Gel Extraction & PCR Purification Combo Kit (#K220001, Thermo Scientific).
Ligation of vector and insert was performed using the T4 DNA-Ligase (#15224041,

Thermo Scientific) in 20 µl sample volume. Vector and insert were typically mixed in a 1:3 ratio. The ligation was incubated for 5 min (RT) and then immediately transformed into chemically competent *E. coli* DH5α cells. The cells were thawed on ice and incubated for 15 minutes with the ligation mixture on ice. A heat shock at 42°C for 45 seconds was carried out and the cells were then placed directly back on ice and YT medium was added. The cells were incubated at 37°C with agitation for 30-60 min and were plated on 2 YT plates with the appropriate antibiotics.
After an overnight incubation at 37°C, single colonies containing the desired plasmid were inoculated into 3 ml of liquid LB media supplemented with the proper antibiotic. Following an overnight growth at 37°C and 200 rpm, plasmid DNA was purified using the PureLink™ Quick Plasmid Miniprep Kit (#K210011, Thermo Scientific). A restriction digest was performed with the isolated plasmids to confirm successful ligation into vectors. 2 µl of purified DNA was cut with 1 µl of the suitable enzymes for 1 h at 500 rpm and 37°C (in 20 µl with 1x NEBuffer). DNA electrophoresis was carried out to approve the presence of the insert in the vector. Samples containing products of expected sizes were sequenced to confirm the correct creation of the plasmid. 50 % glycerol stocks of positive colonies were prepared for long term storage at -80°C.

Tab. 2.1: 2x YT medium

Ingredient	Mass or Volume/5l
1.5 M Tris-HCl pH 7.5	30ml
Tryptone	80g
Yeast extract	50g
NaCl	25g

Tab. 2.2: LB medium (pH 7.0)

Ingredient	Mass or Volume/1l
Tryptone	10g
Yeast extract	5g
NaCl	10g

2.1.2 Transformation and expression of proteins in *E. coli* BL21 cells

Chemically competent One Shot™ BL21 Star™ (DE3) *E. coli* cells (#C601003, Thermo Scientific) were used for protein expression. These cells were treated similarly to DH5α cells. Liquid starter cultures in 2x YT containing the appropriate antibiotic were inoculated with single colonies from overnight agar plates. Bacterial expressions were initiated with 15-30 ml of starter culture in 420 ml 2YT (with antibiotic). The cultures were shaken at 37°C until they reached an optical density at 600 nm (OD600) of 0.5 to 0.8. Protein expression was induced with 1 mM IPTG. Temperature and expression duration differed depending on the construct. Cell pellets were obtained by a 10 min centrifugation at 3450 x g, 4°C (Beckman Coulter JA25.50 rotor). Cell pellets from 1 l expression were resuspended in 40 ml of buffer B with 1 mM DTT and EDTA-free protease inhibitor cocktail (#COEDTAF-RO, Sigma) and stored at – 80°C.

Tab. 2.3: Buffer B

Ingredient	Final concentration	Mass or Volume/1l
Tris-HCl pH 7.5	50mM	50ml (1M stock)
Imidazole	40mM	2,72g
NaCl	150mM	60ml (2.5M stock)
DTT	1mM	1ml (1M stock)
Sucrose	20% (w/v)	200g

2.1.3 Generation of recombinant bacmids

The recombinant vector can be transposed into the baculovirus shuttle vector (bacmid) using the MAX Efficiency DH10Bac™ *E. coli* cells (#10361012, Thermo Scientific). For transformation, 100 µl chemically competent DH10Bac *E. coli* cells were thawed on ice and incubated for 30 min on ice with 5 µl DNA. A heat shock was carried out for 45 s at 42°C and was followed by instant incubation on ice for 2 min. The cells were then rescued in 900 µl S.O.C. medium (#15544-034, Invitrogen) and incubated for 4 h, 300 rpm, 37°C. 100 µl of 1:10 and 1:100 cell dilutions were plated on B2B agar plates supplemented with X-Gal, IPTG, kanamycin, gentamicin and tetracycline.
After incubation for 48 h at 37°C white colonies were picked and added to 3 ml of LB media with gentamycin (7 µg/ml), tetracyclin (10 µg/ml) and kanamycin (50 µg/ml) and

incubated overnight at 37°C, 250 rpm. DNA extraction was performed with the PureLink® Quick Plasmid Miniprep Kit (#K210010, Thermo) following manufacturer's guidelines. In the last step, the presence of the desired construct in the bacmid was approved by PCR with pUC-M13F and pUC-M13R primers. Reaction conditions:

1. First denaturation 98°C 60 s
2. 32 cycles: denaturation 98°C 15 s, annealing 55°C 45 s, extension 72°C 8 min
3. Last extension 72°C 8 min

Tab. 2.4: B2B medium: 500 ml LB medium supplemented with:

Ingredient	Final concentration	Mass or Volume/0.5l
X-Gal	50µg/ml	1.25ml (20mg/ml stock)
IPTG	40µg/ml	84µl (1M stock)
Gentamycin	7µg/ml	70µl (50mg/ml stock)
Kanamycin	50µg/ml	1ml (25mg/ml stock)
Tetracyclin	10µg/ml	0.5ml (10mg/ml stock)
Agar	1.5%	7.5g

2.1.4 Oligonucleotides

All oligonucleotides have been obtained from Eurofins. Constructs were sequenced by GATC Biotech and Eurofins. DNA was analysed with SnapGene or ApE.

Tab. 2.5: Oligonucleotides

Name	**Sequence (5' – 3')**
loop2-GST-EcoR1-fwd	GTGCTGAATTCGATGTCCCCTATACTAGGTT ATTGGAAAATT
loop2_ext HindIII-rev	GATCAAGCTTTCATTTAACAAAATACGGTTC TGCTTGACC
loop2_HindIII-rev	GATCAAGCTTTCAGGTTTACTCAGGCTTGCC
MD9a-forward	AGGATCCATGGATGATTTATGTAGTTTACCT GATTTG
IX-1019-RP	AAAAGCGGCCGCTTACACCTCTTGGTGAAG CAGATC
1019-reverse	TTCTAGACTACTTGTCATCGTCATCCTTGTAA TCCACCTCTTGGTGAGCAGTC
IX-1162-RP	AAAAGCGGCCGCTTATTTTAAAGCTTTAAAT CTTTGTCTTGC
Avi-tag-fwd	GGCCGCAGGTGGCGGTCTGAACGACATCTT CGAGGCTCAGAAAATCGAATGGCACGAAGC
Avi-tag-rev	GGCCGCTTCGTGCCATTCGATTTTCTGAGC CTCGAAGATGTCGTTCAGACCGCCACCTGC
BirASalI_RP	AAAGTCGACCTATTTTTCTGCACTACGC
BirABamHI_FP	AGGATCCAAGGATAACACCGTGCC
CamXBamHIFP	AGGATCCATGGCTGACCAACTGACAGAAG
CamXXhoIRP	ACTCGAGTCACTTTGCTGTCATCATTTGTAC
RLC-BamHI-FP	AAAAAAGGATCCATGTCCAGCAAGCGGGCC AAAGC
RLC-XhoI-RP	TTTTTTCTCGAGCTAGTCGTCTTTATCCTTG GCGC
pUC-M13F	CCCAGTCACGACGTTGTAAAACG
pUC-M13R	AGCGGATAACAATTTCACACAGG

2.2 Biochemical methods

2.2.1 SDS-PAGE

Protein samples were separated by discontinuous Sodium Dodecyl Sulphate Polyacrylamide Gel Electrophoresis (SDS-PAGE) on 7.5 and 15 % gels according to Laemmli (1970) using the BioRad Mini protean Tetra system. For non-muscle IIb constructs commercial precast gradient 4-12 % Bis-Tris Plus gels (#NW04120BOX, Thermo) or 8 % Bis-Tris Plus gels (#NW00080BOX, Thermo) were used, to achieve an optimal separation of ELC and RLC.
Prior to gel electrophoresis, 6 x SDS gel loading buffer was added to the protein samples and mixtures were boiled for 5 min at 98°C. Electrophoresis was performed at a constant voltage of 200 V, first 30 min without samples and then 30 – 60 min with samples. A pre-stained mixture of proteins of known molecular masses between 10 and 245 kDa was used as standard (#A8889, AppliChem). Protein bands are visualised using Coomassie stain.

Tab. 2.6: Separating and stacking gel, Mass or Volume/ 6 gels

Ingredient	Stock	7.5% Sep. gel	15% Sep. gel	Stack. gel
Acrylamide	30%	8ml	16ml	1.7ml
Tris HCl pH 8.8	1.5M	8ml	8ml	1.25ml
SDS	10%	320µl	320µl	100µl
APS	10%	128µl	128µl	100µl
TEMED		13µl	13µl	10µl
H_2O_{dd}		15.5ml	7.5ml	6.8ml

Tab. 2.7: 6x SDS gel loading buffer

Ingredient	Final concentration	Mass or Volume/10ml
Tris-HCl pH 6.8	375mM	1.875ml (2M stock)
SDS	10% (w/v)	1g
Glycerol	50% (v/v)	5ml (99% stock)
β-mercaptoethanol	10%	1ml
Bromophenol blue	0.2% (w/v)	0.02g

Tab. 2.8: SDS running buffer

Ingredient	Mass or Volume/ 1l
Glycine	18.77g
Tris HCl pH 8.3	3g
SDS	1g

2.2.2 Western blots

Proteins were separated by SDS-PAGE and transferred to a Hybond C-extra nitrocellulose membrane (#RPN303E, Amersham Biosciences) according to a modified protocol of Towbin et al. (1979) using the Mini Trans-Blot® module (BioRad). In this wet blotting method, the protein transfer was carried out at 100 V for 60 min. Membranes were blocked for 60 min at RT in 3 % skim milk in PBS with 0.1 % Tween-20. The blocking was followed by incubation with Anti-GST-HRP conjugate antibody (#RPN1236, GE Healthcare) 1:5000 dilution in 3 % skimmed milk for 1 h at RT or overnight at 4°C. The antibody was conjugated with horse radish peroxidase (HRP). After washing the membrane three times with PBS, each 15 min, protein bands were detected with the ECL™ Prime Western Blotting Detection Reagent (#RPN2232,GE Healthcare) and visualized on a ChemiDoc XRS+ (BioRad).

2.2.3 Size-exclusion chromatography

Size exclusion chromatography (SEC) or gel filtration separates molecules based on their size and shape by filtration through a gel. The gel is composed of a porous matrix of beads that have only low reactivity and adsorption properties. Small molecules diffuse into the pores and their flow through the column is slowed down according to their size. In contrast, large molecules do not penetrate the pores and are eluted in the void volume of the column.

During a gel filtration run 500 μl sample was applied to the a Superdex200 Increase 10/300 GL (#28990944, GE Healthcare) on ÄKTA purifier system (GE Healthcare). The column was calibrated with PBS or loop 2 buffer (Struchholz et al., 2009), depending on the experiment. Pressure limits and flow rates were adjusted according to manufacturer's instructions. The absorbance at 280 nm was detected and the peak fractions were analysed by SDS-PAGE.

Tab. 2.9: Loop 2 buffer

Ingredient	Final concentration	Mass or Volume/1l
Tris-HCl pH 7.0	50mM	50ml (1M stock)
NaCl	50mM	20ml (2.5M stock)

2.2.4 Determination of protein concentration

Protein concentration was determined using the Bradford assay and absorbance at 280 nm.
The Bradford assay relies on the absorbance shift of the dye Coomassie Brilliant Blue G-250 (#500-0006, Biorad) from 465 nm to 595 nm when it binds to proteins. Proteins present in an acidic solution of this dye cause a visible colour change from red/brown to blue (Bradford, 1976). A standard BSA curve with known BSA concentrations in the range from 0 – 1 mg/ml was created to quantify the colour change.

The amino acids tyrosine and tryptophan absorb light at 280 nm, which is the basis of the spectrophotometric method to determine protein concentration (Stoscheck, 1990). A Varian Cary UV-spectrophotometer was used, and protein molar concentration c was calculated according to the Beer-Lambert law

$$A = \epsilon l c$$

where A is the absorbance of the protein at the wavelength λ, ϵ is the molar absorption coefficient of the absorbing protein at λ and l is the optical path length (usually 1 cm for standard cuvettes).

2.2.5 Calculation of the ionic strength and free calcium concentration

Ionic strength (I) was calculated as follows:

$$I = \frac{1}{2} \sum_{i=0}^{n} c_i \times z_i$$

where c_i is the molar concentration of ion i and z_i is the charge of ion i.

The free calcium concentration in solution was calculated with an excel program written by Dr. Rogez and was expressed as the negative decadic logarithm of the concentration (pCa).

2.3 Protein expression and purification

2.3.1 Purification of bacterially expressed proteins

Cell pellets from 1 l cultures were thawed in a water bath at 25°C and 1 mM DTT was added. After sonication on ice for 5 min with 1 s on/off bursts with 50 % power (Bandelin HD 2070 sonicator) the cells were centrifuged at 20000 rpm, 4°C for 20 min (Beckman Coulter JA25.50 rotor). The supernatant was filtered through a 0.45 µm syringe filter and loaded automatically on a suitable resin column on ÄKTA Purifier FPLC (GE Healthcare). The column was dependent on the tag of the protein: His- tagged proteins were purified using a 5 ml HisTrap™ FF column (#GE17-5255-01, GE Healthcare), whereas GST- tagged proteins were purified with 5 ml GSTrap™ FF columns (#GE17-5131-01, GE Healthcare) or 5 ml GSTrap™ 4B columns (#GE28-4017-48, GE Healthcare). The column was washed with His-low buffer (His- tagged proteins) or PBS (GST- tagged proteins) to remove nonspecifically bound proteins until the A280 signal reached the baseline. Bound proteins were then eluted from the column by washing with His-high buffer (His-tagged proteins) in a stepwise manner (BirA and CaM: 30, 100 %; ELC and RLC: 3, 30, 100 %) or with reduced gluthathione Tris-buffer (RGT) in three steps (5, 25, 50 %) for GST- tagged proteins. Pressure limits and flow rates were set to 0.5 MPa and 1 ml/min, respectively, according to the manufacturer's instructions. 1 ml fractions corresponding to peaks in the A280 signal were analysed by SDS-PAGE. Clean fractions were pooled, concentrated if necessary, snap-frozen in liquid N_2 and stored at -80°C until use. Biotin ligase BirA was stored with 10 % (v/v) glycerol. ELC and RLC were stored with 20 % (v/v) glycerol.

Tab. 2.10: RGT buffer

Ingredient	Final concentration	Mass or Volume/0.1l
Tris-HCl pH 8.0	50mM	5ml (1M stock)
L-Glutathione	10mM	0.31g

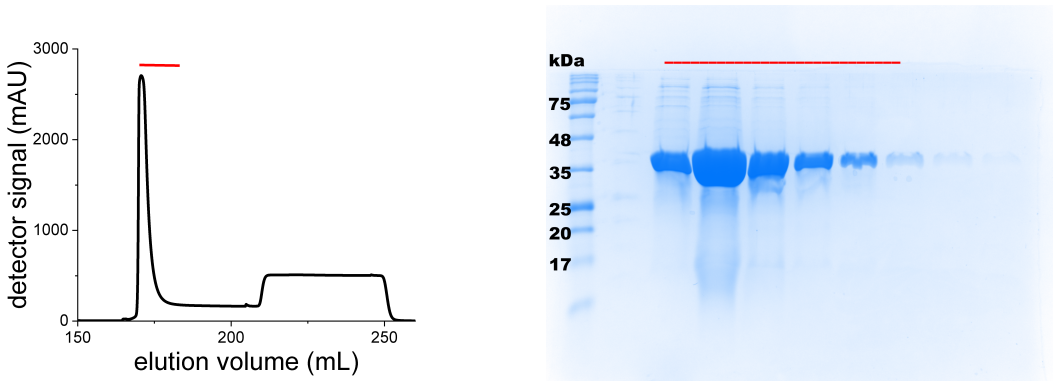

(a) (b)

Fig. 2.1: Representative result of a protein purification using an Äkta FPLC system. (a) Chromatogram of a Ni-NTA (nickel-nitrilotriacetic acid) purification of His-tagged biotin ligase and (b) displays the collected fractions on a SDS-PAGE. Fractions containing the target protein with the expected MW of approx. 37 kDa are indicated in red.

Tab. 2.11: His low buffer

Ingredient	Final concentration	Mass or Volume/1l
Tris-HCl pH 7.5	50mM	50ml (1M stock)
Imidazole	40mM	2.72g
NaCl	500mM	200ml (2.5M stock)

Tab. 2.12: His high buffer

Ingredient	Final concentration	Mass or Volume/1l
Tris-HCl pH 7.5	50mM	50ml (1M stock)
Imidazole	400mM	27.23g
NaCl	500mM	200ml (2.5M stock)

2.3.2 Culture and transfection of Sf21 cells

Gibco® Sf21 cells (#B82101, Thermo Scientific) originally came from the USDA Insect Pathology Laboratory, where they were obtained from the pupal ovarian tissue of the fall army worm, *Spodoptera frugiperda*. They are commonly used to isolate and propagate recombinant baculoviral stocks and for high levels of protein expression using the bac-

ulovirus expression system.
Sf21 cells were cultured in Grace's Insect Medium (#11605086, Thermo) supplemented with 10 % heat-inactivated FBS (#10270106, Thermo), 1 % pluronic® F-68 (#24040032, Thermo) and 1 µg/ml normocin (#ANTNR2, Invivogen). They were maintained in suspension cultures at 27°C, a shaking speed of 140 rpm and at a density of 1.0 x 10^6 cells/ml. For transfection, 0.4 x 10^6 cells/ml were plated into 6-well plates. After 15 min at RT cells were settled and media in wells was exchanged for plating medium (15 % Grace's Insect Medium without antibiotics in unsupplemented Grace's medium (#11595030, Thermo). 100 µl of unsupplemented medium with 8 µl of Cellfectin ® II reagent (#10362100, Thermo) was mixed with 100 µl of unsupplemented medium and 12 µl of bacmid. This mix was incubated for 30 min at RT. Cellfectin is a cationic-lipid reagent that spontaneously forms lipid-DNA compounds that fuse with the plasma membrane. This leads to the uptake and expression of the DNA in these cells. After 30 min the DNA-cellfectin mix was added drop by drop to the Sf21 cells and after 3-5 h incubation at 27°C, the media was replaced against Grace's Insect Medium supplemented with FBS, pluronic and normocin. Plates were incubated in a humid atmosphere at 27°C for 6-9 days. Holes in the cell layer, big and dead cells were signs for a successful virus infection. Viruses (P1 stock) were harvested by centrifugation at 1000 x g, 15 min. In the next step, the virus titer was increased to P3 by subsequent virus amplification in increasing culture volumes. 0.8 x 10^6 cells/ml in 25 ml or 250 ml were infected with 250 µl or 2.5 ml of the previous virus stock, respectively, and grown at 27°C in the dark, 140 rpm. The incubation duration was dependent on the construct. The cell viability should be lower as 50 %, calculated for a 1:1 cell suspension:Trypan Blue (#1450013, Bio-Rad) mix in the TC20™Automated Cell Counter (Bio-Rad). Viruses were harvested by centrifugation at 3450 x g, 15 min, and stored at 4°C.

2.3.3 Myosin

2.3.3.1 Expression and purification of human myosin IXa constructs

Tab. 2.13: Expression conditions of myosin IXa constructs. bv - baculovirus

Construct	cell density (cells/ml)	myosin bv (ml)	CaMX bv (ml)
IXa MD	0.8 - 1.2 x 10^6	40	40
IXa S1	0.8 - 1.2 x 10^6	20	40
IXa MD skeletal	0.8 x 10^6	20-40	/

500 ml cultures of Sf21 cells at a density of 0.8 - 1.2 x 10^6 cells/ml were co-infected with the corresponding amounts of myosin and calmodulin baculovirus (see table 2.13). Proteins were expressed for 72 h at 27°C and a shaking speed of 140 rpm. Pellets were harvested by centrifugation at 3450 x g, 15 min, 4°C and stored at -80°C.
For purification of myosin IXa MD and S1, pellets from 2 l Sf21 were thawed in a water bath at 25°C for 10 min (MD skeletal: 5 l). Pellets were resuspended on ice in 40 ml of myosin extraction buffer (MEB). Myosin IX constructs were biotinylated by adding 2 mM ATP, 4 mM biotin (#B4501, SigmaAldrich) and 1 µM bacterially expressed BirA. Additionally the cell slurry of MD and S1 myosin IX constructs were enriched with 70 nmol of Xenopus calmodulin (CaMX). Cells were sonicated for 5 min with 1 s on/off bursts (40 % power; Bandelin HD 2070 sonicator). This was repeated three times with few minutes breaks in between. The cell slurry was rotated for 1 h at 4°C. Cell lysate was centrifuged for 20 min at 4°C and 20 krpm (Beckman Coulter JA25.50 rotor).

Tab. 2.14: Detailed informations of myosin IXa constructs

Construct	Basepairs	Amino acids	MW (kDa)	ε ($M^{-1}cm^{-1}$)
IXa MD	2715	900	105	80000
IXa S1	3135	1042	135	117000
IXa MD skeletal	2306	737	85	78000

The supernatant was mixed with 0.9 ml of Anti-FLAG® M2 Affinity Gel (#A2220, Sigma Aldrich), which was prepared according manufacturer's instructions. This mix was rotated for 45-60 min at 4°C. The affinity gel with bound protein was collected by low speed centrifugation for 6 min at 1600 rpm and 4°C (Thermo Scientific 75005703 rotor). In the

next step, the resin was resuspended in 10 ml MEB and filled into a disposable 10 ml Poly-Prep® Chromatography column (Bio-Rad). The affinity gel with bound protein was washed two times with 10 ml MEB and twice with 10 ml HMM buffer containing 100 mM NaCl. Elution of myosin IXa protein was performed with 4 ml of 0.1 mg/ml FLAG® peptide (#F3290, Sigma Aldrich) in 100 mM NaCl HMM buffer. This elution was applied directly onto 0.2 ml of a Q Sepharose Fast Flow (#17-0510-10, GE Healthcare), which was prepared following manufacturer's guidelines. Protein was eluted in 0.2 ml fractions of 250 mM and 500 mM NaCl HMM buffer (each 4 fractions). A SDS-PAGE confirmed protein purity, yield and coelution of calmodulin. Proteins were snap-frozen in liquid N_2 with 2 % sucrose and stored at -80°C. Initially, protein drops were frozen in liquid N_2 without additives and stored at -80°C. The protein quality after freezing was dependent on the preparation. For electron microscopy experiments samples were used fresh within few days.

Tab. 2.15: Myosin IX extraction buffer (2x concentrated)

Ingredient	Final concentration	Mass or Volume/1l
MOPS pH 7.2-7.4	20mM	4.2g or 20ml (1M stock)
NaCl	1M	400ml (2.5M stock)
$MgCl_2$	10mM	10ml (1M stock)
EGTA	2mM	4ml (0.5M stock)

Additional Ingredients in 1x concentrated buffer

Ingredient	Final concentration	Mass or Volume/200ml
ATP	3mM	6ml (100mM stock)
DTT	1mM	200µl (1M stock)
Protease Inhibitor		1 tablet

Tab. 2.16: Myosin HMM buffer (2x concentrated)

Ingredient	Final concentration	Mass or Volume/1l
MOPS pH 7.2-7.4	20mM	4.2g or 20ml (1M stock)
EGTA	0.2mM	4ml (0.5M stock)

Additional Ingredients in 1x concentrated buffer

Ingredient	Final concentration	Mass or Volume/200ml
NaCl	100mM/250mM/500mM	2ml/5ml/10ml (2.5M-Stock)
DTT	1mM	50µl (1M stock)

2.3.3.2 Expression and purification of human non-muscle myosin IIb constructs

500 ml cultures of Sf21 cells at a density of 0.8 × 10^6 cells/ml were co-infected with 40 ml myosin IIb, 20 ml RLC and 10 ml ELC baculovirus and incubated at 27°C, 140 rpm (shaking speed) until the viability of the cells was lower than 60 % (usually after 3-4 days). Pellets were harvested by centrifugation at 3450 x g, 15 min, 4°C and stored at -80°C.

For protein purification pellets from 1000 ml Sf21 cells were thawed in a water bath at 25°C for 10 min. Pellets were resuspended on ice in 40 ml of a modified myosin extraction buffer (800 mM KCl instead of NaCl, no EGTA) and sonicated for 5 min with 1 s on/off bursts at 60 % power (Bandelin HD 2070 sonicator). Before sonication bacterially expressed ELC and RLC (each 100 nmol) was added (see section 2.3.1). The cell lysate was then centrifuged at 20000 rpm for 20 min, 4°C (Beckman Coulter JA25.50 rotor). The FLAG-tagged myosin IIb was then purified in the same manner as described above for myosin IXa constructs, except that the FLAG resin was washed twice with the modified myosin extraction buffer containing 3 mM ATP and twice with buffer without ATP. Elution of bound protein was performed in 2x 0.5 ml and 2x 1.5 ml fractions in the modified myosin extraction buffer with 0.1 mg/ml FLAG® peptide. Protein purity and coelution of the light chains were validated by SDS-PAGE. It is important to note that the presence of RLC and ELC was best visualized using the commercial precast gradient 4-12 % Bis-Tris Plus gels (#NW04120BOX, Thermo) or 8 % Bis-Tris Plus gels (#NW00080BOX, Thermo). Proteins were shock-frozen in liquid N_2 and stored with 15 % glycerol at -80°C.

2.3.3.3 Phosphorylation of human non-muscle myosin IIb

Before experiments, frozen non-muscle myosin IIb stocks were thawed and phosphorylated using 20 µg/ml myosin light chain kinase (MLCK, #M9197, Sigma) in a solution containing 1 mM ATP, 5 mM $MgCl_2$, 0.2 mM $CaCl_2$ and 0.5 µM calmodulin. Final myosin IIb concentration was 0.25 mg/ml. After 1 h incubation at 4°C, 200 mM KCl was added to increase the ionic strength to prevent filament formation.

2.3.3.4 Muscle myosin II HMM preparation

Tab. 2.17: Low salt buffer

Ingredient	Final concentration	Mass or Volume/1l
K-Phosphate buffer pH 6.5	20mM	20ml (1M stock)
KCl	40mM	13.3ml (3M stock)
$MgCl_2$	2mM	2ml (1M stock)
DTT	2mM	2ml (1M stock)

Myosin II was prepared by the method of Margossian and Lowey (1982) from a New Zealand white rabbit and stored in 50 % (v/v) glycerol at -20°C (concentration approx. 10 mg/ml).
5 ml of myosin II glycerol-stock solution was mixed with 40 ml of ice cold H_2O_{dd} in a centrifuge tube. This mix was centrifuged for 15 min at 20k rpm and 4°C (Beckman Coulter JA25.50 rotor). The pellet was resuspended in 5 ml 2x high salt buffer and 50 µl of 5 mg/ml chymotrypsin (#C3142, Sigma) were added and the suspension was rigorously vortexed. After precisely 10 min at RT, the proteolysis was terminated by mixing with 50 µl of 10 mg/ml Bowman-Birk-Inhibitor (#T9777, Sigma). Good timing is essential, because too short incubation leads to more uncut myosin II and a too long incubation leads to chymotrypsin splitting the HMM further into S1 and S2 fragments. After an overnight dialysis (Slide-A-Lyzer MWCO 10 000) in 3 l of low salt buffer, the solution was then centrifuged (20k rpm, 30 min, 4°C; Beckman Coulter JA25.50 rotor) to remove all undigested Myosin and LMM. The low salt buffer leads to sticking of the LMM tails to each other, they became heavier and can be separated from HMM by centrifugation. The supernatant was taken and concentration was measured using Bradford and absorbance at 280 nm. For storage 30 % sucrose was added, aliquots were snap frozen in liquid nitrogen and stored at -80°C.

Tab. 2.18: High salt buffer

Ingredient	Final concentration	Mass or Volume/0.1l
K-Phosphate buffer pH 6.5	40mM	4ml (1M stock)
KCl	1M	33ml (3M stock)
$MgCl_2$	4mM	0.4ml (1M stock)
DTT	2mM	0.2ml (1M stock)

2.3.3.5 Preparation of NEM myosin

N-ethylmaleimide (NEM) is a compound to covalently modify cysteine residues in proteins. NEM modified myosin II remains tightly bound to actin in the presence of MgATP (Meeusen and Cande, 1979).
To prepare NEM myosin two times 100 µl myosin II stored in 50 % glycerol (see section 2.3.3.4) were filled into two 2 ml Eppendorf tubes. The tubes were filled up with H_2O_{dd} and centrifuged 13 krpm for 6 minutes at room temperature (Beckman Coulter JA25.50 rotor). The pellet was resuspended in 200 µl high salt buffer and the contents of the two tubes were combined. NEM solution was prepared by dissolving 3 mg NEM (#E1271, Sigma) into 5 µl ethanol and adding 235 µl water. 5.2 µl of NEM solution was added to 250 µl myosin, mixed well and incubated for 75 minutes at RT. The reaction was stopped by adding DTT solution (20 µl 1 M DTT in 1.5 ml water). NEM myosin was then centrifuged at 13 krpm for 6 min (RT). The pellet was resuspended thoroughly in 200 µl 2x high salt buffer and centrifuged again at 13 krpm for 6 min (Beckman Coulter JA25.50 rotor). The NEM modified myosin in the supernatant was placed into a clean tube, stored on ice and used within few days.

2.3.4 Actin

2.3.4.1 Actin purification and polymerization

Actin containing acetone powder was prepared from rabbit skeletal muscle by the method of Pardee and Spudich (1982) and stored at -20°C. 6 g of the powder was mixed with 120 ml ACEX buffer for 30 min, 4°C. The solution was filtered through four layers of cheesecloth and the resulting pellet was mixed with a further 80 ml of ACEX for 10 min. The slurry was filtered a second time and the supernatants were mixed and spun at 20000 rpm in the JA25.50 rotor (Beckman Coulter) for 15 min, 4°C.

Tab. 2.19: ACEX buffer

Ingredient	Final concentration	Mass or Volume/2.5l
Tris-HCl pH 8.0	2mM	2.5ml (2M stock)
ATP	0.2mM	5ml (0.1M stock)
$CaCl_2$	0.2mM	0.5ml (1M stock)
DTT	1mM	2.5ml (1M stock)

The soluble part was brought to a final concentration of 5 mM Tris-HCl pH 8.0, 2 mM $MgCl_2$, 50 mM KCl and 1 mM ATP whilst continuously stirring the solution for 2 h, 4°C. Tropomyosin was removed by adjusting the solution to 800 mM KCl with pH 8.3-8.5 and centrifuged at 70000 rpm, 40 min, 4°C (Ti70 rotor, Beckman Coulter). ACEX buffer was used to soften the pellet for 10 min. The pellet was then homogenized on ice for a further 30 min and the resulting solution was dialysed overnight in ACEX buffer. The next day, the solution was centrifuged at 13000 rpm, 15 min, 4°C (JA25.50 rotor). The purified actin (57 µM) was aliquoted, snap frozen in liquid nitrogen and stored at -80°C. A representative Coomassie Brilliant Blue stained SDS PAGE gel from actin purification is depicted in Fig. 2.2.
Actin polymerization was initiated by adding 1x AB buffer and 0.2 mM ATP. The resulting F-actin was stabilized for at least 1 h with Alexa Fluor 488® phalloidin (#A12379, Thermo), Rhodamine phalloidin (#R415, Thermo) or unlabelled phalloidin (#P3457, Thermo) at a 1:1 molar ratio and stored in the dark at 4°C.
Phalloidin is a small bicyclic peptide that selectively binds to F-actin and inhibits its turnover. Phalloidin is toxic and is originally produced by the fungus *Amanita phalloides*. It has first been isolated at the chemical department of the LMU by Feodor Lynen and Ulrich Wieland in 1938 (Lynen and Wieland, 1938).

2.3.4.2 Preparation of biotinylated actin filaments

20 µg biotinylated G-actin (#AB07, Cytoskeleton) were dissolved in water as described in manufacturer's instructions. Purified G-actin (see section 2.3.4.1, 57 µM) was added at a 1:1 molar ratio and polymerization was started by adding 1x AB buffer and 2 mM ATP. Polymerized F-actin was diluted to 5 µM and labelled for at least 1 h with rhodamine phalloidin in a 1:2.6 molar ratio and stored in the dark at 4°C.

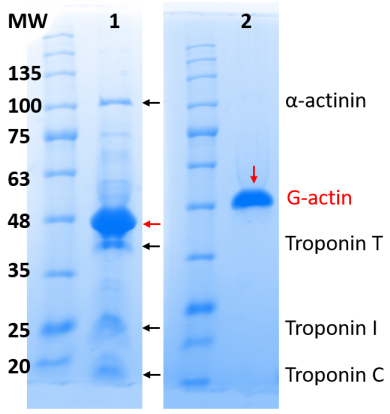

Fig. 2.2: A 7.5 % SDS-PAGE with samples from actin purification.
Lane 1: G-actin (red arrow) and regulatory proteins (black arrows) before high salt cut. G-actin has an expected MW of approx. 42 kDa. Lane 2: Purified G-actin after dialysis. MW - molecular weight markers (kDa).

2.3.4.3 Preparation of polarity-labelled actin filaments

Tab. 2.20: Reaction buffer

Ingredient	Final concentration	Mass or Volume/1l
Tris-HCl pH 7.5	50mM	50ml (1M stock)
$CaCl_2$	0.1mM	0.1 ml (1M stock)
$MgCl_2$	0.1mM	0.2 ml (0.5M stock)
NaCl	30mM	12 ml (2.5M stock)
DTT	1mM	1 ml (1M stock)

Dual-fluorescence-labelled actin filaments were prepared according to the protocol of Herm-Götz et al. (2002) with small modifications. Gelsolin (#HPG6, Cytoskeleton) was dissolved in reaction buffer (RB) as described in manufacturer's instructions. 25 µl purified G-actin (see section 2.3.4.1) was mixed with 0.5 µl gelsolin at a molar ratio of 50:1 and incubated on ice for 10-15 min. The addition of 100 mM KCl (RT) started actin polymerization. The nascent F-actin seeds were stabilized with equimolar rhodamine phalloidin for approx. 1-2 h. Elongation of these seeds is limited to the minus end as their plus ends are blocked by gelsolin. The rhodamine labelled F-actin seeds were diluted to 1 µM in RB buffer. For elongation, a 2-fold excess of unlabelled G-actin was added and polymerization was started with 100 mM KCl. Finallly, the elongated part of the

filaments was stabilized with Alexa Fluor 488 phalloidin for 1 h. This method resulted in rhodamine labelled plus ends and Alexa 488 labelled minus ends. The polarity-labelled actin filaments were stored on ice and used within few days.
They were used *in vitro* motility experiments with myosin IXa constructs. Frames were recorded every 3 s for 20 min in TIRF using the Eclipse Ti microscope (Nikon) with 300 ms exposure time for Rhodamine and 80 ms for Alexa 488.

2.4 Functional *in vitro* assays

2.4.1 *In vitro* motility assay

Tab. 2.21: AB- buffer 10x concentrated (1x stock: I = 41 mM)

Ingredient	Final concentration	Mass or Volume/0.1l
Imidazole pH 7.4	250mM	1.7g
KCl	250mM	8.3ml (3M stock)
$MgCl_2$	40mM	8.0ml (0.5M stock)
EGTA	10mM	2.0ml (0.5M stock)

Tab. 2.22: AB+ buffer 10x concentrated, 20 mM ATP (1x stock: I = 59 mM)

Ingredient	Final concentration	Mass or Volume/0.1l
Imidazole pH 7.4	250mM	1.7g
KCl	250mM	8.3ml (3M stock)
$MgCl_2$	40mM	8.0ml (0.5M stock)
EGTA	10mM	2.0ml (0.5M stock)
ATP	20mM	1.1g

For the *in vitro* motility assay flow chambers were fabricated (see Fig. 2.3). Two stretches of double-sided tape, separated by approx. 5 mm, were stuck to a 76x26 mm Superfrost microscope glass slide (Thermo Scientific, Menzel). A 24x40 mm coverslip (Brand or Marienfeld) was glued on top, creating a flow cell with approx. 10 µl volume.
For the assay of myosin IXa constructs piranha-cleaned glass coverslips were used, which

were pretreated with a 5:1:1 ratio by volume of H_2O:H_2O_2:NH_4OH for 2-3 h at approx. 70°C. In control experiments with rabbit skeletal HMM glass coverslips were coated with a thin layer of 1.5 % nitrocellulose (#R1271, Plano GmbH) in amyl acetate.

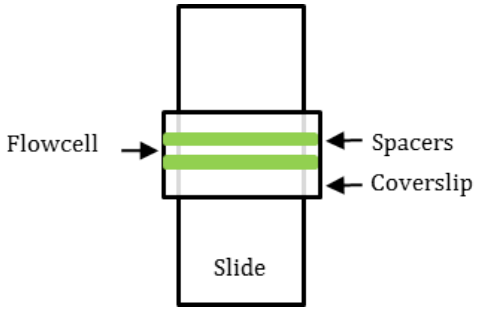

Fig. 2.3: Schematic representation of the assay flow chamber.

In order to accomplish movement of actin filaments by myosin IXa constructs, a specific surface immobilization of the proteins was necessary. 1 mg/ml biotinylated-BSA (#A8549, Sigma) was bound to the coverslip surface for 3 min. Unbound biotinylated-BSA was removed with assay buffer (AB-,Kron and Spudich (1986)) and the flow cell was incubated with 1 mg/ml streptavidin (#S4762, Sigma) for 3 min. Unbound streptavidin was washed out with AB- buffer and 1 -2 µM of biotinylated myosin IXa MD or 0.2 µM myosin IXa MD skeletal were added for 4 min. After wash out of unbound myosin IXa 20 nM Alexa488 or TRITC labelled F-actin was added to the Flow cell, incubated for 3 min and unbound actin was removed by washing with AB-.

Actin filament motility was initiated by addition of an AB+ oxygen scavenger system to reduce photobleaching (with 2 mM ATP, 10 mM DTT, 0.01 mg/ml catalase, 0.05 mg/ml glucose oxidase, 1.5 mg/ml glucose). In experiments with myosin IXa constructs this scavenger contained a total KCl concentration of 100 mM. For myosin IXa skeletal motility the AB+ oxygen scavenger contained additional 10 % (v/v) methylcellulose and short fluorescently labelled actin filaments (for continuous binding and unbinding). Assay buffers were degassed with a vacuum pump before the experiment and stored in disposable hypodermic syringes containing narrow-bore needles to minimize oxygen diffusion into the solution (Veigel et al., 1998).

Motility experiments with myosin IXa MD and IXa skeletal were also performed at > 2 mM ATP. A modified 10x AB+ buffer for 5 and 10 mM ATP was produced (see tables 2.23 and 2.24) to generate buffers with higher $MgCl_2$ concentrations. The $MgCl_2$:ATP

ratio was adjusted to 2:1. In the 10x AB+ buffer with 10 mM ATP no KCl was added, so that the ionic strength did not increase too much (compared to other AB+ buffers).

Tab. 2.23: AB+ buffer 10x concentrated, 50 mM ATP (1x stock: I = 104 mM)

Ingredient	Final concentration	Mass or Volume/0.1l
Imidazole pH 7.4	250mM	1.7g
KCl	250mM	8.3ml (3M stock)
$MgCl_2$	100mM	20.0ml (0.5M stock)
EGTA	10mM	2.0ml (0.5M stock)
ATP	50mM	2.76g

Tab. 2.24: AB+ buffer 10x concentrated, 100 mM ATP (1x stock: I = 154 mM)

Ingredient	Final concentration	Mass or Volume/0.1l
Imidazole pH 7.4	250mM	1.7g
KCl	0mM	0 ml
$MgCl_2$	200mM	40.0ml (0.5M stock)
EGTA	10mM	2.0ml (0.5M stock)
ATP	100mM	5.51g

Frames were recorded every 3 s for 10-20 min in TIRF with an Eclipse Ti microscope (Nikon) equipped with a 60x Apo TIRF objective (NA of 1.49, Nikon) and an Andor CCD camera. The assay was carried out at 23°C. The Fiji plugin MTrackJ was used to manually track individual filaments over time (Meijering et al., 2012). Recordings were analysed using 3-10 frame averaging (dependent on myosin and ATP concentration) and velocities were determined by following moving actin filaments not less than seven consecutive frames.

2.4.2 Inverted *in vitro* motility assay

The principle of the inverted assay (also called landing assay) is very similar to the general *in vitro* motility assay. In the landing assay F-actin is immobilized on a coverslip surface

and fluorescently labelled myosin molecules are added into solution.
The coverslip surface was coated with 1.5 % nitrocellulose and covered with 10 µg/ml NEM modified myosin II (see section 2.3.3.5) for 3 min. Unbound NEM myosin was washed out with assay buffer. Free binding places were blocked with 50 mg/ml BSA for 3 min. After removing of excess BSA with assay buffer 50 nM Alexa 488 labelled F-actin was injected into the flow cell and incubated for additional 3 min. Unbound actin was removed by thorough washing with assay buffer. 50-100 nM IXa MD labelled with a Cy3-FLAG antibody (#A9594, Sigma) or fluorescently labelled myosin V in an AB+ oxygen scavenger system supplemented with 2 mM ATP were introduced into the flow cell. Frames were collected every 3 s on a homemade two-colour TIRF setup on a Olympus IX70 microscope.
A dual band beam splitter allowed simultaneous TIRF excitation of Alexa 488 and Cy3. The emission signal of the dyes was first filtered by a dual band emission filter to block any remaining laser light. After spatial filtering of the image, a second beam splitter splitted the emission from the Alexa488- and Cy3-dye. Each dye was then imaged onto one half of the chip of an EM-CCD camera.

2.4.3 Bundling experiments on NEM myosin surface

10 µg/ml NEM modified myosin II was bound for 3 min to a glass coverslip coated with a thin layer of 1.5 % nitrocellulose in amyl acetate. Unbound NEM myosin was washed out of the flow chamber with assay buffer and 50 mg/ml BSA were injected to block free binding places. After 3 min the flow cell was washed with assay buffer. Myosin IXa MD or MD skeletal was mixed at a 1:1 molar ratio with Alexa 488 labelled actin in solution, incubated for a few minutes and introduced into the flow cell. After 3 min, unbound bundles were washed out with an AB- oxygen scavenger system supplemented with 100 mM KCl. Bundles were imaged in TIRF using Eclipse Ti microscope (Nikon).
In IXa MD labelling experiments, the myosin was incubated with an anti-FLAG antibody labelled with Cye3 (#A9594, Sigma) prior to bundle formation. In experiments with different ATP concentrations, the oxygen scavenger system was prepared with 100 or 250 µM ATP and 100 mM KCl.
ImageJ was used to automatically analyse the images (100 neighbouring fields; total area of 600 × 600 µm^2). A central region of interest (60 × 60 µm^2) was selected within the image to ensure a homogeneous fluorescence excitation. The remaining inhomogeneity was subtracted by dividing by a reference image of the laser-intensity distribution. The total length of actin bundles was calculated using the signal intensity of all pixels within the region of interest (Saczko-Brack et al., 2016).

2.4.4 Bundling experiments on biotin - streptavidin surface

To study the dissociation behaviour of bundles in the presence of ATP a modified bundling assay was developed. In this assay two species of actin filaments were generated. The first species was labelled with rhodamine and contained biotinylated actin monomers (see section 2.3.4.2), whereas the second species of F-actin was labelled with Alexa 488 and was made from non-biotinylated G-actin.
Flow cells were prepared according to the following procedure: A glass coverslip was covered with 1 mg/ml biotinylated-BSA for 3 min. Unbound biotinylated-BSA was removed with assay buffer with a total KCl concentration of 100 mM and incubated with 1 mg/ml of streptavidin for 3 min. Unbound streptavidin was washed out with AB- buffer. Rhodamine labelled biotinylated F-actin was mixed with Alexa 488 labelled non-biotinylated F-actin in a 1:100 molar ratio, incubated with myosin IXa MD in a 1:1 molar ratio and incubated for 20-60 s to ensure to have small bundles consisting of only two actin filaments. The bundles were introduced into the flow cell for 3 min and unbound bundles were removed with an oxygen scavenger system supplemented with 100 mM KCl. The flow cells were stuck to the stage of the microscope to ensure wobble-free frame recording during ATP addition. Frames were recorded every 0.5 s in TIRF using a Nikon Eclipse Ti microscope with 300 ms exposure time for rhodamine and 80 ms for Alexa 488. After 1-2 min recording without ATP, an oxygen scavenger system containing varying amounts of ATP and 100 mM KCl were injected carefully in the flow cell and frames were recorded for additional 30 min.
Images analysis was partly performed with an automated LabVIEW program written by Dr. Nikolas Hundt. In this program bundles were fitted to a 'worm-like' Gaussian function. Non fittable bundles were analysed with the image processing program Fiji.

2.5 Building an optical tweezers setup

In this section I describe the construction of an optical tweezers transducer based on a Leica DMi8 microscope. As seen in Fig. 2.4 the entire trapping setup was mounted on an air damped 1.2 m x 1.2 m vibration isolated workstation to minimize vibrations and facilitate mounting of optical components (#M-SG-44-4, Newport). To reduce vibrations even further, most electrical components with vents were enclosed in a soundproof server rack (#AW-27-C66-DI, 19zoll-tec). The trapping room had a lamella ventilation system with a precise temperature control of 23 ± 0.1°C.
A piezoelectric stage was mounted on a homemade adapter on the microscope stage to permit controlled movements of the sample during the experiments and in order to calibrate the system (stage: #P-541.2DD; controller #E-727.3CDA, Physik Instrumente). The software to control the optical tweezers setup was written in LabView by Dipl.-Ing. Tuan Nam Le. For fast measurement control and data acquisition a multifunctional RIO-FPGA card was used (#PXIe-1073, National Instruments)

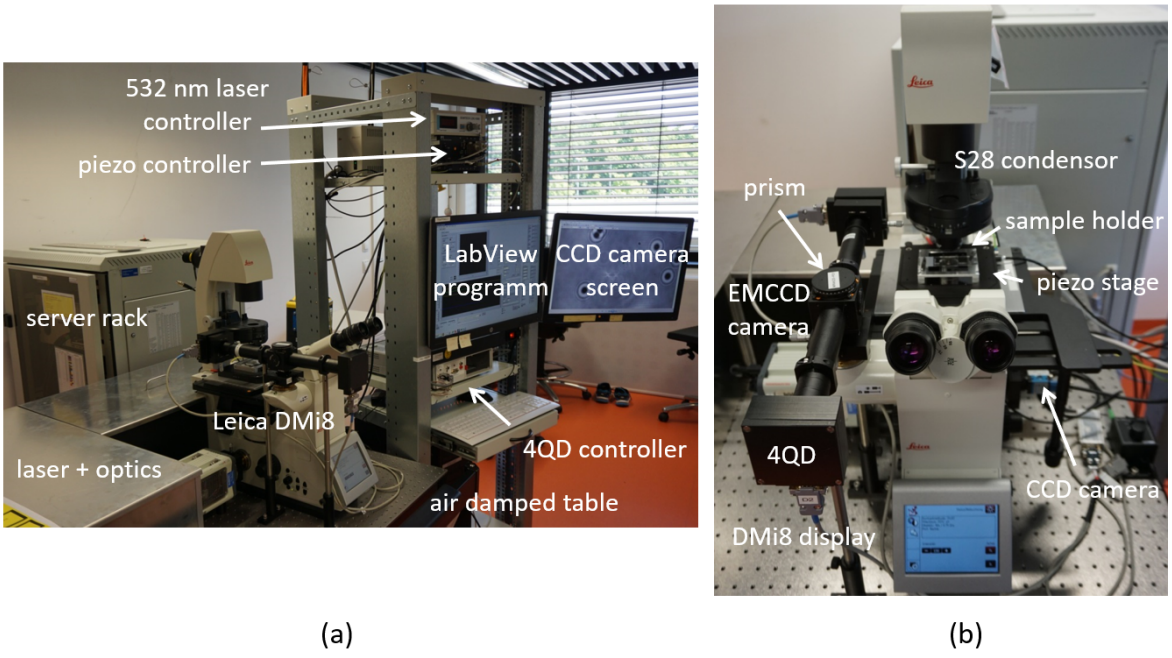

Fig. 2.4: Images of the trapping setup with the most essential parts highlighted. (a) General overview of the setup. The lasers (class 3B and 4) and optics are not visible because they are enclosed for safety reasons. (b) A more detailed image of the modified Leica DMi8 microscope.

2.5.1 Creating a single laser trap

At its most basic level, an optical trap consists of an IR laser that is strongly focused by a lens with a short focal length, usually a high numerical aperture (NA) microscope objective. A 100x oil immersion HC PL APO objective (Leica) with a NA of 1.40 was used in this study. Spherical aberration is the most important lens defect that impairs trapping efficiency and the more expensive lenses may offer important advantages in terms of spherical aberration. The objective was mounted on an extension (#PLE351, Thorlabs) to reach through the piezo stage to the homemade sample holder.
A beam expander was placed before the objective lens, to slightly overfill the approx. 7 mm diameter back aperture. Slightly overfilling the back aperture is preferable to underfilling it. Off-axis rays mainly contribute to the axial gradient force, while the central rays are mostly responsible for the scattering force (see chapter 1.21). Overfilling the objectives back aperture can increase the ratio of gradient to scattering force, which results in a higher trapping efficiency (Rice et al., 2003; Neuman and Block, 2004).
The IR laser is a critical part of the optical trap (class 4 laser; laser head: #BL-106C, power supply: #J20I-8S-12K, Spectra Physics). The IR laser used here was a diode pumped, solid state, continuous wave (cw), single Gaussian transverse emission mode (TEM 0,0) near infra-red laser. The laser material consisted of Nd:YAG and emitted laser light at 1064 nm with over 4 watts of power. The laser beam was vertically polarized and had a diameter of 420 µm on the laser head. To overfill the 7 mm back aperture of the objective, an at least approx. 18 times beam expansion needs to be achieved. The simplest beam expander to build is a Keplerian telescope and it consists of two lenses. In the Keplerian model the focal lengths of both lenses are positive and their addition results in a focal point in the gap between the lenses at the point where the two focal lengths meet (see Fig. 2.5).

The first step in building an optical trap is to create a single stable trap in the centre of the field of view (see Fig. 2.6). For beam adjustment two mirrors were placed before the beam expander and additional two mirrors were installed before the laser entered the infinity port on the back of the microscope. The height of the microscope port specifies the height of the beam path. All optical parts (laser head, mirrors, lens holders) were first adjusted to the same height and then the IR laser was centred using a NIR detector card and a fluorescent alignment disk. To check the laser alignment, it was useful to start without lenses. The IR laser beam needs to enter the objective lens in a parallel way. Once the laser enters the objective, the laser trap was apparent on the screen in a homogenous cloverleaf-like shape (because of glass reflections) and this shape should

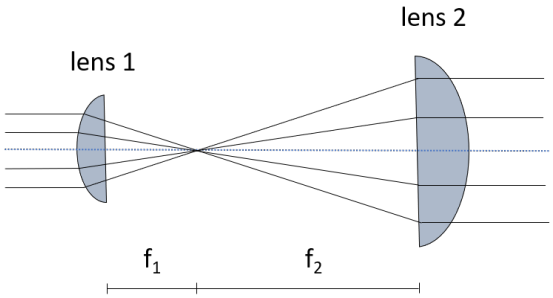

Fig. 2.5: The Kepler beam expander system. The beam expander is made up of two lenses with positive focal lengths that are separated by the sum of their focal lengths. The first lens focusses the beam, whereas the second lens is positioned behind the common focus point and collimates the divergent light again so that the input and the output beam are both parallel to the optical axis. This results in a collimated laser beam with increased diameter.

change in a concentric way when the focus is changed (see Fig. 2.9). The lenses can be mounted and adjusted in the next step so that the beam path goes straight through the lenses and hits them in the centre.

For safety reasons, a shutter was placed directly after the laser head and low laser power was used for laser alignment. Additionally an interlock was installed on the microscope light arm. Tilting this arm resulted in switching off the infrared laser.

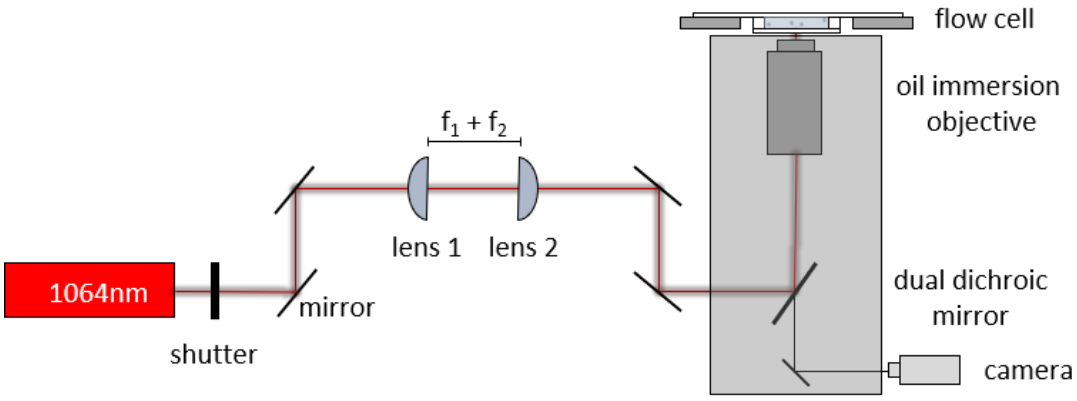

Fig. 2.6: The basic arrangement of lenses and mirrors which are necessary to create a single stable laser trap. Choosing lens 1 with f_1=500 mm and lens 2 with f_2=25.4 mm resulted in a beam expansion of around 20 times, which is sufficient to overfill the approx. 7 mm diameter back aperture of the objective. The grey box marks the optical components inside the microscope.

2.5.2 Creating multiple laser traps with acousto-optical deflectors

Two orthogonally aligned acousto-optic deflectors (AOD) were installed to create multiple traps from a single laser beam and to move the traps quickly (2-axis deflector: #AA.DTSXY-400-1064; electronic synthesizer: #DDSPA2X-D431b-34, Pegasus Optics).

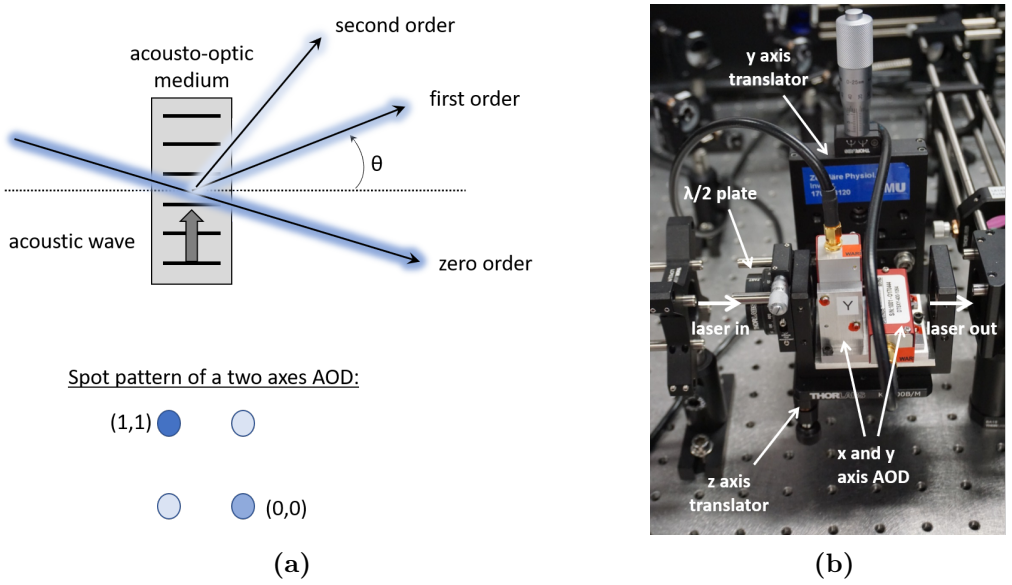

Fig. 2.7: Acousto-optical deflectors (AOD) are used to steer the optical trap. (a) Top: Operating principle of an AOD. Tilting the acousto-optic medium to the Bragg angle θ results that approx. 75 % of the incoming light gets reflected in the first-order deflection. Bottom: When RF power is applied on a two axes AOD, the laser gets diffracted as shown in the image. The efficiency of the diffracted order can be improved by performing slight rotations/translations along the x-axis and y-axis. Figure modified from Reddy and Saggau (2005). (b) A photograph of the two axes AODs mounted on the optical table. The AODs were mounted on x, y and z translators that allow fine adjustment of angle and translation with respect to the input laser beam (x translator is not visible).

In an AOD, a crystalline material is bound to a piezoelectric transducer, which transforms a high-frequency oscillating voltage in the megahertz range into an acoustic wave that propagates through the crystal. The acoustic wave has the same frequency as the applied voltage and has a velocity of 600 m/s. During its travels through the crystal the acoustic wave generates a standing wave pattern of compressions and expansions parallel to the transducer. This density pattern results in periodic changes in the index of refraction of the crystal that periodically shifts the phase of the incident light. The input beam is deflected by diffraction at this phase grating. If the frequency of the applied voltage is

changed, the acoustic wave, the periodicity of the grating and ultimately the deflection angle of the light also changes (Visscher et al., 1996; Spudich et al., 2011).
When the AOD crystal is tilted to the Bragg angle, approx. 75 % of the incoming light is reflected in the so-called first-order deflection, while some light remains undeflected and a small amount of the light is deflected at higher orders (see Fig. 2.7). This means that four zero- and first-order beams are emitted from a set of two orthogonally aligned (X and Y) AODs: one undeflected (0,0), one is only deflected in X direction, one is only deflected in Y direction, and one (maximum about 55 % of the total incident light) that is deflected in both X and Y (1,1). The latter is the selected trapping beam (Rice et al., 2003; Spudich et al., 2011). The diffraction angle is controllable over a range of about 30 mRadians and can be changed within approx. 2 µs. This means multiple optical tweezers can be produced by rapidly scanning a single laser beam between two or more trap positions (time-sharing). This time-sharing approach is based on the fact that viscous drag on a trapped object is high enough that the object remains 'fixed' in its position while the laser beam is in a different position (Molloy et al., 1995; Visscher et al., 1996; Larijani et al., 2006).

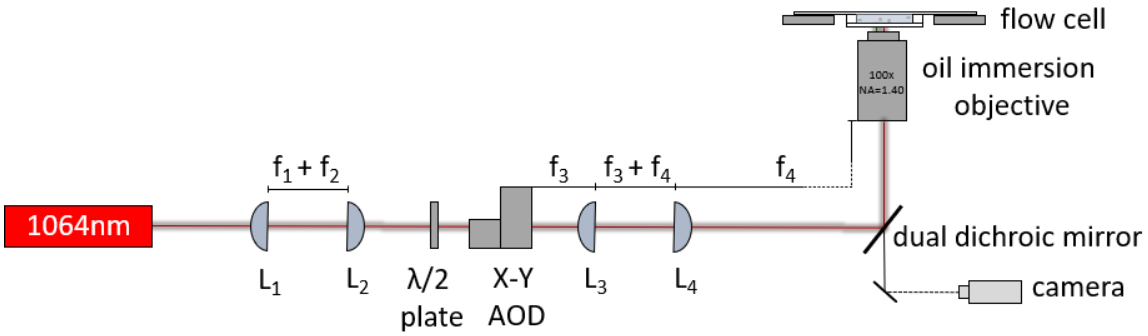

Fig. 2.8: The modified light path after AOD installation. To increase the beam diameter in front of the AOD two lenses with f_1=25.4 mm and f_2=100 mm were installed. Lens 3 and 4 with f_3=150 mm and f_4=500 mm were inserted after the AOD to overfill the back aperture of the objective. These plano-convex lenses were fabricated from N-BK7 glass and have an anti-reflective coating for the range from 1050 nm to 1700 nm.

As shown in Fig. 2.7 the AODs were fixed to x, y and z translators that allow fine adjustment of angle and translation with respect to the input laser beam. According to manufacturer's instructions the beam diameter at the AOD entry side needed to be around 4 mm. The optical light path was therefore modified, so that a 4x beam expander was placed before the AOD (see Fig. 2.8). Additionally, the input laser polarization on the AOD needed to be linear perpendicular. Therefore, a lambda half plate was placed

in front of the AOD to shift laser polarization of 90°.
The AODs were computer controlled on my setup, so that movement of the optical traps was possible with the computer mouse and a variety of pre-programmed waveforms were applicable.

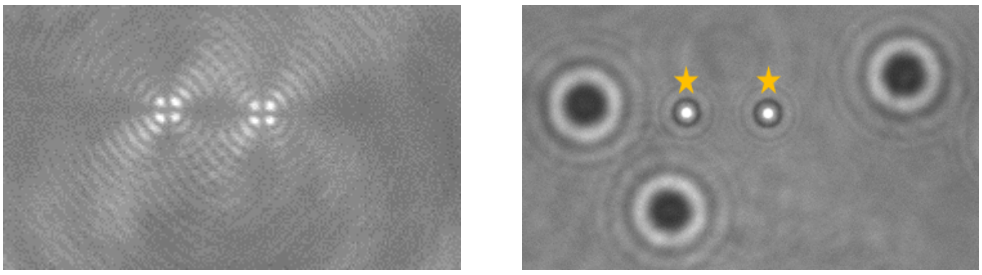

(a) **(b)**

Fig. 2.9: Optical tweezers are apparent on the screen due to glass reflections. (a) The characteristic cloverleaf-like shape of the optical tweezers change its shape in a concentric way when focus is varied. (b) Two 1.1 µm latex beads trapped with optical tweezers (yellow stars; their shape is not visible due to focus change) and three 1.86 µm beads attached to the glass surface.

2.5.3 Light path

The advantage of building an optical tweezers setup around a microscope is that camera ports, objective lens focusing, filter holders, mechanical stage and condenser illumination are all accurately aligned and ergonomically designed.

A dual dichroic mirror (#zt532-543/1064rpc, AHF; size 25.5 x 36.0 x 3.0 mm) that reflects 1064 nm and 532 nm but allows red light to pass through was mounted in the microscope filter block. Samples were visualized using a CCD camera (#DMK33UX290, Imaging Source). Video images from the 1/2.8 inch format CCD camera were captured at 1920 x 1080 pixel resolution, giving 1 pixel corresponded to 29 nm. The CCD camera was mounted on a xy translation stage on a homemade inside blackened adapter and was protected by 1064 nm scattered light by insertion of a shortpass filter (#FES0700, Thorlabs). A built-in optical switch can be used to direct the light path for data acquisition either to the CCD camera or to the four quadrant detectors (4QD).

A high brightness 400 mW LED light source (#M660L4-C2, Thorlabs) was used to illuminate the sample with a wavelength of 660 nm. For contrast enhancement the built-in condenser of the microscope was exchanged against a Leica condenser with a shorter free working distance (28 mm) and a numerical aperture of 0.55.

The image of the bead passes through the objective and the dichroic mirror to the homemade detector. The detector was built on the top port of the microscope through an selfmade adapter where the inner surface was blackened. The detector light path outside the microscope (see Fig. 2.10 (b)) was completely enclosed with Thorlabs equipment. A shortpass filter blocked out any scattered IR laser light (#FESH0800, Thorlabs). A silver coated knife-edge right-angle prism (#MRAK25-P01, Thorlabs) mounted on a rotational platform (#B3CR, Thorlabs) split the detector light path into two parts. As a result, both beads in the three-bead geometry could be observed simultaneously during single-molecule experiments. The image of the bead was projected as a dark silhouette on the 4QD. For maximum resolution of the bead position, the diameter of this silhouette should be around half the size of the 4QD sensor (1130 µm). As 1 μm beads were used in our experiments, and the objective has a magnification of 100x an additional 5x magnification needs to be achieved. With an 1" lens and the magnification $M = (\frac{b}{g}) = 5$ the image distance b can be expressed as $b = 5g$ whereby g is the object distance. Following the lens equation

$$\frac{1}{b} + \frac{1}{g} = \frac{1}{f}$$

with f being focal length, the object distance can be calculated as $g = \frac{6}{5} = 1.2''$.
Each of the 4QD was mounted on a xy translation stage to enable fine positioning of the detector so that the image of the bead was always in the centre of the 4QD to have highest positional sensitivity.

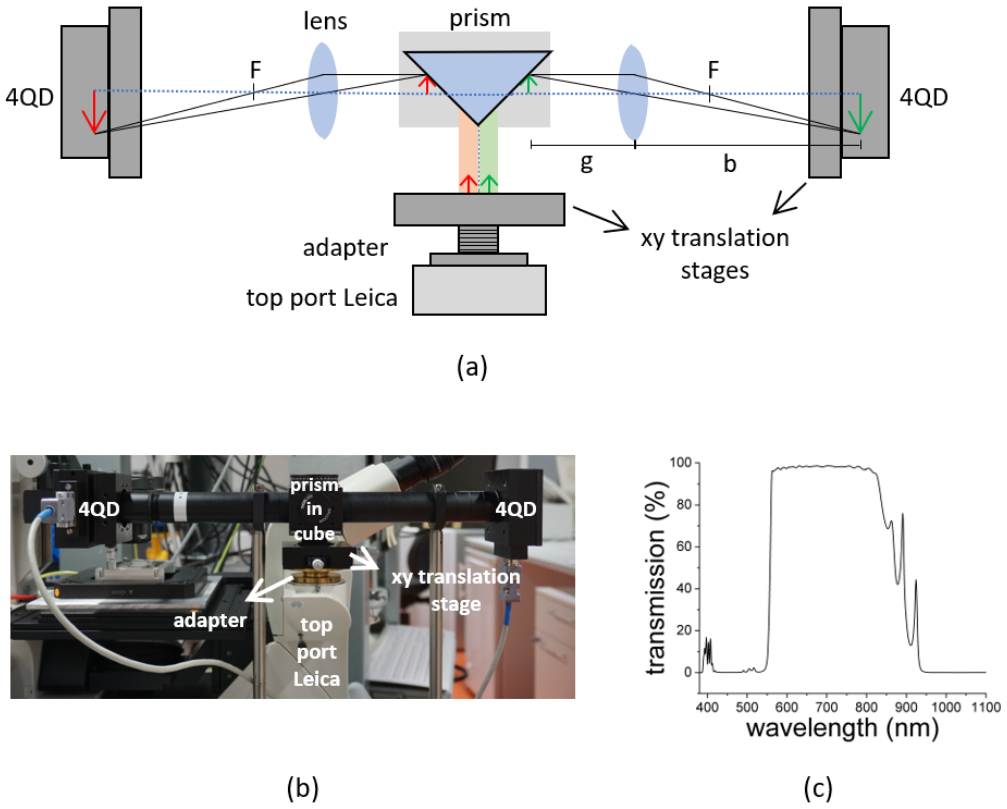

Fig. 2.10: (a) Schematic representation of the detector light path. The silver coated prism splits the light path into two parts permitting both beads (represented as red and green arrows) in the three-bead geometry to be monitored. A lens with f = 1" was inserted into the path to achieve an 5x magnification with g = 1.2" and b = 6". XY translators allowed fine positioning of the quadrant diode so the image of the bead was always in the centre of the 4QD. (b) Image of the homemade detector mounted on the top port of the Leica microscope. (c) Transmission spectra of the dual dichroic mirror mounted in the microscope filter block. The mirror reflects 532 and 1064 nm laser light but has a high transmission for 660 nm red light (AHF, 2021).

2.5.4 Total internal reflection fluorescence microscopy

The phenomenon of total internal reflection (TIR) has been first described by Ambrose (1956) as a surface contact microscopic technique to study cell movements. It is based on the fact that light refracts when it hits the interface between two media with different indices of refraction n (see Fig. 2.11). A collimated light beam that propagates through a medium and reaches such an interface is either refracted or reflected at the interface. Refraction or reflection depends on the angle of incidence and the differences in the refractive index of the two media. For TIR, the medium which the propagating light

encounters, needs to have a lower refractive index (Axelrod, 1981). Snell's Law is valid:

$$n(1) \times \sin\theta(1) = n(2) \times \sin\theta(2)$$

where n(1) is the higher refractive index and n(2) is the lower refractive index. $\theta(1)$ is the angle of the incident ray relative to the normal to the interface and $\theta(2)$ represents the refracted ray angle within the lower index medium. If light hits the interface of the two materials at a large angle, the so-called critical angle θ(c), its direction of refraction becomes parallel to the interface (90° to the normal). At larger angles the light is completely reflected back into the first medium, but creates an evanescent field close to the interface in the lower-index medium. This electromagnetic field decays exponentially in intensity with distance from the interface. The fluorophore excitation is therefore limited to an area that is less than 100 nanometers thick (compared to an optical section thickness of about 1 µm in confocal microscopy). Since only fluorophores are excited in a very thin area, a much higher signal-to-noise ratio is achieved compared to conventional fluorescence microscopy methods. This enables the detection of single molecule fluorescence (Axelrod, 1981; Sako et al., 2000; Ross et al., 2021).
In the three-bead assay there is usually rhodamine fluorescence used to visualize beads and actin filaments. Therefore, a 150 mW 532 nm green laser (#Gem 532, class 4 laser, Laser Quantum) was installed. Additionally, a 50 mW 473 nm blue laser (#DPBL-9050, class 3B laser, Photop Suwtech) was installed to expand the choice of fluorophores. The fluorescence was visualized using an electron-multiplying camera system (#C9100-23B, Hamamatsu) coupled with a IR blocking filter (#FF01-950/SP, Semrock) mounted on a homemade inside blackened adapter. The camera was mounted on the left infinity port of the microscope. Video images were captured at 512 x 512 pixel resolution, giving 1 pixel corresponds to 160 nm.

Both laser beams were coupled into one beam path by using a longpass filter and beam widths of both lasers were expanded using a Kepler beam expander (see Fig. 2.12). The fluorescence laser path was coupled into the IR path after the TIRF lens with a mirror that reflected 1064 nm laser light but passed 473 and 532 nm laser light.
In our objective-based TIRF the fluorescence lasers need to be focused on the back aperture of the objective in order to have an collimated illumination of the sample. Lenses with a high numerical aperture (>1.4 NA) are important to produce the critical incident angle in order to excite the sample with an evanescent field. As seen in Fig. 2.11 a TIRF lens with f = 450 mm was installed. In this optical configuration changing the mirror position will change the incident angle of the lasers on the glass-sample interface allowing

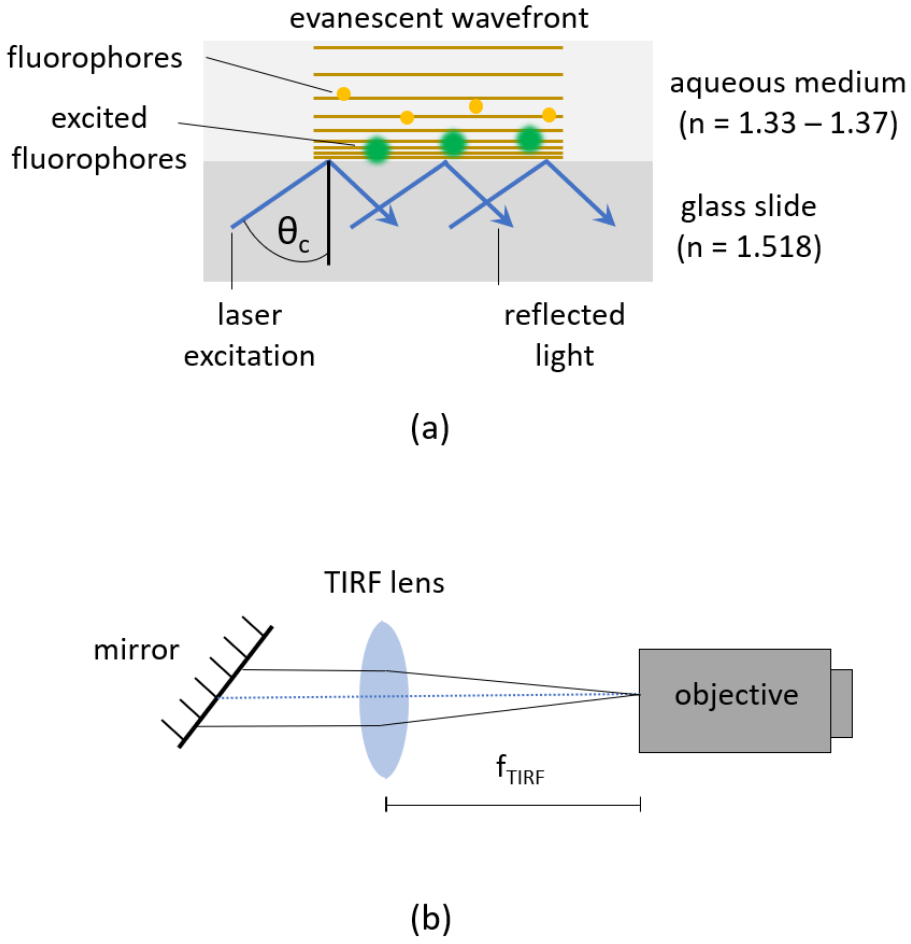

Fig. 2.11: The basic concept of total internal reflection fluorescence (TIRF). (a) The refractive indices of the glass slide (1.518) and the aqueous sample medium (approximately 1.35) are suitable for TIR (Ross et al., 2021). (b) Optical arrangement on the trapping setup for TIRF. The fluorescence lasers are focused on the back aperture of the objective to have a collimated light beam on the sample.

to switch between TIRF and epifluorescence.

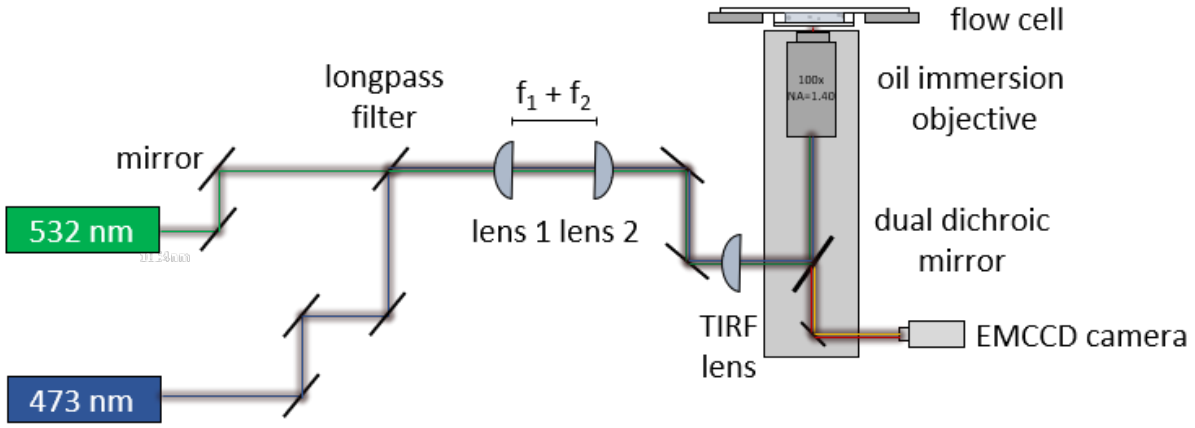

Fig. 2.12: Schematic illustration of the light path of the two fluorescence laser. The beam expander for the 473 and 532 nm lasers consisted out of two plano-convex lenses with f_1=25.4 mm and f_2=300 mm.

2.5.5 Four-quadrant photodetector

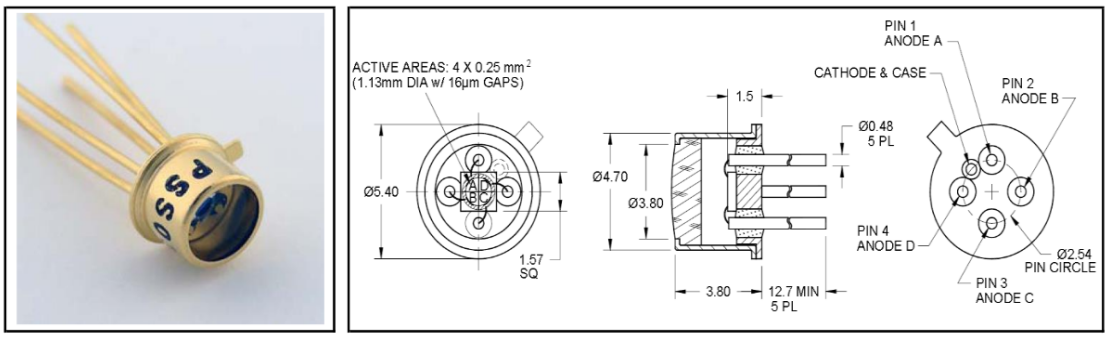

Fig. 2.13: Photograph and technical drawing of the photodiode. The diode generates a current that is amplified from an initial value of ∼1 nA. Figure adapted from FirstSensor (2021).

The imaging system used to record the bead position in the optical trap is critical, as it has to carry out nanometre-precision measurements on millisecond time scales. Four-quadrant photodiode detectors (4QDs) and head stage circuits were built for this purpose, as they are very sensitive to movement in two dimensions.

The 1 mm^2 photodiode (#5000029, First Sensor) consisted of four separated, optical active areas which were separated by a small gap field (see Fig. 2.13). The 4QD compares the voltage response of these four photodiodes to incident light and detects thereby motion in two dimensions (Fig. 2.15). The outputs of the 4QD compare the voltage of the

left two with the right two quadrants, [(1 + 3) - (2 + 4)]/(1 + 2 + 3 + 4), and the upper two with the lower two quadrants [(1 + 2) - (3 + 4)]/(1 + 2 + 3 + 4). If a bead is moved from the centre of the 4QD to the right, the 4QD output will decrease proportionally together with the left-right signal [(1 + 3) - (2 + 4)]/(1 + 2 + 3 + 4). When the edge of the bead crosses the centre of the detector, the 4QD output does not change while the bead is moved. When the bead starts to leave the 4QD and the left-right signal increases, the detector voltage response is brought back to zero (Spudich et al., 2011).

Detector noise can have electrical or optical sources. The sum of these was measured by illuminating the 4QD evenly and recording the output signal. The power density spectrum of this noise is depicted in Fig. 2.14. The bandwidth of the noise is controlled by the electronics of the detector circuit. Feedback resistors of 100 MΩ were used in our 'head-stage' circuit. This gave a good balance between gain (proportional to R), resistor noise (proportional to $R^{0.5}$) and bandwidth (proportional to 1/R). Usually, the overall detector noise is approx. 100-fold smaller than the Brownian motion of a 1.1 μm bead trapped in the optical tweezers (Veigel et al., 1998).
The final output voltage from the 4QDs had an amplitude of 1-10 Volts. A high-speed data acquisition FPGA card was used to record bead position at a high time resolution. The data was viewed and analysed with the software package LabView (National Instruments).

2.5.6 Testing the four-quadrant detector

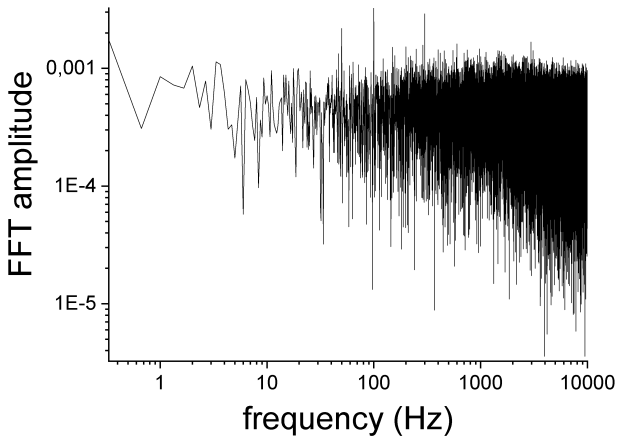

Fig. 2.14: Powerspectrum of the 4QD headstage.

To create a power spectrum of the detector a 1.1 μm silica bead was trapped in the optical tweezers and the noice was recorded for a short time interval (Fig. 2.14). This allows to identify potential unwanted noise sources.
A position sensor with nanometre resolution is created by the final output of the circuit. To achieve highest positional resolution during an experiment it is crucial to position the detector so that the bead is right in the centre of the 4QD (Fig. 2.15).

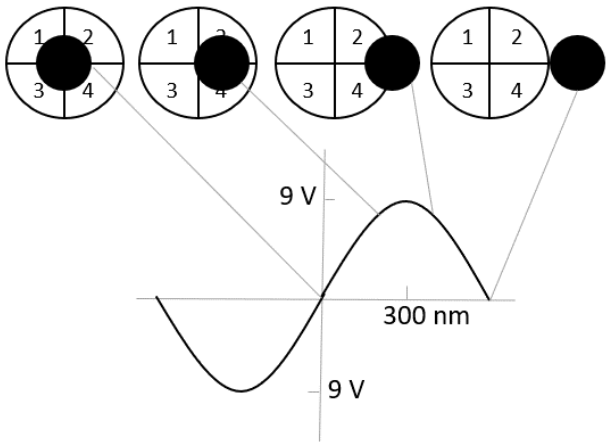

Fig. 2.15: The detector has its highest sensitivity when the bead is in the centre of the 4QD and the diameter of the diode is twice the size of the object diameter. The response of the detector is than linear over a range of 300 nm from the 4QD centre.

2.5.7 AOD calibration and linearity

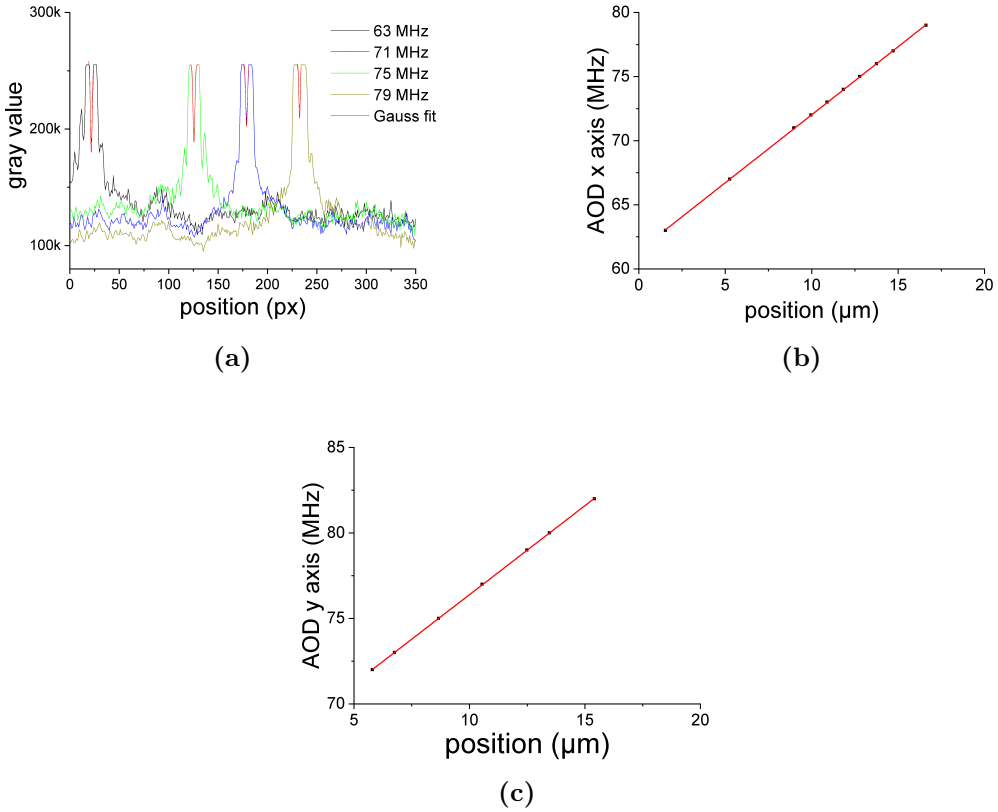

Fig. 2.16: AOD calibration. (a) The optical trap was moved via the AOD to different positions across the screen. The centre position of the trap was determined with a Gaussian fit on a grey value plot for 10 different x axis (b) and 7 different y axis (c) positions. The linear fit gave a calibration factor of 1.063 and 1.041 kHz/nm for the x and y axis, respectively.

The AOD was calibrated to get a conversion factor of the frequency of the applied voltage to nanometre displacement of the optical trap. The centre position of the trap was determined for four different x and y axis positions by fitting a gauss function on their grey value plot in ImageJ (see Fig. 2.16). The position in pixel was then converted to nanometres. This calculation gave a calibration factor of 1.063 kHz/nm for the x axis and 1.041 kHz/nm for the y axis.

To evaluate the linearity of the AOD, a trapped 1.1 μm silica bead was stepped across the screen (x and y position) in 1 µm steps. ImageJ was used to determine the centroid position of each bead in the images and the coordinates were converted from pixels to nanometres.

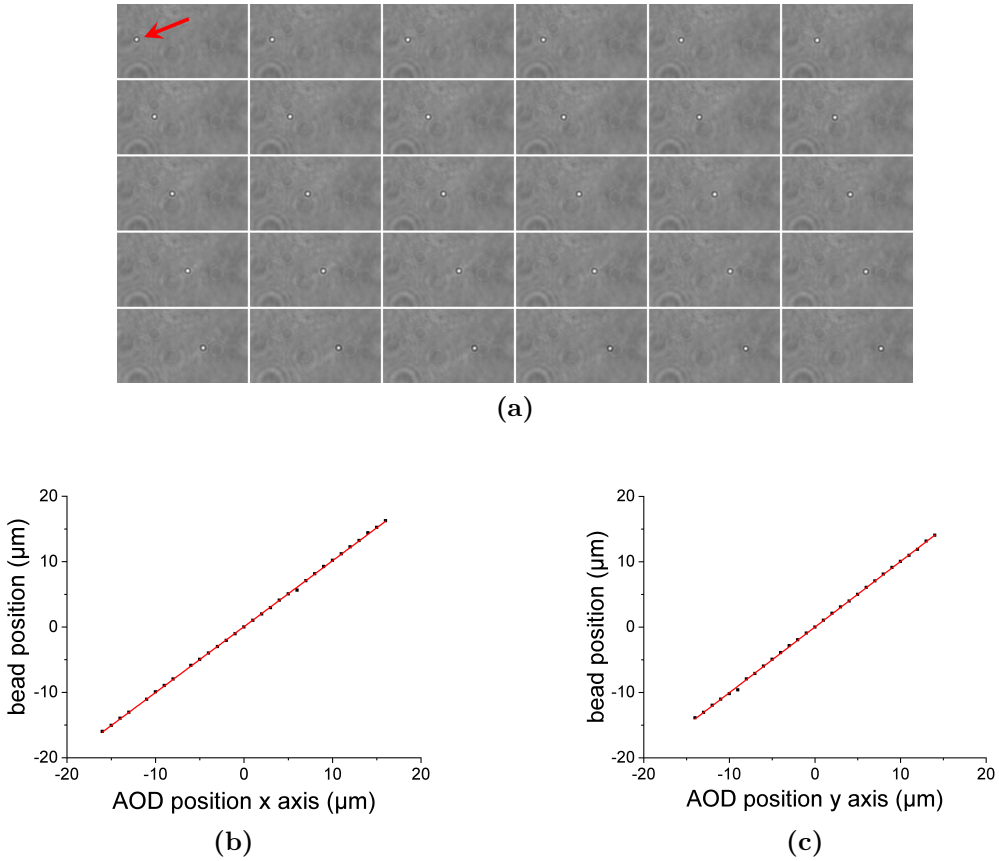

Fig. 2.17: Evaluation of AOD linearity. (a) Stack of 30 images showing a trapped bead (red arrow) stepping across the screen from left to right in 1 μm steps. ImageJ was used to determine the centre position of the bead in each image. The linearity was plotted for the x (b) and y (c) axis. The linear fit resulted in a R^2 of 0.99985 and 0.99974 for the x and y axis, respectively.

2.5.8 Linearity of the piezo stage

The linearity of the piezo stage was reviewed very similar to the AOD linearity. A 1.86 μm bead fixed to the glass surface was moved across the screen in 1 μm steps and the centre position of the bead in each image was determined with ImageJ. Fig. 2.18 shows the almost perfect linearity of the stage with a R^2 of 1.

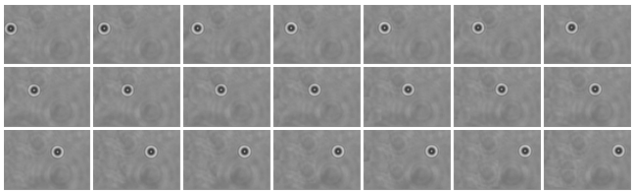

(a)

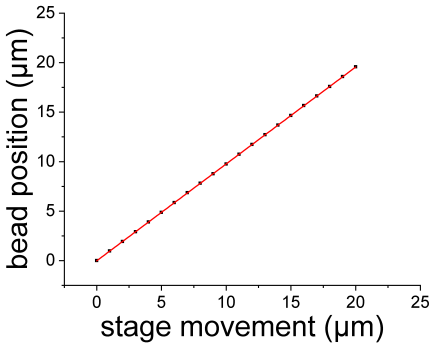

(b)

Fig. 2.18: Evaluation of the linearity of the piezo stage. (a) Stack of 21 images showing a bead (fixed to the glass surface) stepping across the screen in 1 μm steps. (b) The linear fit gave a R^2 of 1.

2.5.9 Stiffness of the optical tweezers

I used two main methods to determine the stiffness of optical tweezers: Stokes calibration and the equipartition theorem (Svoboda and Block, 1994; Veigel et al., 1998). It is important to use trap stiffness's lower than the myosin stiffness to enable accurate estimates of the myosin power stroke. In this study experiments were performed between 0.02-0.04 pN/nm at 22°C. The stiffness was calibrated daily.

2.5.9.1 Stokes Calibration

Stokes calibration involves applying a known viscous drag force to a bead captured in the optical trap and recording how far it is displaced from the tweezers centre. Micron sized particles have very small Reynolds number R_e:

$$R_e = \frac{va\rho}{\eta} \approx 10^{-5}$$

where v is the fluid velocity, ρ is the particle density, a is the particle size and η is the fluid viscosity. Application of a large-amplitude triangular waveform of known size and frequency to the flow cell with the piezoelectric stage produces a viscous drag force on

the trapped bead given by Stoke's law:

$$F = 6\pi\eta r v$$

where r is the radius of the bead and v is the velocity of the stage. By measuring the displacement of the bead the trap stiffness κ_{trap} can be determined (Svoboda and Block, 1994):

$$\kappa_{trap} = \frac{\text{Force}}{\text{Displacement}}$$

2.5.9.2 Equipartition Principle

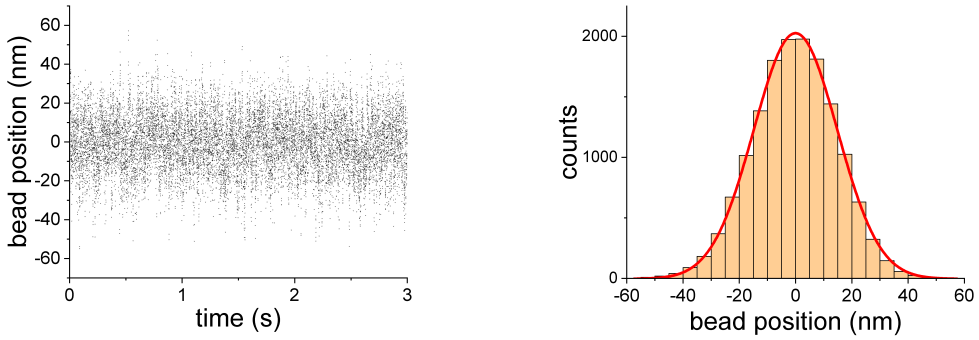

(a) **(b)**

Fig. 2.19: Calibration of trap stiffness by analysis of the Brownian motion. (a) A single 1.1 μm bead is trapped in the optical tweezers and data is sampled at 5 kHz. The graph displays the bead position vs. time. (b) Shows the same data plotted as a histogram. The gauss fit centred at 0.013 ± 0.025 nm (R^2=0.999) and the variance is determined by the vibration due to Brownian noise.

Microscopic objects in a viscous medium show significant Brownian motion. This motion of a bead captured in the optical tweezers can be used to measure the trap stiffness κ_{trap} by the equipartition theorem. In thermal equilibrium the mean energy of a system is spread equally over all degrees of freedom (hence the name 'equipartition') and is directly proportional to the absolute temperature T:

$$\frac{1}{2}k_B T = \frac{1}{2}\kappa_{trap}\langle x\rangle^2$$

where k_B is Boltzmann's constant and x is the displacement of the particle from its trapped equilibrium position (Svoboda and Block, 1994; Neuman and Block, 2004). Thus, the trap stiffness can be determined from the positional variance of a single trapped bead.

2.6 Optical trapping methods

2.6.1 Bead preparation

Most optical tweezers experiments involve the use of micron-sized polystyrene or silica beads, which are connected via diverse methods to the proteins under investigation. The use of beads has many advantages: They are available in a wide variety of sizes and surface chemistries and can be labelled with different (fluorescent) dyes. In our optical tweezers measurements we are using 1.0 µm polystyrene beads coated with neutravidin (#F8777, Thermo), so that they can be connected to biotinylated actin filaments. Those beads are very stably trapped using 1064 nm laser light and also give a high-contrast image on the 4QD.

The beads were labelled with rhodamine according the following protocol: 10 µl of neutravidin coated latex beads were mixed with 50 µl phosphate buffer and spun down at 3650 x g, 2 min, room temperature. The pellet was resuspended gently in 50 µl phosphate buffer. 10 µl of 1 M glycine and 5 µl of 10 mg/ml Rhodamine-BSA were added to the beads and incubated for 20 min at RT in the dark. To remove excess dye 250 µl of phosphate buffer was added and first spun down 5 min at 540 x g, RT and then another 4 min at 3650 x g, RT. This washing step was repeated one time. Finally, the pellet was resuspended in 50 µl of phosphate buffer and stored at 4°C. Beads were used fresh within 2 days.

Tab. 2.25: Phosphate buffer (adding KH_2PO_4 to K_2HPO_4 until pH 7.0 is reached)

Ingredient	Mass or Volume/120ml
K_2HPO_4	70ml (50mM stock)
KH_2PO_4	∼50ml (50mM stock)

2.6.2 Optical trapping procedure

For optical trapping experiments special flow chambers were constructed. Custom-built spacer coverslips (3x40 mm, Marienfeld) were glued with a UV-curing epoxy adhesive (Henkel) onto 76x26 mm Superfrost microscope glass slides (Menzel) so that they had the same width as the coverslips (22 mm). 1.86 µm glass microspheres (#SiO2MS-1.8, Cospheric) were spread on a coverslip surface (24x40 mm, Brand) as a suspension in 0.1 % (w/v) nitrocellulose in amylacetate (Kron and Spudich, 1986). Optimal surface density of about one microsphere per 10 μm^2 was controlled with bright-field microscopy. The

coverslips were then glued onto the spacers, which created a ∼100 µl flow cell. The flow cells were exposed to UV light for 20-30 min. UV-curing epoxy adhesive gives good z axis (focus) stability during the experiments (Veigel et al., 1998).
In control experiments with muscle myosin II HMM and in first experiments with myosin IXa motor constructs, the motor proteins were diluted in AB- to approx. 2 ng/ml (HMM) and 10–50 ng/ml (MD) and applied directly to the nitrocellulose surface for 4 min. In later experiments with myosin IXa motor constructs and non-muscle myosin IIb, proteins were bound via a monoclonal anti-FLAG antibody to the surface (#A8592, Sigma). In those experiments the anti-FLAG antibody was diluted to 1 ng/ml in PBS and incubated for 4 min. Then the flow cell was washed with 200 µl PBS. In experiments with myosin VI variants, proteins were bound with 1 ng/ml of an anti-tail antibody to the surface (B4-2; gift from F. Buss, University of Cambridge). Additionally, 1 mg/ml calmodulin was added to myosin VI variants before experiments.
The following procedure was the same for all studied myosins. The surface was blocked with 0.5 mg/ml BSA in AB- for 3 min. The concentration of BSA was increased up to 50 mg/ml if the surface was sticky. Afterwards dead heads were blocked with 100 nM phalloidin-labelled short actin filaments in AB- containing ATP. After blocking, the solution was replaced with AB+ Scavenger (AB- supplemented with various ATP concentrations, 10 mM DTT, 0.01 mg/ml catalase, 0.05 mg/ml glucose oxidase, 1.5 mg/ml glucose, 0.5 mg/ml BSA) containing an ATP backup system (2 mM creatine phosphate, 0.1 mg/ml creatine phosphokinase). Additionally, this trapping mixture also contained 1-4 nM rhodamine labelled biotinylated actin and rhodamine labelled neutravidin coated beads.

Tab. 2.26: AB- buffer 10x concentrated, with creatine phosphate

Ingredient	Final concentration	Mass or Volume/0.1l
Imidazole pH 7.4	250mM	1.7g
KCl	250mM	8.3ml (3M stock)
$MgCl_2$	40mM	8.0ml (0.5M stock)
EGTA	10mM	2.0ml (0.5M stock)
Creatine phosphate	20mM	0.51g

Using fluorescence microscopy a biotinylated actin filament was attached between two beads that were trapped by two independently controlled optical tweezers. This was usually done by keeping the traps in fixed positions and controlling the stage with the mechanical x-y controls. A pretension was applied to the actin filament by moving one of the traps along the actin filament axis and detecting the motion of the bead kept in the stationary trap. Then the so-called actin dumbbell was moved in such a way that each bead image was optimally projected into the centre of its respective 4QD. The two mechanical x-y translators on the photodetectors were used to make a final alignment. A 100 nm 100 Hz sinusoidal oscillation was applied to one of the optical traps (Veigel et al., 1998).
The actin dumbbell was than positioned over a third, myosin coated, surface bead. Fine positioning of the third bead was done with the computer-controlled piezo stage. Surface beads were visualized by bright-field microscopy with proper Köhler illumination. The condenser port was opened fully to allow precise control of the z-axis (focus) and the focus was adjusted until myosin binding events with actin were monitored. It is important to defocus the bead image to enhance the contrast between the bead and the background in order to have a good detector signal. Interactions between a single myosin motor and the actin dumbbell were measured from the motion of a bright-field image of the two trapped beads cast onto two 4QDs (Veigel et al., 1998). Interactions were measured at optical tweezers stiffness's between 0.02-0.04 pN/nm at 23°C. Data was sampled at 5 kHz.

2.6.3 Optical trapping data analysis

Data analysis of optical tweezers measurements was performed with a python script provided by Andreas Graw (versions 0.3.10, 0.3.11 and 0.3.13). Single-molecule binding events were detected using a running variance calculation (160 data points). Data was smoothed using a running median of 40 points. By manually thresholding the variance, events were identified in the data set. This threshold was adjustable in order to allow for changes in stiffness over time. The displacement due to myosin binding events was determined by the difference between the local mean bead position during intervals of bound and unbound myosin to actin (see Fig. 2.21). Furthermore, the duration of the event was also recorded by the program.

In optical tweezers measurements a statistically large data set must be recorded. In contrast to bulk measurement techniques (*in vitro* motility assay, solution kinetics) optical trap measurements allow to collect data from single myosin molecules. If the data set from one myosin molecule is large enough (>100 events) it is possible to determine the

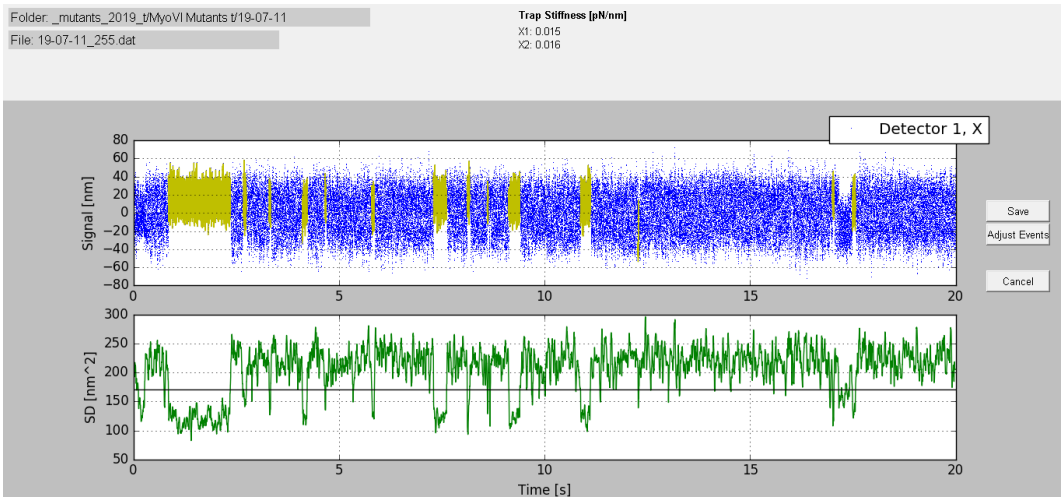

Fig. 2.20: Data analysis. Front end of the python script to detect single myosin VI binding events. The upper trace (blue) shows the original raw data of detector 1. The lower trace (green) shows the calculated variance. Myosin binding events (yellow in the upper trace) were identified by a drop of variance below the manually set threshold (solid black line in the lower trace).

orientation of the actin filament in the bead-actin-bead dumbbell. In that way data sets from different myosin molecules can be pooled and analysed together.

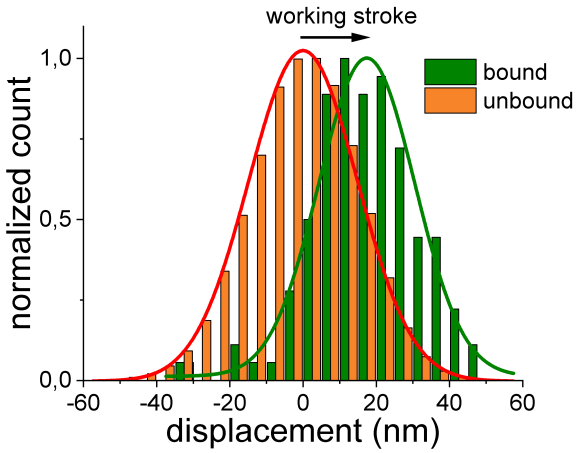

Fig. 2.21: Analysis of actomyosin binding events. The orange coloured histogram with the red fit line is a Gaussian distribution from the bead positional noise in the absence of binding events. The distribution centres at 0.013 ± 0.025 nm (R^2=0.999). The olive histogram shows the distribution of event amplitudes obtained using human myosin VI interacting with rabbit actin at 100 µM ATP and 0.02 pN/nm single trap stiffness. The centre of the distribution is shifted from zero by the magnitude of the working stroke, and the width is shaped by the trap stiffness and size of the applied oscillation. In this example the working stroke of human myosin VI is 17.4 ± 0.7 nm (R^2=0.966).

2.6.4 Series compliance

The displacement data from single-molecule measurements needs to be corrected for series compliance that results from the connection between the neutravidin coated beads and the actin filament. The bead-actin-bead structure is not completely rigid, and this system can be thought about as a series of springs (see Fig. 2.22). The binding of myosin to actin creates a mechanical connection between the trapped beads and the ground. The actin-bead connection stiffness κ_{con} is linked in series with the myosin stiffness κ_{myo} and these are combined in parallel with the trap stiffness κ_{trap}. A small portion of the myosin power stroke is absorbed by the compliance of the connection. Thus, the measured bead displacement must be corrected for the effects of series compliance in the following way:

$$\text{Correction factor} = \frac{\kappa_{trap}}{\kappa_{con}}$$

During periods of myosin attachment, κ_{con} is calculated as follows:

$$\kappa_{con} = \frac{F}{(\Delta_R - \Delta_L)}$$

with

$$F = (\Delta_O - \Delta_R) \times \kappa_{trap}$$

where Δ_O is the amplitude of the applied oscillation. The peak-to-peak amplitudes of the driven (Δ_R) and passive (Δ_L) beads during binding events are calculated from the complex amplitude of the sinusoidal component of the motion (Veigel et al., 1998; Larijani et al., 2006).

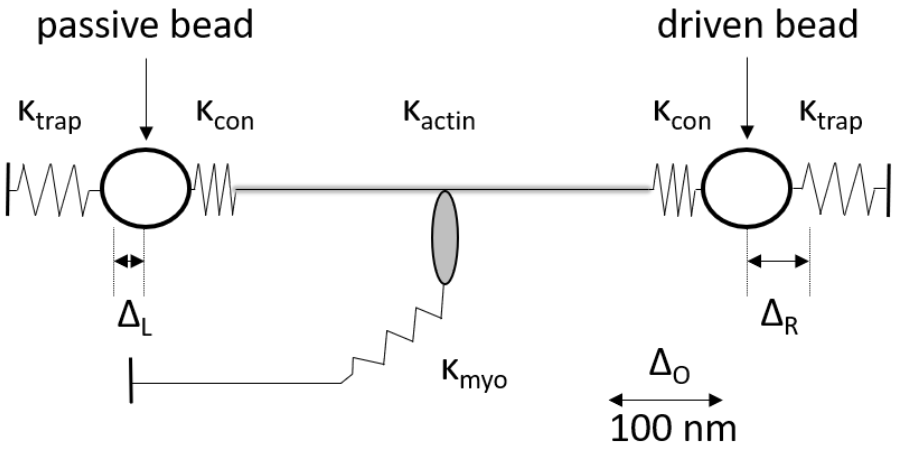

Fig. 2.22: Series compliance. Schematic illustration of the different mechanical components in the three bead geometry. An external sinusoidal oscillation Δ_O results in an amplitude of the driven bead Δ_R and a damped amplitude (because of κ_{con}) of the passive bead Δ_L. Figure modified from Veigel et al. (1998).

.

2.6.5 Stiffness calculation

The stiffness of single myosin molecules was determined using two 4QD detectors. A 100 Hz 100 nm sinusoidal waveform was applied to one bead (called driven bead) in the bead-actin-bead dumbbell. The other bead followed this waveform in a passive manner (called passive bead), because of mechanical connection through the actin filament with the driven bead (see Fig. 2.22).
With a given dumbbell where $\kappa_{con} \gg \kappa_{trap}$ the amplitude reduction of the sinusoidal waveform of the passive bead increases with higher myosin stiffness. The myosin stiffness κ_{myo} is calculated as follows (Veigel et al., 1998):

$$\kappa_{myo} = \frac{\kappa_{trap}}{X_{resp}} \times (\Delta_O - \Delta_R - \Delta_L)$$

where κ_{trap} is the trap stiffness, Δ_O is the amplitude of the oscillation (usually 100 nm) and Δ_R is the amplitude of the driven bead.
A discrete Fourier transformation (DFT) was used to determine the amplitudes of the raw data using a running window of one period length. With a sampling frequency of 5 kHz and a 100 Hz 100 nm sinusoidal waveform, the period length corresponded to 10 ms (50 data points). The final stiffness data was smoothed using an running median (see Fig. 2.23).

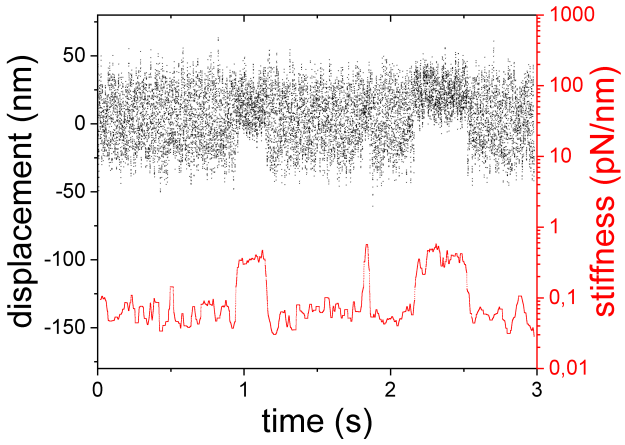

Fig. 2.23: Stiffness calculation. Exemplary raw data from single myosin VI binding events at 100 µM ATP are shown in black. A discrete Fourier transformation (DFT) analysis was used to calculate the amplitude of the data. The resulting stiffness smoothed by a running median (window size 200 points) is plotted in red and shows a sharp increase after an acto-myosin binding event.

2.7 Data analysis

Data was analysed using Origin 2018b. Mean and standard error of the mean (SEM) are shown unless indicated otherwise. Python scripts were run with version 2.7.10. DNA and protein sequences were analysed with SnapGene and ApE.

3 Results

3.1 Single-molecule & biochemical studies of human myosin IXa

This section introduces human myosin IXa. In general, class IX myosins are thought to act as motorized signalling molecules, as they contain a Rho-GTPase activating domain (RhoGAP) in the tail, which can alter the dynamics of the actin cytoskeleton. Myosin IXa is localised in actomyosin networks at cell-cell adhesions, where it was identified as a key requirement for collective cell migration (Omelchenko and Hall, 2012; Wood and Olson, 2012). Many processes depend on the movement of groups of cells: During tumour progression cancer cells invade the tissue surrounding a primary tumour, while in wound healing epithelial cells have to move close to the wound.

In this study I expressed a variety of human myosin IXa constructs comprising the motor domain and the calmodulin-binding lever arm. The first part describes structure-function studies on various myosin IXa domains including the large loop 2 and the six IQ domains in the lever arm using the in vitro motility assay. In the second part I performed quantitative TIRF microscopy showing that myosin IXa assembles actin into bundles of up to seven or even more filaments. I show that loop 2 is the molecular basis for this bundling capability. A collaboration project using transmission electron microscopy combined with single particle image processing revealed that the bundles consisted of a highly ordered 2D actomyosin network. The third part describes single-molecule measurements using an optical tweezers setup. This measurements explain and supplement the results from the first section, showing the substantial influence of loop 2 on the kinetics of myosin IXa. In the last part I give an outline of different attempts to express and purify loop 2, including a bioinformatic structure prediction approach to get structural informations about the unique large loop 2 of myosin IXa.

3.1.1 Design of human myosin IXa constructs

Fig. 3.1 shows a schematic overview of myosin IXa constructs used in this study. The IXa motor domain (MD) construct encompasses amino acids 149-1019 of human myosin IXa (NCBI no. AAI40870.1). This construct includes the full head domain with the class IX specific loop 2 insert, the actin- and ATP binding sites but does not contain the N-terminal extension.

To study the impact of the >200 aa loop insert, a MD mutant was developed where the loop was replaced by the much shorter loop 2 (17 aa) of human skeletal muscle myosin (see section 3.1.4.4; Saczko-Brack et al. (2016)). A third S1 construct contained all structural features of the MD construct and additional the neck region with six IQ motifs for putative light chain binding (amino acids 149-1162). This construct was used to assess the impact of the neck region on motor functions.

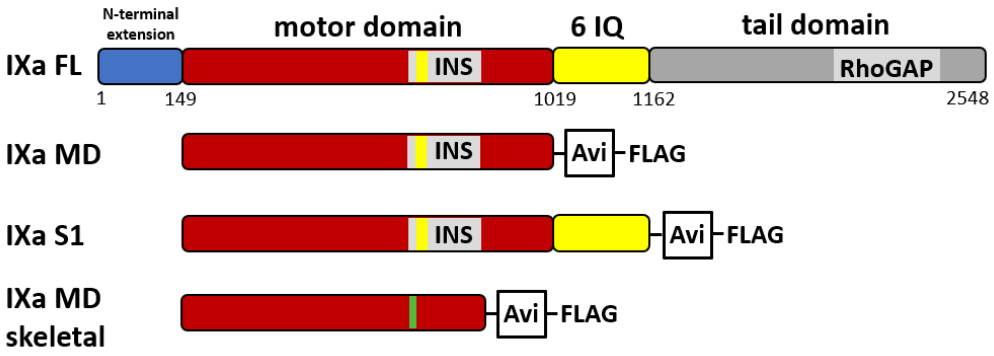

Fig. 3.1: A simplified depiction of the domain organisation of full length human myosin IXa and the constructs used in this study. Numbers of important amino acids within the myosin IXa sequence are shown. All constructs contained a C-terminal Avi- and FLAG-tag. The N-terminal extension (1-148 aa) and loop 2 insert (INS) are indicated. Note there are altogether seven putative calmodulin-binding sites: One in the insert (yellow box) and six in the neck region. In the MD mutant (IXa skeletal) the class IX specific loop 2 was replaced by the much shorter loop 2 of human skeletal muscle myosin (indicated by green box). RhoGAP: Rho GTPase-activating protein.

All constructs contained a C-terminal FLAG-tag for protein purification. Additionally, the constructs contained an Avi-tag. In the presence of biotin and ATP, biotin ligase (BirA) catalyses an amide linkage between the biotin and the specific lysine of the 15 aa Avi-Tag peptide. This highly specific *in vitro* biotinylation was used to site specifically bind the myosin to glass surfaces (Fairhead and Howarth, 2015).

3.1.2 Cloning of myosin IXa constructs

Full-length human myosin IXa cDNA (7647 bp; NCBI no. AAI40870.1) was synthesized and cloned into pUC57 (GenScript). The sequence was codon-optimized for the expression in insect cells. This construct was used as a template to clone the myosin IXa motor domain (MD) construct (base pairs 444-3057 encoding amino acids 149-1019) and myosin IXa S1 construct (bp 444-3492; aa 149-1164) into the pFBNX vector using PCR and BamHI/XbaI restriction sites. The reverse primer included a FLAG-tag sequence (DYKDDDK) upstream of the stop codon. In addition, an Avi-Tag (GLNDIFEAQKIEWHE) was inserted C-terminal of the myosin IXa sequence (Saczko-Brack et al., 2016).

3.1.3 Purification of myosin IXa constructs

Recombinant baculoviruses expressing myosin IXa MD and S1 were produced and proteins were expressed and purified as described in chapters 2.3.2 and 2.3.3.1. Following FLAG purification, the eluted protein was bound to an ion exchange resin and eluted with increasing salt concentrations. The latter purification step was useful to concentrate the protein. This two-step purification protocol resulted in homogenous myosin IXa preparations that achieved a purity of about 90 % as calculated by gel densitometry analysis. Moreover, ion exchange chromatography resulted in separation of two myosin species: with and without bound calmodulin. The species without bound calmodulin did not exhibit any motor activity in the *in vitro* motility assay and therefore was not used for further experiments. Enzymatically active myosin IXa MD eluted from the ion exchange resin at 250 mM NaCl, whereas active myosin IXa S1 eluted at 500 mM NaCl (see Fig. 3.2). Protein yield and activity varied from preparation to preparation, especially for the S1 construct.

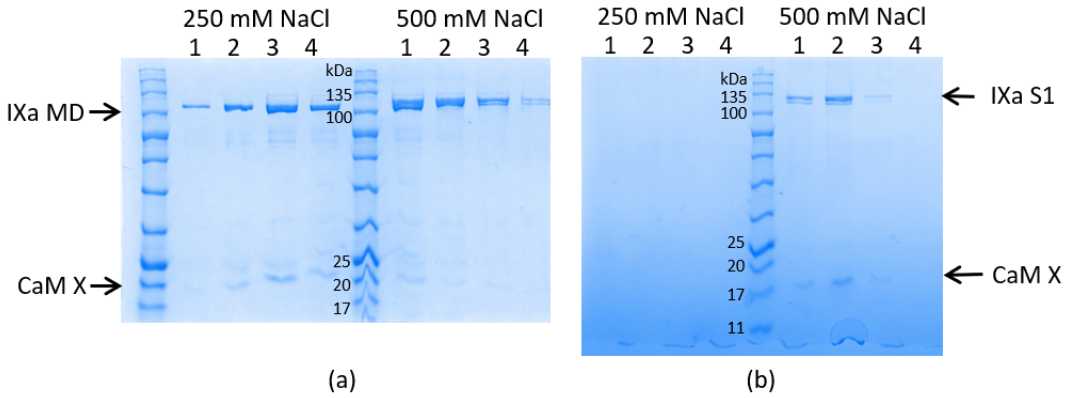

Fig. 3.2: A two-step purification protocol resulted in highly pure myosin IXa preparations. Representative 7.5 % SDS-PAGE gels displaying purification steps of myosin IXa MD (a) and myosin S1 (b). The construct was purified using FLAG affinity chromatography. Proteins present after FLAG elution were applied to an ion exchange chromatography resin and eluted in fractions with 250 mM and 500 mM NaCl. Myosin IXa MD was found in two fractions: with bound calmodulin (eluting at 250 mM NaCl) and without bound calmodulin (eluting at 500 mM NaCl). The majority of IXa S1 eluted at 500 mM NaCl.

3.1.4 *In vitro* motility assays on myosin IXa constructs

This section investigates the mechanical properties of human myosin IXa. Site-specific attachment via a streptavidin-biotin linkage resulted in an active translocation of actin filaments. In this study I show that replacement of the large myosin IXa loop 2 by the much shorter loop 2 of skeletal muscle myosin II resulted in an increased actin gliding velocity. Although the head domain contains an calmodulin-binding site in the loop 2, the velocity is just slightly increased in the presence of calcium. Furthermore, this study clearly reveals that human myosin IXa is a plus-end directed molecular motor and its directionality is not influenced by calcium.

3.1.4.1 Introduction

The *in vitro* motility assay was first described by Kron and Spudich (1986) and is widely used in the motor molecules field (applicable also for kinesin and dynein) with many different adaptions. This assay allows investigations of myosin properties through observation of actin filament propulsion by surface-bound myosin motors. It can provide a deeper understanding of how various chemicals in bulk solutions (e.g. ions, drugs and other proteins) influence the functionality of myosins. The *in vitro* motility assay is an easy and fast method to evaluate the quality of a myosin preparation before technically more sophisticated experiments (i.e. single-molecule experiments with optical tweezers) are carried out.

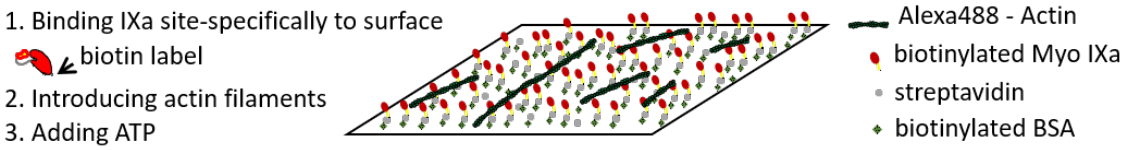

Fig. 3.3: A simplified illustration of the *in vitro* motility assay of myosin IX constructs. The motor molecules are site-specifically attached to the surface. The coverslip is coated with biotin-BSA and streptavidin. In the next step C-terminal biotinylated myosin IX is introduced into the flow cell. After injection of Alexa 488-labelled actin filaments, motility is initiated by the addition of ATP.

The technique is described in detail in chapter 2.4.1. Briefly, a glass coverslip is coated with nitrocellulose and myosin is bound nonspecifically to the surface. Further binding places are blocked with BSA. Fluorescently labelled actin filaments are introduced into the flow cell. After addition of ATP, surface-attached myosins begin to interact with actin filaments, which results in movement of these filaments.
Non-specific binding of myosin to nitrocellulose can lead to different geometries of myosin

motors on the surface. This could orient myosin molecules in such a way that they are unable to perform a complete power stroke and therefore impede the motility. There are two main ways to bind myosins to the surface in a certain conformation: Attachment via the biotin streptavidin linkage, where the myosin has a biotin attached at a specific site (defined with the Avi-tag) and the coverslip surface is coated with streptavidin. The second way is specific attachment via an antibody raised against a C-terminal part of a myosin (i.e. tail) or a C-terminal tag (i.e. FLAG). Such site-specific immobilization aligns the N-terminal myosin heads towards the interior of the flow cell and allows complete power strokes that lead to movement of actin filaments.

3.1.4.2 Control measurements with skeletal muscle myosin II

Heavy meromyosin (HMM) of skeletal muscle myosin II was used as a control in the *in vitro* motility assay. 0.2 mg/ml rabbit skeletal HMM was applied to a flow cell constructed of a coverslip covered with nitrocellulose. After blocking of free binding places with BSA, Alexa 488-labelled actin was introduced and motility was started by adding ATP. Fluorescent actin was excited in TIRF mode and images were acquired in 300 ms intervals. Skeletal muscle myosin II robustly moved actin filaments in the presence of ATP. The Fiji plugin MTrackJ was used to manually track single filaments (Meijering et al., 2012) and a velocity distribution graph was generated (Fig. 3.4 (a)). Rabbit skeletal HMM propelled actin filaments with a velocity of 4.04 ± 0.03 µm/s at 2 mM ATP, which corresponds well with previously reported values (Sheetz et al., 1984; Kron and Spudich, 1986; Homsher et al., 2003).

Furthermore, the steady-state ATP affinity of rabbit skeletal HMM was also examined by calculating the average sliding speeds of HMM at different ATP concentrations (Fig. 3.4 (b)). The actin gliding velocity increased with rising ATP concentration and data points were fitted to Michaelis-Menten kinetics. The half-maximal velocity was reached at K_{ATP} = 126.17 ± 52.09 µM (23°C).

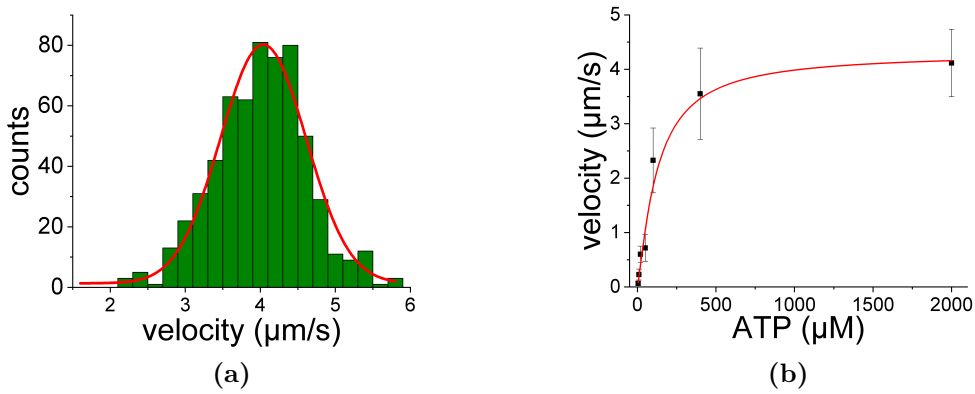

Fig. 3.4: The *in vitro* motility assay of rabbit skeletal HMM. (a) The velocity distribution plot of HMM at 2 mM ATP. A total of 635 filaments from three different flow cells were tracked. Data was fitted with a Gaussian distribution (R^2=0.966) and gave a velocity of 4.04 ± 0.03 µm/s at 23°C. (b) The dependence of HMM velocity on ATP concentration. Data was fitted to Michaelis-Menten kinetics (R^2=0.951) and the half maximal velocity was reached at K_{ATP}=126.17 ± 52.09 µM. In total 702 filaments were included in this analysis.

3.1.4.3 Site-specifically attached myosin IXa actively transports actin

Initial attempts by previous lab members to bind the myosin IXa motor domain nonspecifically to a nitrocellulose-covered coverslip did not result in actin translocation. Therefore, biotinylated IXa MD was used to bind it site-specifically to a piranha-cleaned glass coverslip (Warchol, 2016). Briefly, biotin-BSA was introduced into the flow chamber, followed by streptavidin and 0.1-0.2 mg/mL IXa-MD and Alexa 488 actin. Fluorescent actin filaments were visualised using TIRF and images were recorded every 3 s for 10-20 min on a Nikon Eclipse Ti microscope. The assay buffer was supplemented with 2 mM ATP and 100 mM KCl. Compared to the original assay buffer from Kron and Spudich (1986), containing 25 mM KCl, the salt concentration in this experiments was increased to adapt to physiological conditions.

IXa MD site-specifically bound to the flow cell surface actively moved actin filaments (Fig. 3.5). The mean velocity obtained from 1012 filaments was 23.9 ± 0.2 nm/s, which confirms that the myosin was mechanically active. The velocity was ∼170 times lower than that of skeletal muscle myosin measured above (4 µm/s at 2 mM ATP).

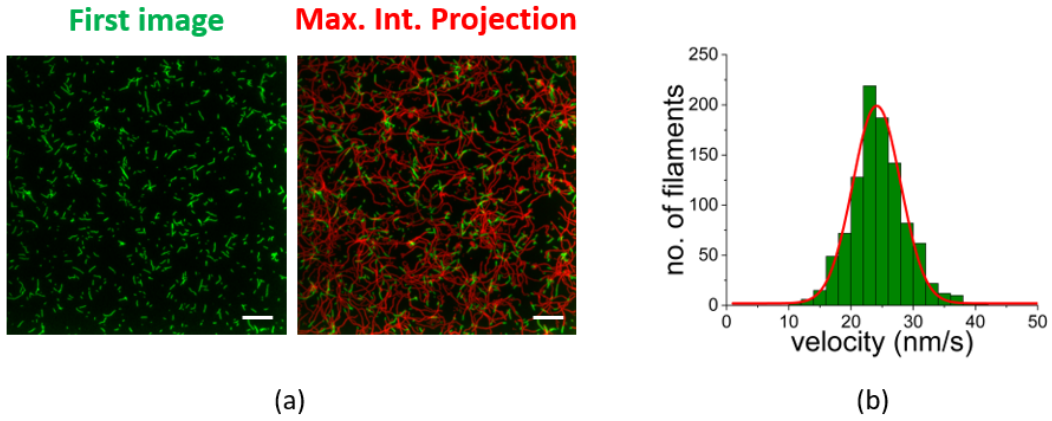

Fig. 3.5: IXa MD specifically attached to the surface via a streptavidin-biotin linkage actively moves actin filaments. (a) The first image and the maximum intensity projection (indicating the cumulative pixel intensity from several frames) are shown revealing translocation of actin filaments (right image: actin paths in red). Scale bar is 10 µm. (b) A histogram of the velocity distributions of IXa-MD. 1012 single filaments from three independent myosin purifications were used to collect the data. Data was fitted with a Gaussian distribution (R^2=0.980) and gave a velocity of 23.9 ± 0.2 nm/s at 2 mM ATP.

3.1.4.4 Removal of the IX specific loop 2 insert increases actin velocity in the *in vitro* motility assay

To investigate the mechanical role of the loop 2 in detail, a MD construct was developed where the IXa specific loop 2 (approx. 200 aa) was replaced by the much shorter loop 2 (∼20 aa) of human skeletal muscle myosin. Amino acids residues 692-887 of human myosin IXa sequence were replaced by the following sequence: SGAQAGEEGGGGKKG-GKKKG. The MD skeletal was assembled from synthetic oligonucleotides and inserted into the pFastBac1 vector (ThermoFisher). The MD skeletal sequence was followed by a glycine linker and the Avi-Tag sequence (GLNDIFEAQKIEWHE). Additionally, a 3x FLAG-tag sequence (DYKDHDGDYKDHDIDYKDDDDK) was added C-terminally to the construct. Recombinant bacmids were obtained as described in chapter 2.1.3 and successful transposition was confirmed by PCR (Fig. 3.6 (b)). Recombinant baculoviruses expressing IXa MD skeletal were generated as previously mentioned. Proteins were expressed and purified as described above, except that 5 L of Sf21 were necessary to get a sufficient protein amount. In contrast to the MD construct the MD skeletal protein eluted in the 500 mM NaCl fraction after the ion exchange chromatography (Fig. 3.6 (c)).

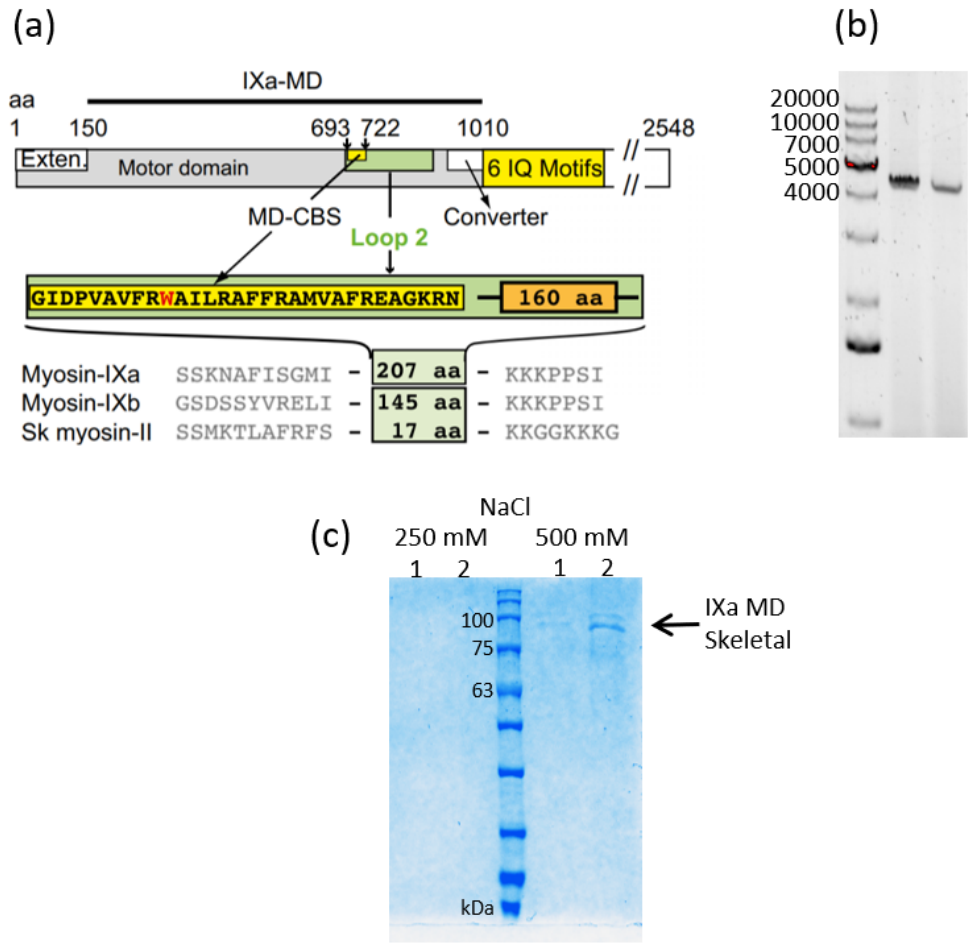

Fig. 3.6: Cloning and expression of a myosin IXa motor mutant with replaced loop 2. (a) Domain architecture of myosin IXa, showing the motor domain (grey), N-terminal extension (white), and calmodulin-binding site in loop 2 (MD-CBS). The neck domain is depicted in yellow with six calmodulin-binding motifs. The tail domain is indicated in white. In the MD skeletal mutant the IXa specific loop 2 (∼200 aa) was replaced by loop 2 (20 aa) of human skeletal muscle myosin (Saczko-Brack et al., 2016). (b) The MD skeletal DNA sequence was purchased from ThermoFisher in a pFastBac1 vector. *E.coli* DH10Bac cells were transformed with this vector and recombinant bacmids were generated. Successful transformation was validated by PCR. Products were examined by gel electrophoresis, revealing bands of correct sizes (∼4.7 kbp). (c) A representative 7.5 % SDS-PAGE gel of purified IXa MD skeletal from 5 L Sf21 cells. The purified protein corresponds well with the expected molecular weight (∼85 kDa).

To test the functionality of the purified IXa mutant, an *in vitro* motility assay was performed. 0.02 mg/mL MD skeletal was site-specifically attached to a glass coverslip via the biotin streptavidin linkage as described previously. Alexa 488 actin was applied to the flow chamber and frames were acquired every 3 s for 10-20 min. Additionally, the

assay buffer contained 100 mM KCl. In the presence of ATP, only individual dissociation and binding events of actin filaments were detected, but no continuous movement of filaments. Increasing the motor concentration on the surface up to 0.2 mg/mL or decreasing the ionic strength of the assay buffer did not result in filament movement. These results suggest that at least a small part of the motors on the glass surface are enzymatically active because they release and rebind actin filaments.

Previous studies on myosin IX of *C. elegans* indicated that the viscosity reagent methylcellulose was necessary to keep actin filaments near the myosin heads for a robust motility (Liao et al., 2010; Elfrink et al., 2014). Methylcellulose has the capability to compensate for decreased actin binding by myosins (Joel et al., 2001). Therefore, the assay buffer was supplemented with 0.5 % (w/v) methylcellulose. Indeed, this viscosity agent increased significantly the amount of moving actin filaments. The mean velocity of actin filaments at 2 mM ATP was 181.0 ± 7.1 nm/s (115 filaments). Compared to IXa MD (23.9 nm/s) the velocity of MD skeletal was more than seven times faster. This result indicated that the removal of the IXa-specific loop 2 insert alters the actin affinity of the motor. This is in good agreement with previous results on isolated loop 2 of rat IXb which bound stoichiometrically and with high affinity to F-actin (Struchholz et al., 2009). Furthermore, it had been proposed by several groups that the loop 2 insertion of myosin IX might act as an actin tether to prevent dissociation from actin filaments (Reinhard et al., 1995; Post et al., 2002; Inoue et al., 2002; Nalavadi et al., 2005; Nishikawa et al., 2006; Kambara and Ikebe, 2006; Liao et al., 2010; Elfrink et al., 2014).
In order to get the steady-state ATP affinity of myosin IXa MD skeletal the average sliding velocity of the motor was calculated over different ATP concentrations (Fig. 3.7 (b)). The actin gliding velocity increased with increasing ATP concentration and the data were fitted to Michaelis-Menten kinetics. The half-maximal velocity was reached at K_{ATP} = 1.1 ± 0.7 mM. Interestingly, the actin gliding velocity did not saturate at 2 mM but reached a V_{max} of 294.1 ± 91.7 nm/s at around 10 mM ATP. The KCl concentration in the assay buffer was adjusted (see Fig. 3.7 (c)) in order to keep the ionic strength at ∼120 mM.

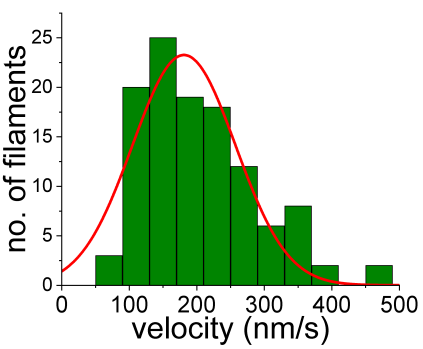

(a)

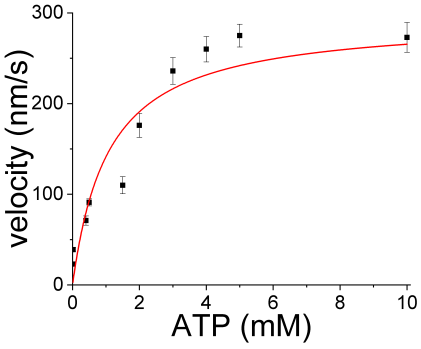

(b)

ATP (mM)	Ionic strength (mM)	KCl (mM)	ATP (mM)	Ionic strength (mM)	KCl (mM)
0.01	116	100	2	120	86
0.02	116	100	3	120	70
0.1	117	100	4	120	52
0.4	120	100	5	120	40
0.5	120	100	7.5	141	25
1.5	120	90	10	150	0

(c)

Fig. 3.7: The *in vitro* motility assay of IXa MD skeletal. (a) A histogram of velocity distributions of MD skeletal. 115 individual filaments from two independent myosin purifications were analysed and the average speed was 181.0 ± 7.1 nm/s (R^2=0.868). (b) The dependence of MD skeletal velocity on ATP concentration. Data was fitted to Michaelis-Menten kinetics and the half maximal velocity was reached at K_{ATP} = 1.1 ± 0.7 mM (R^2=0.678). Each data point represents the average (±SEM) of 30 to 100 tracked filament velocities. (c) Table shows the ionic strength and KCl concentrations in the buffers used to determine the actin gliding velocity. Note that the 10 mM ATP buffer did not contain any KCl, in order to keep the ionic strength low.

3.1.4.5 The 6 IQ domains in the neck region of myosin IXa act as a lever arm

Previous studies on *C. elegans* myosin IX reported unclear results on the velocity of head-neck constructs compared to myosin IX head constructs (Liao et al., 2010). They observed varying acting gliding velocities depending on the myosin preparation. Some head-neck preparations yielded clearly faster velocities, whereas other preparations resulted in the same velocities as the head construct.

To investigate the role of the neck domain of human myosin IXa, *in vitro* motility as-

says with specific biotin-streptavidin linkage were carried out. Motility assays with the biotinylated myosin IXa-S1, containing the motor domain with the six IQ motifs, were performed as described above. In contrast to the IX MD construct, translocation of actin filaments was only observed in the presence of exogenous calmodulin. In the absence of calmodulin only single dissociation and binding events of actin filaments were noted, but no active movement of filaments occurred.

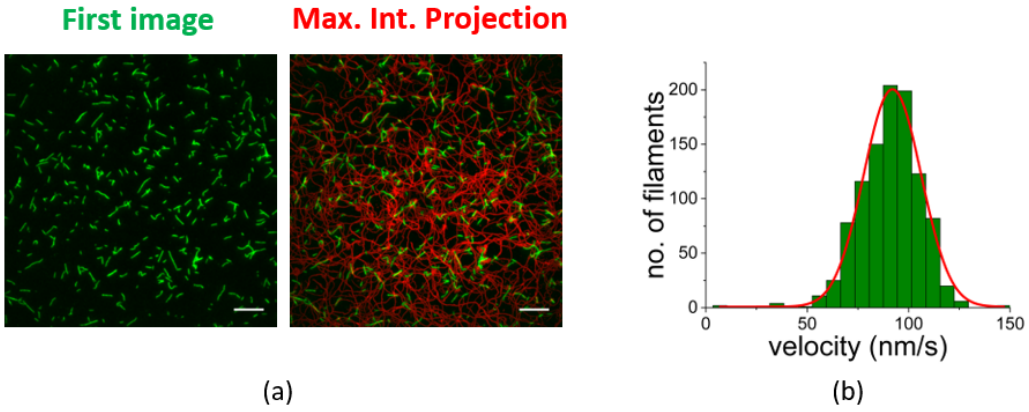

Fig. 3.8: Human myosin IXa S1 translocates actin filaments solely with a 10-fold molar excess of exogenous calmodulin. (a) 0.1-0.2 mg/mL biotinylated IXa S1 was bound site-specifically to a biotin-BSA and streptavidin covered glass coverslip. Unbound myosin was removed with assay buffer and the surface was blocked with BSA. Alexa 488 labelled actin filaments were added to the flow cell and imaged in TIRF on a Nikon Eclipse Ti microscope as described before. Motility was initiated by the addition of an oxygen scavenger system supplemented with ∼15 µM CaMX, 2 mM ATP and 100 mM KCl. Frames were acquired every 3 s for 10-20 min. The Maximum Intensity Projection (representing the collective pixel intensity from several frames) is shown revealing translocation of actin filaments (right image; actin paths in red). Scale bar: 10 µm (b) A velocity distribution plot of myosin IXa S1. 1016 individual filaments from two independent IXa preparations were tracked to collect the data. Data was fitted with a Gaussian distribution (R^2=0.982) and gave a velocity of 91.0 ± 0.9 nm/s at 2 mM ATP.

The mean sliding velocity of IXa S1 was 91.0 ± 0.9 nm/s (N = 1016) – about 4 times faster than that of IXa MD (23.9 nm/s). The increased velocity of IXa S1 compared to IXa MD is clearly visible in the Maximum Intensity Projection by an increased length of the filament traces (compare Fig. 3.5 with 3.8).
These results clearly suggest that the neck domain of human myosin IXa acts as a lever arm to increase the actin gliding velocity. Although not all myosin IXa S1 preparations resulted in a robust translocation of actin filaments, preparations with a stable translocation where

always faster than the head construct of myosin IXa. This is in great contrast to the study of Liao et al. (2010) mentioned above.
Compared to IXa MD the S1 construct contains six additional CaM- binding sites. It might have been expected that the gliding velocity of the S1 construct is 6 times faster compared to the MD construct. It is plausible than one or more IQ motifs in the neck domain do not have a calmodulin bound, or some motifs have a very weak affinity to CaM. This could lead to the lever arm becoming unstable and thus the power stroke being inhibited. Supplementing the assay buffer with up to a 20x molar excess of exogenous calmodulin did not increased the actin velocity in the *in vitro* motility assay.

3.1.4.6 Influence of calcium on the *in vitro* gliding velocity of myosin IXa

Binding of calcium ions to calmodulin was shown to strongly modulate the mechanics and activation level of several myosins (Batters and Veigel, 2016). Solution kinetics studies on human myosin IXa indicated that, in the presence of 100 µM free calcium, the ATPase of the motor domain was stimulated five fold by actin. This data revealed that myosin IXa is regulated by calcium (Saczko-Brack et al., 2016). Since calmodulin binds to the N-terminal portion of loop 2, I investigated the effect of calcium on the actin gliding velocity of IXa MD in the *in vitro* motility assay.
0.1 mg/ml biotinylated IXa MD was immobilized on a coverslip surface via biotin-BSA and streptavidin. Free binding sites were blocked with BSA and Alexa 488-labelled actin was introduced into the flow cell. The assay buffer was supplemented with 2 mM ATP, 100 mM KCl and 0.1 mM free calcium (pCa 4). Subsequent frames were collected as before. As shown in Fig. 3.9 a free calcium concentration of pCa 4 slightly, but significantly increased the actin gliding velocity from 28.1 ± 0.28 nm/s to 33.6 ± 0.33 nm/s.
Solution kinetics studies on *C. elegans* myosin IX showed that the kinetics of the head domain was reduced by a factor of 5 in the presence of 50-100 µM free calcium. Interestingly, the head-neck construct showed a two-fold activation of the maximal F-actin-activated ATPase activity in the presence of calcium (Liao et al., 2010). This result suggests that calcium binding to the neck region of myosin IX affects the motor properties of myosin IXa. As myosin IXa contains six putative calmodulin binding sites in the neck region the effect of calcium was studied also with the myosin IXa S1 construct. Fig. 3.10 shows the summarized results of this *in vitro* motility experiments. Interestingly, 0.1 mM free calcium significantly decreased the actin gliding velocity from 74.1 ± 1.0 nm/s to 30.3 ± 0.8 nm/s. This result lead to the hypothesis that calcium binding to neck-bound calmodulin of myosin IXa could destabilize the lever arm in such a way that it is hampered to make a complete power stroke. Even though calcium binding to head-bound calmodulin increases

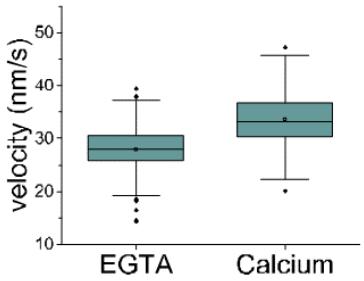

(a)

condition	velocity (nm/s)	SEM	N
EGTA	28.06	0.28	221
Calcium	33.57	0.33	212

(b)

Fig. 3.9: The effect of calcium on the velocity of IXa MD. (a) Box plot of actin gliding velocities in the absence (EGTA) and presence of 0.1 mM free calcium (pCa 4). The data for each condition was collected from three independent flow cells. A statistical analysis using the two-sample student's t-test indicated a significant difference between the two conditions ($p < 0.001$). (b) Average values of the actin gliding velocities of myosin IXa motor domain in the absence and presence of calcium. In total 433 filaments were included in this analysis.

the actin gliding velocity, the destabilizing effect on the neck region is predominant.

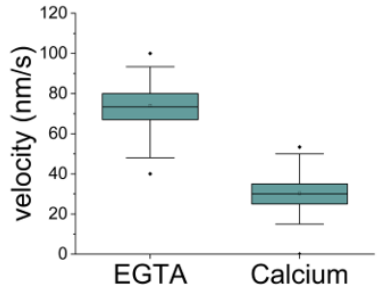

(a)

condition	velocity (nm/s)	SEM	N
EGTA	74.13	0.97	119
Calcium	30.35	0.78	110

(b)

Fig. 3.10: The effect of 0.1 mM free calcium on the actin gliding velocity of myosin IXa S1. (a) A box plot shows that calcium significantly decreases the actin velocity in the *in vitro* motility assay ($p < 0.001$, two-sample student's t-test). The data for each condition was collected from three independent flow cells and is summarized in the table shown in (b).

3.1.4.7 Myosin IXa moves towards the plus end of dual-labeled actin filaments

In vitro motility assay with polarity labelled actin filaments on tail-less myosin IXb constructs showed that it moves towards the minus end of the actin filaments (Inoue et al., 2002). However, experiments on full-length myosin IXb indicated that it is a plus-end-directed motor (O'Connell and Mooseker, 2003). These results indicate that the tail domain of myosin IXb regulates motor directionality.

To determine the directionality of myosin IXa constructs I performed motility experiments with polarity labelled actin filaments. In those experiments biotinylated myosin IXa MD was site-specifically bound to a glass coverslip coated with biotin BSA and streptavidin. Free binding places were blocked with BSA and 10 nM polarity labelled actin filaments were introduced into the flow cell. The assay buffer was supplemented with 2 mM ATP and 100 mM KCl. Actin filaments were visualised using TIRF on a Nikon Eclipse Ti microscope. Filament movement was manually tracked, and colour of the leading filament end was registered. For a filament to be considered for analysis, each filament had to show precisely two well defined parts of different labelling, and the filaments entire length had to be visible for at least 5 consecutive frames of filament movement.

In order to verify the correct polarity labelling of actin filaments, directionality was first determined for muscle myosin II HMM and full-length myosin VI, i.e. for motor proteins of known direction of movement. For HMM, 94 dual-labelled filaments from 3 different flow cells were analysed (Fig. 3.11). 92 (97.9 %) of these filaments showed a leading

plus end, thus HMM was identified as plus end-directed motor. The evaluation of 106 filaments from myosin VI samples resulted in 94.3 % of the filaments exhibiting a leading minus end. Therefore, myosin VI motor movement was determined as minus end-directed.

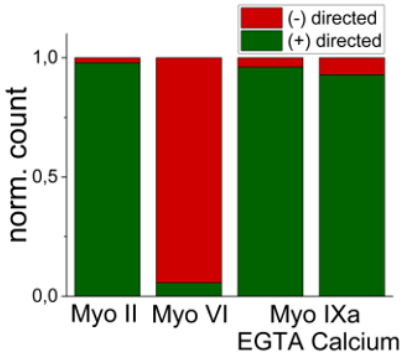

(a)

	(+) directed	(-) directed
Myo II HMM	92	2
Myo VI	6	100
Myo IXa MD EGTA	97	4
Myo IXa MD Calcium	104	8

(b)

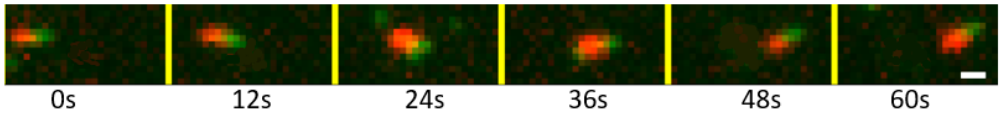

(c)

Fig. 3.11: Determination of motor directionality in gliding filament assays with dual-labelled F-actin. (a) Relative comparison of filaments indicating plus end- or minus end-directed movement of muscle myosin II HMM, chicken full-length myosin VI, and human IXa MD. Control experiments with myosin II and VI verified the applied method. Myosin IXa MD was found to be a plus end-directed motor in the absence and presence of calcium (pCa 4). (b) A table showing the absolute number of filaments used in the evaluation. At least three independent flow cells for each motor protein or condition were used to collect the data. (c) Sequential images of dual-labelled actin sliding on a surface covered with myosin IXa in the absence of calcium: the leading Alexa 488-labelled minus end (green) demonstrates movement of myosin IXa towards the Rhodamine-labeled plus end (red). Scale bar: 1 µm

As these findings were in agreement with the literature (Huxley, 1969; Sheetz and Spudich, 1983; Wells et al., 1999), gliding filament assays with myosin IXa MD were performed. 5 flow cells were prepared and in total 101 filaments were analysed. 97 of these filaments (96.0 %) showed a leading plus end. Therefore, myosin IXa MD was identified as a plus end-directed motor protein. This is the first study to show that human myosin IXa moves towards the plus-end of actin filaments.

As *in vitro* motility assay experiments in the presence of calcium showed a slight but

significant increase of the actin gliding velocity (see above), I investigated the effect of calcium on the directionality of actin filaments. Experiments were performed as above, except that the assay buffer was additionally supplemented with 0.1 mM free calcium (pCa 4). 112 filaments of 6 different flow cells were analysed and 104 of them (92.9 %) showed plus-end directed movement. These results indicate that calcium does not change the polarity of actin filaments in the *in vitro* motility assay.

3.1.5 Single-molecule measurements using optical tweezers

This section describes the first optical tweezers measurements on human myosin IXa. Single-molecule experiments were performed with different myosin IXa constructs, revealing the distinct function of the neck domain and the loop 2 insert. Initially, I show that site-specific immobilization of the motor protein on a glass surface is necessary to observe a reasonable power stroke size. Optical tweezers measurements on a loop 2 mutant of myosin IXa indicate, that this ∼200 aa sized loop 2 insert affects the kinetics of the motor protein, but does not have any impact on the power stroke size. This result explains the observed increased in vitro motility assay velocity measured in section 3.1.4.4. Furthermore, I show that the six IQ domains of myosin IXa act as a lever arm and produces a working stroke of ∼24 nm.

3.1.5.1 Control experiments with skeletal muscle myosin II

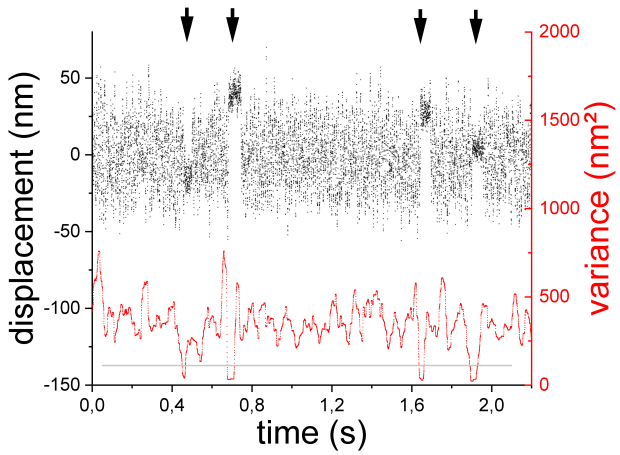

Fig. 3.12: Single-molecule binding events in an optical trap setup. The time trace in black shows the displacement of one dumbbell bead cast on the 4QD detector. Binding events of a single muscle myosin II HMM molecule with the bead-actin-bead dumbbell are highlighted with arrows (20 µM ATP). The reduction in amplitude below a certain threshold (grey line) of the variance (shown in red) was used to identify individual binding events. Data was obtained at 0.02 pN/nm single trap stiffness and 22°C.

Control measurements were performed with skeletal muscle myosin II HMM. Trapping flow chambers with 2.1 µm glass microspheres on a 0.1 % nitrocellulose surface were prepared as described in chapter 2.6.2. 2 ng/mL HMM was bound to the flow cell surface for 3 min. Unbound myosin was washed out with assay buffer and unspecific binding places on the glass surface were blocked with BSA for 3 min. After blocking, the solution was replaced with an oxygen scavenger system supplemented with various ATP concentrations,

an ATP backup system, rhodamine labelled actin filaments and neutravidin coated beads. All experiments were performed at 22°C, using a trap stiffness of 0.02 pN/nm per trap. A 100 nm 100 Hz sinusoidal oscillation was applied to one of the optical traps. Data was collected at 5 kHz.
When an actomyosin crossbridge between the constructed bead-actin-bead dumbbell and a myosin bound on a third surface bead formed, the overall system stiffness increased. This created a reduction in the thermal motion and applied sinusoidal oscillation. Single-molecule binding events were identified from changes in variance in the data (Fig. 3.12). This data can then be used to determine the myosin power stroke size, lifetimes, rate constants and stiffness of the myosin.

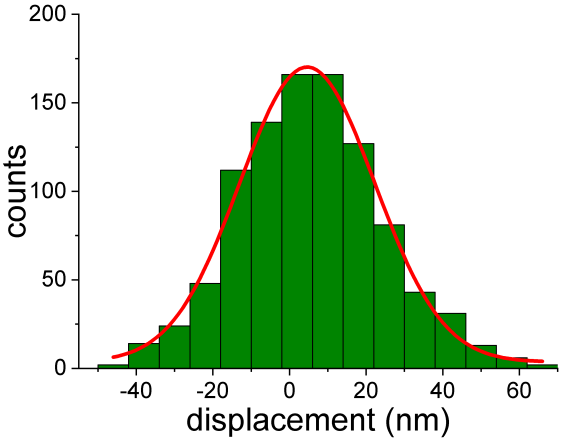

Fig. 3.13: Frequency distribution of the displacements of single muscle myosin II HMM binding events. Measurements were obtained from 4 separate actin filaments and combined to give one large data set (N=974). Data was fitted with a Gaussian distribution (R^2=0.989) and gave a displacement of 4.6 ± 0.5 nm. Measurements were obtained at 20 µM ATP, 0.02 pN/nm single trap stiffness and 22°C.

For the determination of the power stroke size of muscle myosin II HMM, data from 4 filaments (and therefore from several single myosins) was collected and pooled to give in total 974 individual binding events. Fig. 3.13 shows a histogram of the amplitude of the displacements. The histogram shows a large distribution due to the background thermal vibration and the applied sinusoidal oscillation of 100 nm and 100 Hz. The raw data was corrected to allow for series compliance (approximately 10 %). The correction factor was determined from the ratio of bound and detached stiffness's (see chapter 2.6.4). The data was fitted with a Gaussian distribution and gave a displacement of 4.6 ± 0.5 nm.

The lifetime of a single event depends on the probability that an event will end, and

that probability depends on the kinetics of the myosin being measured. Although binding events are stochastic, their average lifetime is typical for the myosin. Fig. 3.14 shows the distribution of event lifetimes at 10 and 20 µM ATP obtained from 274 and 974 individual myosin II events, respectively. The data can be fitted with a single exponential decay with the characteristic half-life $t_{1/2}$ of 87.60 ± 3.06 ms and 30.85 ± 0.51 ms for 10 and 20 µM ATP, respectively. This time parameters describe the ATP dependent detachment time of myosin from actin.

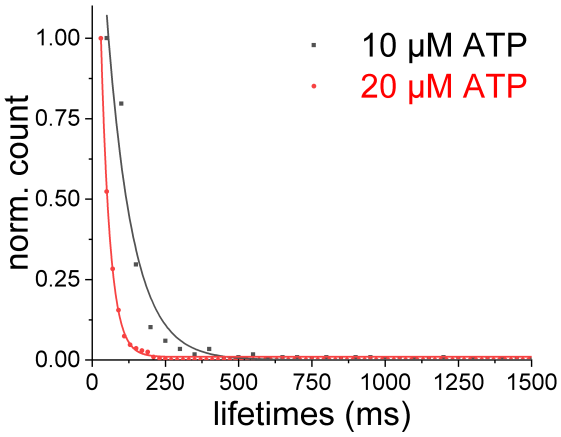

Fig. 3.14: Lifetime distribution of rabbit skeletal myosin II HMM at 10 and 20 µM ATP demonstrates the stochastic nature of events. At 10 µM ATP a single exponential fit revealed a half-life $t_{1/2}$ of 87.60 ± 3.06 ms (N=274; R^2=0.966), whereas at 20 µM ATP $t_{1/2}$ was 30.85 ± 0.51 ms (N=974; R^2=0.999). This gives an average detachment rate of myosin II from actin of 1.4 μM^{-1} s^{-1}.

The homogeneity of the analysed datasets can be reviewed by plotting the displacement vs. lifetime or displacement vs. recording time (see Fig. 3.15). These plots allow the investigator to control whether the data has any anomalies, e.g. if the data contains more than one distribution, or if the distribution changes over time.

As the measured displacements and lifetimes of rabbit skeletal myosin II HMM were homogenous and in agreement with the literature (Molloy et al., 1995; Veigel et al., 1998; Tyska and Warshaw, 2002) single-molecule mechanical experiments with myosin IXa could be performed.

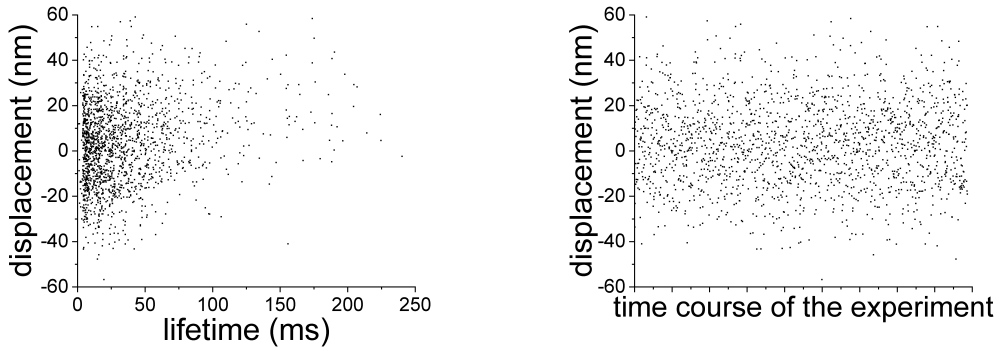

(a) (b)

Fig. 3.15: Plots to review the homogeneity of single-molecule data sets. A displacement vs. lifetime plot (a) and a displacement vs. recording time plot (b) of raw data points of the myosin II HMM data set shown in Fig. 3.13. These plots shows if there is any clustering or discrepancy in the data. In this example the data set is homogeneous.

3.1.5.2 Myosin IXa motor domain nonspecifically attached to surface produces a very small power stroke

First single-molecule mechanical experiments with myosin IXa MD were performed with the motor protein nonspecifically bound to a nitrocellulose coated glass surface similar as in control experiment with muscle myosin II. Non-specific binding of myosin to nitrocellulose leads to different orientations of molecules on the surface. As a single-molecule method is applied, the investigator scans several surface beads with the bead-actin-bead dumbbell until binding events are detected. This means that solely such myosins are selected that can perform a complete power stroke .
10-50 ng/mL IXa MD was injected into the trapping flow cell and incubated for 3 min. After blocking with BSA, an oxygen scavenger system supplemented with various ATP concentrations, 100 mM KCl, an ATP backup system, rhodamine labelled actin filaments and neutravidin coated beads were introduced into the flow cell. Experiments were performed at a trap stiffness of 0.02 pN/nm per trap and 22°C.
Fig. 3.16 shows single-molecule binding events of myosin IXa MD. IXa produced single, intermittent interactions with actin and no processive steps were observed, which is consistent with a nonprocessive motor. Analysis of the power stroke size of 397 single interactions from 3 different filaments revealed a power stroke size of 0.24 ± 0.66 nm.

Trapping experiments were performed at 50 and 100 µM ATP and the distribution of event lifetimes showed a single exponential decay with a half-life $t_{1/2}$ of 90.4 ± 15.6 ms and 56.1 ± 6.3 ms for 50 and 100 µM ATP, respectively. Data was obtained from 108 (50

µM ATP) and 253 interactions (100 µM ATP).

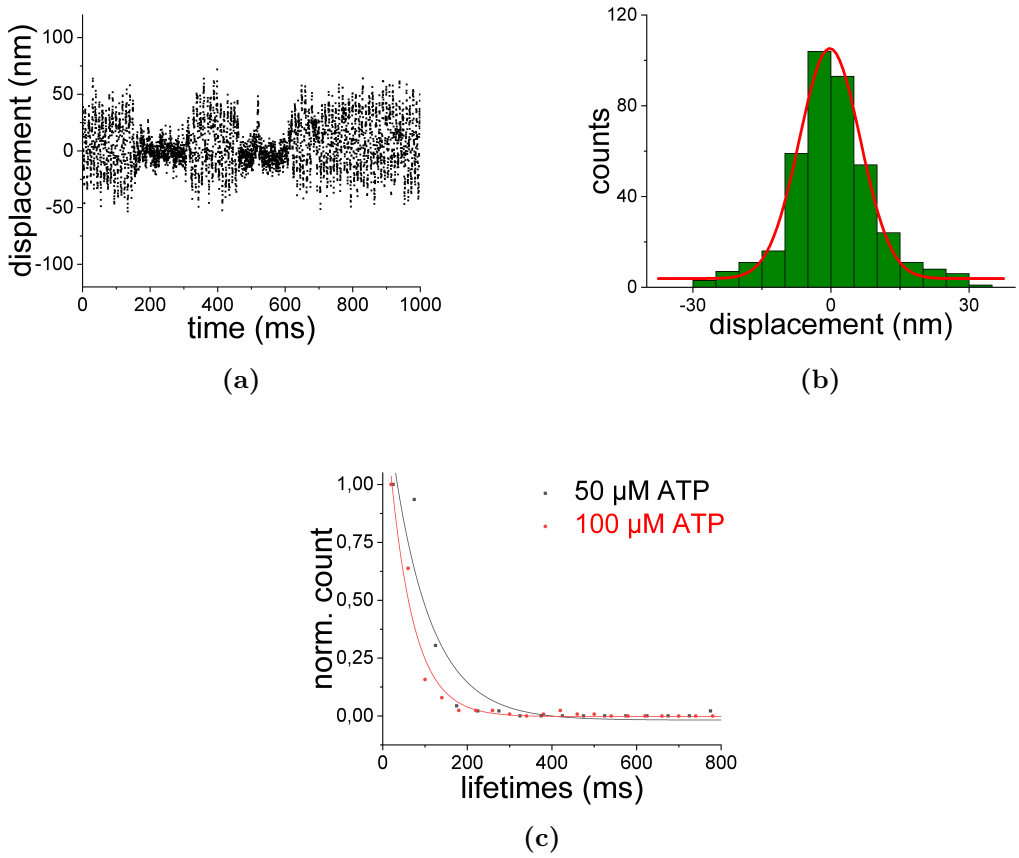

Fig. 3.16: Single-molecule trapping experiments with myosin IXa nonspecifically attached to a nitrocellulose surface. (a) Original file traces of the interaction of a single IXa MD molecule with the bead-actin-bead dumbbell. Trace shows the displacement of one dumbbell bead cast on the 4QD detector. (b) Distribution of mean displacement during 397 attachments of IXa MD. Data was fitted with a Gaussian distribution (R^2=0.985) and gave a displacement of 0.24 ± 0.33 nm. (c) Histogram of dwell times of single MD interactions in the presence of 50 and 100 µM ATP. The solid line shows a single exponential fit with a half-life $t_{1/2}$ of 90.4 ± 15.6 ms (R^2=0.914) and 56.1 ± 6.3 ms (R^2=0.974) for 50 and 100 µM ATP, respectively.

The power stroke of IXa MD obtained in these experiments is very small. From the kinetic measurements at 50 and 100 µM ATP an average detachment rate constant of 0.2 μM^{-1} s^{-1} can be determined. At 2 mM ATP this gives an average binding event duration of 2.5 ms. Together with the measured power stroke size of 0.24 nm a maximal velocity v can be determined:

$$v = \frac{\text{power stroke size}}{\text{binding event duration}} = \frac{0.24\text{nm}}{2.5\text{ms}} = 96\text{nm/s}$$

This means that single-molecule data suggests a maximal velocity of myosin IXa MD of around 100 nm/s at 2 mM ATP. Compared with the measured velocity in the *in vitro* motility assay (24 nm/s; see section 3.5), this value deviates by a factor of 4.
The small power stroke size might be explained by the fact, that myosin IXa MD was nonspecific bound to the nitrocellulose coated coverslip. The molecules might have a preferred position to bind to the surface so that the distribution of different geometries is not random. The observed binding events in the above experiments could be explained by myosin molecules, which are able to bind actin but are bound in such a geometry on the surface, that they are incapable of undergoing a complete power stroke.
On the other hand, the myosin IXa construct used in the above experiments comprises solely the motor domain without a neck domain. The expected power stroke must be quite small as expected from single-molecule studies with smooth muscle HMM molecules, where the neck domain length was artificially modified by either deleting or adding light chain binding sites (Warshaw et al., 2000). In this study the neckless myosin mutant generated an average displacement of 2.0 nm, which is much bigger than the value obtained in the experiments presented here.

3.1.5.3 Site specific attachment of myosin IXa increases power stroke size

To test if a specific attachment of IXa MD molecules to the glass surface could alter the measured power stroke, the nitrocellulose coated surface of the trapping flow cells was covered with a FLAG antibody. The myosin IXa sequence contains a C-terminal FLAG sequence for purification and can therefore be bound to the surface in such a way that the N-terminal head region is free to interact with actin. 1 ng/ml anti-FLAG antibody was injected into the flow cell and incubated for 4 min. After a thorough wash with PBS, ∼20 pM myosin IXa was introduced into the flow cell and then the surface was blocked with BSA. Afterwards, dead myosin heads were blocked with phalloidin labelled actin. This solution was replaced by an oxygen scavenger system with different ATP concentrations, 100 mM KCl, an ATP backup system, rhodamine labelled biotinylated F-actin and beads. Fig. 3.17 (a) shows raw data traces of single myosin IXa interactions with actin. Similar to Fig. 3.16 single intermittent interactions with actin were observed and no processive steps could be detected. Evaluation of 321 single-molecule interactions from two independent MD preparations filaments showed a power stroke size of 4.8 ± 0.2 nm (see Fig. 3.17 (b)), 20 times greater than the power stroke obtained from measurements of non specific attachments of myosin IXa to a nitrocellulose surface. This result clearly demonstrates that site specific attachment of myosin IXa alters the power stroke. By binding the

myosin to the surface with an anti-FLAG antibody, the molecules are oriented in such a way that the myosin heads can move freely for a complete power stroke. Because of this pronounced effect of the site-specific binding, all further trapping experiments with myosin IXa constructs were carried out with the anti-FLAG antibody.
The power stroke measured here fits well with previous studies on neckless myosin mutants (see above, Warshaw et al. (2000); Ruff et al. (2001)) and suggests that the fulcrum for lever arm rotation lies a few nanometres inside the C-terminus of the head domain. This hypothesis is also supported by *in vitro* motility assay measurements in this work, which show that the motor domain of myosin IXa alone is sufficient to produce movement.

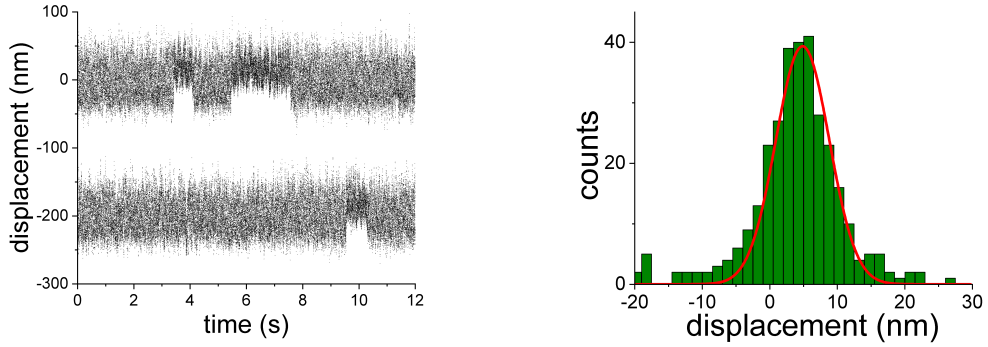

(a) **(b)**

Fig. 3.17: Site specific attachment of myosin IXa MD to a glass surface with an anti-FLAG antibody alters the displacement. (a) Original file traces of single IXa MD interactions with actin at 2 mM ATP and a single trap stiffness of 0.02 pN/nm. Two time traces with each 12 s show the displacement of one dumbbell bead cast on the 4QD detector. (b) Frequency distribution of the displacement during 321 attachments of IXa MD at 100 µM ATP. Fitting the data to a Gaussian distribution (R^2=0.910) gave a displacement of 4.8 ± 0.2 nm. Data was obtained from two independent IXa MD preparations.

3.1.5.4 Kinetics

Optical trapping measurements with site specific attachment of the IXa MD construct were performed with three different ATP concentrations (10, 100 and 2000 µM). Interestingly, unusual long binding events were visible in the data traces, sometimes lasting longer than 10 s (see Fig. 3.18 (a)). In total 8-10 % of the data consisted of events longer than 1000 s and the amount depended on the ATP concentration. The origin of those long events from so-called dead heads, inactive or denatured myosin motors (e.g. due to oxidation at the actin binding site) that are unable to unbind from an actin filament after attaching, could not be excluded. However, the presence of one or several short lived (<1000 ms) events after a long event (as seen in Fig. 3.18 (a)) suggested that the par-

ticular myosin head was still enzymatically active and able to bind and unbind from actin.

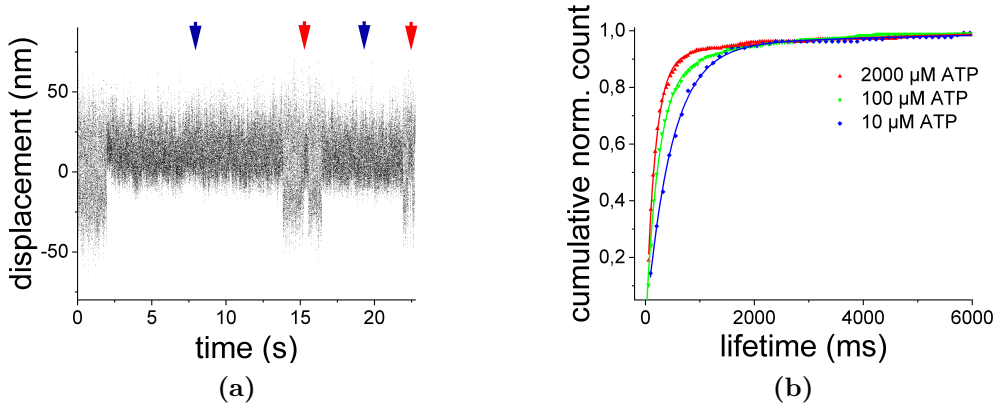

Fig. 3.18: Lifetime analysis of site specific attached myosin IXa MD. (a) Analysis of the kinetics revealed the presence of atypical long binding events (blue arrows). The raw data trace at 2 mM ATP shows two long binding events followed by short binding events (red arrows), indicating that the long attachment events originate from an enzymatically active head. (b) Cumulative histogram of dwell times of IXa MD interactions in the presence of 10, 100 and 2000 µM ATP (N=130, 500 and 300). The solid lines show a double exponential fit (R^2=0.998 for all three ATP concentrations).

Despite the presence of those long events, the myosin IXa MD construct showed an ATP dependent behaviour as shown in Fig. 3.18 (b) and was consistent with the motility assay data.

3.1.5.5 Removal of myosin IXa specific loop 2 insert does not change power stroke size but affects kinetics

In vitro motility experiments on the MD skeletal mutant, where the loop 2 of myosin IXa was exchanged against the much shorter loop 2 of skeletal myosin II, showed a seven times increased actin gliding velocity (180 nm/s) compared to IXa MD (24 nm/s) at 2 mM ATP (see section 3.1.4.4). From a single-molecule point of view several explanations could explain this observation: A) The power stroke size of MD skeletal increases compared to MD while the kinetics remains unchanged. In this scenario myosin IXa skeletal would be able to make a bigger power stroke in the same period of time, which would result in a increased actin gliding velocity. B) The power stroke size remains the same, but the kinetics alters. C) Both parameters are changing, kinetics as well as power stroke size.

To test which explanation describes the increased velocity in the *in vitro* motility assay, trapping experiments were performed as described above. Around 5-10 µg/mL (approx.

50 nM) IXa MD skeletal were introduced into a flow cell, which was covered with the anti-FLAG antibody. Fig. 3.19 (a) shows the Gaussian distribution of 739 individual MD skeletal binding events giving a displacement of 4.9 ± 0.2 nm, very similar to the value obtained for IXa MD (4.8 ± 0.2 nm). A unpaired Student's t test revealed that the difference between the working stroke size values was not statistically significant (two-tailed p value <0.01).

Analysis of the lifetimes at 100 and 2000 µM ATP and comparison with the MD construct showed a clear difference in the kinetics between the two constructs. For both ATP concentrations the MD skeletal was characterized by a faster kinetics than the MD construct (see Fig. 3.19 (b) and (c)).

These results clearly demonstrate that the increased velocity in the *in vitro* motility assay can be explained by a molecular perspective. Without the IXa specific loop 2 insert, myosin IXa is still able to perform a power stroke with the same size as wildtype MD. Nevertheless, the kinetic is faster for MD skeletal compared to wildtype MD indicating that the loop 2 insert of IXa has some impact on the ATPase cycle or interacts with the actin binding capability. The latter hypothesis is in good agreement with previous studies on loop 2, where it was proposed that the loop 2 insertion of myosin IX might function as an actin tether to prevent dissociation from actin filaments (Struchholz et al., 2009; Elfrink et al., 2014).

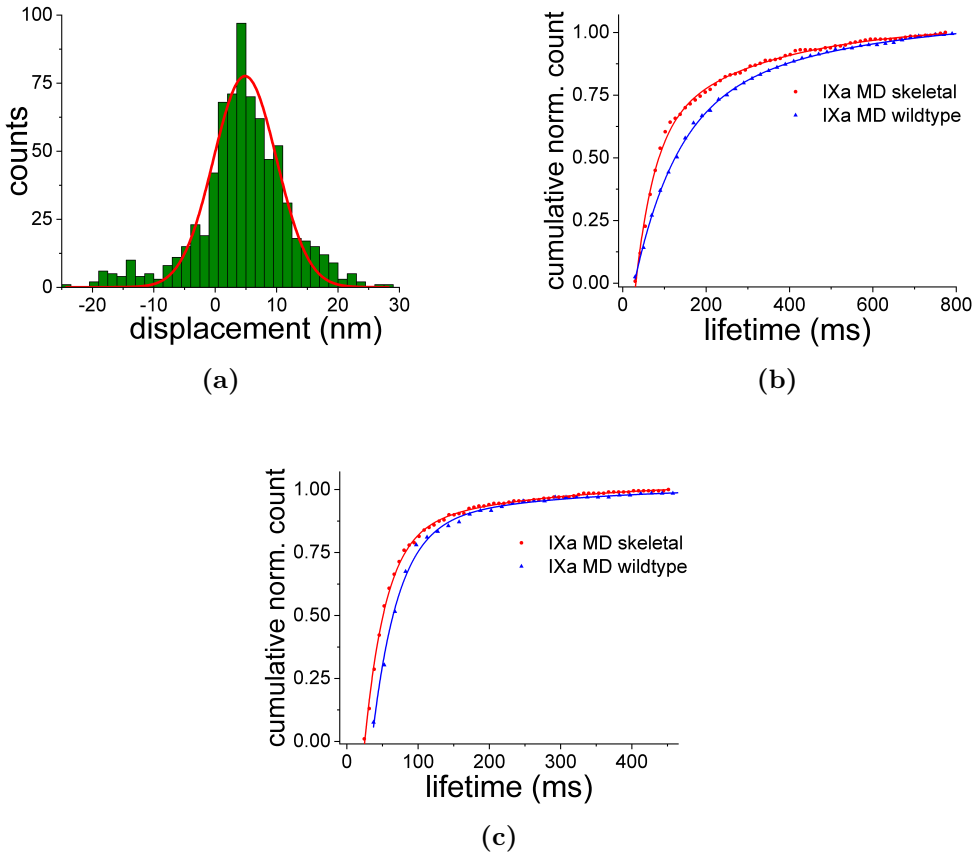

Fig. 3.19: Exchange of the IXa specific loop 2 accelerates kinetics but does not affect the power stroke size of myosin IXa. (a) Myosin IXa MD skeletal was site specific attached to a glass surface via an anti-FLAG antibody. Analysis of 739 single-molecule attachments resulted in a displacement of 4.9 ± 0.2 nm at 2 mM ATP and 0.02 pN/nm single trap stiffness (R^2=0.935). This value is similar to the displacement of IXa MD molecules. Data was obtained from two independent IXa MD skeletal preparations. (b) & (c) Comparison of the kinetics at 100 (b) and 2000 µM ATP (c) revealed a clear difference between MD skeletal (red datapoints) and MD (blue datapoints). Data was fitted with a double exponential fit (solid lines) with a R^2 of 0.997 (N=260) and 0.998 (N=250) for MD skeletal and a R^2 of 0.999 (N=270) and 0.996 (N=210) for MD wildtype at 100 and 2000 µM ATP, respectively.

3.1.5.6 Removal of loop 2 insert decreases motor stiffness

To assess the effect of the class IX specific loop 2 insert on the mechanical properties in further detail, stiffness measurements were carried out with MD skeletal and MD wildtype. If a sinusoidal waveform (100 Hz, 100 nm peak-to-peak) is applied to one bead in the bead-actin-bead dumbbell, the second bead follows this signal in a passive manner. The amplitude reduction is used to calculate the stiffness of the myosin head (see chapter 2.6.5).

As shown in Fig. 3.20 (a) a binding event is followed by a sharp stiffness increase. Each

data point in the raw optical trapping trace was used to calculate the stiffness and a histogram was plotted for MD wildtype and MD skeletal (Fig. 3.20 (b) and (c)). The data was fitted to a logarithmic normal distribution and centered at 0.39 ± 0.002 pN/nm for MD wildtype and 0.26 ± 0.005 pN/nm for MD skeletal. The data clearly shows that MD skeletal has a lower stiffness than MD wildtype.

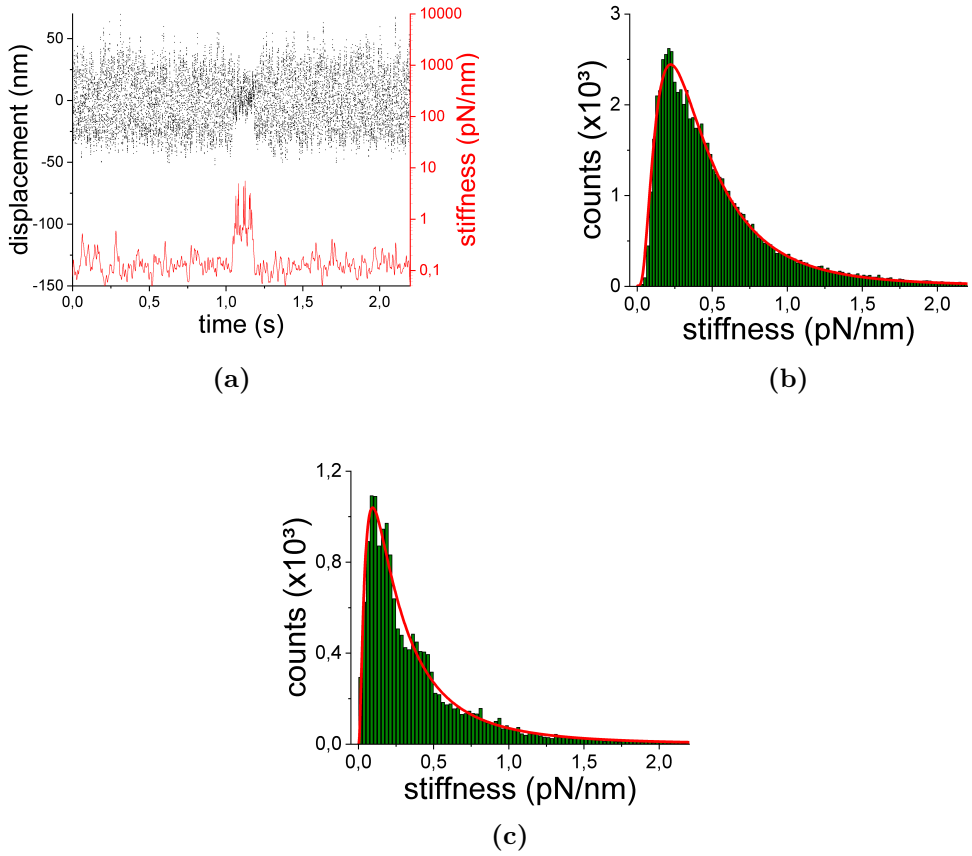

Fig. 3.20: The class IX specific loop 2 insert affects the stiffness of myosin IXa. (a) Exemplary raw data from a single myosin IXa MD wildtype binding event at 2 mM ATP is shown in black. A discrete Fourier transformation analysis was used to calculate the stiffness plotted in red. (b) Several binding events were used to calculate the stiffness for myosin IXa MD wildtype. Data was fitted with a logarithmic normal distribution and centered at 0.39 ± 0.002 pN/nm (R^2=0.993). (c) Stiffness evaluation of MD skeletal events showed a decreased stiffness with the fit centering at 0.26 ± 0.005 pN/nm (R^2=0.980).

These results indicate that the unique >200 aa loop 2 insert does not only influences the kinetics of the actomyosin interaction, but also effects the stiffness of the binding events.

3.1.5.7 The head-neck construct creates a working stroke of ∼24 nm

In vitro motility experiments with myosin IXa S1, containing the motor domain with six IQ motifs ('neck'), exhibited a four times faster actin gliding velocity (91 nm/s) at 2 mM ATP compared to the 'neckless' myosin IXa MD construct (24 nm/s; see section 3.1.4.5). This increased velocity suggests a lever arm effect of the IQ motifs which was also shown for *Dictyostelium* myosin II mutants, where the sliding speed was linearly dependent on the neck domain length (Uyeda et al., 1996).

On a single-molecule level this lever arm effect should be apparent in an increased power stroke of IXa S1 compared to the MD construct. To test this hypothesis, optical trapping measurements were performed as described above. 5-10 ng/ml (20-40 nM) myosin IXa S1 was bound site specifically to a surface coated with an anti-FLAG antibody. Dead myosin heads were blocked with phalloidin labelled actin. This solution was replaced by an oxygen scavenger system with different ATP concentrations, 100 mM KCl, an ATP backup system, rhodamine labelled biotinylated F-actin and beads. Additionally, similar to the *in vitro* motility experiments a 10 times molar excess of calmodulin was added to the trapping mix.

Fig. 3.21 shows the power stroke analysis of 397 single myosin IXa S1 interaction from 2 different filaments. Surprisingly, the distribution showed two main peaks. Data was fitted with a double Gaussian distribution and resulted in peaks at -1.3 ± 0.5 nm and 23.7 ± 0.3 nm.

A peak at around 0 nm appeared also in other, smaller datasets at 100 µM ATP and was also present at 10 µM ATP (data not shown). This '0 nm peak' could represent loop 2 interactions with actin. The 200 amino acid sized loop 2 is unable to make a conventional power stroke, but could bind and unbind to actin filaments in a stochastic manner. This idea is supported by biochemical studies on isolated loop 2 of rat myosin IXb, which showed that loop 2 can bind to F-actin in solution (Struchholz et al., 2009). In this scenario myosin IXa S1 would be able to make two different kind of interactions: A 24 nm power stroke performed by the catalytic head-neck domain and a 0 nm interaction of the loop 2.

If the 0 nm peak represents loop 2 interactions with actin, than this peak should be present also in myosin IXa MD interactions. Indeed, a closer look at the displacement histogram of IXa MD (see Fig. 3.17) shows that a slight shoulder is apparent at ∼0 nm. It remains unclear why the 0 nm peak is so prominent in the S1 construct (peak is almost twice as high as the 24 nm peak), whereas it is inconspicuous in the MD construct.

Compared to the displacement of site specific bound myosin IXa MD (4.8 nm) the not-zero displacement of the head-neck construct was about 5 times bigger. To a similar

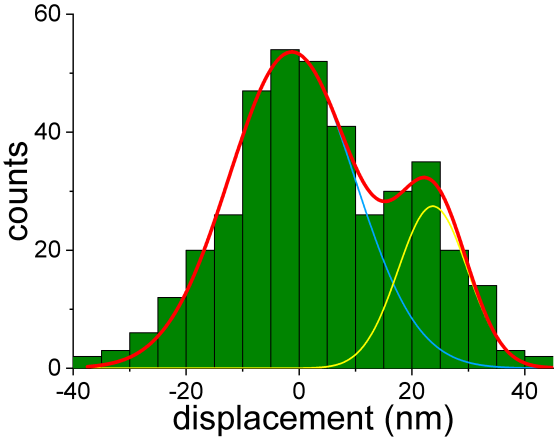

Fig. 3.21: Power stroke analysis of myosin IXa S1, containing the motor domain with six IQ motifs. Myosin IXa S1 was site specifically bound to the surface with an anti-FLAG antibody and single-molecule interactions were measured at 100 µM ATP and 0.02 pN/nm single trap stiffness. Interestingly, the distribution of mean displacements during 397 attachments showed two main peaks. Data was fitted with a double gauss fit (red line) and gave peaks at -1.3 ± 0.5 nm and 23.7 ± 0.3 nm (R^2=0.973). Single Gaussian distributions of the main peaks are shown in yellow and blue.

extent, also the actin gilding velocity in the *in vitro* motility assay was about 4 times greater for the S1 compared to the MD construct. The single-molecule measurements presented here support the idea that the neck domain of human myosin IXa act as a lever arm. Although the S1 construct contains six putative calmodulin (CaM) binding sites and exogenous CaM was present during optical trapping measurements, it is possible that one or two IQ motifs are not saturated with CaM or they have a very weak affinity to CaM.

It is worth mentioning that some datasets resulted in a power stroke size of <20 nm (data not shown). This supports the above mentioned idea, that the neck domain is not completely saturated with calmodulins and therefore leads to a destabilization of the lever arm.

In contrast to optical tweezers studies on human myosin IXb no processive steps could be detected in my measurements (Nishikawa et al., 2006). In this study the head-neck construct took several, approx. 20 nm steps before it detached from an actin filament. Interestingly, they pointed out that processive movement was not observed for all molecules and they observed also isolated single step displacements with a smaller amplitude (13 nm). Nishikawa et al. (2006) speculated that myosin IXb exists in two forms, one with processive motility and the other form has no processive motility. Therefore, processivity could be regulated by an currently unknown mechanism (e.g. phosphorylation). Such

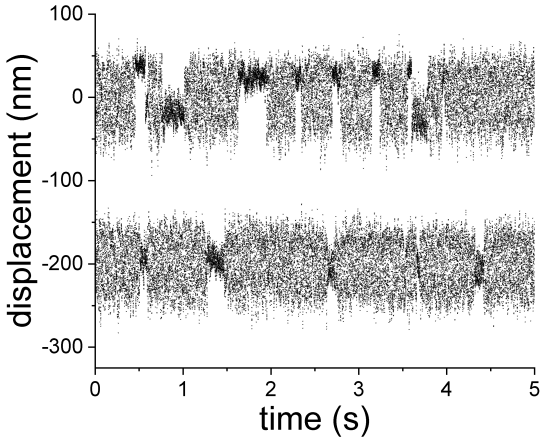

Fig. 3.22: Raw data traces of single myosin IXa S1 interactions. The head-neck constructs produced single, intermittent interactions with actin and no processive steps were observed, which is consistent with a nonprocessive motor. Data was obtained at 100 µM ATP and a single trap stiffness of 0.02 pN/nm.

a regulation mechanism could be also plausible for human myosin IXa, although there exists no experimental evidence that would suggest a processive behaviour of myosin IXa.

3.1.6 Actin bundling induced by myosin IXa

This section investigates the actin bundling capability of human myosin IXa. Using TIRF microscopy I show that the class IX specific loop 2 is the molecular basis for bundle formation and creates a second actin binding site in the head domain of myosin IXa. A quantitative analysis revealed that up to seven filaments could be resolved in the bundles. Transmission electron microscopic data showed that the bundles consisted of highly ordered lattices. The myosin IXa motor domains formed cross-links with a repetition distance of exactly 36 nm, which matches the helical repeat of actin. Intriguingly, this experiments showed that actin bundles could still be formed in the presence of millimolar ATP concentrations. Furthermore, I show that bundle dissociation occurs in discrete, ATP dependent events.

3.1.6.1 A modified in vitro motility assay shows that myosin IXa forms actin bundles

Recent studies indicated a central role of myosin IXa in regulating the collective migration of epithelial cells through the formation of actin bundles near cell–cell adhesions (Wood and Olson, 2012; Omelchenko and Hall, 2012). However, the detailed molecular mechanisms involved in class IX myosins organising the actin cytoskeleton are not known. Moreover, the velocity of myosin IXa in the *in vitro* motility assay measured in the section above is very slow compared with other myosins (e.g. skeletal myosin II with 4 µm/s) suggesting a more structural role.

To investigate this topic in further details, I performed a slight modification of the inverted motility assay (see Fig. 3.23 (a)). NEM modified myosin II was immobilized on a nitrocellulose coated coverslip and free binding places on the glass surface were blocked with BSA. Myosin IXa MD was mixed at a 1:1 molar ratio with Alexa 488 labelled actin in solution and was introduced into the flow cell. After addition of an AB- oxygen scavenger system supplemented with 100 mM KCl, bundles were imaged using a two-colour TIRF setup based around a Olympus IX70 microscope. This allowed a simultaneous TIRF excitation of Alexa 488 and Cy3. Each dye was then imaged onto one half of the chip of an EM-CCD camera.
As shown in Fig. 3.23 (b) high and low intensity signals of actin filaments were observed, which corresponded to a different amount of bundled actin filaments. They were equally distributed over the entire field of view. Long actin filaments bundles with a high intensity were mostly accompanied with low intensity signals at their filament ends. To elucidate

the role of myosin IX in this bundles, an anti-FLAG antibody labelled with Cy3 was added to the oxygen scavenger system. The antibody solely labelled the high intensity actin bundles, which indicates that myosin IXa was present there. The greater the intensity signal in the actin channel, the higher the intensity in the myosin IXa channel. This experiments clearly showed that myosin IXa has the ability to bundle actin filaments. The bundles were up to 100 µm in length and its intensity was dependent on the duration of IX-actin incubation and the concentration of myosin IX. No labelling of myosin was observed on actin filaments with a low intensity, showing that myosin IXa did not bind to single actin filaments.

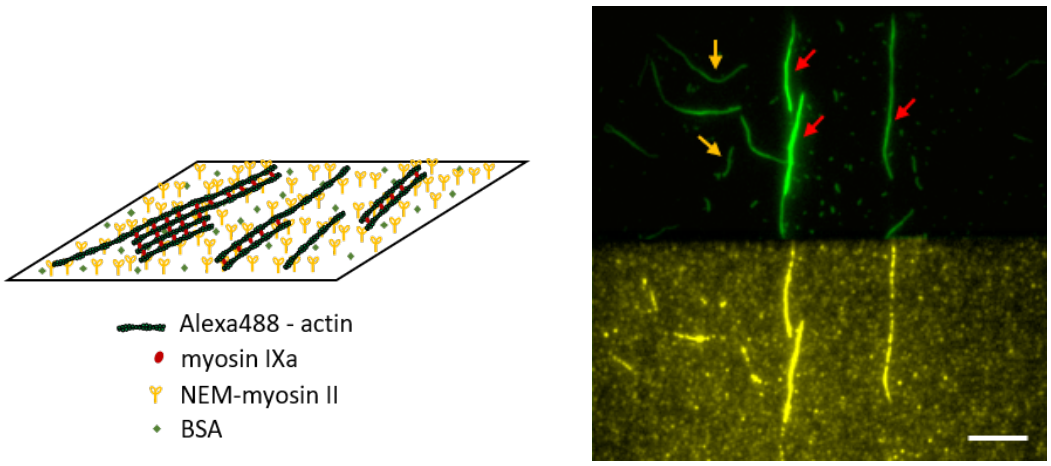

(a) **(b)**

Fig. 3.23: Myosin IXa induced the formation of actin bundles. (a) A schematic depiction of the bundling assay. NEM modified myosin II was immobilized on a nitrocellulose covered glass coverslip. Free binding positions on glass were blocked with BSA. Myosin IXa MD and fluorescently labelled actin were premixed in solution at a 1:1 molar ratio and injected into the flow cell. Frames were collected every 3 s on a homemade two-colour TIRF setup based around a Olympus IX70 microscope. (b) Two channel recording of the same field of view. Top: Alexa 488 labelled actin filaments are present in bundles (red arrows) and as single actin filaments (orange arrows). Bottom: Myosin IXa labelled with an anti-FLAG Cy3 antibody was uniquely present in the bundles and not on single actin filaments. Scale bar: 10 µm

3.1.6.2 Loop 2 is necessary for bundle formation

Considering these results on bundle formation the question arises how does a single myosin IX is able to cross-link and bundle actin filaments? Studies showed that the class IX specific loop 2 insertion in the head domain binds to F-actin with high affinity (Struchholz et al., 2009). This leads to the hypothesis that myosin IXa contains a second actin-binding site in the motor domain that can cross-link actin filaments. To test this hypothesis the above-mentioned experiment was repeated with MD skeletal, a construct where the myosin IXa–specific loop 2 was substituted for a human skeletal muscle loop 2 (see section 3.1.4.4). IXa MD skeletal was mixed with Alexa 488 actin in solution and applied to a nitrocellulose coated coverslip covered with NEM modified myosin II. Following addition of an AB- oxygen scavenger system supplemented with 100 mM KCl, images were acquired in TIRF. Even at a 2:1 molar ratio of variant IXa MD to actin, no bundling was observed and exclusively single actin filaments were visible (see Fig. 3.25 (a)).
These fluorescence studies clearly indicated that the loop 2 insert is the molecular basis for the actin cross-linking properties of myosin IXa. The loop 2 insert is necessary for bundle formation (Saczko-Brack et al., 2016).

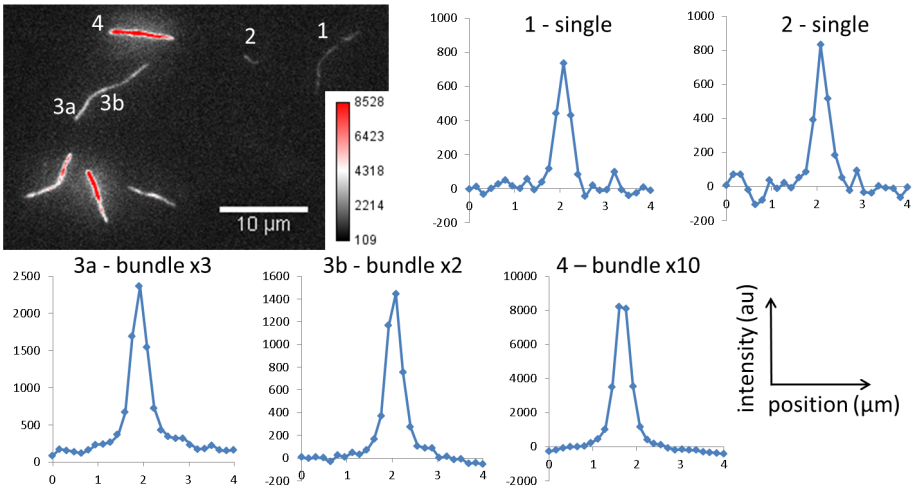

Fig. 3.24: The number of actin filaments inside individual bundles were determined by analysing the fluorescence intensity. ImageJ was used to analyse the fluorescence intensity of crosscut single and bundled actin filaments. Filaments 1 and 2 were single actin filaments and their fluorescence intensity values were around 800 au. The bundled actin filament 3 has different intensities along the bundle and was therefore subdivided into 3a and 3b. Analysis of the fluorescence intensity revealed that the bundle at position 3a contained three actin filaments, whereas at position 3b solely two actin filaments. Cross section of bundle 4 gave a fluorescence intensity of around 8000 au, indicating that this bundle consisted of around 10 individual actin filaments (data from Dr. Rogez).

3.1.6.3 Quantitative analysis of bundles

To get a more sophisticated look on the bundling capability of myosin IXa the bundles were analysed in a quantitative way. The bundles were characterized by analysing the fluorescence intensity of cross sectioned single actin filaments and comparing it with the intensity of crosscut bundles. As shown in Fig. 3.24 the number of actin filaments in a bundle could be determined with this method.

A similar fluorescence intensity analysis can be performed also along an individual actin bundle. As shown in Fig. 3.25 (b) and (c) the fluorescence intensity increased in a stepwise quantized manner along the bundle from * to **, which indicated that the bundle size increased one by one actin filament. The intensity raised until it reached the saturation level of the CCD camera.
This intensity analysis can also be done in an automatized way with many bundles. For this image analysis, 100 neighbouring fields with a total area of 600 × 600 µm^2 were recorded by systematically moving the microscope stage. A central region of interest within the image was identified to ensure a homogeneous fluorescence excitation. The signal intensity of all pixels within the region of interest was used to calculate the total length of the actin bundles. The histogram in Fig. 3.25 shows that up to seven actin filaments could be resolved with this analysis (Saczko-Brack et al., 2016).

3.1.6.4 Effect of calcium on actin bundling

Calcium ions are some of the most versatile signalling molecules and can regulate many cellular processes. As the calcium-binding protein calmodulin is binding to the IXa specific loop 2 extension in the myosin head domain, it is interesting to speculate that calcium affect its interaction with actin and therefore regulates IXa bundling behaviour.
To investigate the effect of calcium on bundling activity of myosin IXa MD, a bundling assay was performed as described above. Briefly, NEM modified myosin II was bound on a nitrocellulose coated coverslip and free binding places on the glass surface were blocked with BSA. Myosin IXa MD and Alexa 488 labelled actin were independently incubated at pCa 4, mixed at a 1:1 molar ratio and injected into the flow cell. The AB- oxygen scavenger system was supplemented with 0.1 mM free calcium (pCa 4) and 100 mM KCl. In the absence of calcium, bundles were created in the same way, except that the scavenger system without calcium was used. Bundles were imaged in TIRF using the Nikon Eclipse Ti microscope. At 0.1 mM free calcium actin bundles as well as single actin filaments were visible in the microscope field of view. This situation was similar to IXa-actin bundles in the absence of calcium. At pCa 4 the bundles were several tenths of micrometers in length

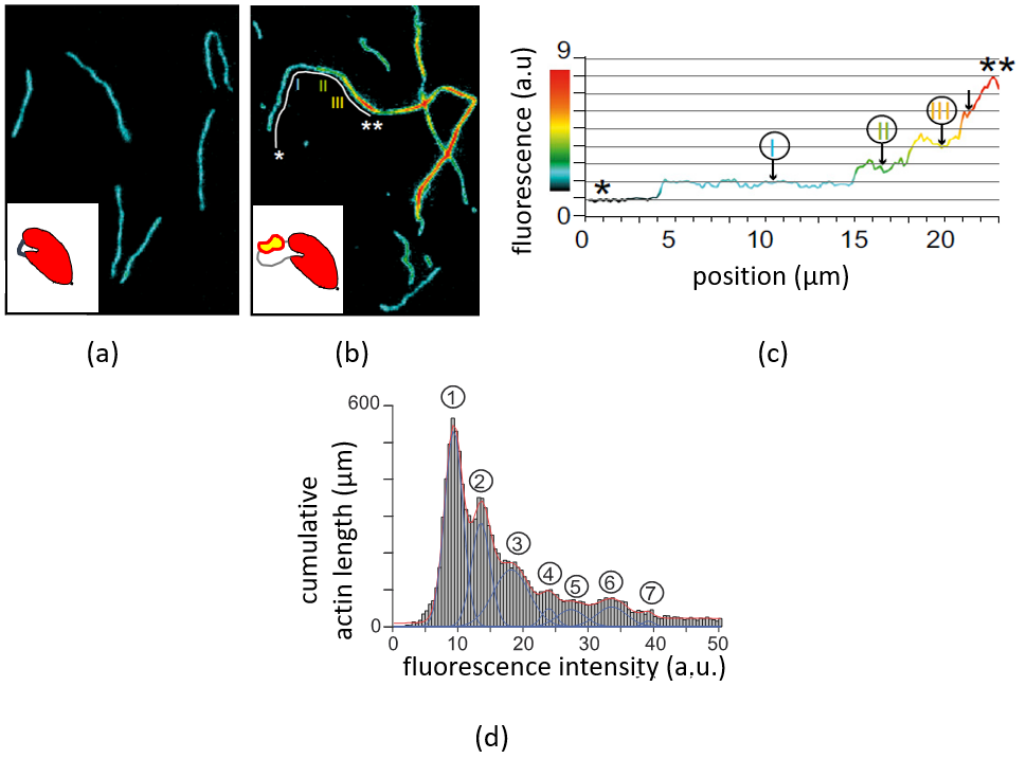

Fig. 3.25: Quantitative bundle analysis. Alexa 488 labelled actin filaments in the presence of IXa skeletal (a) or wildtype IXa MD (b) at a molar ratio of 1:1. (c) The actin bundle shown in (b) was analysed by determining the fluorescence intensity along the bundle and indicates a stepwise increase in fluorescence intensity marked from * to **. The colour code in (a) and (b) shows fluorescence intensity and actin bundling. It is apparent that in the presence of the variant lacking the class IX specific loop 2 insert no actin bundling was observed. d) The accumulated length of actin filaments and bundles was calculated using an automated pixel intensity analysis of 100 images. With this method up to seven filaments could be resolved in the bundles. The blue lines show single Gaussian distributions below each peak (Saczko-Brack et al., 2016).

and its fluorescence intensity was dependent on the duration of IX-actin incubation and the concentration of myosin IXa.

Fig. 3.26 shows the result of analysing the pixel intensity values of 100 images (each 81 x 81 µm^2) of IXa bundles in the absence and presence of 0.1 mM calcium. The cumulative length of actin filaments and actin bundles was determined and up to six filaments in the bundles could be identified for both conditions. These results clearly show that also in the presence of calcium IXa MD is bundling actin filaments and there is no difference in bundling activity from a quantitative perspective.

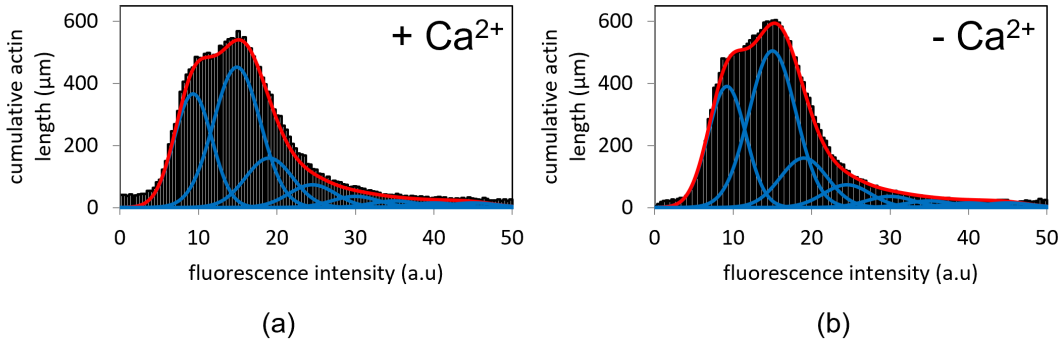

Fig. 3.26: Calcium has no influence on bundling activity of myosin IXa MD. (a) Also in the presence of 0.1 mM free calcium IXa cross-links actin filaments. Quantitative bundle analysis revealed that up to six actin filaments could be resolved in the bundles, similar as in the absence of calcium (b). The blue lines show single Gaussian distributions (data from Dr. Rogez).

3.1.6.5 High resolution images of bundles using STORM

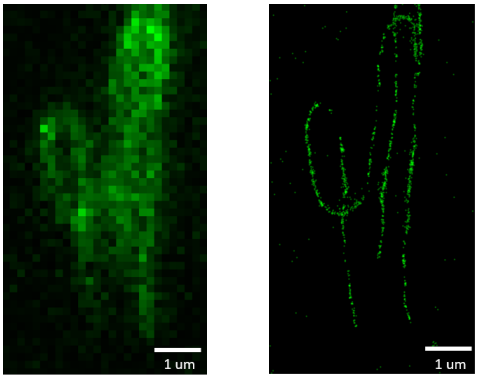

Fig. 3.27: Comparison of the resolution obtained by conventional widefield microscopy (a) and STORM (b). The STORM image of an actin filament labelled with Alexa Fluor 488 was reconstructed from 5000 images with a total acquisition time of 7 min (images from Dr. Rogez).

In collaboration with Dr. Rogez stochastic optical reconstruction microscopy (STORM) was performed with myosin IXa induced actin bundles. STORM and related super resolution microscope techniques can achieve resolutions far below the diffraction limit. The Nobel Prize in Chemistry was awarded to Eric Betzig, W.E. Moerner and Stefan Hell in 2014 for "the development of super-resolved fluorescence microscopy" (Sahl et al., 2017). Fig. 3.27 shows the power of this technique by comparing a conventional widefield image

of actin with a reconstructed STORM image.
STORM uses optically switchable fluorophores, which can be switched between a non-fluorescent and a fluorescent state by exposure to light. This allows to localise multiple fluorescent molecules positioned in close proximity with high precision because the images of individual molecules are not overlapping. After deactivation of the fluorescent molecules a new subset is activated to the fluorescent state and these newly activated fluorophores are localised. Repeating this process of activation, localisation and deactivation, the positions of many fluorophores can be determined and thus an complete image can be reconstructed. The disadvantage of this technique is the long acquisition time (several minutes to hours), which limits the possibility of studying dynamic processes (Kamiyama and Huang, 2012; Sahl et al., 2017).
Fig. 3.28 (a) shows a reconstructed image of myosin IXa MD bundles mixed with actin in a 1:1 molar ratio. Bundles were bound to a glass surface covered with NEM modified myosin II and actin was fluorescently labelled with Alexa Fluor 488.

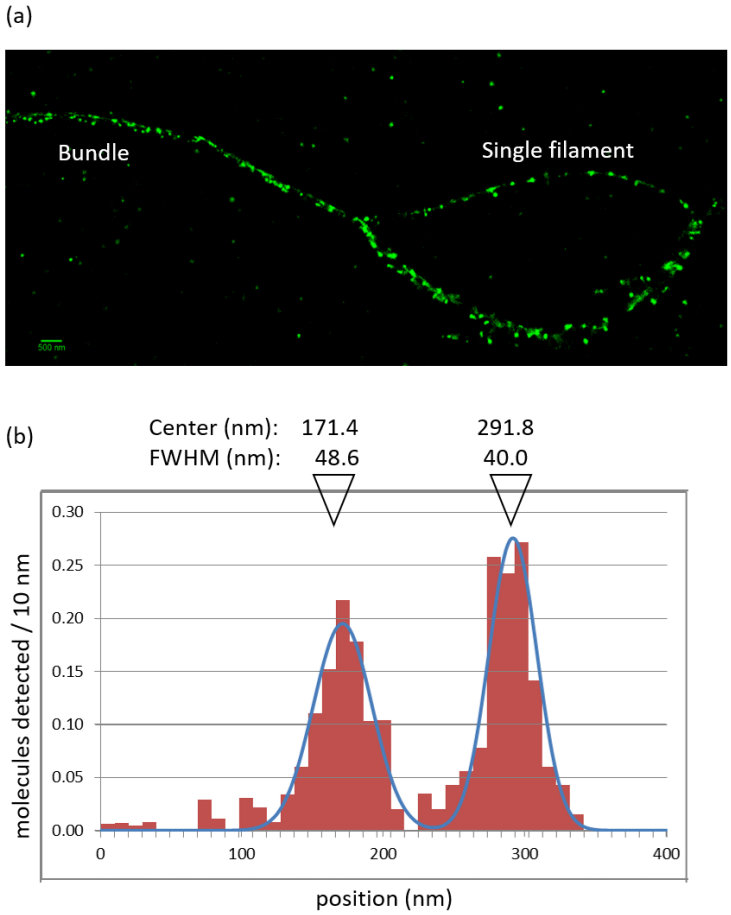

Fig. 3.28: STORM and myosin IXa. (a) Reconstructed STORM image of myosin IXa MD induced actin bundles bound to a glass surface via NEM myosin II. A clear distinction can be made between single and bundled actin filaments. (b) Quantitative evaluation of two actin filaments lying 120 nm apart from each other. The resolution here is 40-50 nm (data from Dr. Rogez).

3.1.6.6 Myosin IXa bundles form a highly regular network observed in TEM experiments

In order to make the bundling of actin filaments by myosin IXa directly visible, the cross-links were investigated using transmission electron microscopy in collaboration with Dr. Saczko-Brack. Phalloidin stabilized F-actin and IXa MD were mixed at 0.5:1 molar ratio, applied to carbon grids and negatively stained using uranyl acetate. In the absence of nucleotide, IXa MD bundled actin filaments and formed clearly visible ladder-like patterns (see Fig. 3.29). The bundles consisted of a very regular network of actomyosin cross-links linking up to five actin filaments. Averaging over 981 images revealed that individual cross-links were separated by 36 nm, which matches the helical repeat of actin.

Binding of IXa MD to single actin filaments was never detected and we did not find any additional motor molecules between the 36 nm pattern, which suggests that binding was highly cooperative between IXa MD and actin (Saczko-Brack et al., 2016).

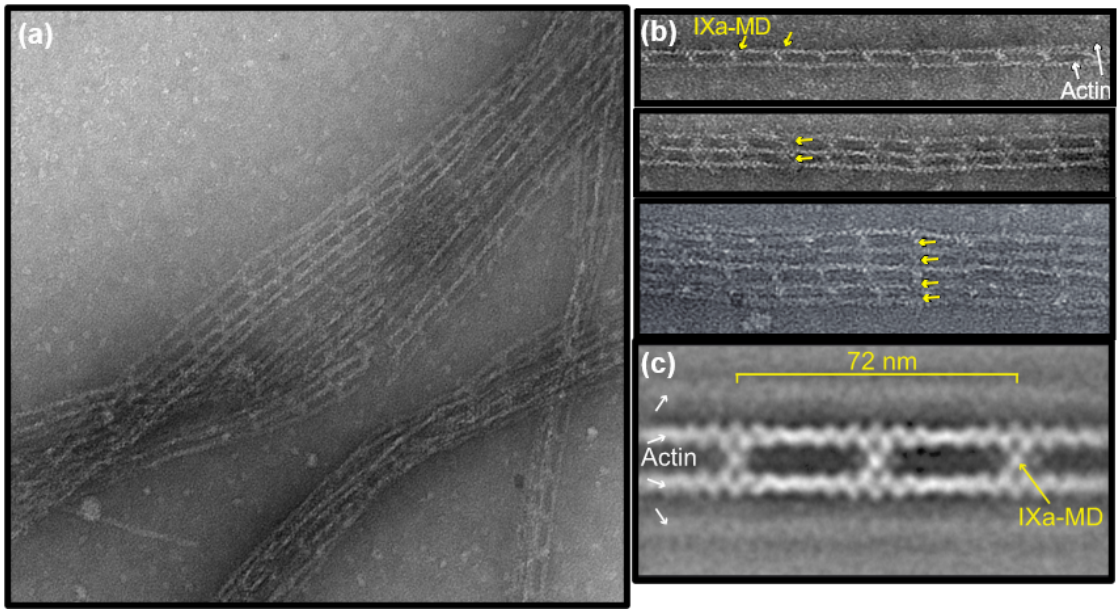

Fig. 3.29: Negative-stain EM showed that IXa MD leads to the formation of a highly regular actomyosin network. (a) IXa MD was mixed with F-actin at a 0.5:1 molar ratio. (b) Examples of actin bundles made up of two to five actin filaments. IXa MD (shown with yellow arrows) formed cross-links in ladder-like patterns. (c) 981 images of two or more actin filaments were used to make an ensemble average and clearly demonstrated that IXa motor domain formed cross-links with a repetition distance of exactly 36 nm (Saczko-Brack et al., 2016).

Three different conformations could be identified by classifying the IXa MD images based on the myosin connections to the four actin monomers. Two of these conformations formed a cross-link between the actin filaments (Fig. 3.30): The diagonally shaped cross-link (conformation I) and the bent cross-link (conformation II), both with an occurrence of 44 % and 29 %, respectively. The remaining 27 % were in an inchworm conformation, where the IXa MD molecules did not cross-link, but rather formed a bridge between two neighbouring actin monomers on the same actin filament (conformation III; Saczko-Brack et al. (2016)).

The polarity and phase of the actin filaments cross-linked by myosin IXa could be also resolved in those EM images. It was determined by fitting models of filaments with parallel or anti-parallel polarity, in-phase or out-of-phase, to the EM data. The analysis revealed that 97 % of the cross-links were created between parallel actin filaments. The hotspots of variability between the images were analysed using the variance and they were localised

at the junction between the central myosin mass (bound to one actin monomer) and a second actin monomer, either on the same or on the opposite actin filament. This result fits very well with the image classification in three myosin IXa conformations (Fig. 3.30 (d), pink spots).

In order to better understand the EM data of the actin cross-links, a modelled crystal structure of an actomyosin-Ie complex was fitted to the data (PDB ID code 4A7F; Behrmann et al. (2012)). Fig. 3.30 (e) shows that the actomyosin-Ie complex, which is superimposed on the averaged EM data could belong to both actin monomers on the bottom actin filament (green) and for the central body of the myosin IXa cross-links (blue). The three variable parts in the EM average (shown as white circles) were not covered by the model structure and therefore presumably belong to the extended loop 2 (approx. 200 aa). A calmodulin–peptide complex was fitted to the N-terminus of loop 2 in the myosin-Ie structure to include the calmodulin on loop 2 (Saczko-Brack et al., 2016).

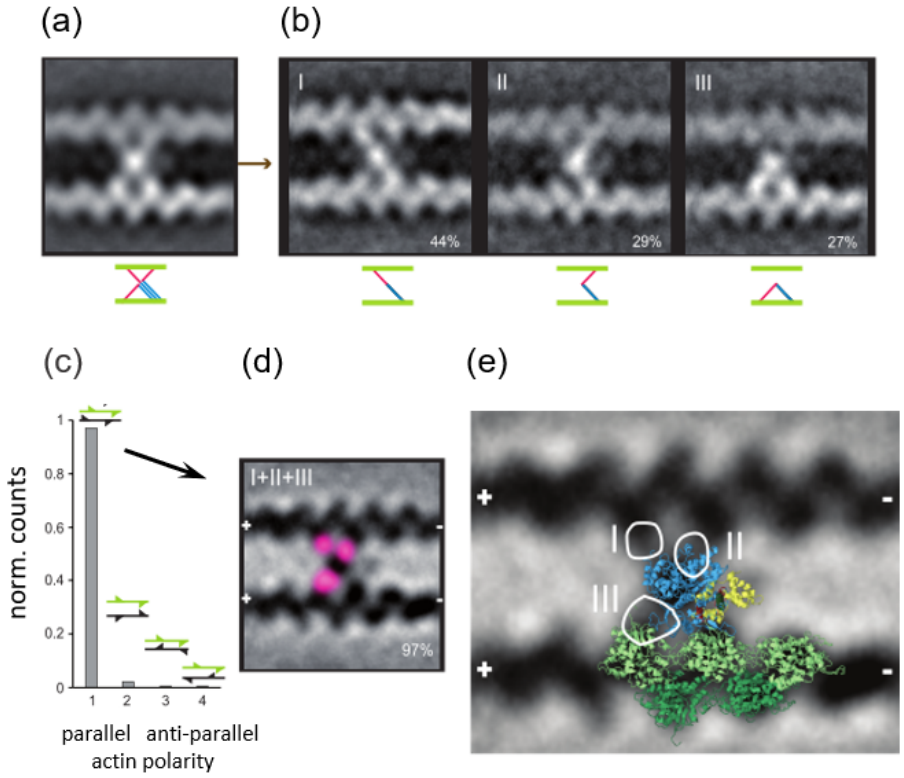

Fig. 3.30: Extended analysis of the IXa MD induced actin cross-links.
(a) Class average of 981 myosin IXa actomyosin-IXa cross-links. (b) The classification indicated three different conformations. (c) Analysis of the polarity of the actin filaments bundled by myosin IXa MD revealed that 97 % of the cross-links were formed between parallel actin filaments. (d) Analysis of the variance between the realigned cross-links showed three variable sections (pink), which indicate three secondary myosin-binding sites on actin. (e) Interpretation of the cross-links using a modelled crystal structure of myosin Ie, together with a calmodulin modelled onto loop 2. The model was superimposed onto the real-EM class average (myosin IXa MD: blue; calmodulin bound to loop 2: yellow; actin monomers: green). The circles indicate the variance hotspots seen in (d), and the Roman numbers label the different conformations presented in (b) (Saczko-Brack et al., 2016).

3.1.6.7 Calcium changes the polarity of myosin IXa-actin bundles

The fluorescence studies in section 3.1.6.4 showed that the presence of 0.1 mM calcium (pCa 4) had no influence on bundling activity and bundle size of IXa MD. Nevertheless, bundles were investigated using negative stain electron microscopy in collaboration with Dr. Saczko-Brack to have a closer look on the molecular mechanism. Phalloidin stabilized F-actin at pCa 4 and IXa MD at pCa 4 were mixed at a 0.5:1 molar ratio, applied to carbon grids and were negatively stained. At high calcium concentrations IXa MD formed a very regular network of actomyosin cross-links (Fig. 3.31) similar to the ladder-like patterns observed in the absence of calcium. The repeat distance between the individual cross-links

was 36 nm and averaging over 201 images revealed three different conformations of the cross-links: diagonal-, bent-, and an inchworm-type. These results were consistent with the data obtained at low calcium concentrations. Interestingly, preliminary evaluation of the actin polarity in the bundles indicated that at pCa 4 approx. 75 % of the filaments seem to adopt anti-parallel polarity. As a reminder, in the absence of calcium approx. 97 % of the filament in the bundles were aligned in parallel and in-phase.

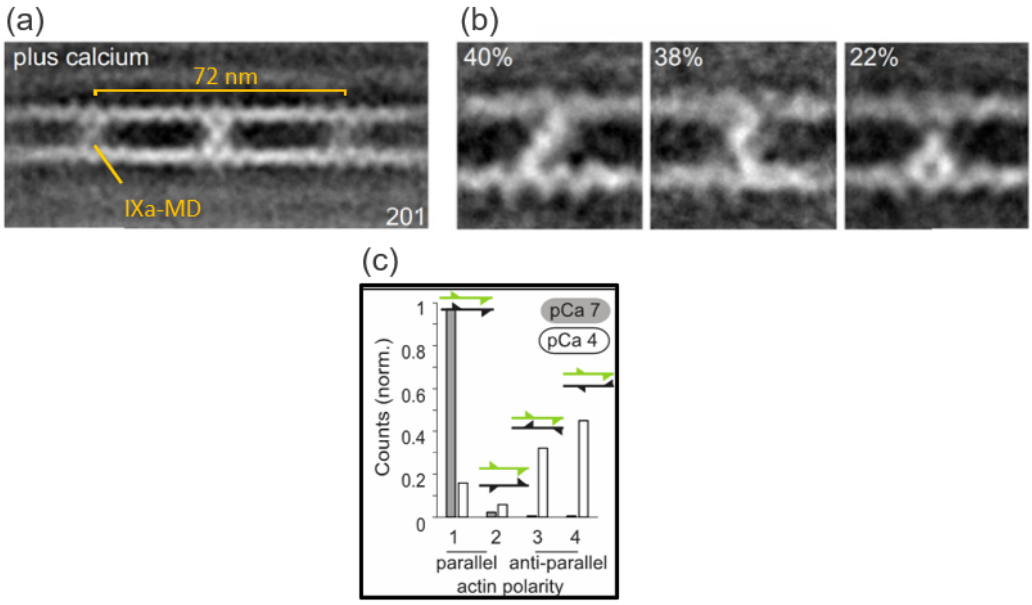

Fig. 3.31: Calcium changes polarity of the actin filaments crosslinked by myosin IXa MD. (a) At 0.1 mM free calcium myosin IXa and actin are forming highly regular ladder-like patterns with a repeat distance of 36 nm, similar as in the absence of calcium. (b) The cross-links can be classified into diagonal-, bent-, and inchworm-conformations. The distribution of conformations seemed unchanged by calcium. (c) At low calcium concentrations approx. 97 % of the filament in the bundles were aligned in parallel and in-phase, while at pCa 4 approx. 75 % seem to be anti-parallel (a and b: Saczko-Brack et al. (2016); c: preliminary data from Dr. Saczko-Brack).

In summary these electron microscopic data revealed that the IXa MD induced actin cross-links are made up of a very regular actin network with parallel actin polarity in the absence of calcium. The IXa motor domain formed cross-links at a repeat distance of 36 nm. Furthermore, single-particle image processing determined three different conformations of myosin IXa in those bundles: A diagonally shaped cross-link, a bent cross-link and an inchworm conformation. In the latter conformation the myosin binds just to a single actin filament. Bundles were even formed in the presence of high calcium concentrations (pCa 4). The striking property here was that the polarity of the actin filaments in the myosin IXa induced bundles seems to be regulated by calcium. At pCa 4 approx. 75 % of the

filament in the bundles were aligned anti-parallel, whereas at low concentrations approx. 97 % were parallel and in-phase. These leads to the hypothesis that this pronounced change in the polarity of the actin network is caused by calcium binding to the calmodulin at the loop 2 insert on IXa MD, inducing a structural reorganisation of this loop.

3.1.6.8 Bundle dissociation dynamics

3.1.6.8.1 IXa induced bundles are formed even in the presence of ATP The results of the myosin IXa induced actin networks described in the previous section were all performed in the absence of ATP. This might rise the question why an ATP dependent motor protein has such structural functions. To answer this question and to apply the experiments at more physiological conditions, I performed the bundling assay in the presence of nucleotide. Bundles were formed as described previously and bound to a coverslip surface coated with NEM modified myosin II. The oxygen scavenger system was supplemented with 100 mM KCl and different amounts of ATP. As described in chapter 2.4.3 the number of pixels at different fluorescence intensities was determined and used to compute the cumulative length of actin bundles. Fig. 3.32 shows the fluorescence intensity distribution over 100 fields of view (60×60 µm^2) at 100 µM ATP and indicates that up to seven filaments were identified in a bundle. Bundles were still visible even at 250 µM ATP, although the amount of filaments in the bundles was significantly reduced. This suggests that bundle formation is completely reversible and depends on the nucleotide concentration (Saczko-Brack et al., 2016).

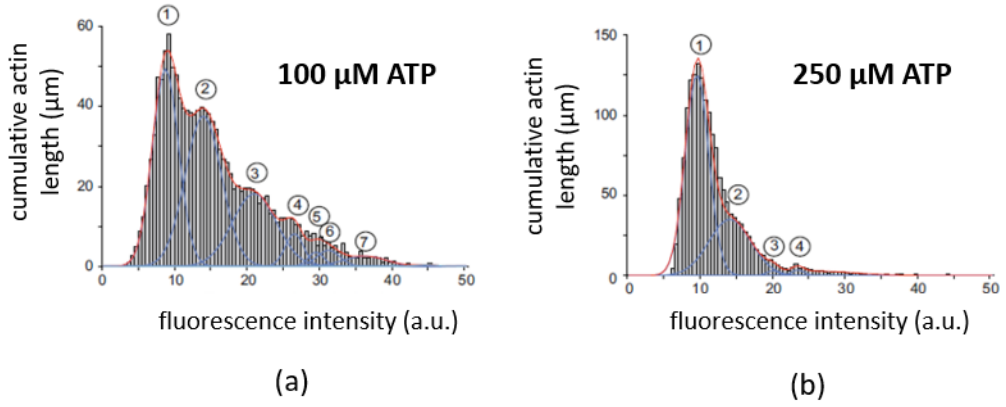

Fig. 3.32: IXa MD forms bundles even in the presence of ATP.
(a) Distribution of fluorescence intensities over 100 fields of view at an ATP concentration of 100 µM. The computer-based analysis revealed up to seven actin filaments in the bundles. (b) Even at 250 µM ATP bundles are still present, but with reduced numbers of filaments (Saczko-Brack et al., 2016).

3.1.6.8.2 Bundle dissociation occurs in discrete, ATP dependent events To study the dynamic assembly and disassembly of IXa induced bundles in the presence of ATP in further detail, a modified bundling assay was developed (see Fig. 3.33 (a)). In this assay the dissociation behaviour of small bundles consisting of only two actin filaments were analysed. For this purpose, two species of actin filaments were generated. The first species was labelled with rhodamine and contained biotinylated actin monomers, whereas the second species of F-actin was labelled with Alexa 488 and was constructed out of the usual non-biotinylated G-actin. The surface of a piranha cleaned glass coverslip was covered with biotin BSA and streptavidin and free binding places were blocked with BSA. Rhodamine labelled biotinylated actin was mixed in a 1:100 molar ratio with Alexa 488 labelled actin. This actin mixture was then combined with IXa MD at a 1:1 molar ratio in solution (final myosin concentration was 2 µM), incubated for 20-60 s to ensure having small bundles and injected into the flow cell. The oxygen scavenger system was supplemented with 100 mM KCl and frames were recorded every 500 ms in TIRF using a Nikon Eclipse Ti microscope. After recording a few frames, indicated amounts of ATP were gently added to the flow cell.

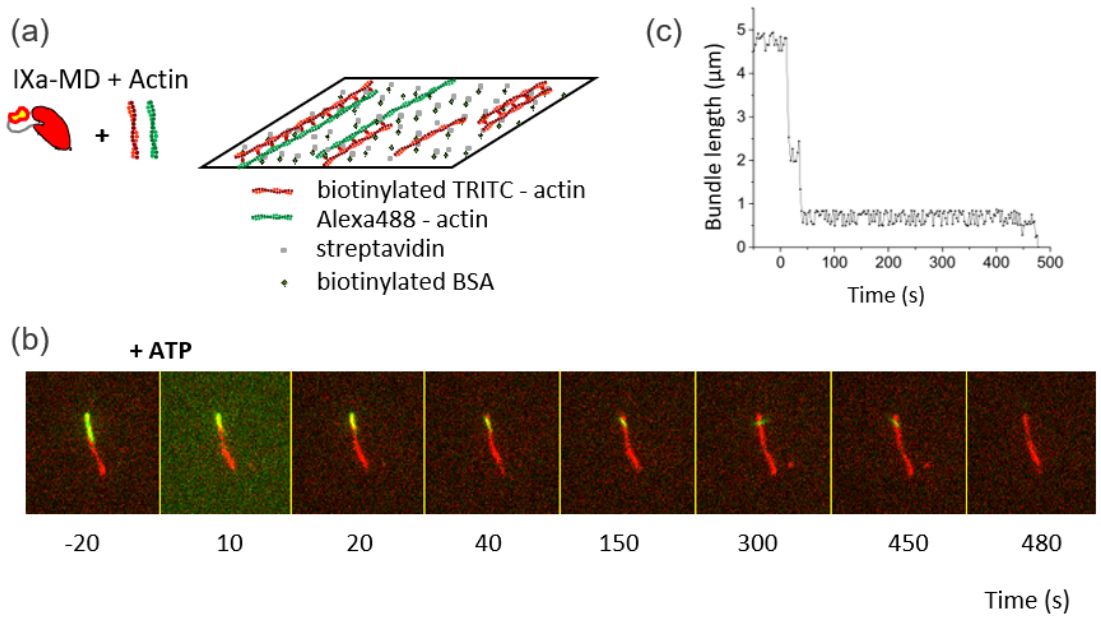

Fig. 3.33: Bundle dissociation occurs in discrete events. (a) A schematic depiction of the assay. Biotinylated rhodamine labelled actin filaments (red) and non-biotinylated Alexa 488 labelled actin filaments (green) were mixed with myosin IXa MD in a 1:1 molar ratio and bound to a glass coverslip via streptavidin. Only the red actin filaments bind tightly to the surface, whereas the green filaments can only bind to the surface via an IXa-actin bundle. (b) An exemplary sequence of frames shows that the green filament dissociates in a sequential manner from the red filament. Indicated time in seconds after ATP addition. (c) A detailed analysis of the bundle length over the time course of the experiment shows a stepwise dissociation process.

Fig. 3.33 (b) shows a typical sequence of frames of such an experiment. The rhodamine labelled biotinylated actin (red) is tightly bound to the streptavidin coated glass coverslip and does not change its position over the time course of the experiment. The shorter Alexa 488 labelled actin (green) is bundled via myosin IXa MD to the red actin filament. This actin species made of non-biotinylated actin monomers cannot interact with the surface and its appearance on the surface is limited to bundles. After addition of ATP the green actin filament started to dissociate in a discrete stepwise manner from the red filament. Fig. 3.33 (c) shows the graph of the dissociation process of a typical experiment, which demonstrates the sequential decrease of bundle length.

In those experiments frames were acquired every 500 ms, so the time resolution was sufficient to observe discrete dissociation events. Moreover, the spatial resolution was 1 pixel corresponding to 180 nm, which was also adequate to measure amplitudes in the range of micrometers.

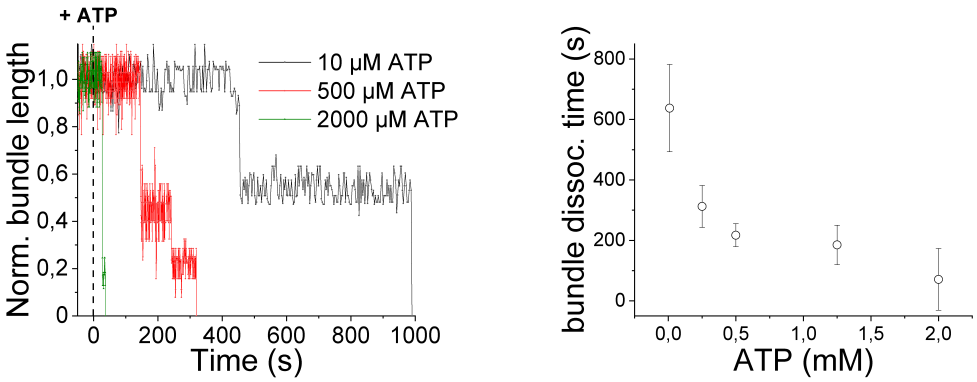

(a) (b)

Fig. 3.34: Bundle dissociation showed a clear ATP dependence. (a) Overlay of exemplary experiments at 10, 500 and 2000 µM ATP. Time 0 corresponds to ATP addition (black dashed line). (b) Bundle dissociation kinetics was evaluated for 49 bundles and displayed an ATP dependent behaviour. Bundle dissoc. time corresponds to the time interval until the complete dissociation of a myosin IXa-actin bundle.

The dissociation experiment was repeated at five different ATP-concentrations (10, 250, 500, 1250 and 2000 µM). Three exemplary experiments at 10, 500 and 2000 µM ATP are plotted in Fig. 3.34 (a) (ATP addition is timepoint 0). The striking differences in the dissociation kinetics is immediately visible. At low ATP concentrations bundle dissociation was much slower than at high ATP concentrations (Fig. 3.34 (b)). At 2 mM ATP complete bundle dissociation occurred on average in ∼71 s, whereas at 10 µM ATP it took ∼638 s (approx. 10 min).

For a more detailed analysis of the discrete bundle dissociation process the time interval from ATP addition (time=0) until the first bundle dissociation event (BDE) was defined as dwell time before BDE. In a similar fashion the time interval from the end of the first BDE until the second BDE was set as dwell time after BDE. As shown in Fig. 3.35 (b), the dwell time before BDE decreases significantly with increasing ATP concentrations. In total 67 bundles of a least three different samples per ATP concentration were evaluated for this analysis. A similar ATP dependent behaviour was noticeable for the dwell time after BDE (N=28; Fig. 3.35 (c)).

As already indicated from Fig. 3.34 (a) also the BDE amplitude showed an ATP dependent attitude (Fig. 3.35 (d)). Closer inspection of 71 bundles of a least three different samples per ATP concentration revealed that the first BDE amplitude increased from 1.50 ± 0.20 µm at 10 µM ATP to 2.69 ± 0.28 µm at 2 mM ATP.

IXa MD bundle dissociation occurred in single or multiple events (up to 5 events). At low ATP concentration multiple events occurred more frequently than at high ATP concentrations (see Fig. 3.36).

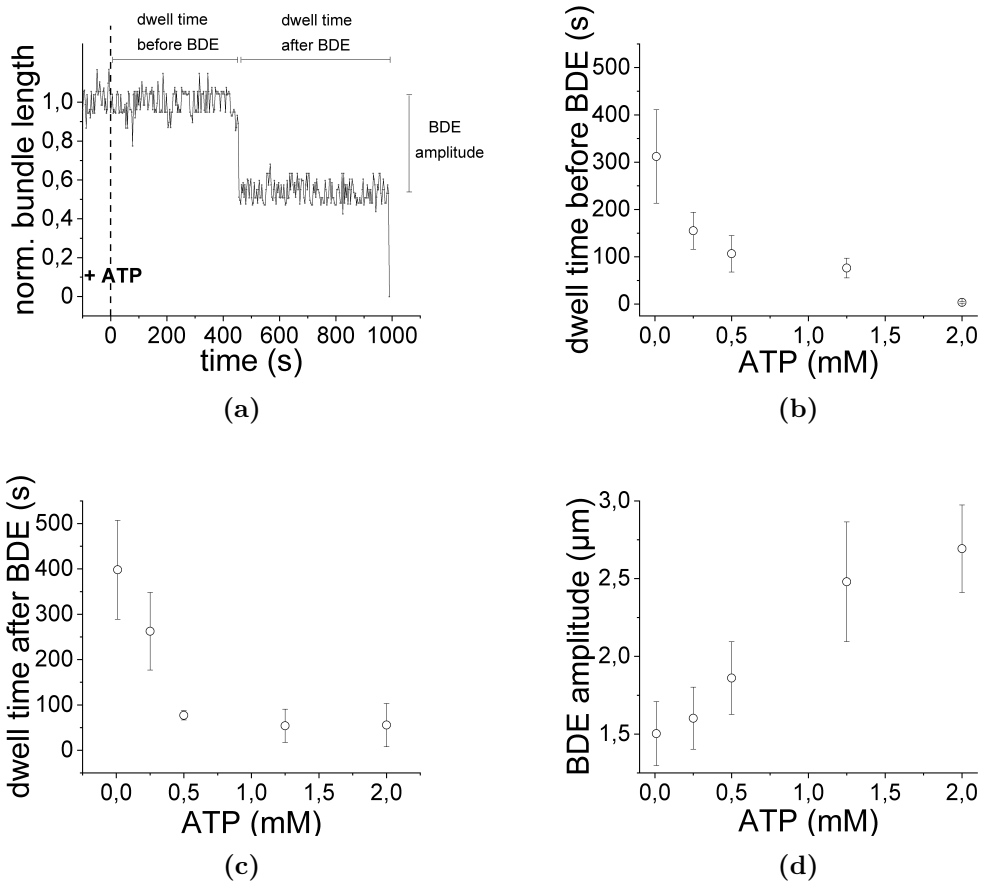

Fig. 3.35: A detailed analysis showed that single parameters of the discrete dissociation process displayed an ATP dependence. (a) Graphical depiction of the different evaluated parameters (BDE=bundle dissociation event). (b) The time interval from ATP addition until the first BDE was defined as dwell time before BDE and was analysed for 67 bundles. This dwell time decreased with increasing ATP concentrations. (c) The time interval from the end of the first BDE until the second BDE was set as dwell time after BDE. Similar to (b) also this dwell time showed an ATP dependent behaviour (N=28). (d) The first BDE amplitude of IXa MD bundle dissociation was analysed for 71 bundles.

In summary this experiments showed that the myosin IX induced actin bundles are still present at micromolar ATP concentrations. This indicates that the bundles have physiological relevance to create a dynamic actomyosin network. The ATP dependent motor protein is a molecular switch in the network, to regulate the assembly and disassemble of actin bundles at different time scales.

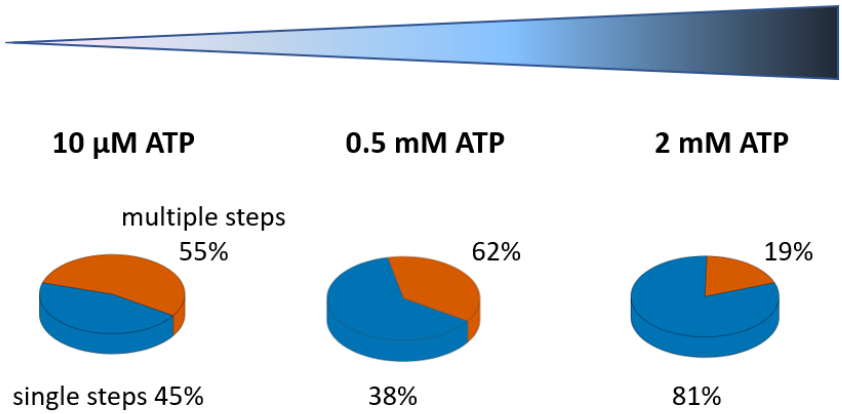

Fig. 3.36: Bundle dissociation took place in single or multiple events.

3.1.7 Cloning and purification of myosin IXa loop 2 constructs

This section describes the cloning, expression and purification strategy of different loop 2 constructs. The 200 aa loop 2 of human myosin IXa was fused to glutathion-S-transferase (GST) to enhance its expression and solubility. Although the fusion protein was solely present in the void volume after gel filtration, I was able to express and to purify small amounts of the protein. Additionally, I used two different structure prediction algorithms to get insights into the three-dimensional structure of the loop 2, which revealed a high α-helical content.

3.1.7.1 Introduction

Class IX myosin contain a unique insertion in the loop 2 of the motor domain. It had been proposed by several groups that this insertion might act as an actin tether to prevent dissociation from actin filaments (Reinhard et al., 1995; Post et al., 2002; Inoue et al., 2002; Nalavadi et al., 2005; Nishikawa et al., 2006; Kambara and Ikebe, 2006; Liao et al., 2010; Elfrink et al., 2014). This is consistent with results on isolated loop 2 of rat IXb which bound stoichiometrically and with high affinity to F-actin (Struchholz et al., 2009). However, the exact three-dimensional structure of the loop 2 insert is not known. Single-molecule AFM force spectroscopy experiments on myosin IXb loop 2 have shown that it contains a lot of secondary structure, but it still remains flexible with spring-like properties and a high affinity for actin (Struchholz et al., 2009).
Currently, there is no biochemical or structural information about myosin IXa loop 2. Fig. 3.37 shows the amino acid sequence of loop 2 and gives an overview about various protein parameters. The basic isoelectric point (pI) of 10.5 is similar to the pI of rat myosin IXb loop 2 (11.9; Struchholz et al. (2009)) suggesting that the interaction with actin is electrostatic also for IXa. A 1-8-14 calmodulin-binding site was identified at the N-terminus of the loop 2 insert. This calmodulin binding sequence is highly conserved in class IX myosins and only exists in class IX myosins (Liao et al., 2010). Comparison between the loop 2 of different myosin IX isoforms and of skeletal muscle myosin II revealed that loop 2 of IXa is more than 10x bigger than that of myosin II (see Fig. 3.6 (a)).
In the present work the loop 2 of myosin IXa was cloned into pGEX as a fusion protein with glutathion-S-transferase (GST). It is known from studies with isolated loop 2 of rat IXb that a high amount of this protein is insoluble. Therefore it was purified under denaturing conditions and refolded by stepwise dialysis in decreasing urea concentrations (Struchholz et al., 2009). To circumvent this laborious and problematic method we fused the loop 2 with the 211 amino acid protein GST (26 kDa) in order to enhance its expression and

solubility, as GST quickly folds into a stable and highly soluble protein during translation (Frangioni and Neel, 1993).

1	GIDPVAVFR**W**	AILRAF**F**RAM	VA**F**REAGKRN	IHRKTGHDDT
41	APCAILKSMD	SFSFLQHPVH	QRSLEILQRC	KEEKYSITRK
81	NPRTPLSDLQ	GMNALNEKNQ	HDTFDIAWNG	RTGIRQSRLS
121	SGTSLLDKDG	IFANSTSSKL	LERAHGILTR	NKNFKSKPAL
161	PKHLLEVNSL	KHLTRLTLQD	RITKSLLHLH	K

(a)

number aa	191
molecular weight	21.8 kDa
theoretical pI	10.46
total number of negatively charged residues (Asp + Glu)	17
percentage	9 %
total number of positively charged residues (Arg + Lys)	33
percentage	17 %
extinction coefficient	12615 M^{-1} cm^{-1}

(b)

Fig. 3.37: Sequence and general informations about the unique loop 2 of human myosin IXa. (a) Amino acid sequence 692-883 of human myosin IXa, indicating the 1-8-14 calmodulin-binding site at the N-terminal site (bulky hydrophobic amino acids at positions 1, 8 and 14 of the CaM-binding site are highlighted in red). Those characteristic residues form important interactions with calmodulin (Yap et al., 2000; Liao et al., 2010). (b) Outline of diverse protein parameters of the loop 2-sequence.

3.1.7.2 Cloning and purification of a loop 2-GST fusion protein

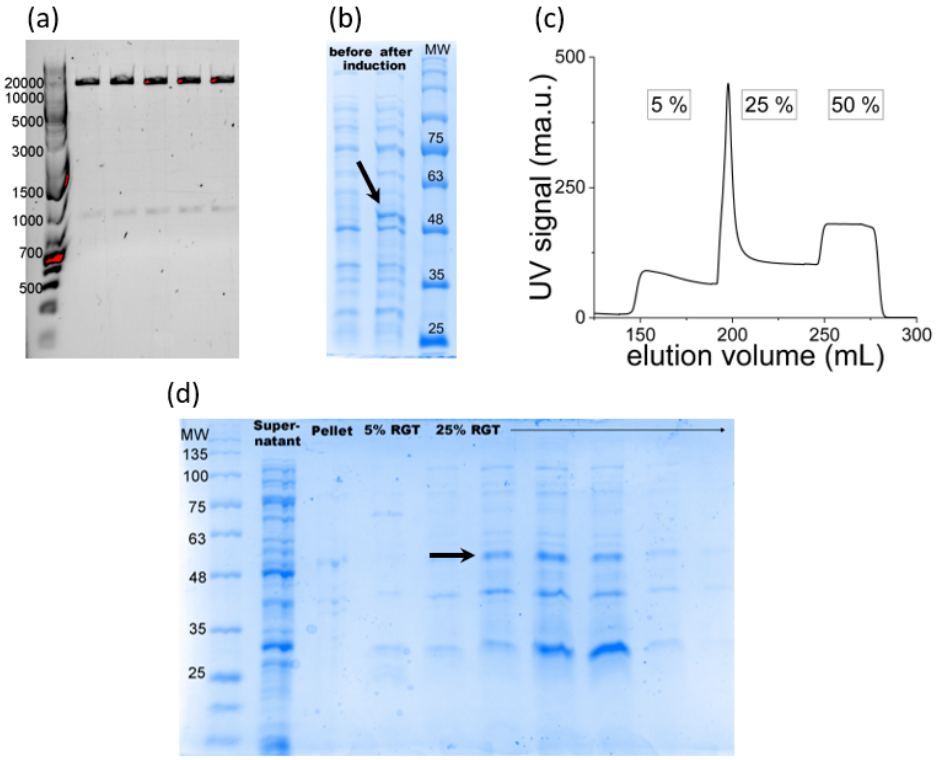

Fig. 3.38: Cloning, expression and purification of a loop 2–GST fusion protein. (a) His tagged human myosin IXa loop 2 was assembled from synthetic nucleotides (ThermoFisher) and cloned into pGEX-6P1. Correct insertion of the construct into the vector was verified by a test digestion with BamHI and XhoI. DNA electrophoresis, as expected, showed the presence of two fragments: a pGEX-6P1 vector backbone (∼5 kbp) and His tagged loop 2 (∼650 bp). Those samples were sequenced and used to transform *E. coli*. (b) The fusion protein was expressed in *E. coli* BL21 for 4 h at 16°C. A 7.5 % SDS PAGE of whole cell samples confirms the expression of a protein with the expected size (50 kDa) after IPTG induction (black arrow). (c) 3 l of expression were purified using two 5 ml GSTrap ff columns connected in series on an Äkta® FPLC system. UV/Vis absorbance curve shows the total protein concentration in real time that passes through the absorbance detector. Elution was performed with 5, 25 and 50 % reduced gluthathione Tris-buffer (RGT). (c) shows the collected fraction on a 7.5 % SDS-PAGE. The black arrow indicates the desired loop 2–GST fusion protein at the correct size (50 kDa), although there are also contaminants present.

Nucleotides 2068-2703 encoding amino acids 690-901 of human myosin IXa (NCBI no. AAI40870.1) were codon-optimized, assembled from synthetic oligonucleotides and inserted into the pRSET A vector (ThermoFisher). A 6x His tag sequence was added N-terminally to the construct and it was flanked by BamHI and XhoI. Using this restriction sites loop 2 was subcloned into pGEX-6P1 (with N-terminally GST). Protein was

expressed in *E. coli* BL21 at 16°C for 4 h. As shown in Fig. 3.38 (b) a clear band was visible in the whole cell sample after expression at around 50 kDa, corresponding to a loop 2-GST fusion protein (loop 2: 26 kDa; GST: 26 kDa). This 50 kDa protein was still present after GST purification (see Fig. 3.38 (c) and (d)) using two 5 ml GSTrap ff columns connected in series on an Äkta® FPLC system. However, two contamination proteins at around 30 and 40 kDa were also present. The 30 kDa protein could represent GST alone (26 kDa) without any fused protein.

To separate the loop 2–GST fusion protein from the other contaminants, a gel filtration with a Superdex 200 Increase column was performed. 500 µl pooled and concentrated sample from the His purification was applied to the column at room temperature. Fig. 3.39 (a) shows the UV/Vis absorbance curve of the gel filtration and a corresponding 7.5 % SDS PAGE of the different fractions. Besides the void volume peak at 7.9 ml two additional peaks were present in the elution profile. The first peak at 13.9 ml contained mostly GST (26 kDa) as confirmed with SDS PAGE and western blot using an anti–GST antibody (see Fig. 3.39 (b) and (c)), whereas the second peak at 19.0 ml contained only traces of GST. Low concentrations of loop 2–GST were present in the later fractions of the void volume as confirmed by SDS PAGE and western blot. Although the fusion protein could be separated clearly from the 30 kDa contaminant, the desired protein was present in the void volume indicating that it formed big aggregates. Therefore, the aggregated molecules were excluded from the gel filtration matrix because they were larger than the largest pores and passed directly through the packed bed. Consequently, those aggregates were present in a very early fraction of the gel filtration.
Another possibility that loop 2-GST was found in the void volume of the column is that it formed big oligomers. This would increase the proteins molecular weight and would result in an early elution of the protein.

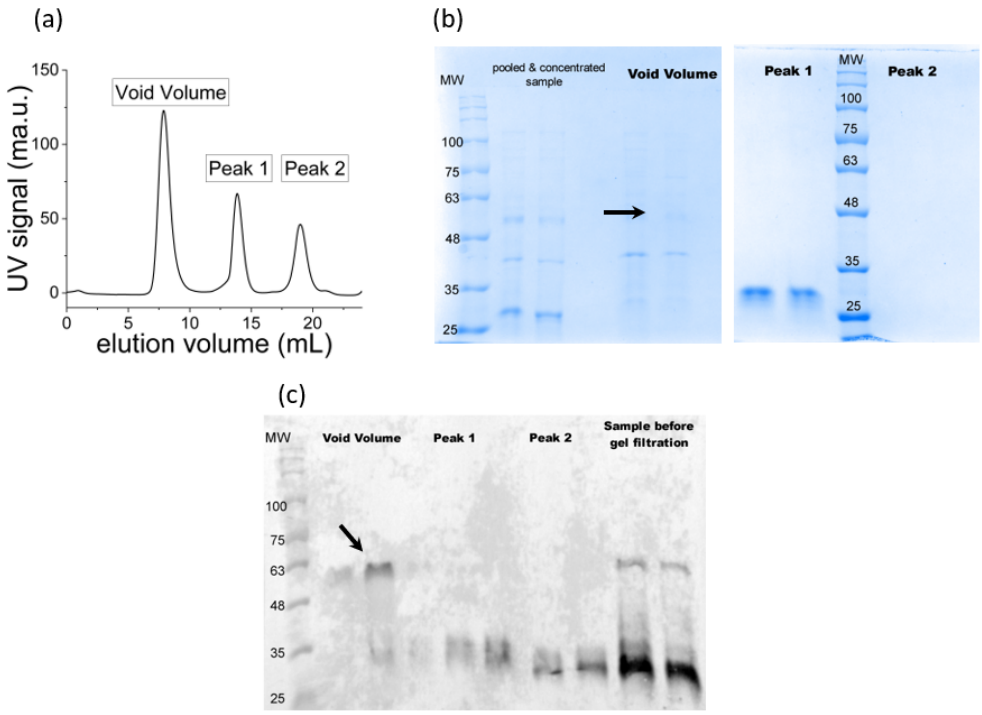

Fig. 3.39: A second purification step with a Superdex 200 Increase column was performed on an Äkta® FPLC system. (a) Typical elution profile of loop 2–GST. (b) A 7.5 % SDS PAGE of indicated fractions shows that GST (26 kDa) could be separated from loop 2–GST, but the desired protein was present in the void volume of the column. (c) Western blot against GST confirmed the successful separation of GST (peak 1 and 2) and loop 2-GST (void volume peak).

3.1.7.3 Optimization of loop 2 purification

Overnight dialysis of loop 2–GST after purification in a loop 2-buffer with a lower ionic strength (50 mM Tris pH 7.0 and 50 mM NaCl; Struchholz et al. (2009)) and performing gel filtration in this buffer did not changed the elution profile.

Sequence analysis revealed a calmodulin-binding site near the N-terminus of the loop 2 insert. Therefore, calmodulin was added at a 1:1 molar ratio to 2 mg/ml of the pooled and concentrated loop 2–GST sample and gel filtration was performed on a Superdex 200 Increase in loop 2–buffer. Fig. 3.40 shows a typical elution profile with the corresponding SDS PAGE. Although after calmodulin addition an additional peak appeared at 12.3 ml elution volume, loop 2–GST was still present in the void volume indicating its aggregation or oligomerisation behaviour.

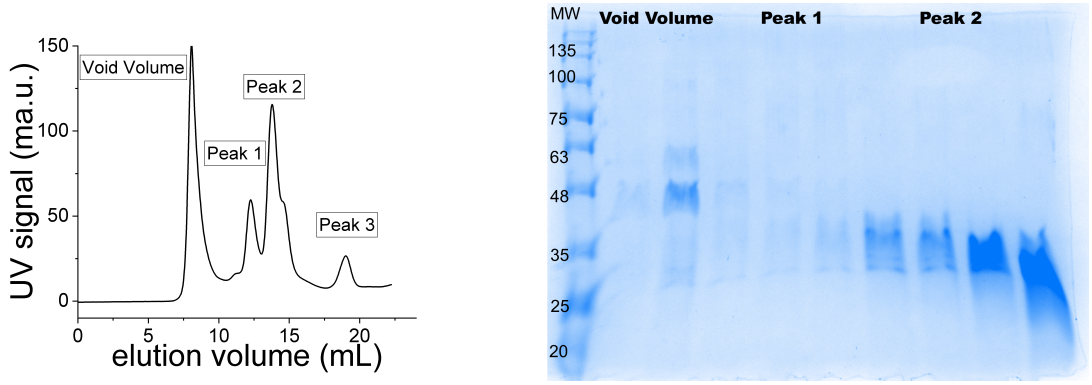

(a) **(b)**

Fig. 3.40: Gel filtration of loop 2–GST in the presence of equimolar amounts of calmodulin. (a) 500 µl pooled and concentrated loop 2–GST from 6 l of *E. coli* expression culture were applied to a Superdex 200 Increase column. Gel filtration was performed in buffer from Struchholz et al. (2009). The elution profile showed an additional peak at 13.3 ml compared to the elution profile shown in Fig. 3.39. (b) A 7.5 % SDS PAGE of indicated fractions showed that even in the presence of calmodulin loop 2–GST was present in the void volume.

Supplementing the loop 2–buffer with 0.1 mM calcium (pCa 4) and incubation for 1 h with loop 2–GST before performing gel filtration at pCa 4 did not shifted the fusion protein into later fractions of the elution profile.

In summary, the expression of a loop 2-GST fusion protein in *E. coli* was successful, although a further purification step on a Superdex 200 Increase column showed that most of the expressed protein was aggregated or formed big oligomers. Furthermore, the concentration of loop 2–GST derived from the SDS PAGE after gel filtration was small compared to the contaminant at around 40 kDa. Therefore, I decided to improve the expression conditions for getting a higher amount of the protein with higher quality.

3.1.7.4 Co-expression of loop 2 with calmodulin

Expressing the myosin IXa motor domain in a baculovirus system in Sf21 cells requires co-expression with calmodulin, otherwise only low amounts of active motors are obtained (data not shown). This leads to the hypothesis, that calmodulin is already required during the expression of IXa for a correct binding and folding of loop 2 and the motor domain. Therefore, loop 2 and calmodulin were integrated into a pET-Duet vector to express them simultaneously with their own promotors in *E. coli*.
Loop 2-GST was amplified via PCR out of pGEX-6P1 with forward and reverse primers containing restriction sites for EcoRI and HindIII and inserted into the multiple cloning

site 1 (MCS 1) of pET-Duet. Xenopus calmodulin was inserted into MCS 2 of the duet–vector via NdeI and XhoI. Successful insertion was confirmed by test digestion (see Fig. 3.41 (a) and (b)) and sequencing. The proteins were expressed in *E. coli* for 4 h at 20°C. As initial attempts purifying the fusion protein via the GST–tag were not successful, purification was performed with a 5 ml HiTrap ff as loop 2-GST contained a N-terminally 6x His tag. Fig. 3.41 (c) and (d) shows the elution profile and the corresponding 15 % SDS PAGE of the purification of 1 l *E. coli* culture in an Äkta FPLC system. Although there are still a lot of proteins present after His–purification a prominent band appeared at around 40 kDa. A western blot against GST was carried out (Fig. 3.41 (e)), which showed only a weak band at the expected size of the desired loop 2–GST fusion protein (50 kDa).

In summary, co-expression of loop 2–GST with calmodulin did not increase the amount of protein. The pET-Duet vector was expressed also in a *E. coli* rosetta strain, which are BL21 derivatives intended to improve the expression of eukaryotic proteins containing codons that are rarely utilised in *E. coli*. This strain exchange did not increased the amount of purified protein. Taken together, this suggests that the expression of loop 2 needs further optimization.

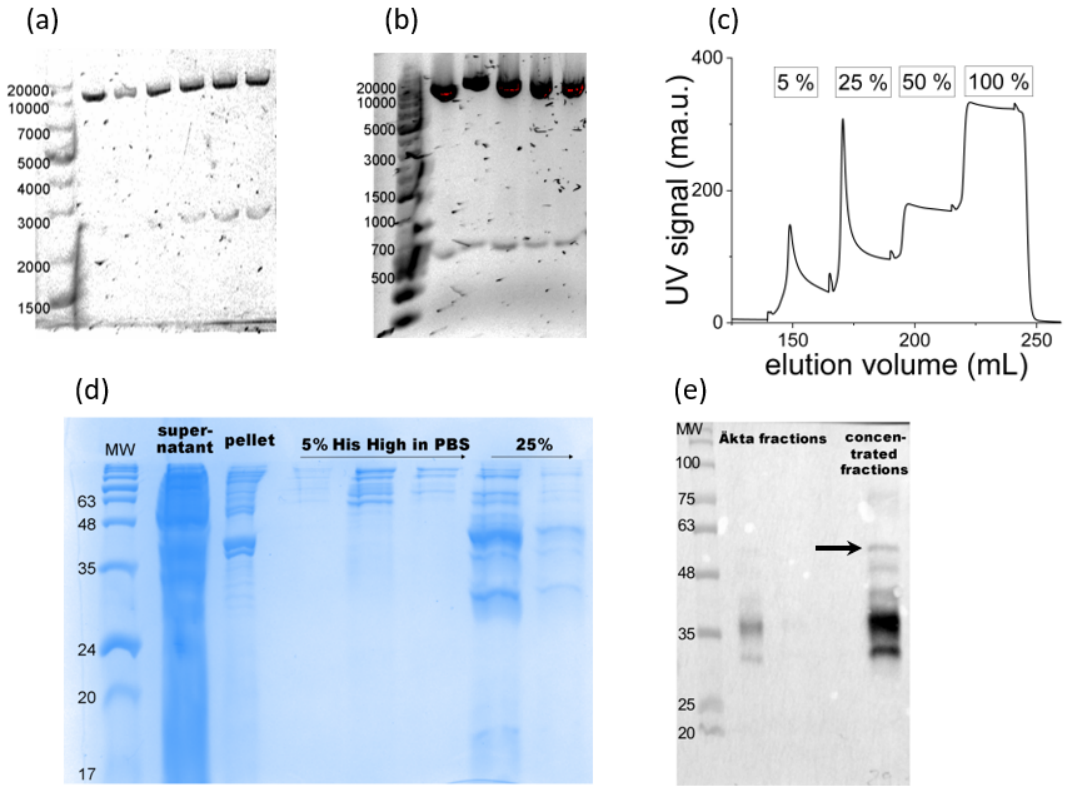

Fig. 3.41: Cloning and purification of a loop 2–GST fusion protein together with calmodulin in a pET-Duet vector. (a) PCR amplified loop 2-GST was inserted into MCS 1 of pET-Duet with the restriction sites EcoR1 and HindIII. Successful insertion was verified by a test digestion with those enzymes. DNA electrophoresis showed the presence of two fragments with ∼5400 bp (vector backbone) and ∼1300 bp (loop 2-GST). (b) Xenopus calmodulin (CamX) was inserted into MCS 2 of the Duet vector. A test digestion with NdeI and XhoI showed the presence of a ∼450 bp (CaMX) and the remaining vector (∼6250 bp). Samples which contained both constructs were sequenced and used to transform *E. coli*. (c) 1 l of *E. coli* BL21 culture were expressed for 4 h at 20°C and purified with a 5 ml HiTrap ff column. The elution profile showed a highest protein peak with 25 % His high in PBS. (d) 15 % SDS PAGE of indicated fractions showed a prominent band at around 40 kDa besides other higher and lower molecular weight proteins. (e) A western blot with an anti–GST antibody showed that the 40 kDa band did not correspond to loop 2-GST. A band at the desired size of 50 kDa is present (see black arrow), although the concentration is very low.

3.1.7.5 Structure prediction of loop 2

Although there exists no structural data about the myosin IXa loop 2, bioinformatical structure prediction algorithms can be used to predict and analyse protein structures. Some of the most widely used modelling tools are I-TASSER and Phyre2. They are validated in international blind trials of protein structure prediction methods (critical assessment of protein structure prediction or CASP; Kryshtafovych et al. (2019)) and both

tools show superior performance.
I-TASSER uses a multiple threading alignment method to find structural templates in the protein data bank (PDB). Full-length three-dimensional (3D) models are then constructed through iterative fragment assembly simulations (Yang and Zhang, 2015). Phyre2 utilises an advanced remote homology detection approach to build 3D models. In this tool the sequence of interest is compared with a large database of sequences and a evolutionary profile is constructed that is used to scan known structures. The resulting alignment can be used to build a model of the unknown sequence based on the available structure of the homologous protein (Kelley et al., 2015).

Fig. 3.42 shows the Phyre2 result of the predicted protein structure of myosin IXa loop 2. Most of the protein contained α-helices (82 %), whereas no β-sheet was detected. In total five α-helices were detected, whereby the first and last helices showed the highest confidence level (see colour-coded 'SS confidence' line). More than half of the protein sequence (56 %) was classified as disordered. The weakest region of α-helix prediction coincided with a strong disorder prediction. The I-TASSER web server indicated very similar results, although the amount of helical structures was reduced. Similar to Phyre2 the α-helices at the C- and N-terminal end showed the highest confidence score.

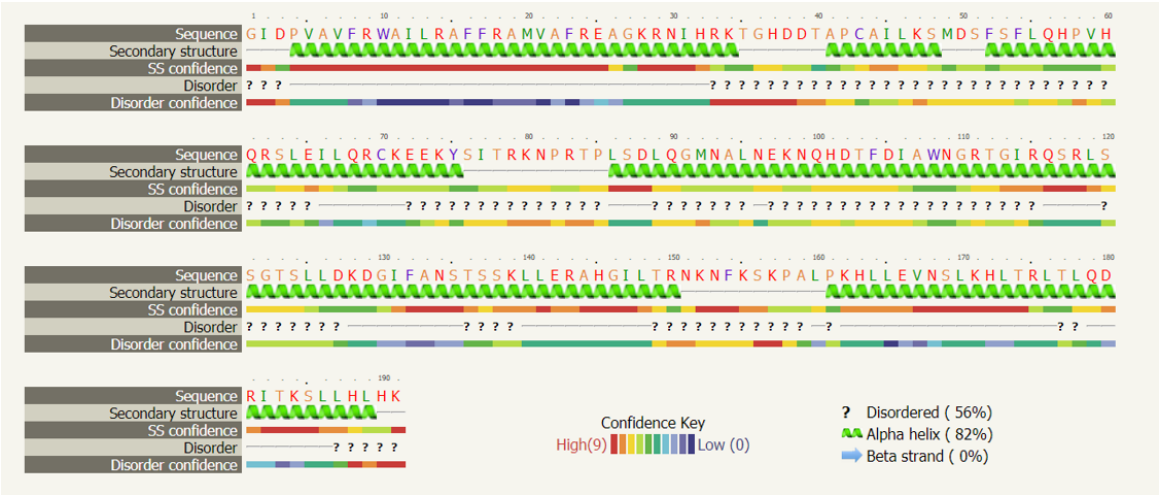

Fig. 3.42: Predicted secondary structure of the loop 2 of human myosin IXa. The online modelling tool Phyre2 was used to predict and analyse the loop 2 structure. In total five α-helices have been detected, with the first and last helices having the highest helical confidence and the lowest disorder confidence level. The amino acid residues are coloured based on a property-based scheme and are grouped into small (polar), hydrophobic, charged and aromatic (together with cysteine) amino acids (Kelley et al., 2015).

Fig. 3.43 shows the predicted I-TASSER 3D structure of human myosin IXa loop 2 with the highest confidence score. Several structural templates have been identified in the PDB. The topology of the model was then constructed by reassembling the constantly-aligned fragment structures from the templates. Unaligned regions have been modelled *ab initio* using Monte Carlo simulations (Yang and Zhang, 2015).

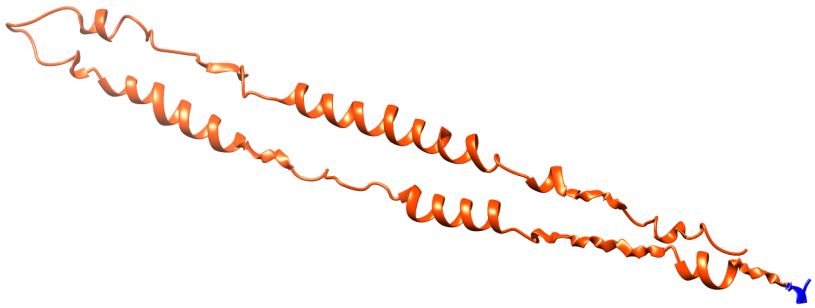

Fig. 3.43: Predicted 3D model of human myosin IXa loop 2 using I-TASSER. The model shows several α-helices with the N-terminal end coloured in blue. The figure was made with UCSF chimera.

Interestingly, the prediction tool Pyre2 found a homologous protein structure to the C-terminal part of loop 2 (residues 97-176). Parts of the crystal structure of myosin Vc in the pre-power stroke (PDB: 4ZG4; Wulf et al. (2016)) showed a 91 % probability being homologous to the loop 2 sequence.

3.2 Single-molecule studies of human non-muscle myosin IIb

This section focuses on the non-muscle isoform IIb (NMIIb), which plays an important function in fundamental cellular processes such as cytokinesis and cell migration. In this work I compared the single-molecule properties of single and double-headed human NMIIb to investigate the cooperativity of the myosin heads. I show that single and double headed NMIIb produces two types of power strokes: A ∼5 nm working stroke known also from other myosin II isoforms, and close-to-zero attachment events. In contrast to other NMIIb studies this 0 nm binding events do not show a lifetime dependence and are present in both short and long events. Furthermore, stiffness analysis of single binding events showed that short events had a slight lower stiffness than long events. These results indicate that the short events could represent transient, weak binding states of myosin to actin. Interestingly, the kinetics was very similar between single and double headed NMIIb, indicating that the single myosin heads act in an independent, non-cooperative manner.

3.2.1 Design of human non-muscle myosin IIb constructs

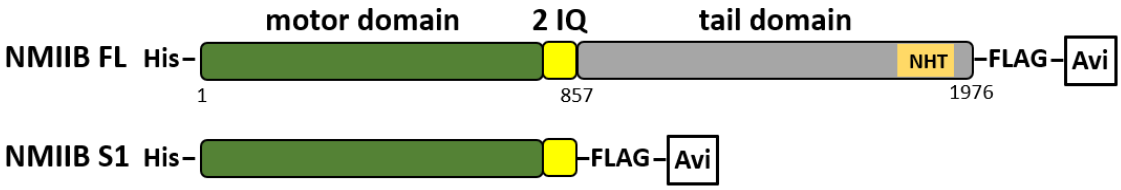

Fig. 3.44: Schematic illustration of the human NMIIb constructs developed in this work. Numbers of important amino acids within the NMIIb sequence are shown. The S1 construct comprised only the head domain with the two IQ motifs, which are binding sites for the regulatory (RLC) and essential (ELC) light chain. Without the coiled-coil motif this construct is unable to polymerize into larger structures and is therefore single-headed. In contrast the full-length (FL) NMIIb construct contains this motif in the tail and is therefore able to form a double-headed dimer. A short nonhelical tail region (NHT) terminates the heavy chain.

Two HNMIIb constructs were used and developed in this study and are schematically represented in Fig. 3.44. The 1976 aa-sized full-length construct comprises the full head domain, the neck domain with two binding motifs for the essential (ELC) and regulatory light chain (RLC) and the tail domain. The latter contains an α -helical coiled-coil motif, which leads to homodimerisation of two HNM heavy chains and to a double-headed structure. To study the behaviour of single-headed HNMIIb a truncated construct

was developed, which contained solely the head and neck domain (amino acids 1-857). Without the coiled-coil motif this construct is unable to form dimers. Both constructs contained a N-terminal FLAG-tag for affinity purification and an Avi-tag for site-specific surface binding via biotin/streptavidin.

3.2.2 Cloning of myosin IIb constructs

Codon-optimized full-length human non-muscle myosin IIb cDNA (5931 bp; NCBI no. AAI17692.1) was chemically synthesized and cloned into pFastBac1 using BamHI/NotI restriction sites (Thermo). Similarly, the NMIIb S1 construct (bp 1-2571 encoding amino acids 1-857) was synthesized and cloned into pFastBac1. Both constructs contained a FLAG-tag, separated by a 3x glycine-linker from the NMIIb sequence and an C-terminally Avi-tag (split apart by a 3x glycine linker from the FLAG-tag). Additionally, both constructs contained a N-terminal 6x His tag separated by a glycine-serine-glycine linker from the myosin sequence.
Recombinant baculoviruses were produced as described in chapter 2.3.2.

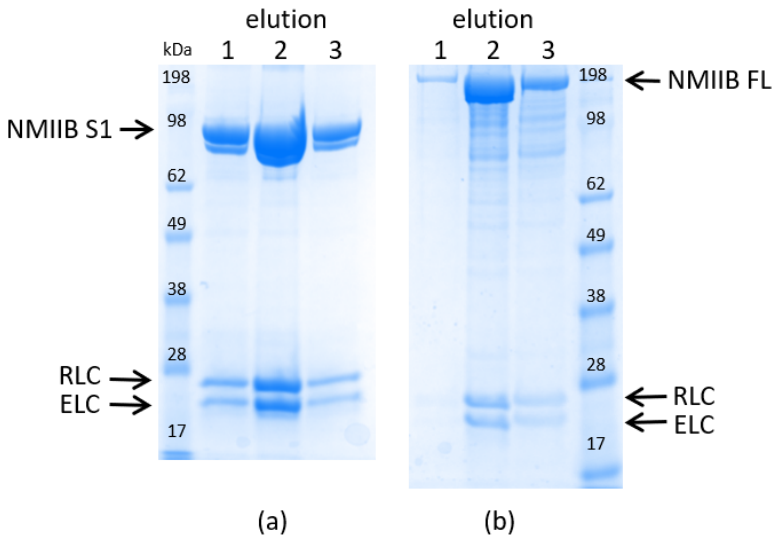

Fig. 3.45: Representative 4-12 % gradient Bis-Tris SDS-PAGE gels showing purified full-length (a) and S1 (b) human NMIIb. The neck-bound essential (ELC, 19 kDa) and regulatory light chains (RLC, 26 kDa) are clearly visible on the gel. Positions of the myosin heavy chain and light chains are shown by arrows.

3.2.3 Purification of myosin IIb constructs

Proteins were expressed and purified as described in chapter 2.3.3.2. Similar as for myosin IXa constructs, a FLAG affinity purification was carried out which resulted in homogenous NMIIb preparations (see gels in Fig. 3.45). It is important to note that bacterially expressed ELC and RLC was added during purification, which increased the quality of the myosin preparation.

3.2.4 Single- and double headed non-muscle myosin IIb produces two types of binding events

Single-molecule experiments using an optical tweezers transducer were performed with myosin IIb site-specifically bound to a glass coverslip via an anti-FLAG antibody. As the FLAG-tag is located on the C-terminus of the myosin heavy chain, the myosin molecules are oriented in such a way that the head domain is freely movable to undergo a complete power stroke.

Trapping flow cells were prepared according to the protocol described in chapter 2.6.2. Briefly, 1 ng/ml anti-FLAG antibody was injected into the flow chamber and incubated for 4 min. Unbound antibody was removed with PBS and 1-5 µg/ml freshly phosphorylated NMIIb were introduced into the flow cell, incubated for 4 min and then the surface was blocked with BSA. Subsequently, dead myosin heads were blocked with phalloidin labelled actin. This solution was replaced by an oxygen scavenger system containing 50 µM ATP, an ATP backup system, rhodamine labelled biotinylated F-actin and neutravidin coated beads. Experiments were carried out at a single trap stiffness of 0.02 pN/nm and 22°C. Data was collected at 5 kHz.

Fig. 3.46 (a) shows raw data traces of single full-length myosin IIb interactions with actin. Mostly single interactions were observed and only rare, spontaneous processive steps were detected. Interestingly, evaluation of the power stroke size of 727 single interactions showed a distribution with two mean peaks (see Fig. 3.46 (b)). Data was fitted with a double gauss fit and gave peaks at 0.43 ± 0.25 nm and 6.06 ± 0.19 nm.

To compare the single-molecule behaviour of double-headed full-length with single-headed S1 NMIIb, the displacement was also evaluated for the latter construct. As shown in Fig. 3.46 (c) also the single-headed construct showed two main peaks at 0.15 ± 0.09 nm and 4.67 ± 0.14 nm.

Neglecting the approx. 0 nm power stroke, the displacements measured in this study are very similar to the values for myosin II molecules found in the literature (Molloy et al., 1995; Tyska and Warshaw, 2002; Veigel et al., 2003; Nagy et al., 2013). In an optical

tweezers study, Tyska et al. (1999) showed that the power stroke sizes of double-headed smooth and skeletal muscle myosins were about twice as large as those of the single-headed construct. They introduced the idea of 'two heads are better than one' and proposed that the second, not actively attached myosin head, could orient the attached head in that way to produce maximal force and motion.

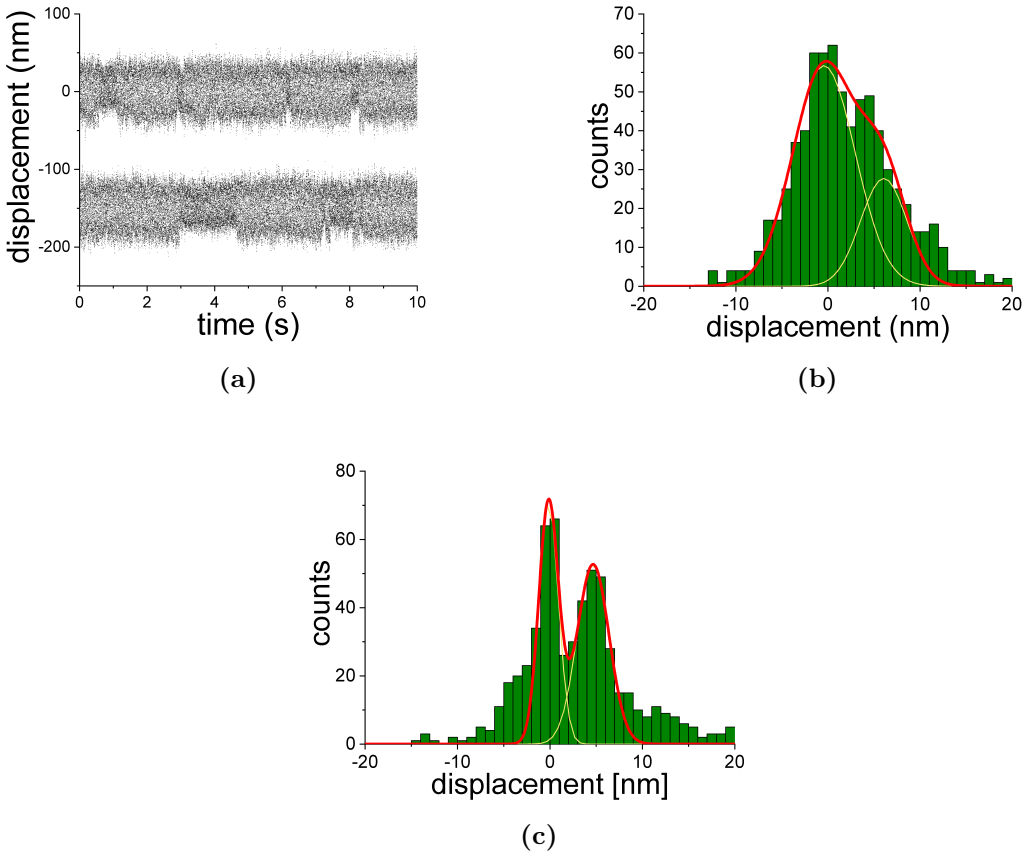

Fig. 3.46: Single- and double headed non-muscle myosin IIb produce similar working strokes. (a) Raw data traces of double-headed full-length NMIIb site specific bound to a glass surface via an anti-FLAG antibody. Trace shows the displacement of one dumbbell bead cast on the 4QD detector. Single-molecule interactions were measured at 50 µM ATP and 0.02 pN/nm single trap stiffness. (b) Analysis of the power stroke size of 727 single interactions of three different filaments showed a distribution with two mean peaks. A double gauss fit (red line) of the data gave peaks at 0.43 ± 0.25 nm and 6.06 ± 0.19 nm (R^2=0.933). Single Gaussian distributions of the main peaks are shown in light yellow. (c) Interestingly, also the evaluation of the power stroke size of single-headed NMIIb S1 resulted in a two-peak distribution (N=595). Fitting the data resulted in peaks at 0.15 ± 0.09 nm and 4.67 ± 0.14 nm (R^2=0.926).

In the present study the working stroke sizes of single and double headed NMIIb were similar. This difference could arise from the preparation of single headed myosin species.

In our study subfragment 1 was recombinantly expressed and purified out of insect cells, whereas in the Tyska et al. (1999) study the single-headed species was generated by proteolytic digestion of full-length myosins. After the digestion, the two fractions were separated by chromatography. Protease treatment of myosins often leads to the cleavage of surface loops in the head domain or partial cleavage of the light chains in the neck region. On the other hand, non-muscle myosin II could behave differently regarding single/double headed compared to smooth and skeletal muscle myosin II. This could be also an explanation for the deviating results.

In an optical trapping study using also human NMIIb, Nagy et al. (2013) measured working strokes of 6.9 ± 1.2 nm for double-headed NMIIb-HMM and 4.8 ± 1.3 nm for an artificial single-headed NMIIb-SH-HMM. The single-headed construct was generated by co-expressing NMIIb-HMM with subfragment 2 (S2). This strategy leads to a mixed population of double (NMIIb-HMM) and single headed (NMIIb + S2) myosin molecules. Only after a second purification step using subfragment 2 as a purification target (using a different tag) single headed myosin IIb could be extracted. Although, double-headed NMIIb-HMM cannot entirely be excluded by this two-step purification protocol especially when performing a single-molecule method, the values from Nagy et al. (2013) were very similar to the power strokes measured in this study.

3.2.5 Kinetics is very similar between single- and double headed non-muscle myosin II

In both above mentioned trapping studies using human NMIIb (Nagy et al., 2013) or smooth and skeletal muscle myosin II (Tyska et al., 1999) the kinetics of single- and double headed molecules were comparable. Therefore, I proceeded to analyse the dwell times of the single-molecule interactions. Fig. 3.47 (a) shows the cumulative histogram of lifetimes of single- and double-headed NMIIb interactions with actin. Evaluation of 656 single interactions of full-length NMIIb and 555 NMIIb S1 interactions along with fitting the data using a double exponential function indicated very similar time parameters of the two constructs (Fig. 3.47 (b)).

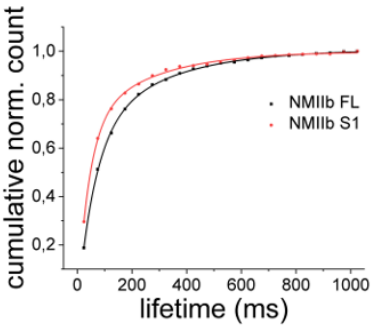

(a)

construct	t_1 (ms)	t_2 (ms)	R^2
NMIIb FL	62.97 ± 3.57	280.70 ± 23.47	0.999
NMIIb S1	42.94 ± 3.46	247.72 ± 24.57	0.999

(b)

Fig. 3.47: Single- and double headed NMIIb have very similar kinetics. (a) Cumulative histogram of dwell times of full-length (FL) and S1 NMIIb in the presence of 50 µM ATP and 0.02 pN/nm single trap stiffness (N=656 and 555 for FL and S1, respectively). Data was fitted with a double exponential fit (solid lines), with characteristic time and fitting parameters shown in (b).

In the trapping study of Nagy et al. (2013) with human NMIIb they observed two different types of events. Short-lived events (<100 ms) with a power stroke size close to 0 nm and longer events with a 5-7 nm power stroke. The short events accounted for 80-90 % of all observed events and were approx. 50 times faster than the long-lived events. They hypothesized that the short-lived interactions represent transient, nonproductive, weak binding events between NMIIb and actin, whereas only the longer events represent full, complete power strokes.

In the measurements presented here only 50-60 % of all events were shorter than 100 ms. Fig. 3.48 shows a displacement vs. lifetime plot of single- and double-headed NMIIb interactions and demonstrates the different situation in the measurements presented here.

Close-to-zero and approx. 5 nm power strokes were equally clustered especially for short lifetimes.

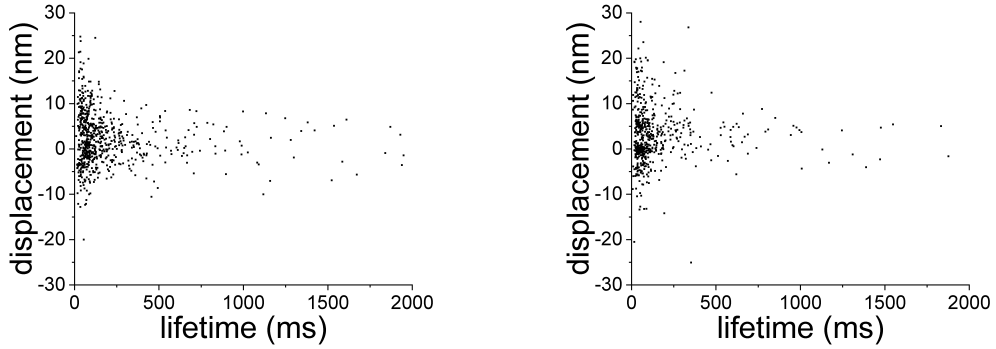

Fig. 3.48: The power stroke size of single- and double headed NMIIb is lifetime-independent. Displacement vs. lifetime plots of S1 NMIIb (a) and full-length NMIIb (b) interactions shown in Fig. 3.46 indicate that the average displacement does not seem to change with the lifetime. In total 727 interactions of full-length NMIIb and 595 S1 NMIIb interactions were included in this analysis (50 µM ATP and 0.02 pN/nm single trap stiffness).

Sorting the single-molecule binding events according to their lifetimes and plotting them as a histogram illustrates this difference even further. The histograms are shown in Fig. 3.49 and clearly show that 0 and 5 nm power strokes are both present at short (<100 ms) and long events. It seemed that for events longer than 500 ms the relative amount of 5 nm compared to 0 nm power strokes is higher for single-headed NMIIb and the situation is reversed for double-headed NMIIb, although the count numbers are quite low.

The question arises why the measurements presented here show a lifetime-independent power stroke size of human NMIIb, whereas in the study of Nagy et al. (2013) a clear distinction between short 0 nm interactions and long approx. 5 nm interactions was possible. Nagy et al. (2013) applied a 200 nm 200 Hz sinusoidal forcing function to one of the optical traps, whereas in the present study the forcing function had lower frequency (100 Hz) and amplitude (100 nm, peak-to-peak). Even though an increased oscillation of the optically trapped beads increases the signal-to-noise ratio of the attachment events, it also increases the load on the myosin head. It has been already shown that some myosins act load-dependent (Veigel et al., 2003, 2005; Sellers and Veigel, 2010; Greenberg et al., 2012; Hundt et al., 2016). The different load conditions in the trapping experiments could explain the divergent results.

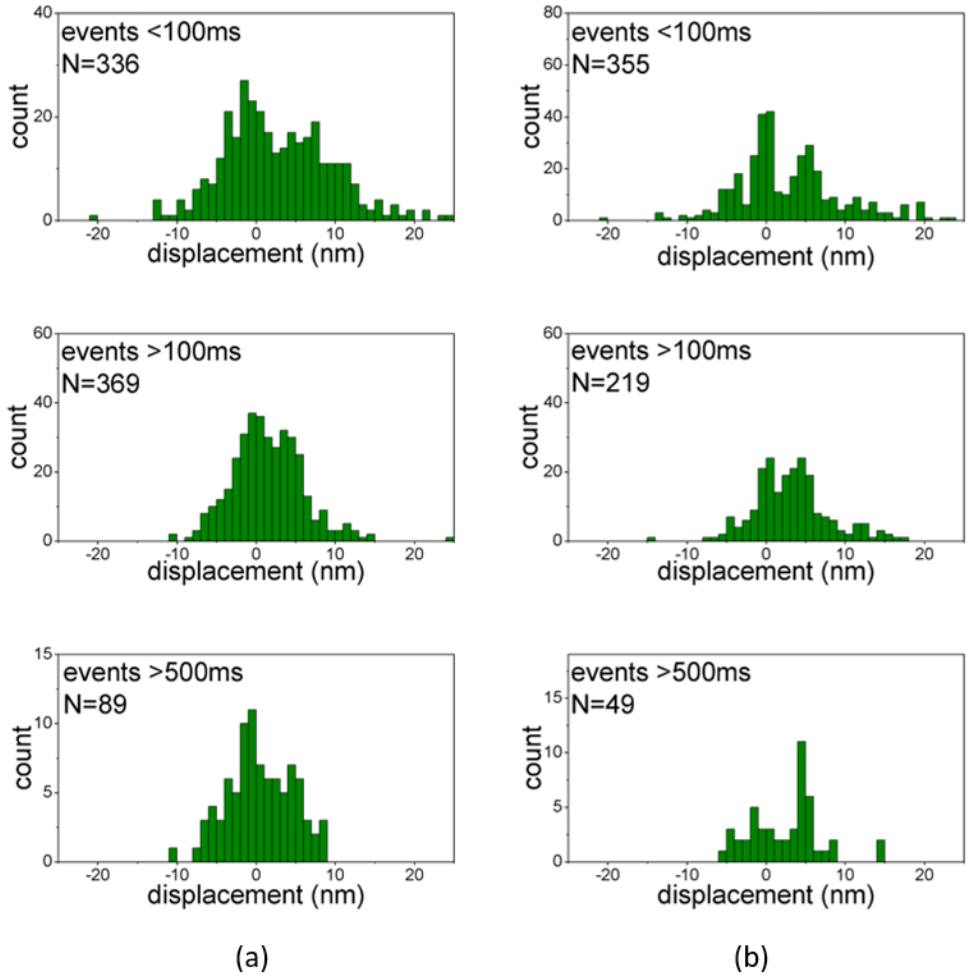

Fig. 3.49: An additional visualization of lifetime-independent power stroke sizes of NMIIb. Single-molecule interactions of double- (a) and single-headed (b) NMIIb shown in Fig. 3.46 were sorted according to their lifetimes and displacement histograms were plotted in three different groups: events <100 ms, events >100 ms and events >500 ms (50 µM ATP and 0.02 pN/nm single trap stiffness). The plots show that close-to-zero and 5 nm displacements are equally distributed over the dwell times.

3.2.6 Stiffness measurements on single- and double headed non-muscle myosin IIb

Optical trapping data is rich in information about power stroke size, processivity and kinetics of single-molecule interactions. When a sinusoidal forcing function is applied to one of the optical traps additional informations about the stiffness of the myosin can be obtained (see chapter 2.6.5). A 100 Hz 100 nm sinusoidal waveform was applied to the driven bead in the bead-actin-bead dumbbell. The other bead follows this waveform

in a passive manner, because of mechanical connection through the actin filament with the driven bead. The larger the amplitude reduction of the passive bead, the higher the resulting myosin stiffness.

Fig. 3.50 shows a comparison of stiffness measurements on single- and double headed NMIIb. 51 single-molecule interactions of full-length and 22 interactions of S1 NMIIb were analysed (50 µM ATP and single trap stiffness of 0.02 pN/nm for both constructs). The data was fitted with a logarithmic normal distribution and gave peaks at 0.2 ± 0.001 pN/nm and 0.38 ± 0.001 pN/nm for full-length and S1 NMIIb, respectively.

This result shows that single-headed non-muscle myosin II is stiffer than double-headed and can be mainly explained by the size of the molecule and their attachment mode to the surface. The small S1 head is tagged with a FLAG-tag directly after the lever arm and is bound via an anti-FLAG antibody to the glass surface. Double-headed full-length NMIIb is FLAG-tagged C-terminally at the end of the tail and therefore has a high degree of freedom and flexibility, because the tail domain is not firmly attached to the glass surface which leads to a lower myosin stiffness.

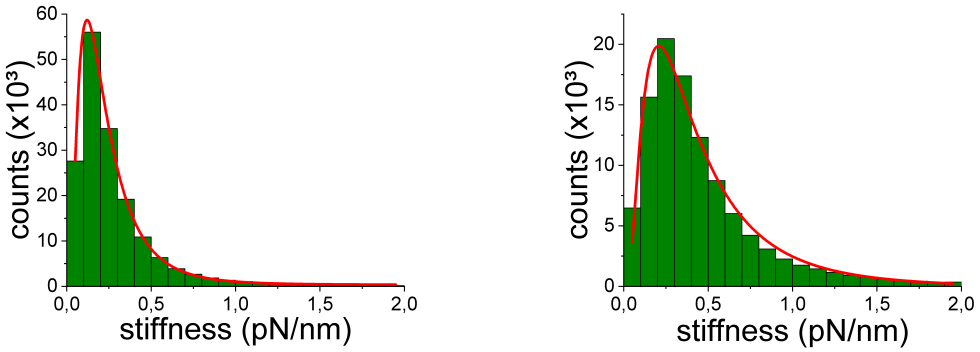

Fig. 3.50: Single-headed has a higher stiffness than double-headed NMIIb. A 100 nm 100 Hz sinusoidal waveform was applied to one of the optical traps and both 4QD detector signals were analysed. This method was used to calculate the stiffness of single-molecule interactions of NMIIb. Data was fitted with a logarithmic normal distribution and gave peaks at 0.2 ± 0.001 pN/nm (N=51; R^2=0.999) for full-length (a) and 0.38 ± 0.001 pN/nm (N=22; R^2=0.973) for S1 NMIIb (b). Data was measured at 50 µM ATP and with a single trap stiffness of 0.02 pN/nm.

Furthermore the lifetime dependence of NMIIb interactions was investigated. As shown in Fig. 3.51 events were sorted according to their lifetime and stiffness histograms were plotted in three different groups: events <50 ms, events >50 ms and events >250 ms. The stiffness values for events longer than 50 or 250 ms were very similar with about 0.2 pN/nm, whereas the stiffness for events shorter than 50 ms was slightly lower (0.13

pN/nm).

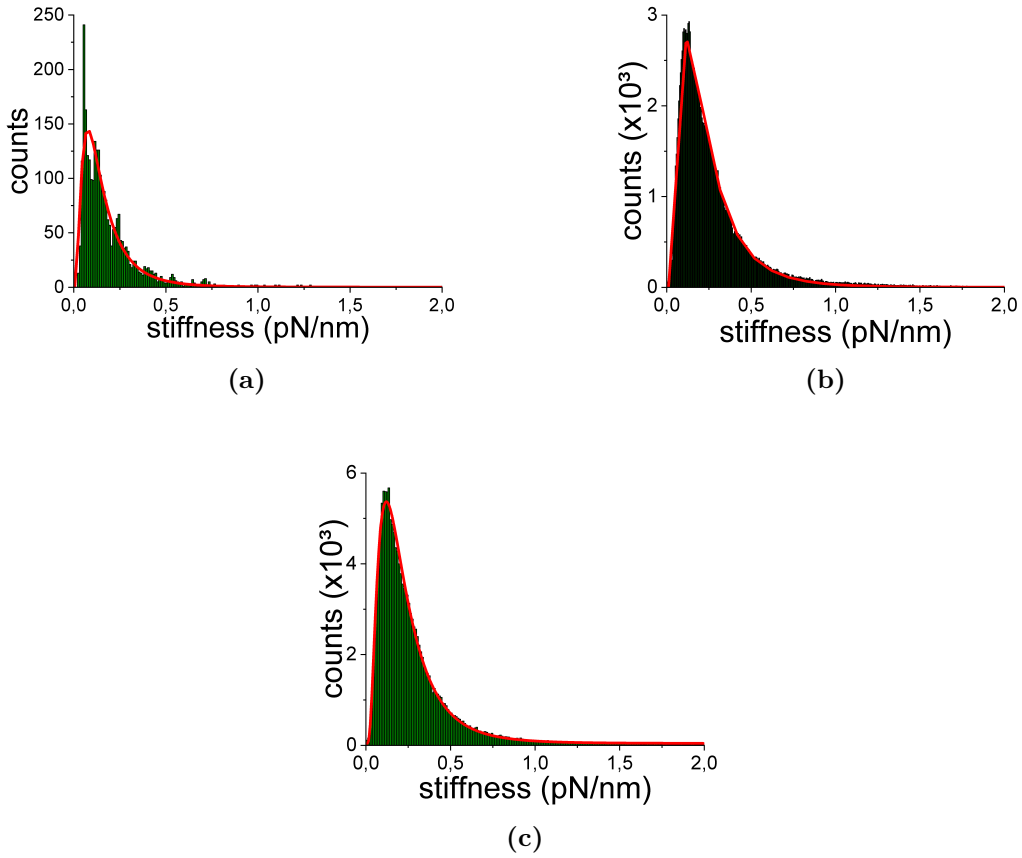

Fig. 3.51: Analysis on the lifetime dependence of NMIIb interactions. 32 events of full-length NMIIb interactions were grouped into three lifetime categories and stiffness was calculated. Data was obtained at 50 µM ATP and at 22°C. Fitting the data to logarithmic normal distributions resulted in peaks at 0.13 ± 0.003 pN/nm for events <50 ms (a), 0.20 ± 0.001 pN/nm for events >50 ms (b) and 0.20 ± 0.001 pN/nm for events >250 ms (c, R^2=0.899, 0.996 and 0.996 for the three groups, respectively). Note that the stiffness distribution of events <50 ms was unsteady and showed several peaks.

3.3 Influence of phosphorylation on the mechanical properties of human myosin VI

Myosin VI is distinguished from other members of the myosin superfamily in that it moves towards the minus end of actin filaments (Wells et al., 1999). This ubiquitously expressed molecular motor is involved in intracellular vesicle and organelle transport. Not much is known about the regulation of myosin VI by post-translational modifications (Buss and Kendrick-Jones, 2008). This section focuses on a recently found phosphorylation site (S267) in the head domain of myosin VI using mass spectrometry (F. Buss, University of Cambridge). This serine side chain is located very close to the unique insert 1, which has been shown by several studies to regulate nucleotide affinity and gating of the heads of dimeric myosin VI (Ménétrey et al., 2005; Sweeney and Houdusse, 2007; Pylypenko et al., 2011).
The results show that S267 phosphorylation has huge impacts on the in vitro properties of myosin VI. The actin gliding velocity in the motility assay was increased three-fold in the phosphorylated variant compared to unphosphorylated and wild type myosin VI. To unravel the observed increased velocity at the single-molecule level, optical trapping experiments were performed. They revealed that phosphorylation does not influence the power stroke size of myosin VI, but rather accelerates the ADP release and ATP binding rate in the actomyosin ATPase cycle. Finally, I show that S267 phosphorylation does not influence the stiffness of myosin VI.

3.3.1 Generation of myosin VI phosphovariants

To study how phosphorylation affects the mechanical properties of human myosin VI in *in vitro* assays, two phosphorylation variants have been developed by the Buss lab. The S267A variant contains a non-phosphorylatable alanine and mimics the non-phosphorylated wild type myosin VI protein. In contrast, the so-called phospho-mimetic variant S267E imitates the phosphorylated myosin VI because of the structural and electrostatic similarity between phosphoserine and glutamate (Fig. 3.52, (Wang et al., 1998)).
Additionally, artificially dimerised myosin VI constructs have been developed using a leucine zipper (after aa991) included at the C-terminus. Those constructs also contained a C-terminal GFP.
Recombinant human myosin VI bacmid DNA (NCBI no. 4646) was generated by the Bac-to-Bac® method and proteins were expressed using ExpiSf9 cells. The phosphovariants were purified using His-tag purification (Buss lab).

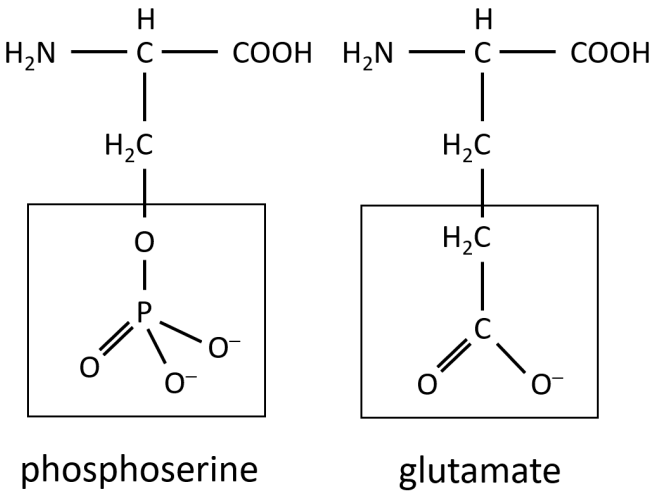

Fig. 3.52: Structural comparison of phosphoserine and glutamate. Despite the similar size, glutamate also carries a negative charge and can be used instead of phosphoserine to mimic the phosphorylated protein state.

3.3.2 The phospho-mimetic variant shows an increased actin gliding velocity

To investigate the phosphorylation effect on the actin gliding velocity, *in vitro* motility assays with both phosphovariants and wild type myosin VI were carried out by J. De Jonge and Dr. C. Batters (CIMR, University of Cambridge). Myosin VI was immobilized on a coverslip covered with nitrocellulose. After blocking of free binding places with BSA, TRITC-phalloidin labelled actin was injected. Motility was started by adding 2 mM ATP in assay buffer. TRITC-actin was excited in TIRF mode with a xenon lamp on a Zeiss Axio-observer microscope. Frames were recorded every 10 s for totally 300 s.
Myosin VI actively translocated actin filaments in the presence of ATP. As shown in Fig. 3.53 (a) the S267A variant translocated fluorescent actin with a velocity of 61.4 ± 15.2 nm/s (mean ± SD), which is a very similar velocity to wild type myosin VI (55.4 ± 14.9 nm/s). Interestingly, the phospho-mimetic variant S267E showed a nearly three-fold increased actin gliding velocity (153.8 ± 43.6 nm/s).
In addition, *in vitro* motility assays with artificially dimerised myosin VI constructs have been performed. The C-terminal GFP was used to bind the motor site-specifically to a nitrocellulose coated coverslip using a GFP nanobody. Experiments have been carried out as described above and showed similar tendencies (see Fig. 3.53 (b)). The dimerised S267A variant translocated actin filaments with a velocity of 34.6 ± 10.4 nm/s. In contrast, the S267E variant showed a two-fold increase in the actin gliding velocity (57.0 ±

21.0 nm/s).

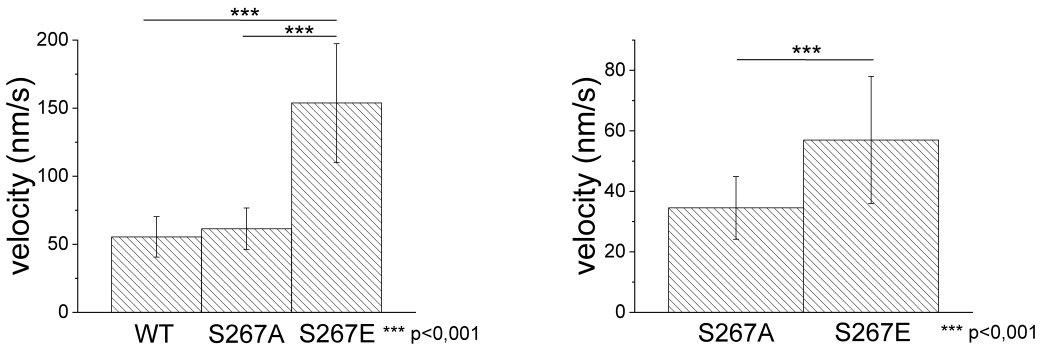

Fig. 3.53: The phospho-mimetic S267E variant increases the actin gliding velocity. (a) Bar chart displaying the velocities of fluorescently labelled actin filaments translocated by myosin VI phosphovariants and wildtype (WT). Data was collected from a minimum of three separate flow cells from three independent protein purifications (380, 375, 376 filaments for WT, S267A and S267E respectively; mean ± SD). A statistical analysis using the two-sample student's t-test revealed significant differences between the constructs with indicated p-values. (b) Summary of *in vitro* motility assay data from artificially dimerised myosin VI phosphovariants. In total 196 filaments were evaluated in this analysis (mean ± SD). All assays were carried out at 22°C (data from Buss lab).

3.3.3 The power stroke size does not differ between the two phosphovariants

In order to investigate the phosphovariants at the single-molecule level and to elucidate the nature of the increased actin gliding velocity of the phospho-mimetic variant observed in the experiments presented above, I performed optical trapping experiments with both variants. Hypothetically, the increased actin gliding velocity can be explained in two ways: 1. The working stroke size increases or 2. the overall kinetics of the motor increases.
The phosphovariants were site-specifically bound to the coverslip surface using an antibody against the N-terminal part of the tail (aa 920 - 1034; without globular domain). Unbound myosin was washed out with assay buffer and unspecific binding places on the glass surface were blocked with BSA. After blocking, the solution was replaced with an oxygen scavenger system supplemented with 100 µM ATP, an ATP backup system, rhodamine labelled actin filaments and neutravidin coated beads. Experiments were carried out with a single trap stiffness of 0.02 pN/nm and at 22°C. Data was collected at 5 kHz. Fig. 3.54 shows exemplary raw data traces with single interactions of the S267A and S267E variant with actin. Analysis of the power stroke size of 363 single S267A interactions from

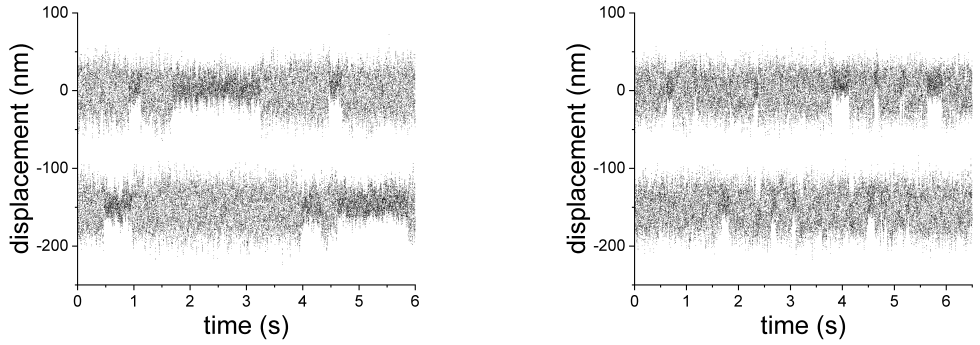

Fig. 3.54: Raw data. Original file traces of single interactions of S267A (a) and S267E variant (b) with actin. The traces show the displacement of one dumbbell bead cast on the 4QD detector. Interactions were measured at 100 µM ATP and 0.02 pN/nm single trap stiffness.

three different filaments revealed a working stroke size of 17.4 ± 0.7 nm. Intriguingly, the power stroke size of the S267E variant was very similar with 18.2 ± 0.7 nm (N=312). A Student's t test (unpaired) revealed that the difference between the values for the working stroke size was not statistically significant.

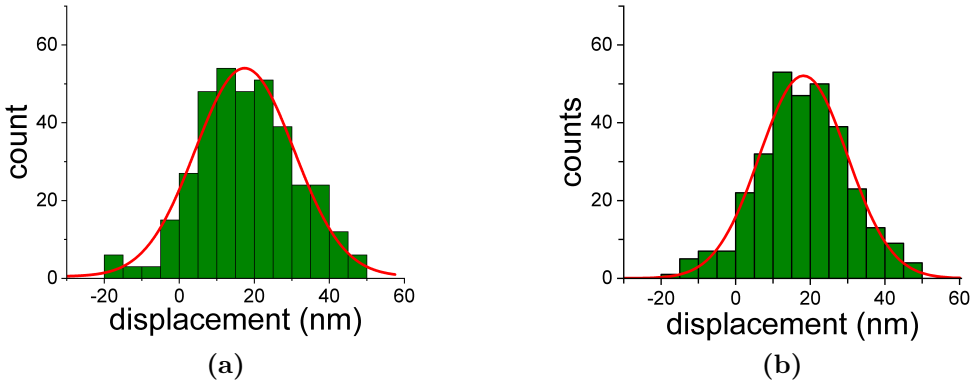

Fig. 3.55: Both phosphovariants have a very similar working stroke size. (a) Distribution of mean displacement during 363 attachments of the non-phosphorylatable variant S267A. Data was fitted with a Gaussian distribution (R^2=0.965) and resulted in a displacement of 17.4 ± 1.38 nm. (b) Analysis of the power stroke size of 312 single interactions of the phospho-mimetic variant S267E revealed a power stroke size of 18.2 ± 1.33 nm (R^2=0.972), very close to the measurements shown in (a).

The power stroke measurements of myosin VI variants presented here are very similar to wild type, which was determined to be 18 nm in optical trapping experiments (Lister et al., 2004).

3.3.4 The phospho-mimetic variant has faster kinetics compared to the non-phosphorylatable variant

The raw data traces presented in Fig. 3.54 already suggest that the S267E variant produced shorter and more frequent binding events. The overall lifetime was notably reduced in this variant compared to S267A. Optical trapping experiments were performed at two ATP concentrations (10 and 100 µM). The data was fitted with a double exponential fit and the characteristic time parameters t_1 and t_2 were extracted (see Fig. 3.56). Closer inspection of the time parameters revealed that t_2 showed a striking ATP dependence. Therefore, this ATP-dependent time parameter describes the ATP binding in the actomyosin ATPase cycle (see chapter 1.21.2). Interestingly, the ATP binding rate was very similar for both variants and was determined to $\sim$0.05 $\mu M^{-1}s^{-1}$. In contrast, the time parameter t_1 was very similar between the two measured ATP concentrations and therefore describes the ADP release. For the S267A variant the ADP release rate was determined to 5 s^{-1}. Intriguingly, this rate was nearly fourfold bigger than for the phospho-mimetic variant at 100 µM ATP and more than twice as big at 10 µM ATP.

This optical tweezers measurements clearly demonstrate that the increased velocity in the *in vitro* motility assay of the phospho-mimetic variant can be explained by a faster kinetics, whereas the power stroke size does not changes. A more detailed analysis revealed that the ADP release rate was increased by a factor 2-4 for the S267E variant. In contrast, the ADP release rate of the S267A variant was very similar to previous published values (De La Cruz et al. (2001): 6.4 s^{-1}; Lister et al. (2004): 5 s^{-1}). Furthermore, the ATP binding rate did not differ between the two variants and was around twice as high as in values found in the literature (Altman et al. (2004): 0.03 $\mu M^{-1}s^{-1}$; Lister et al. (2004): 0.02 $\mu M^{-1}s^{-1}$).

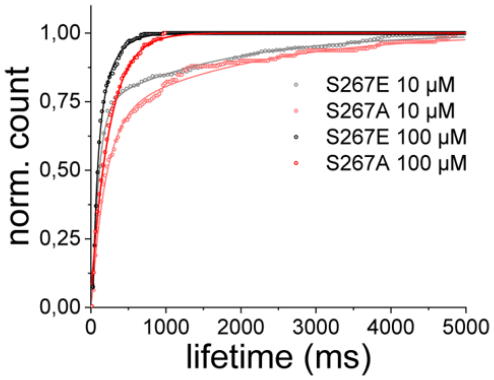

(a)

	t_1 (ADP release)		t_2 (ATP binding)	
	10µM	**100µM**	**10µM**	**100µM**
S267E	90,4 ms (±3,03)	54,5 ms (±6,29)	1703,6 ms (±42,19)	195,7 ms (±14,49)
	11,1 s^{-1}	18,3 s^{-1}	0,059 $\mu M^{-1}s^{-1}$	0,051 $\mu M^{-1}s^{-1}$
S267A	188,2 ms (±6,11)	244,3 ms (±4,49)	1931,8 ms (±47,54)	244,3 ms (±5,01)
	5,3 s^{-1}	4,1 s^{-1}	0,052 $\mu M^{-1}s^{-1}$	0,041 $\mu M^{-1}s^{-1}$
WT	6,4 s^{-1} (De La Cruz et al. 2001) 5 s^{-1} (Lister et al. 2004)		0,03 $\mu M^{-1}s^{-1}$ (Altman et al. 2004) 0,02 $\mu M^{-1}s^{-1}$ (Lister et al. 2004)	

(b)

Fig. 3.56: The ADP release rate is increased in the phospho-mimetic variant S267E. (a) Cumulative histogram of dwell times of single MD interactions in the presence of 10 and 100 µM ATP. The data was fitted with a double exponential fit (solid line) and the t_1 (ADP release) and t_2 (ATP binding) values were determined (S267E: R^2=0.994 and 0.997 for 10 and 100 µM ATP, respectively. S267A: R^2=0.992 and 0.999 for 10 and 100 µM ATP, respectively). (b) Tabular representation of the measured time parameters, their calculated rates and their comparison with the literature (WT: wildtype). In total 675 S267E and 393 S267A interactions were evaluated.

3.3.5 Phosphorylation does not affect the stiffness of the myosin VI head

To study the effect of S267 phosphorylation on the structure and dynamics of the myosin VI motor domain, molecular dynamics (MD) simulations were performed in cooperation with Dr. S. Boyd (CompChem Solutions, Cambridge). Preliminary 10 ns simulations showed substantial movement within the motor domain of the unphosphorylated myosin VI, whereas serine-phosphorylation at position 267 caused a conformational stabilization of the motor domain. This stabilization could lead to a more compact structure of the myosin VI head and hence to an increased myosin stiffness. To test this hypothesis the stiffness was measured and compared between the two phosphovariants. As shown in Fig. 3.57 the stiffness was determined to 0.25 ± 0.001 pN/nm for the S267E variant, which was very similar to the S267A variant (0.33 ± 0.002 pN/nm).

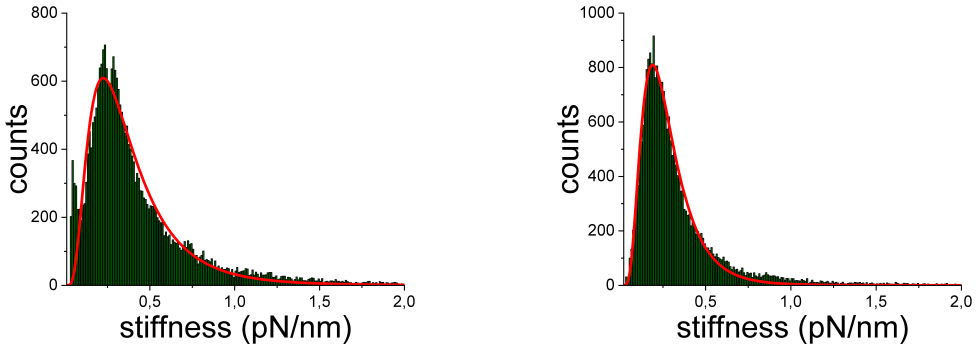

Fig. 3.57: Stiffness measurements on myosin VI phosphovariants. (a) The applied 100 nm 100 Hz sinusoidal waveform to one optical trap was used to calculate the stiffness of single-molecule interactions of myosin VI phosphovariants. Data was fitted with a logarithmic normal distribution and gave peaks at 0.33 ± 0.002 pN/nm for S267A (N=23; R^2=0.937) and 0.25 ± 0.001 pN/nm (N=18; R^2=0.990) for S267E (b). Data was obtained at 100 µM ATP and with a single trap stiffness of 0.02 pN/nm.

4 Discussion

4.1 Human myosin IXa

Class IX myosins have several unique structural features. They contain a large insertion (100-200 aa) in the loop 2 region of the head domain, which is known to bind to F-actin. Additionally, they contain a Rho-GTPase–activating protein (RhoGAP) domain in the tail, which suppresses the activity of the GTPase Rho. The presence of such an for myosins unusual protein domain connects this motor protein with signal transduction functions (Bähler et al., 2011).
By using the highly versatile baculovirus/insect cell system our laboratory was able to express and purify enzymatically active human myosin IXa fragments for the first time (Saczko-Brack et al., 2016). Despite low expression levels and prep-to-prep variability I was able to express and purify different myosin IXa constructs and to characterize them with different biophysical ensemble assays as well as single-molecule methods.
The results presented in chapter 3.1 clearly indicated that human myosin IXa is a mechanically active motor that can bind and translocate actin filaments in an ensemble *in vitro* motility assay and on the single-molecule level with an optical tweezers transducer. Furthermore, I showed that the unique loop 2 insert is responsible to cross-link actin filaments into highly ordered networks, which links this motor protein to structural functions in the cytoskeleton.

4.1.1 Human myosin IXa is an active motor protein and the neck domain acts as a lever arm

The motor domain (MD) construct, including residues 149-1019, contained the unique ∼200 aa loop 2 insert together with a calmodulin-binding IQ motif. Site-specific immobilization of IXa MD via the biotin-streptavidin linkage on a glass surface resulted in translocation of actin filaments with a velocity of ∼24 nm/s at 2 mM ATP, about 170

times slower than that of skeletal muscle myosin II. Interestingly, the head of myosin IXa without the neck domain produced the actin filament movement, suggesting that the pivot point over which the neck domain swings is located N-terminally of the last amino acid of the MD construct.

The myosin IXa S1 construct contained the motor domain and six IQ motifs (neck) and moved actin in the *in vitro* motility assay with a velocity of 91 nm/s at 2 mM ATP. This velocity is about 4 times faster than the actin gliding velocity of the MD construct and clearly shows that the neck domain of myosin IXa functions as a lever arm. These results are in good agreement with measurements of previous lab members, although Warchol (2016) observed a six times increased velocity of the S1 versus MD construct (from ∼35 to ∼204 nm/s).

In this work I performed the first single-molecule measurements on the myosin IXa isoform using an optical tweezers transducer. Initially, human myosin IXa MD was unspecifically bound to a nitrocellulose-coated surface. Although actomyosin binding events were observed, their working stroke size and kinetic did not match the kinetic data obtained in the ensemble assay mentioned above. Therefore, IXa MD was site-specifically attached to the glass surface using an anti-FLAG antibody. This attachment method, using the C-terminal FLAG-tag on the myosin IXa sequence, oriented the myosin molecules in such a way, that their heads could move freely to bind actin and to perform complete power strokes. This modification resulted in a power stroke size of 4.8 nm.

Interestingly, the S1 (head-neck) construct produced a 23.7 nm working stroke (besides ∼0 nm binding events), which is about five times bigger than the power stroke obtained from myosin IXa MD experiments. These single-molecule results match the findings of the ensemble measurements mentioned above in a good way, where a four times faster velocity of the head-neck construct compared to the head construct was measured. Both single-molecule and ensemble techniques suggest that the neck domain of human myosin IXa functions as a lever arm as shown in Fig. 4.1. This lever arm effect was also shown for *Dictyostelium* myosin II and smooth muscle mutants with different biophysical techniques (Uyeda et al., 1996; Warshaw et al., 2000; Ruff et al., 2001). Furthermore, optical trapping measurements on myosin V, which also contains six IQ motifs in the neck domain revealed a power stroke size of 25 nm (Veigel et al., 2002), which is very similar as in the measurements presented here.

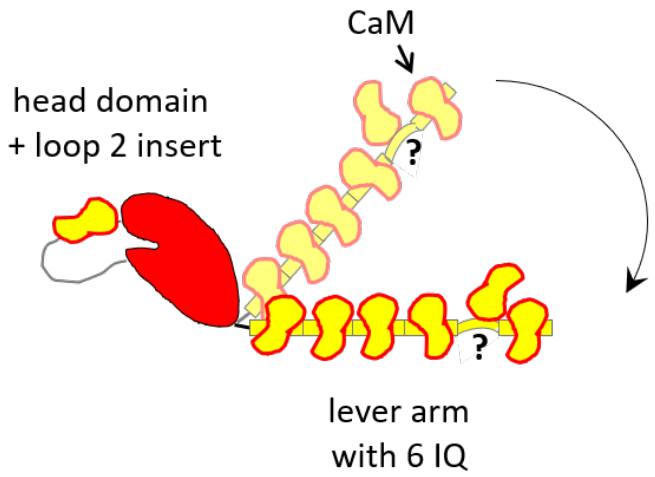

Fig. 4.1: The six IQ domain of myosin IXa acts as a lever arm. *In vitro* motility assay and optical trapping experiments clearly showed that the six IQ domain of myosin IXa increases the actin gliding velocity in ensemble measurements and enlarges the working stroke in single-molecule experiments. Note that the fifth calmodulin (CaM) in the neck domain is only loosely bound at the C-terminal lobe and probably does not contribute to the effective lever arm because of a kink at this IQ motif position (details see text).

The neck domain of human myosin IXa contains six IQ motifs, which can bind theoretically a total of six calmodulins (CaM). Therefore, it might have been expected that the actin gliding velocity of the head-neck construct is six times faster than the head construct. In a similar way, also the power stroke of the S1 construct might be six times bigger than of the MD construct. My measurements showed a four fold increase of the actin velocity in the *in vitro* motility assay and a five fold increase in the power stroke size in optical tweezers measurements. This leads to the hypothesis that one or two IQ motifs in the neck domain do not have calmodulin bound, or they have a very weak affinity to CaM. This could result in an instability in the lever arm and therefore to slower velocities and smaller power strokes. This hypothesis is supported by protein band densitometry measurements of previous lab members, which showed that the neck domain binds only five calmodulins. Interestingly, this study pointed out that the fifth IQ motif in the neck region of myosin IXa has glycine replaced for lysine at position 7 of the consensus sequence IQxxxRGxxxR (Warchol, 2016). It is predicted that this sequence substitution binds to CaM in an extended conformation at the C-terminal lobe only and could lead to a total loss of calmodulin binding. Both the N- and C-terminal lobes of CaM bind to unsubstituted IQ motifs in a compact conformation (Terrak et al., 2005; Liao et al., 2010). Intriguingly, also one of the IQ motifs of myosin IX from *C. elegans* has this glycine substitution and it was shown that the neck domain only binds four instead of

five calmodulins (Liao et al., 2010). The biophysical experiments presented in this study support these findings, indicating that only 4-5 of the six IQ domains contribute to the effective lever arm, because one or two IQ motifs are not mechanically stabilized by a calmodulin.
The idea that CaM binding to the neck domain of myosin IXa plays an important role for stabilizing the lever arm is emphasized by the fact that a 5-10 fold excess of exogenous CaM was necessary to obtain robust translocation of actin filaments in the *in vitro* motility assay of the head-neck construct. Additionally, exogenous calmodulin was also necessary to add during purification to increase the quality of the preparation.

4.1.2 Mechanical functions of the extended loop 2 in myosin IXa

Class IX myosins contain a unique large insertion (100-200 aa) in the loop 2 region of the head domain. Studies with isolated loop 2 of rat myosin IXb showed that this peptide bound stoichiometrically and with high affinity to F-actin (Struchholz et al., 2009). These results indicated that the myosin IX-specific loop 2 insertion is involved in the interplay of myosin IX with F-actin besides the conventional actin-binding site.

To address the effect of the loop 2 on the mechanical functions of human myosin IXa, I developed a mutant MD skeletal construct, where the characteristic loop 2 of IXa (∼200 aa) was replaced against the much shorter loop 2 of skeletal muscle myosin II (∼20 aa). Interestingly, the MD skeletal construct was more than seven times faster in the *in vitro* motility assay as the MD construct. Furthermore, robust translocation of actin filaments was only observed in the presence of 0.5 % methylcellulose, a viscosity substance that was previously used to compensate for insufficient actin binding by smooth muscle myosin and myosin IXb (Joel et al., 2001; Liao et al., 2010; Elfrink et al., 2014). These results clearly demonstrated that the removal of the IXa-specific loop 2 insert alters the actin affinity of the motor. Binding of the loop 2 insert to actin acts as a 'molecular break' in the motility assay and thereby decreases the actin gliding velocity.
Nevertheless, the increased actin velocity in the *in vitro* motility assay after the removal of the loop 2 insert is in great contrast to the study of Elfrink et al. (2014), where they observed a reduced actin gliding velocity after loop 2 removal. This discrepancy could be explained by the fact that in our study the entire loop 2 of myosin IXa was replaced by the loop 2 sequence of skeletal muscle myosin whereas in Elfrink et al. (2014) only the loop 2 insert was removed. The different loop 2 sequences (this work: skeletal myosin II; Elfrink et al. (2014): *C. elegans* myosin IXb) could alter the actin binding in a severe way

as exchange of flexible loops between different members of class II myosins was shown to affect the ATPase rates and the mechanochemical coupling (Uyeda et al., 1994; Rovner et al., 1995). In addition, myosin IX from *C. elegans* was used in the study of Elfrink et al. (2014), which could explain the deviating results further. This invertebrate species contains only a single myosin class IX gene, with a smaller loop 2 insert compared to myosin IXa.

The increased actin gliding velocity was also investigated on a single-molecule level using an optical tweezers transducer. Although the power stroke size did not differ between the MD and the MD skeletal construct, the kinetics was faster for the mutant lacking the myosin IX specific loop 2. These results are in good agreement with the motility assay data and indicate that the loop 2 insert is not required to perform a complete power stroke, but influences the ATPase cycle or interacts with the transition of weak to strong actin binding states.
Intriguingly, the actin velocity in the *in vitro* motility assay of MD skeletal did not saturate at 2 mM ATP compared with skeletal myosin II measured in this work and by others (Sheetz et al., 1984; Kron and Spudich, 1986; Homsher et al., 2003). The actin gliding velocity increased up to ∼300 nm/s at 10 mM ATP. In contrast, the actin gliding velocity of the MD construct saturated at 2 mM ATP (preliminary data, not shown). A more detailed understanding of this processes could be addressed in future experiments, also based on solution kinetic experiments.

The bundling experiments clearly demonstrated that a single myosin IXa head is able to cross-link actin filaments due to the presence of the unique loop 2 insert. These results indicate that myosin IXa contains a second actin binding site in the head domain besides the conventional binding site (CBS; see Fig. 4.2). With the exception of monomeric myosin I, that contains a second actin-binding site in the tail domain, no other member of the myosin superfamily is known to bundle actin filaments (Lynch et al., 1986; Stafford et al., 2005).
Those two binding sites allow myosin IXa to bundle actin filaments in a very regular and ordered way and leads to the following question: Are single-molecule methods able to differentiate between the two binding states? Closer investigation of the stiffness of single-molecule binding events revealed that the MD skeletal mutant had a 1.5 times lower stiffness than the MD wildtype. This result indicates that binding of the ∼200 aa loop 2 to actin contributes significantly to the overall myosin IXa stiffness. This finding is supported by transmission electron micrographs showing that both binding sites of the

myosin head can simultaneously bind to a single actin filament in the inchworm conformation.

Another possibility to differentiate between the two binding sites would be to consider the power stroke size. Loop 2 binding to actin is expected to produce a binding event close to 0 nm as no active movement can be produced by this flexible peptide. Indeed, evaluation of the power stroke size of the head-neck (S1) construct showed a main peak at around 0 nm, although only a small shoulder at 0 nm was observed with the head (MD) construct. Future experiments could work out why the 0 nm peak is so prominent in the head-neck construct, whereas it is inconspicuous in the MD construct. The generation of a S1 skeletal construct, lacking the loop 2, could reveal if the myosin IXa specific loop 2 insert is responsible for the 0 nm power stroke.

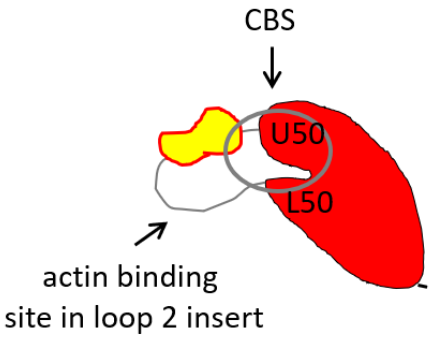

Fig. 4.2: A single myosin IXa head has two actin binding sites. The conventional actin binding site (CBS) is located in the loop 2 region and involves also parts of the upper and lower 50 kDa catalytic domain (U50 and L50). The second actin binding site is found in the ∼200 aa loop 2 insert.

4.1.3 Actin bundling induced by myosin IXa

The presence of a second actin-binding site within a single myosin IXa head and recent studies indicating a major role of IXa-actin bundles in regulating the collective migration of epithelial cells (Wood and Olson, 2012; Omelchenko and Hall, 2012), suggest a structural function of this motor protein.

Using qualitative and quantitative total internal reflection fluorescence (TIRF) microscopy I was able to show that human myosin IXa bundles actin and they contain up to seven actin filaments. The MD skeletal mutant did not cross-link filaments, clearly demonstrating that the loop 2 insert is responsible for the bundling capability of myosin IXa. In collaboration with Dr. Saczko-Brack the actomyosin bundles were directly visualized us-

ing transmission electron microscopy. The data showed highly ordered lattices, where the motor domain of IXa formed cross-links at a repeat distance of exactly 36 nm. Classification of around 1000 images resolved three distinct conformations of myosin IXa within the bundles: A diagonally shaped cross-link, a bent cross-link and an inchworm conformation, where the myosin IXa did not cross-link but binds with both actin binding sites to the same filament.

Based on these results we proposed a model (see Fig. 4.3) for generating lattice-like actomyosin networks caused by myosin IXa (Saczko-Brack et al., 2016): 1) A myosin IXa MD binds to an actin filament either via the loop 2 insert or the conventional actin binding site. 2) If a second actin filament of the same polarity comes nearby, myosin IXa is able to form a cross-link between two filaments. In this state, the flexible insert in loop 2 with its second binding is able to freely move around in search of other actin monomers. 3) The cross-linking activity positions the two actin filaments in parallel polarity. Further myosin IXa molecules are binding and extend the cross-linking process, which stabilizes the actin network even more. The position of new cross-links is determined by the 36 nm periodicity. This creates a free energy landscape which has minima at this preferred binding positions. Myosin IXa can adopt three distinct conformations within these cross-links, depending on the binding position of the flexible loop 2 on actin: the diagonal conformation (I), the bent conformation (I) or the inchworm conformation (III). The latter one does not cross-link two filaments and is bound with both actin binding sites on one single actin filament.

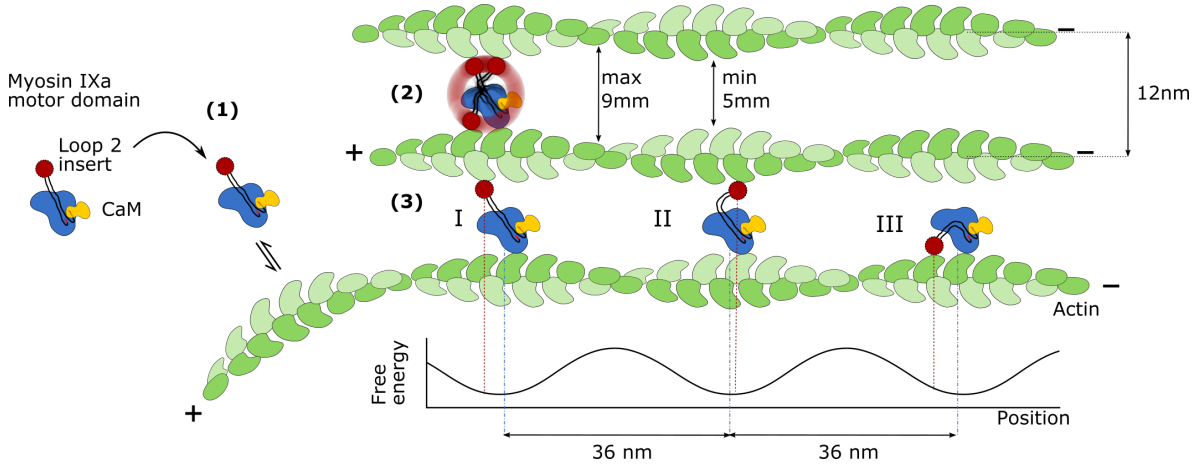

Fig. 4.3: Suggested model to explain the self-organisation of actin networks by myosin IXa. Actin filaments with parallel polarity are bundled by the myosin in a highly ordered fashion. IXa molecules can adopt three interchangeable conformations (inchworm, diagonal or bent) that are found at binding sites with free-energy minima. The exact 36 nm spacing is obtained due to the length restriction and flexibility of loop 2 and the distances between actin filaments defined by their three-dimensional structures (Saczko-Brack et al., 2016).

In future studies it is planned to investigate the myosin IXa induced actin bundles using cryo-EM in collaboration with Dr. Saczko-Brack. In this stain-free technique, developed by Adrian et al. (1984) many drawbacks of negative staining can be overcome. Fig. 4.4 shows preliminary raw cryo micrographs, where actomyosin bundles are clearly visible (red arrows). The contrast is rather low in those raw micrographs, but the regular arrangement of myosin IXa-crosslinks is recognisable. Those data will be analysed in order to get high resolution images of myosin IXa in the bundles and possibly informations about the three-dimensional arrangement of the extended loop 2 within the myosin head.

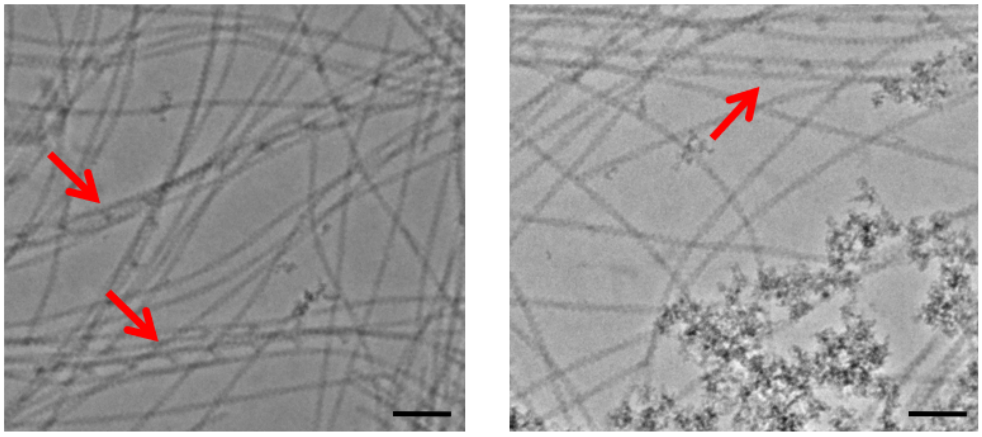

Fig. 4.4: Cryo-EM raw micrographs of myosin IX induced actin bundles. IXa MD was mixed with F-actin at a 1:1 molar ratio and applied to cryo-grids. Myosin IXa formed cross-links in ladder-like patterns (red arrows). Scale bar is 50 nm (images from Dr. Saczko-Brack).

4.1.3.1 Bundle dissociation dynamics

Interestingly, bundles were still present at millimolar ATP concentrations (up to 2 mM). Even at this high ATP concentrations small bundles were observed, which dissociated very fast into single filaments. To study the dissociation behaviour of small actin bundles consisting of only two actin filaments a new type of bundling assay was developed. In this assay two species of actin were used. The first species contained biotinylated actin monomers and was able to bind to a glass surface covered with streptavidin. The second species was made of non biotinylated G-actin and was labelled with a different dye than the first species. In the presence of myosin IXa, actin filaments got bundled. Only those bundles, with a surface-bound biotinylated actin and a non biotinylated actin bundled to this via myosin IXa, were selected for analysis. Intriguingly, the ATP-induced dissociation did not occur in a gradual manner as expected but happened in discrete events.

Complete bundle dissociation took place in single or multiple events with up to 5 events. The size decrease of the bundles and the duration between single events showed an ATP dependent behaviour.

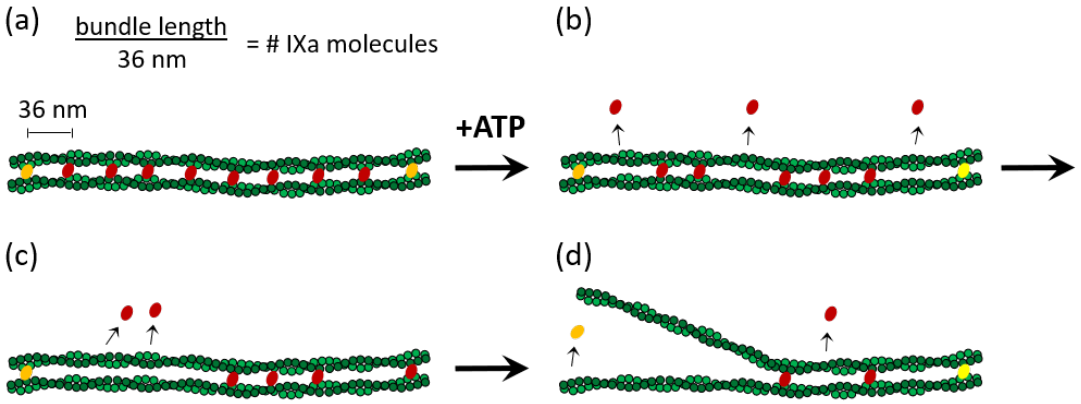

Fig. 4.5: A possible theoretical explanation of bundle dissociation occurring in ATP dependent events. (a) In this schematic cartoon a bundle is shown consisting of two actin filaments crosslinked by several myosin IXa molecules with a distance of 36 nm. Because of the precise spacing of myosin IXa in the bundles, the bundle length can be used to determine the amount of crosslinked myosin IXa molecules. (b) & (c) In the presence of ATP, the conventional binding site of myosin IXa unbinds from actin. At which position along the bundle the unbinding occurs is stochastic but the unbinding probability is dependent on the ATP concentration. (d) Only if the myosin molecule at the bundle end (coloured in yellow) unbinds from actin, a bundle dissociation event happens.

A possible explanation of the dissociation events takes the persistence length of actin filaments into account, which is in the order of micrometers (Milo and Phillips, 2016), whereas the spacing between two myosin IX-crosslinks is only 36 nm. A single or even several ATP-induced unbinding of myosin IXa from actin will not be detected in the bundling assay, because the actin filament is rigid and remains at its position. An actin dissociation event only occurs when enough myosin IXa molecules unbind from actin and this filament part get bended into solution and it is no longer visible in TIRF microscopy (see Fig. 4.5). The unbinding probability of myosin IXa from actin depends on the amount of available ATP molecules in solution. Therefore, the dissociation process is ATP dependent. Interestingly, the crosslinking myosin IXa at the bundle end (coloured in yellow in Fig. 4.5) plays a crucial role: As long as this myosin IXa does not unbind from actin, no bundle dissociation can occur.

These theoretical considerations are emphasized by preliminary TEM experiments in col-

laboration with Dr. Saczko-Brack, which showed 'holes' in the regular actin network in the presence of ATP (see Fig. 4.6). Without nucleotides an irregular actomyosin network with 'empty' binding places was never observed. These experiments and the possibility of a quantitative description of the bundle dissociation process, would allow to generate a theoretical model in future work.

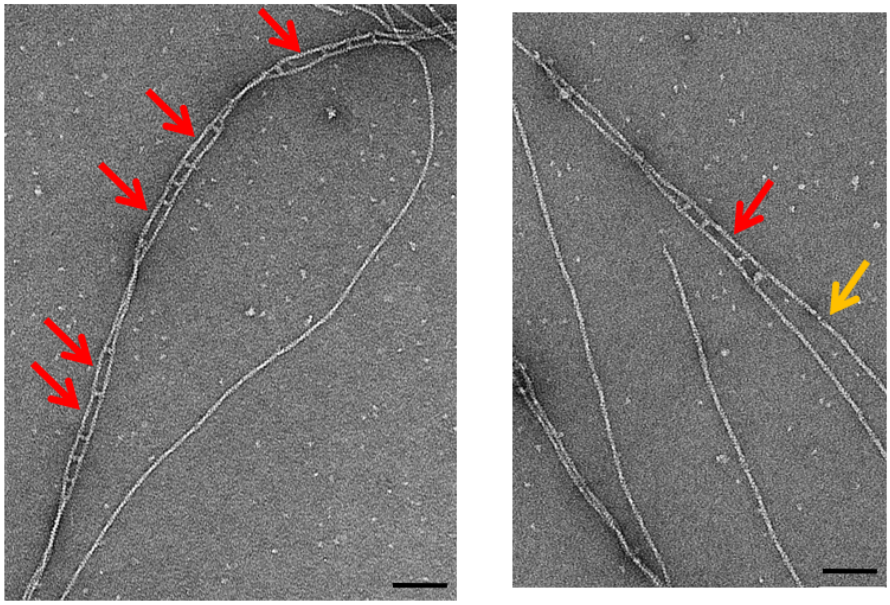

Fig. 4.6: Preliminary TEM micrographs of myosin IXa-induced actin bundles in the presence of 10 µM ATP. Phalloidin stabilized F-actin and IXa MD were mixed at a 1:1 molar ratio and incubated for several minutes with 10 µM ATP. The specimen was applied to carbon grids and negatively stained using uranyl acetate. The amount of bundles on the grids was highly reduced with ATP. The red arrows indicate 'holes' in the actomyosin network, suggesting individual myosin IXa dissociation events from actin leading to dissociation of the bundles (orange arrow). Scale bar is 100 nm (images from Dr. Saczko-Brack).

In summary, these results showed that the myosin IXa-induced actin lattices can still be formed in the presence of ATP. Fluctuations in the intracellular ATP concentration allow to regulate the dynamic assembly and disassembly of the actin network. Other crosslinking proteins such as fascin, α-actinin, fimbrin or filamin (Blanchoin et al., 2014) are not sensitive to ATP and cannot adapt in that extent to various intracellular nucleotide concentrations. Additionally, the cross-linking myosin IXa is also sensitive to calcium, which is a further regulatory mechanism and allows to adjust the polarity of the actin lattices (see below). This might provide specific tracks for other myosin motors tunable by intracellular ATP and calcium concentrations. Furthermore, these networks could also represent platforms, which allows specific RhoGAP activity from the tail of myosin IXa

to be focused on specific locations inside the cell, e.g. near the plasma membrane at cell-cell adhesions. Indeed, spatial regulation of RhoGAP activity is known for several members of this protein family to control cytoskeleton dynamics and to provide positional information for signalling (Machacek et al., 2009; Pertz, 2010; Müller et al., 2020).

4.1.4 The regulatory function of calcium

Besides a second actin-binding site the unique loop 2 of myosin IXa contains a calmodulin binding sequence. Sequence analysis showed that this motif belongs to the family of 1-8-14 calmodulin-binding sites, whereas the numbers indicate the positions of bulky hydrophobic residues that form important interactions with calmodulin. This motif is highly conserved within the myosin IX family but only present in class IX myosins (Yap et al., 2000; Liao et al., 2010).

Many studies showed that calcium binding to calmodulin regulates the mechanics and activation level of various myosins (Szent-Györgyi, 2007; Buss and Kendrick-Jones, 2008; Batters and Veigel, 2016). *In vitro* motility experiments of a head construct of *C. elegans* myosin IX showed no actin translocation in the presence of calcium. Interestingly, the actin gliding velocity increased by a factor of 2.5 for the head-neck construct at pCa 4 (0.1 mM free calcium). Similar tendencies were also observed in solution kinetics measurements (Liao et al., 2010).

Motility experiments on the motor domain of human myosin IXa performed by previous lab members did not showed any differences in the gliding velocity in the absence or presence of pCa 4. Intriguingly, solution kinetics studies revealed that the ATPase of the MD construct was activated five-fold by actin in the presence of calcium. Furthermore, the motility of the head-neck construct of myosin IXa was fully inhibited at pCa 4 (Warchol, 2016).

These results on *C. elegans* myosin IX and human myosin IXa clearly show that class IX myosins are regulated by calcium, but there exist big differences between the two isoforms in terms of calcium regulation. These differences might be based on sequence variabilities between the two isoforms or due to experimental challenges in performing the motility experiments. In order to achieve an overview by myself, I performed motility experiment with the MD and the S1 (head-neck) construct in the absence and presence of 0.1 mM free calcium. The actin gliding velocity of the MD construct increased only slightly but significantly at pCa 4. It is surprising that the actin-activated ATPase activity of the motor domain is stimulated five-fold by calcium (Warchol, 2016), but the actin gliding velocity only increases slightly. A possible explanation might be, that the ATPase was measured in solution, whereas the motility assay was performed with site-specific immo-

bilized myosin IXa on a glass surface. This oriented attachment mode could alter the kinetic properties of myosin IXa, or could prevent specific parts of the motor domain to interact with distinct sites within the head domain.
In actin gliding experiments with the head-neck (S1) construct I observed a significant decrease of the gliding velocity, whereas Warchol (2016) described a complete inhibition in the presence of pCa 4. Calcium binding to neck-bound calmodulin could lead to a complete loss of single or several CaM, which could destabilize the lever arm to be unable to perform a complete power stroke. Indeed, preliminary optical trapping measurements with the S1 construct at pCa 4 (data not shown) revealed variable stiffness values of single-molecule binding events, suggesting the presence of varying number of calmodulins bound to the lever arm of myosin IXa.

Preliminary TEM data in collaboration with Dr. Saczko-Brack showed that the polarity of actin filaments in the myosin IXa induced actin networks is regulated by calcium. At low calcium concentration (pCa 8) ∼97 % of the actin filaments in the bundles showed a parallel polarity, whereas at high calcium concentrations (pCa 4) intriguingly ∼75 % of the filaments adopted an anti-parallel polarity. This dramatic effect on the polarity of the actin lattices might be explained by calcium binding to calmodulin bound to the class IX specific loop 2 insert. This binding could induce a structural reorganisation of the loop 2. The detailed mechanism is still unclear and could not be resolved in TEM experiments.
In order to investigate the binding of myosin IXa to actin in the absence and presence of calcium in further detail, *in vitro* motility experiments with polarity labelled actin filaments were carried out. These filaments are generated with gelsolin, that binds to the plus end of actin filaments and prevents further polymerization. Different fluorescent actin labels were used before and after gelsolin incubation, which leads to distinct labelled plus- and minus ends. In the absence of calcium 96 % of actin filaments showed a leading plus-end, which is in accordance with other myosin IX isoforms (O'Connell and Mooseker, 2003; Liao et al., 2010). This is the first direct confirmation that human myosin IXa moves towards the plus-end of actin filaments.
Interestingly, in the presence of 0.1 mM free calcium the directionality of myosin IXa did not changed and 93 % displayed a plus-end directed movement. It might have been expected that the directionality of actin filaments changes in the presence of calcium as the polarity in the actin networks is switched in the TEM data. The motility experiments suggest that the conventional actin binding sites, which is mainly responsible for active actin translocation, is only slightly calcium sensitive. The speed of actin translocation of the motor domain increased only minimal in the presence of calcium (see above), whereas

the directionality of actin filaments in the motility assay is not influenced by pCa 4. These results suggests that the unique loop 2 insert with the calmodulin binding site is the main candidate for calcium sensitivity. A structural reorganisation of the loop 2 insert induced by calcium would have no or only a little effect in the *in vitro* motility assay, because actin translocation does not require a insert-actin interaction. In contrast, insert-actin interplay is required during bundling as a second actin-binding site is needed to establish a stable cross-link between the head of myosin IXa and actin. Therefore, the calcium sensitivity of the loop 2 insert plays a major role in bundling and not in the motility assay.

The pronounced calcium effect on the polarity of myosin IXa induced actin networks, could have important physiological relevance in cell types, which use calcium transients for signalling purposes such as the neuromuscular junction (NMJ) in motor neurons. Indeed, mutations in the myosin IXa gene have been identified in patients with congenital myasthenic syndrome (CMS), an inherited neuromuscular disorder which is characterized by muscle weakness often affecting facial muscles (O'Connor et al., 2016, 2019). These patients have defects in the NMJ and underline the involvement of myosin IXa in motor axon functionality. A calcium mediated switch of actin polarity in myosin IXa-actin lattices could have pronounced effects on the directionality of vesicle transport in NMJ. The exact molecular mechanism and the action of myosin IXa pathophysiology in CMS still remains unclear and needs further investigation.

4.1.5 Structure of the loop 2 of myosin IXa

The unique loop 2 insert of human myosin IXa with a length of ∼200 aa contains a 1-8-14 calmodulin-binding site and a second actin binding site which enables a single myosin IXa head to cross-link actin filaments. The precise structure of the loop 2 insert is not known. However, single-molecule AFM force spectroscopy studies on rat myosin IXb loop 2 revealed that it did not provide much resistance to mechanical unfolding. This result does not exclude that the loop 2 insert contains folded structures, but also shows that it can act as a flexible linker. The persistence length was determined to ∼0.3 nm, which is a quite low value and is typical for a flexible peptide behaving like an entropic spring. The isolated loop 2 bound actin in a 1:1 stoichiometric ratio and with high affinity (Struchholz et al., 2009).

At present, there are no structural or biochemical details known about the loop 2 insert of myosin IXa. In this work I cloned, expressed and purified different IXa loop 2 constructs. Although I was able to express and purify small amounts of a loop 2-GST

fusion protein, gel filtration analysis revealed that it formed aggregates or big oligomers. Varying the ionic strength of the elution buffer, adding 0.1 mM calcium or equimolar amounts of calmodulin did not changed the elution profile of the gel filtration column. This observation could be explained by two possibilities: 1) The right conditions for correct protein folding are not found yet and need further optimization. Increasing the ionic strength above ∼160 mM (PBS) during gel filtration would be one option, as also the actin gliding velocity of myosin IXa showed a broad ionic strength dependence (Warchol, 2016). 2) The isolated loop 2 of myosin IXa does form aggregates or big oligomers as a consequence of its amino acid composition. DLS measurements would be able to determine the hydrodynamic size of the (small) aggregates and it would be possible to differentiate between aggregates and oligomers.
Studies on isolated loop 2 of rat myosin IXb indicated that most of this peptide was insoluble. Therefore it was purified under denaturing conditions and refolded by stepwise dialysis in decreasing urea concentrations (Struchholz et al., 2009). In my work the main part of the expressed loop 2-GST fusion protein was found in the supernatant of bursted and centrifuged *E. coli* cells, showing that a large proportion of the expressed protein was soluble. Nevertheless, the amount of expressed protein was quite low, suggesting that the expression conditions were not optimal. Variation of the expression temperature and duration did not increased the amount of soluble protein, neither coexpression of loop 2 with calmodulin in a pET-Duet vector. Also the expression of the pET-Duet vector in a different *E. coli* strain did not augmented the protein quantity.

Many eukaryotic proteins need post-translational modifications in order to fold properly into their three-dimensional structure. Changing the expression host to an eukaryotic organism could have substantial impact on the quality and quantity of the expressed protein (Tokmakov et al., 2012). Although expression of loop 2 was not successful in a insect cell line (Sf21; personal communication with Dr. Chris Batters), using an mammalian expression system (e.g. HeLa cells) in future studies could increase the protein quality.
Due to the lack of structural data about the loop 2 of myosin IXa, I used two different structure prediction algorithms to get insights into the three-dimensional (3D) structure. I-TASSER and Phyre2 are widely used modelling tools, which compare the unknown protein sequence with a large database of known structures and predict secondary structures to build 3D models. Although their general working principle is similar, they differ in great extent in their detailed operating pipeline. I-TASSER uses a multiple threading alignment method to find structural templates in the protein data bank (PDB), whereas Phyre2 uses homology detection methods (Yang and Zhang, 2015; Kelley et al., 2015).

Interestingly, both tools predicted several α-helices in the loop 2-sequence, but no β-sheets have been detected. This result is in line with previous AFM force spectroscopy studies on purified myosin IXb loop 2, which indicated that loop 2 contains a considerable amount of secondary structure with elastic properties (Struchholz et al., 2009). α-helices would fit into this concept, providing a high flexibility to loop 2 for actin binding.
Furthermore, the modelling tool Phyre2 found a highly homologous part in the myosin Vc structure to the C-terminal part of loop 2. Besides myosin Vc, several other myosin isoforms have been found being homologous to the C-terminal part, even though they had a lower confidence level than myosin Vc. In contrast, the N-terminal part of loop 2 did not show considerable homology to PDB protein structures. This may reflect the fact that this part contains the 1-8-14 calmodulin-binding site, which is only present in class IX myosins and is highly conserved within this isoform (Liao et al., 2010). This highlights the unique nature of the calmodulin-binding site and its regulatory functions.

The predicted I-TASSER 3D structure of human myosin IXa loop 2 had a high confidence score, indicating that the core of the protein is modelled with great accuracy. Nevertheless, one should be careful with this 3D models, as both algorithms also predicted a relatively high amount of disordered structures. Additionally, flexible surface loops are generally problematic for structure prediction tools (Fiser et al., 2000), although the length of myosin IXa loop 2 ($\sim$200 aa) may suggest that it adopts a stable 3D fold.

4.2 Human non-muscle myosin IIb

Class II myosins comprise a multitude of diverse myosin motors including skeletal, cardiac, and smooth muscle myosin II, with a high tissue specificity and so-called non-muscle myosin II isoforms which are ubiquitously expressed throughout different cell types. Humans express three non-muscle (NM) myosin II isoforms named NMIIa, NMIIb, and NMIIc. Those isoforms play a key role in many essential cellular processes such as cytokinesis, cell migration, cell adhesion and control of cell morphology (Berg et al., 2001; Heissler and Manstein, 2013). The importance of NMII isoforms for cellular homeostasis and developmental mechanisms are highlighted by the fact that NMII knock-out mice die during embryogenesis (Vicente-Manzanares et al., 2009).

Similar to many other classes of the myosin superfamily, NMII's are characterized by their 'double-headed' structure, with each head behaving as a single molecular motor, which can hydrolyse ATP and interact with actin. However, the functional relevance of this dimeric structure is still not completely understood. In this work I focused on the NMIIb isoform, which is highly enriched in neuronal tissues and in cardiac muscle (Rochlin et al., 1995). I cloned, expressed, and purified single- (S1) and double-headed (FL) human NMIIb constructs and compared their mechanical and kinetic behaviour at the single-molecule level using an optical tweezers transducer. The aim was to investigate the cooperativity of the myosin heads.

The results indicated that the power stroke size was very similar between the single- and double-headed NMII constructs. Besides ∼0 nm attachment events (see below), the full-length (FL) construct showed a ∼6 nm power stroke, whereas the S1 construct revealed a ∼5 nm power stroke. Both values were similar to previous measurements with myosin class II molecules (Veigel et al., 1999; Yanagida et al., 2000; Veigel et al., 2003). Additionally, the values obtained in this work are very close to an optical tweezers study of Nagy et al. (2013) with single and double headed human NMIIb. A major plus point of my work is the generation of a recombinant single headed construct. Compared to previous studies on single- and double headed myosin molecules, the single-headed myosin species were generated using proteolytic digestion (Tyska et al., 1999) or by co-expression of NMIIb-HMM with subfragment 2 (Nagy et al., 2013). Both methods cannot completely rule out the generation of double-headed myosin species, especially with subsequent single-molecule measurements. Recombinant expression of a S1 construct eliminates this problem, because S1 lacks a coiled-coiled sequence enabling it to form dimers and filaments.

Interestingly, the kinetic measurements in this work were very similar between single- and double-headed NMIIb constructs. This indicates that the single myosin heads act in an independent, non-cooperative manner. As both parameters, working stroke size and kinetics, did not vary between single- and double-headed NMIIb, supports the idea that only one of the two heads of dimeric NMIIb are interacting with actin at a time in the presence of ATP. This hypothesis is also supported by the fact, that the stiffness of the full-length construct was not higher as for the single-headed construct. Intriguingly, the stiffness of the S1 head was higher compared to the full-length construct, which can be attributed to the attachment mode to the surface via the anti-FLAG antibody. The FLAG-tag is directly attached C-terminally to the lever arm of the S1 construct and gives the small head a rigid surface anchor. In contrast, the double-headed construct contains its FLAG-tag at the end of the tail and therefore the heads experience a high degree of freedom, because the tail domain is not rigidly attached to the surface, which leads to a lower myosin stiffness (see Fig. 4.7).

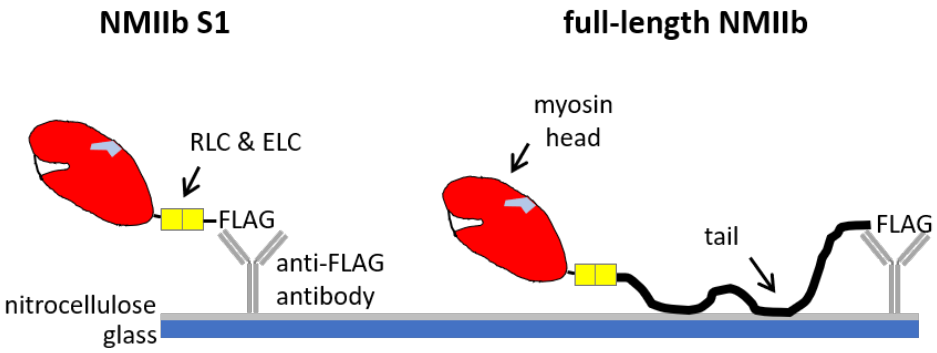

Fig. 4.7: Schematic illustration of the different attachment modes of S1 and full-length NMIIb. An anti-FLAG antibody is immobilized on a nitrocellulose covered glass surface. NMIIb is site-specifically attached to the surface via the antibody. Because of the missing tail domain the S1 construct is more rigidly attached to the surface than the full-length construct. This results in different stiffness values for the two proteins. The ∼2 µm surface beads used in the three-bead assay were omitted for simplicity.

Myosin V is an example, where two stiffness levels were observed at stall forces, which can be explained by a one- and two-headed attachment (Veigel et al., 2002). However, it cannot be excluded that a similar situation exists also for NMIIb, but at faster time scales that are beyond the detection limit of the optical trap setup.

In my optical tweezers measurements with NMIIb I observed mostly single interaction with actin, and only seldom processive steps were detected. This was a very similar observation to the study of Nagy et al. (2013) but in contrast to optical tweezers measurements of Norstrom et al. (2010) with chicken NMIIb, where they detected several forward and backward steps along the actin filament. The differences might be explained by the fact, that the data from my measurements and in the study of Nagy et al. (2013) were collected using a sinusoidal oscillation of one of the beads in the bead-actin-bead dumbbell, whereas Norstrom et al. (2010) did not applied such a forcing function. This suggests a load dependency of NMIIb. The sinusoidal oscillation imposes a small load onto the myosin molecule, which might prevent the myosin from making processive steps along an actin filament. It has been already shown by several studies that loads affects the kinetics of other myosins (Veigel et al., 2003, 2005; Sellers and Veigel, 2010; Greenberg et al., 2012; Hundt et al., 2016). Interestingly, Kovacs et al. (2007) demonstrated that load regulates the rate of ADP release in human NMIIb. This load-dependency might have important physiological consequences as NMIIb has been implicated in maintaining cortical tension (Bridgman et al., 2001) and smooth muscle function (Morano et al., 2000).

4.2.1 NMIIb produces two types of binding events

The present work clearly showed that two types of attachment events were visible in single-molecule optical trapping experiments. Both single and double-headed NMIIb constructs showed attachment events at around 0 nm and 5-6 nm. The latter can be assigned to the typical working stroke size of myosin II motors (see above), whereas it remains ambiguous where the 0 nm attachment events arise from. Similar 0 nm events have been previously observed in an optical trapping study of Nagy et al. (2013) with human NMIIb, although they were restricted to short lifetimes. In great contrast, the 0 nm attachment events of this work were equally distributed over short and long lifetimes. Nagy et al. (2013) hypothesized that the close-to-zero attachment events represent nonproductive, weak binding interactions between NMIIb and actin, whereas only the longer events represent full, complete working strokes. This hypothesis can also be transferred to this work, with the extension that 0 nm events also occurred at longer lifetimes.

This 0 nm attachment events might represent nonproductive bindings to actin, which are not coupled to the hydrolysis of ATP. This idea is supported by trapping measurements on *Drosophila* myosin XVIII, which produces also close-to-zero events and does not hydrolyse ATP (Guzik-Lendrum et al., 2011). Although the myosin head binds actin during these transient events, it cannot transform into a strong actin binding state because of the lack of nucleotide. This weak binding interactions could have important cellular relevance to bind and tether the NMIIb myosin filament to actin without the consumption of further ATP, especially as this NMII isoform is known to be involved in tension maintenance and structural anchoring (Vicente-Manzanares et al., 2009). In this regard, binding events without ATP consumption would make sense for NMIIb also for longer events. Further measurements in the absence of ATP could elucidate the nature of this close-to-zero attachment events.

In this work I performed the first stiffness measurements on the NMIIb isoform using an optical tweezers transducer. Interestingly, short events had a lower stiffness than long events. This is in line with the hypothesis, that the 0 nm events represent weak actin binding states and are therefore characterized by a low myosin stiffness.

4.3 Human myosin VI

Although there exist more than 35 classes of molecular motors within the myosin superfamily, only myosin VI is known to move toward the minus-end of actin filaments. Myosin VI is involved in diverse cellular processes including endocytosis, secretion and cell migration (Sweeney and Houdusse, 2007). It is still largely unknown how this multitude of functions are regulated on a molecular scale. The motor protein must be tightly regulated and coordinated in a spatial and temporal manner in order to maintain cellular organisation and correct localization of components. Regulatory mechanisms include expression of alternatively spliced isoforms, modulation through calcium/calmodulin, phosphoinositides (PIP2) but also posttranslational modifications such as phosphorylation (Buss and Kendrick-Jones, 2008).

4.3.1 S267 phosphorylation influences kinetics of human myosin VI

Initial evidence for myosin VI phosphorylation came from cell biological studies, which showed that stimulation of a human epithelial carcinoma cell line with epidermal growth factor (EGF) increased the amount of myosin VI phosphorylation. Furthermore, myosin VI was recruited to newly formed membrane ruffles at the leading edge of the cells, suggesting an important function for phosphorylated myosin VI in membrane trafficking on secretory and endocytic pathways. Studies indicated that threonine at position 406 in the cardiomyopathy loop in the motor domain might be phosphorylated by a p21-activated kinase (PAK, Buss et al. (1998)). The cardiomyopathy loop is located between the upper and lower 50 kDa domain in near proximity to the actin binding interface. Although the location of this phosphorylation site suggests a regulatory function, it did not alter myosin VI *in vitro* kinetic parameters (De La Cruz et al., 2001; Morris et al., 2003).
In great contrast to T406 phosphorylation, the phosphorylation site S267 identified by Buss et al. (unpublished data) and studied in this work has pronounced effects on the *in vitro* properties of myosin VI. Initial *in vitro* motility assays have clearly shown that the actin gliding velocity is increased two- to three-fold in the presence of the phosphomimicking mutant S267E. Mutagenesis studies on *Acanthamoeba* myosin I revealed that the phosphorylated and unphosphorylated states are mimicked by replacement of the phosphorylatable serine with a glutamate or alanine residue, respectively (Wang et al., 1998). Similar to the myosin I study, also the non-phosphorylatable mutant S267A had the same actin gliding velocity as wild type myosin VI.
In this work I performed single-molecule optical trapping experiments to characterize

the phospho-mutants in further detail. Intriguingly, the ADP release rate of the S267E mutant was increased 2-4 fold compared to the S267A mutant and wildtype myosin VI (De La Cruz et al., 2001; Lister et al., 2004). The ATP binding rate did not differ between the two mutants and was around twice as high as the values found in the literature (Altman et al., 2004; Lister et al., 2004). Furthermore, the working stroke size was determined to 17-18 nm for both mutants, which is very close to prior determined values (Lister et al., 2004).
In line with my optical tweezers measurements, solution kinetic studies using stopped-flow performed by Dr. C. Johnson at the University of Kent (UK) revealed that the S267E mutant had a five-fold increased ADP dissociation rate and a two-fold increased ATP-binding rate compared to wildtype or S267A.

In summary, these results indicate that serine-phosphorylation at position 267 has a major impact on the kinetic properties of myosin VI. This is not surprising, as S267 is located in the upper 50 kDa domain in the proximity of the unique insert 1 of myosin VI. Insert 1 is found near the nucleotide binding pocket and has been shown to regulate nucleotide binding and release as well as gating of the heads of dimeric myosin VI (Ménétrey et al., 2005; Pylypenko et al., 2011). In the structural study of Pylypenko et al. (2011) they showed that the insert 1, and in particular L310, restricts the size of the entry of the nucleotide binding pocket and therefore influences the rate of ATP binding and unbinding. Their solution kinetics measurements indicated a three-fold increase in ADP-dissociation rates for a myosin VI mutant without the insert 1 and also for a L310G mutant. Additionally, they also observed a 10-fold increase in ATP-induced binding and dissociation rates for actin binding.

Altogether the above-mentioned studies indicate that S267 is well positioned near the nucleotide binding site (see Fig. 4.8) and phosphorylation of this residue could modify nucleotide binding properties and influences the overall kinetics of myosin VI. Interestingly, preliminary molecular dynamics (MD) simulations showed that S267 phosphorylation stabilizes the motor domain and decreases the nucleotide entry site and size of the binding pocket (experiments performed by Dr. Boyd, CompChem Solutions, Cambridge). The simulations also revealed that the unphosphorylated myosin VI has more flexibility in the motor domain and is not that rigid as the phosphorylated form. To test if this increased rigidity of the motor domain translates also to the whole myosin VI molecule, I performed stiffness measurements on single-molecule binding events. Interestingly, the stiffness analysis did not show any difference between the two phospho-mutants, indicat-

ing that the postulated local stiffness increase around the nucleotide binding pocket is not transmitted to the entire myosin VI molecule. The local increase of rigidity could be compensated by other structural elements in the head domain.

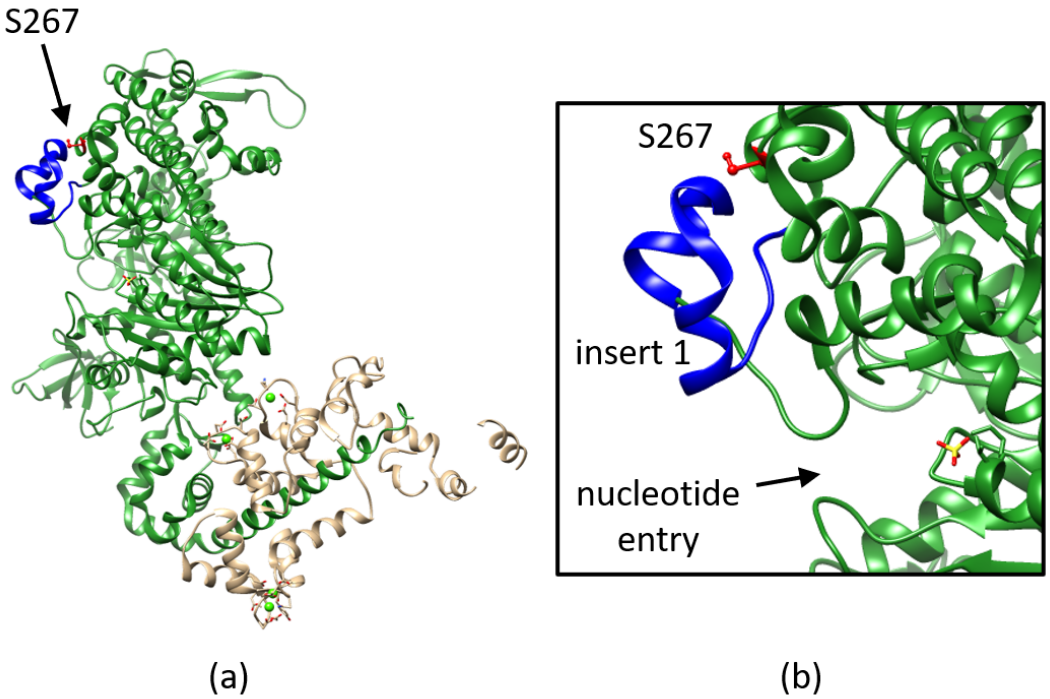

Fig. 4.8: Location of S267 in the motor domain of myosin VI. (a) Schematic illustration of the head domain of myosin VI (green) with bound calmodulins (grey). The serine residue at position 267 is coloured in red as ball and stick model. The myosin VI-specific insert 1 (C278-A303) is coloured in blue. (b) The close-up illustrates the vicinity of S267 to insert 1 and the nucleotide binding pocket. The figure was made with UCSF chimera (PDB: 2bki; Ménétrey et al. (2005)).

It is still unclear how the smaller size of the nucleotide entry site and binding pocket can explain the increased kinetics of the phospho-mimetic mutant observed in single-molecule and solution kinetic studies. A longer simulation time interval (up to 100 ns) could provide more detailed insights into the mechanochemical processes induced by S267 phosphorylation.

In a cell biological context an increased myosin VI activity after S267 phosphorylation could raise membrane dynamics at the leading edge of migrating cells. Indeed, cell biological experiments suggested that the expression of the phospho-mimetic mutant S267E enhanced the ability of a plus-end directed myosin VI to induce filopodia at the cell surface compared to wildtype myosin VI (performed by J. De Jonge, University of Cambridge).

In this plus-end directed myosin VI mutant, the reverse gear, the IQ motif and the lever arm extension were replaced by the lever arm of myosin V, which leads to a reversal of myosin VI motility (Masters and Buss, 2017). Additionally, experiments also demonstrated that phosphorylation stimulates *Salmonella enterica* entry into HeLa cells. It has been shown in recent studies that myosin VI gets highjacked by *Salmonella* virulence factors and facilitates the uptake of the pathogen (Brooks et al., 2017). The number of pathogens taken up by HeLa cells was significantly higher in cells transfected with the S267 phospho-mimetic mutant.
In summary, those cell biological experiments clearly illustrate that phosphorylation S267 has dramatic effects on myosin VI activity in membrane dynamics and cytoskeletal organisation.

Declaration

Eidesstattliche Erklärung

Ich versichere hiermit an Eides statt, dass die vorgelegte Dissertation von mir selbstständig und ohne unerlaubte Hilfe angefertigt wurde. Des Weiteren erkläre ich, dass ich nicht anderweitig ohne Erfolg versucht habe, eine Dissertation einzureichen oder mich der Doktorprüfung zu unterziehen. Die folgende Dissertation liegt weder ganz, noch in wesentlichen Teilen einer anderen Prüfungskommission vor.

Markus Kröss
München, 23. September 2021

Statutory Declaration

Hereby, I declare that I have authored this thesis independently, that I have not used other than the declared sources/references. As well I declare that I have not submitted a dissertation without success and not passed the defense. The present dissertation (neither the entire dissertation nor parts) has not been presented to another examination board.

Markus Kröss
Munich, 23rd September 2021

Acknowledgements

Throughout the preparation and writing of this dissertation I received a lot of support and assistance.

I would first like to thank my supervisor **Prof. Dr. Claudia Veigel** for giving me the possibility to research in her laboratory. I gained a lot of methodical and technical experiences in performing many different biochemical and biophysical techniques including the fascinating but simultaneously very challenging optical tweezers measurements. In our numerous discussions she encouraged me to sharpen my thinking and helped me to develop as a scientist and human being.
I would also like to acknowledge **Prof. Dr. Kirsten Jung** from the faculty of Biology, who took the time and supervised me as an external PhD candidate. I would also like to thank the entire thesis examination committee for their interest in my work.
Special thanks go to my supervisor **Dr. Christopher Batters**, which thankfully proofread parts of this manuscript and always had open ears for my questions and ideas. His exceptional biochemical expertise and calm character were very helpful in carrying out the different projects.
Many thanks to the cooperation partner in the myosin VI project, **Prof. Dr. Folma Buss** from the University of Cambridge (UK).
I would like to give credit also to **CeNS** (Center for NanoScience) and the **'Science Rocks!'-community** for great talks, fantastic workshops and stimulating discussions.

Finally, I could not have completed this dissertation without the support of all the current and past group members **Antonino, Beate, Christian, Christoph, Constanze, Heike, Ibrahim, Johannes, John, Michael, Michaela, Nam, Nicole, Rogez B., Sabine, Sascha, Shin and Simon**. Special thanks goes to the following persons, who worked with me on different projects over the years:
Andreas Graw: Andi supported me a lot with the single molecule measurements and was a helping hand during the building of the optical trapping setup. I want to thank you deeply for your patient support in all my scientific and personal issues.

Dr. Dario Saczko-Brack: Dario performed all the EM measurements and was always very reliable and precise, although he had to struggle with the quality of the highly variable myosin IXa preparations. I really appreciated to work with you!
Francesco Ippolito: Francesco supported me a lot during the last period of my dissertation by performing most of the optical tweezers measurements on myosin IXa. I am very grateful for your very systematic and reliable work and I really enjoyed doing sports together.
Dr. Nikolas Hundt, Ana Petrova, Felix Zierhut: Thanks so much for your countless advices, suggestions and many helpful discussions.
Marilou Fraek, Roswitha Maul, Irene Schneider & Robert Waberer: Your invaluable work in the background laid the foundation of this thesis. Many thanks for always taking care of the cells, equipment, reagents and good mood.

My deepest appreciation belongs to my family, who supported me on every step of my work with endless confidence and patience. Together with my wife **Claudia** and my son **Felix** I am looking forward to an exciting future.

Bibliography

M. Abouhamed, K. Grobe, I. V. Leefa Chong San, S. Thelen, U. Honnert, M. S. Balda, K. Matter, and M. Bähler. Myosin IXa Regulates Epithelial Differentiation and Its Deficiency Results in Hydrocephalus. *Molecular Biology of the Cell*, 20(24):5074–5085, Dec. 2009. URL https://www.molbiolcell.org/doi/10.1091/mbc.e09-04-0291.

M. Adrian, J. Dubochet, J. Lepault, and A. W. McDowall. Cryo-electron microscopy of viruses. *Nature*, 308(5954):32–36, 1984.

AHF. Dual Line Strahlenteiler zt532-543/1064rpc, Apr. 2021. URL https://www.ahf.de/produkte/spektralanalytik-photonik/optische-filter/strahlenteiler/laser-strahlenteiler/langpass-laser-strahlenteiler/dual/2996/dual-line-strahlenteiler-zt532-543/1064rpc.

D. J. Aidley and D. J. Ashley. *The physiology of excitable cells*, volume 4. Cambridge University Press Cambridge, 1998.

D. Altman, H. L. Sweeney, and J. A. Spudich. The mechanism of myosin VI translocation and its load-induced anchoring. *Cell*, 116(5):737–749, 2004.

E. J. Ambrose. A Surface Contact Microscope for the study of Cell Movements. *Nature*, 178(4543):1194–1194, Nov. 1956. URL http://www.nature.com/articles/1781194a0.

L. Aschenbrenner, T. Lee, and T. Hasson. Myo6 facilitates the translocation of endocytic vesicles from cell peripheries. *Molecular biology of the cell*, 14(7):2728–2743, 2003.

A. Ashkin. Acceleration and Trapping of Particles by Radiation Pressure. *Physical Review Letters*, 24(4):156–159, Jan. 1970. URL https://link.aps.org/doi/10.1103/PhysRevLett.24.156.

A. Ashkin. Optical trapping and manipulation of neutral particles using lasers. *Proc. Natl. Acad. Sci. USA*, page 8, 1997.

A. Ashkin and J. M. Dziedzic. Optical trapping and manipulation of viruses and bacteria. *Science*, 235(4795):1517–1520, Mar. 1987. URL https://science.sciencemag.org/content/235/4795/1517.

A. Ashkin, J. M. Dziedzic, J. E. Bjorkholm, and S. Chu. Observation of a single-beam gradient force optical trap for dielectric particles. *Optics Letters*, 11(5):288–290, May 1986. URL https://www.osapublishing.org/ol/abstract.cfm?uri=ol-11-5-288.

A. Ashkin, J. M. Dziedzic, and T. Yamane. Optical trapping and manipulation of single cells using infrared laser beams. *Nature*, 330(6150):769–771, 1987.

K. B. Avraham, T. Hasson, K. P. Steel, D. M. Kingsley, L. B. Russell, M. S. Mooseker, N. G. Copeland, and N. A. Jenkins. The mouse Snell's waltzer deafness gene encodes an unconventional myosin required for structural integrity of inner ear hair cells. *Nature Genetics*, 11(4):369–375, Dec. 1995. URL https://www.nature.com/articles/ng1295-369.

D. Axelrod. Cell-substrate contacts illuminated by total internal reflection fluorescence. *The Journal of Cell Biology*, 89(1):141–145, Apr. 1981. URL https://rupress.org/jcb/article/89/1/141/59168/Cellsubstrate-contacts-illuminated-by-total.

Y. S. Babu, J. S. Sack, T. J. Greenhough, C. E. Bugg, A. R. Means, and W. J. Cook. Three-dimensional structure of calmodulin. *Nature*, 315(6014):37–40, 1985.

M. Baehler, I. Kehrer, H. E. Stoeffler, L. Gorden, and A. S. Olsen. Physical mapping of human myosin-IXB (MYO9B), the human orthologue of the rat myosin myr 5, to chromosome 19p13.1. *Genomics*, 43(1), July 1997. URL https://www.osti.gov/biblio/588661.

A. Bahloul, G. Chevreux, A. L. Wells, D. Martin, J. Nolt, Z. Yang, L.-Q. Chen, N. Potier, A. V. Dorsselaer, S. Rosenfeld, A. Houdusse, and H. L. Sweeney. The unique insert in myosin VI is a structural calcium–calmodulin binding site. *Proceedings of the National Academy of Sciences*, 101(14):4787–4792, Apr. 2004. URL https://www.pnas.org/content/101/14/4787.

I. Banga and A. Szent-Györgyi. Preparation and properties of myosin A and B. *Stud. Inst. Med. Chem. Univ. Szeged*, 1:5–15, 1942.

C. Batters and C. Veigel. Mechanics and Activation of Unconventional Myosins. *Traffic*, 17(8):860–871, 2016. URL https://onlinelibrary.wiley.com/doi/abs/10.1111/tra.12400.

C. Batters, K. A. Woodall, C. P. Toseland, C. Hundschell, and C. Veigel. Cloning, Expression, and Characterization of a Novel Molecular Motor, *Leishmania* Myosin-XXI. *Journal of Biological Chemistry*, 287(33):27556–27566, Aug. 2012. URL http://www.jbc.org/lookup/doi/10.1074/jbc.M112.381301.

C. Batters, H. Ellrich, C. Helbig, K. A. Woodall, C. Hundschell, D. Brack, and C. Veigel. Calmodulin regulates dimerization, motility, and lipid binding of Leishmania myosin XXI. *Proceedings of the National Academy of Sciences*, 111(2):E227–E236, Jan. 2014. URL https://www.pnas.org/content/111/2/E227.

E. Behrmann, M. Müller, P. Penczek, H. Mannherz, D. Manstein, and S. Raunser. Structure of the Rigor Actin-Tropomyosin-Myosin Complex. *Cell*, 150(2):327–338, July 2012. URL http://www.sciencedirect.com/science/article/pii/S0092867412007076.

W. M. Bement, T. Hasson, J. A. Wirth, R. E. Cheney, and M. S. Mooseker. Identification and overlapping expression of multiple unconventional myosin genes in vertebrate cell types. *Proceedings of the National Academy of Sciences*, 91(14):6549–6553, July 1994. URL http://www.pnas.org/cgi/doi/10.1073/pnas.91.14.6549.

J. S. Berg, B. C. Powell, and R. E. Cheney. A Millennial Myosin Census. *Molecular Biology of the Cell*, 12(4):780–794, Apr. 2001. URL https://www.molbiolcell.org/doi/10.1091/mbc.12.4.780.

R. Bergmann, A. Afifi, and P. Heidger. Anatomy Atlases: Atlas of Microscopic Anatomy: Section 1 - Cells, 2020. URL https://www.anatomyatlases.org/MicroscopicAnatomy/Section05/Plate0566.shtml.

V. Betapudi, L. S. Licate, and T. T. Egelhoff. Distinct Roles of Nonmuscle Myosin II Isoforms in the Regulation of MDA-MB-231 Breast Cancer Cell Spreading and Migration. *Cancer Research*, 66(9):4725–4733, May 2006. URL http://cancerres.aacrjournals.org/lookup/doi/10.1158/0008-5472.CAN-05-4236.

N. Billington, A. Wang, J. Mao, R. S. Adelstein, and J. R. Sellers. Characterization of Three Full-length Human Nonmuscle Myosin II Paralogs. *Journal of Biological Chemistry*, 288(46):33398–33410, Nov. 2013. URL http://www.jbc.org/lookup/doi/10.1074/jbc.M113.499848.

L. Blanchoin, R. Boujemaa-Paterski, C. Sykes, and J. Plastino. Actin Dynamics, Architecture, and Mechanics in Cell Motility. *Physiological Reviews*, 94(1):235–263, Jan. 2014. URL https://www.physiology.org/doi/10.1152/physrev.00018.2013.

S. M. Block, L. S. Goldstein, and B. J. Schnapp. Bead movement by single kinesin molecules studied with optical tweezers. *Nature*, 348(6299):348–352, 1990.

M. M. Bradford. A Rapid and Sensitive Method for the Quantitation of Microgram Quantities of Protein Utilizing the Principle of Protein-Dye Binding. *Analytical biochemistry*, 72(1–2):248–254, 1976.

P. C. Bridgman, S. Dave, C. F. Asnes, A. N. Tullio, and R. S. Adelstein. Myosin IIB is required for growth cone motility. *Journal of Neuroscience*, 21(16):6159–6169, 2001.

A. B. E. Brooks, D. Humphreys, V. Singh, A. C. Davidson, S. D. Arden, F. Buss, and V. Koronakis. MYO6 is targeted by Salmonella virulence effectors to trigger PI3-kinase signaling and pathogen invasion into host cells. *Proceedings of the National Academy of Sciences*, 114(15):3915–3920, Apr. 2017. URL https://www.pnas.org/content/114/15/3915.

F. Buss and J. Kendrick-Jones. How are the cellular functions of myosin VI regulated within the cell? *Biochemical and biophysical research communications*, 369(1):165–175, 2008.

F. Buss, J. Kendrick-Jones, C. Lionne, A. E. Knight, G. P. Côté, and J. Paul Luzio. The Localization of Myosin VI at the Golgi Complex and Leading Edge of Fibroblasts and Its Phosphorylation and Recruitment into Membrane Ruffles of A431 Cells after Growth Factor Stimulation. *Journal of Cell Biology*, 143(6):1535–1545, Dec. 1998. URL https://rupress.org/jcb/article/143/6/1535/15974/The-Localization-of-Myosin-VI-at-the-Golgi-Complex.

F. Buss, J. P. Luzio, and J. Kendrick-Jones. Myosin VI, a new force in clathrin mediated endocytosis. *FEBS letters*, 508(3):295–299, 2001.

F. Buss, G. Spudich, and J. Kendrick-Jones. Myosin VI: cellular functions and motor properties. *Annu. Rev. Cell Dev. Biol.*, 20:649–676, 2004.

M. Bähler. Are class III and class IX myosins motorized signalling molecules? *Biochimica et Biophysica Acta (BBA)-Molecular Cell Research*, 1496(1):52–59, 2000.

M. Bähler, K. Elfrink, P. Hanley, S. Thelen, and Y. Xu. Cellular functions of class IX myosins in epithelia and immune cells. *Biochemical Society Transactions*, 39(5):1166–1168, Oct. 2011. URL https://portlandpress.com/biochemsoctrans/article/39/5/1166/86577/Cellular-functions-of-class-IX-myosins-in.

R. E. Cheney and M. S. Mooseker. Unconventional myosins. *Current opinion in cell biology*, 4(1):27–35, 1992.

E. Chieregatti, A. Gartner, H. E. Stoffler, and M. Bahler. Myr 7 is a novel myosin IX-RhoGAP expressed in rat brain. *Journal of Cell Science*, 111(24):3597–3608, Dec. 1998. URL https://jcs.biologists.org/content/111/24/3597.

L. M. Coluccio. Myosins and Disease. In *Myosins*, pages 245–316. Springer, 2020.

P. B. Conibear, C. R. Bagshaw, P. G. Fajer, M. Kovács, and A. Málnási-Csizmadia. Myosin cleft movement and its coupling to actomyosin dissociation. *Nature Structural & Molecular Biology*, 10(10):831–835, 2003.

M. A. Conti, S. Kawamoto, and R. S. Adelstein. Non-Muscle Myosin II. In L. M. Coluccio, editor, *Myosins: A Superfamily of Molecular Motors*, Proteins and Cell Regulation, pages 223–264. Springer Netherlands, Dordrecht, 2008. ISBN 978-1-4020-6519-4. URL https://doi.org/10.1007/978-1-4020-6519-4_7.

L. S. Costanzo. *Physiology*. Elsevier, Philadelphia, PA, 6. edition edition, May 2017. ISBN 978-0-323-47881-6.

D. S. Courson and R. E. Cheney. Myosin-X and disease. *Experimental Cell Research*, 334(1):10–15, May 2015. URL http://www.sciencedirect.com/science/article/pii/S0014482715001081.

L. P. Cramer. Organization and polarity of actin filament networks in cells: implications for the mechanism of myosin-based cell motility. *Biochemical Society Symposium*, 65:173–205, 1999.

J. L. Cyr, R. A. Dumont, and P. G. Gillespie. Myosin-1c Interacts with Hair-Cell Receptors through Its Calmodulin-Binding IQ Domains. *The Journal of Neuroscience*, 22 (7):2487–2495, Apr. 2002. URL http://www.jneurosci.org/lookup/doi/10.1523/JNEUROSCI.22-07-02487.2002.

G. A. Dabiri, J. M. Sanger, D. A. Portnoy, and F. S. Southwick. Listeria monocytogenes moves rapidly through the host-cell cytoplasm by inducing directional actin assembly. *Proceedings of the National Academy of Sciences*, 87(16):6068–6072, 1990.

P. F. Davies. Hemodynamic shear stress and the endothelium in cardiovascular pathophysiology. *Nature clinical practice. Cardiovascular medicine*, 6(1):16–26, Jan. 2009. URL https://www.ncbi.nlm.nih.gov/pmc/articles/PMC2851404/.

E. M. De La Cruz and E. M. Ostap. Relating biochemistry and function in the myosin superfamily. *Current Opinion in Cell Biology*, 16(1):61–67, Feb. 2004. URL https://linkinghub.elsevier.com/retrieve/pii/S0955067403001698.

M. De La Cruz, Enrique M, E. M. Ostap, and H. L. Sweeney. Kinetic mechanism and regulation of myosin VI. *Journal of Biological Chemistry*, 276(34):32373–32381, 2001.

H. Defacque, M. Egeberg, A. Habermann, M. Diakonova, C. Roy, P. Mangeat, W. Voelter, G. Marriott, J. Pfannstiel, and H. Faulstich. Involvement of ezrin/moesin in de novo actin assembly on phagosomal membranes. *The EMBO journal*, 19(2):199–212, 2000.

R. Dominguez and K. C. Holmes. Actin structure and function. *Annual review of biophysics*, 40:169–186, 2011.

R. Dominguez, Y. Freyzon, K. M. Trybus, and C. Cohen. Crystal Structure of a Vertebrate Smooth Muscle Myosin Motor Domain and Its Complex with the Essential Light Chain: Visualization of the Pre–Power Stroke State. *Cell*, 94(5):559–571, Sept. 1998. URL http://www.sciencedirect.com/science/article/pii/S0092867400815986.

F. Donaudy, R. Snoeckx, M. Pfister, H.-P. Zenner, N. Blin, M. Di Stazio, A. Ferrara, C. Lanzara, R. Ficarella, F. Declau, C. M. Pusch, P. Nürnberg, S. Melchionda, L. Zelante, E. Ballana, X. Estivill, G. Van Camp, P. Gasparini, and A. Savoia. Nonmuscle Myosin Heavy-Chain Gene MYH14 Is Expressed in Cochlea and Mutated in Patients Affected by Autosomal Dominant Hearing Impairment (DFNA4). *The American Journal of Human Genetics*, 74(4):770–776, Apr. 2004. URL http://www.sciencedirect.com/science/article/pii/S0002929707619041.

A. C. Dosé and B. Burnside. Cloning and Chromosomal Localization of a Human Class III Myosin. *Genomics*, 67(3):333–342, Aug. 2000. URL http://www.sciencedirect.com/science/article/pii/S0888754300962566.

T. A. Dunn, S. Chen, D. A. Faith, J. L. Hicks, E. A. Platz, Y. Chen, C. M. Ewing, J. Sauvageot, W. B. Isaacs, and A. M. De Marzo. A novel role of myosin VI in human prostate cancer. *The American journal of pathology*, 169(5):1843–1854, 2006.

E. Eisenberg and L. E. Greene. The Relation of Muscle Biochemistry to Muscle Physiology. *Annual Review of Physiology*, 42(1):293–309, Oct. 1980. URL http://www.annualreviews.org/doi/10.1146/annurev.ph.42.030180.001453.

K. Elfrink, W. Liao, U. Pieper, S. J. Oeding, and M. Bähler. The Loop2 Insertion of Type IX Myosin Acts as an Electrostatic Actin Tether that Permits Processive Movement. *PLoS ONE*, 9(1):e84874, Jan. 2014. URL https://dx.plos.org/10.1371/journal.pone.0084874.

R.-J. Essiambre. In memory of Arthur Ashkin. *Nature Photonics*, 15(3):167–168, Mar. 2021. URL https://www.nature.com/articles/s41566-021-00768-0.

M. Fairhead and M. Howarth. Site-specific biotinylation of purified proteins using BirA. *Methods in molecular biology (Clifton, N.J.)*, 1266:171–184, 2015. URL https://www.ncbi.nlm.nih.gov/pmc/articles/PMC4304673/.

W. O. Fenn. A quantitative comparison between the energy liberated and the work performed by the isolated sartorius muscle of the frog. *The Journal of Physiology*, 58 (2-3):175–203, 1923. URL https://physoc.onlinelibrary.wiley.com/doi/abs/10.1113/jphysiol.1923.sp002115.

M. A. Ferenczi, Z.-H. He, R. K. Chillingworth, M. Brune, J. E. Corrie, D. R. Trentham, and M. R. Webb. A new method for the time-resolved measurement of phosphate release in permeabilized muscle fibers. *Biophysical journal*, 68(4 Suppl):191S, 1995.

J. T. Finer, R. M. Simmons, and J. A. Spudich. Single myosin molecule mechanics: piconewton forces and nanometre steps. *Nature*, 368(6467):113–119, 1994.

FirstSensor. First Sensor QP Data Sheet, June 2021. URL https://www.first-sensor.com/cms/upload/datasheets/QP1-6_TO_5000029.pdf.

A. Fiser, R. K. G. Do, and A. Šali. Modeling of loops in protein structures. *Protein Science*, 9(9):1753–1773, Jan. 2000. URL https://onlinelibrary.wiley.com/doi/abs/10.1110/ps.9.9.1753.

J. V. Frangioni and B. G. Neel. Solubilization and Purification of Enzymatically Active Glutathione S-Transferase (pGEX) Fusion Proteins. *Analytical Biochemistry*, 210(1):179–187, Apr. 1993. URL http://www.sciencedirect.com/science/article/pii/S000326978371170X.

T. Fujii, A. H. Iwane, T. Yanagida, and K. Namba. Direct visualization of secondary structures of F-actin by electron cryomicroscopy. *Nature*, 467(7316):724–728, 2010.

M. Furch, M. A. Geeves, and D. J. Manstein. Modulation of actin affinity and actomyosin adenosine triphosphatase by charge changes in the myosin motor domain. *Biochemistry*, 37(18):6317–6326, 1998.

S. Galler. Molecular basis of the catch state in molluscan smooth muscles: a catchy challenge. *Journal of muscle research and cell motility*, 29(2-5):73, 2008.

M. A. Geeves. The dynamics of actin and myosin association and the crossbridge model of muscle contraction. *Biochemical Journal*, 274(1):1–14, Feb. 1991. URL https://portlandpress.com/biochemj/article/274/1/1/26375/The-dynamics-of-actin-and-myosin-association-and.

M. A. Geeves and P. B. Conibeart. The Role of Three-State Docking of Myosin Si with Actin in Force Generation. *Biophysical Journal*, 68:6, 1995.

M. A. Geeves and K. C. Holmes. Structural Mechanism of Muscle Contraction. *Annual Review of Biochemistry*, 68(1):687–728, June 1999. URL http://www.annualreviews.org/doi/10.1146/annurev.biochem.68.1.687.

M. A. Geeves and K. C. Holmes. The molecular mechanism of muscle contraction. *Advances in protein chemistry*, 71:161–193, 2005.

M. A. Geeves, R. S. Goody, and H. Gutfreund. Kinetics of acto-S1 interaction as a guide to a model for the crossbridge cycle. *Journal of Muscle Research and Cell Motility*, 5 (4):351–361, Aug. 1984. URL http://link.springer.com/10.1007/BF00818255.

M. A. Geeves, R. Fedorov, and D. J. Manstein. Molecular mechanism of actomyosin-based motility. *Cellular and Molecular Life Sciences CMLS*, 62(13):1462–1477, 2005. Publisher: Springer.

M. Glotzer. The Molecular Requirements for Cytokinesis. *Science*, 307(5716):1735–1739, Mar. 2005. URL https://science.sciencemag.org/content/307/5716/1735.

Y. E. Goldman, M. G. Hibberd, J. A. McCray, and D. R. Trentham. Relaxation of muscle fibres by photolysis of caged ATP. *Nature*, 300(5894):701–705, 1982.

S. W. Gorman, N. B. Haider, U. Grieshammer, R. E. Swiderski, E. Kim, J. W. Welch, C. Searby, S. Leng, R. Carmi, V. C. Sheffield, and D. M. Duhl. The Cloning and Developmental Expression of Unconventional Myosin IXA (MYO9A) a Gene in the Bardet–Biedl Syndrome (BBS4) Region at Chromosome 15q22–q23. *Genomics*, 59 (2):150–160, July 1999. URL https://linkinghub.elsevier.com/retrieve/pii/S0888754399958676.

M. J. Greenberg, T. Lin, Y. E. Goldman, H. Shuman, and E. M. Ostap. Myosin IC generates power over a range of loads via a new tension-sensing mechanism. *Proceedings of the National Academy of Sciences*, 109(37):E2433–E2440, 2012.

S. Guzik-Lendrum, A. Nagy, Y. Takagi, A. Houdusse, and J. R. Sellers. Drosophila melanogaster myosin-18 represents a highly divergent motor with actin tethering properties. *Journal of Biological Chemistry*, 286(24):21755–21766, 2011.

A. Hall. Rho GTPases and the actin cytoskeleton. *Science*, 279(5350):509–514, 1998.

J. A. Hammer and J. R. Sellers. Walking to work: roles for class V myosins as cargo transporters. *Nature reviews Molecular cell biology*, 13(1):13–26, 2012.

P. J. Hanley, Y. Xu, M. Kronlage, K. Grobe, P. Schön, J. Song, L. Sorokin, A. Schwab, and M. Bähler. Motorized RhoGAP myosin IXb (Myo9b) controls cell shape and motility. *Proceedings of the National Academy of Sciences*, 107(27):12145–12150, July 2010. URL https://www.pnas.org/content/107/27/12145.

P. J. Hanley, V. Vollmer, and M. Bähler. Class IX Myosins: Motorized RhoGAP Signaling Molecules. In *Myosins*, pages 381–389. Springer, 2020.

K. E. Heath, A. Campos-Barros, A. Toren, G. Rozenfeld-Granot, L. E. Carlsson, J. Savige, J. C. Denison, M. C. Gregory, J. G. White, D. F. Barker, A. Greinacher, C. J. Epstein, M. J. Glucksman, and J. A. Martignetti. Nonmuscle Myosin Heavy Chain IIA Mutations Define a Spectrum of Autosomal Dominant Macrothrombocytopenias: May-Hegglin Anomaly and Fechtner, Sebastian, Epstein, and Alport-Like Syndromes. *The American Journal of Human Genetics*, 69(5):1033–1045, Nov. 2001. URL http://www.sciencedirect.com/science/article/pii/S0002929707613196.

S. M. Heissler and D. J. Manstein. Nonmuscle myosin-2: mix and match. *Cellular and Molecular Life Sciences*, 70(1):1–21, 2013.

A. Herm-Götz, S. Weiss, R. Stratmann, S. Fujita-Becker, C. Ruff, E. Meyhöfer, T. Soldati, D. J. Manstein, M. A. Geeves, and D. Soldati. Toxoplasma gondii myosin A and its light chain: a fast, single-headed, plus-end-directed motor. *The EMBO Journal*, 21(9):2149–2158, May 2002. URL https://www.ncbi.nlm.nih.gov/pmc/articles/PMC125985/.

H. Higuchi and S. A. Endow. Directionality and processivity of molecular motors. *Current Opinion in Cell Biology*, 14(1):50–57, Feb. 2002. URL http://www.sciencedirect.com/science/article/pii/S0955067401002939.

K. C. Holmes. The swinging lever-arm hypothesis of muscle contraction. *Current Biology*, 7(2):R112–R118, Feb. 1997. URL http://www.sciencedirect.com/science/article/pii/S0960982206000510.

K. C. Holmes and M. A. Geeves. The structural basis of muscle contraction. *Philosophical Transactions of the Royal Society of London. Series B: Biological Sciences*, 355(1396):419–431, 2000.

K. C. Holmes, D. Popp, W. Gebhard, and W. Kabsch. Atomic model of the actin filament. *Nature*, 347(6288):44–49, Sept. 1990. URL https://www.nature.com/articles/347044a0.

K. C. Holmes, I. Angert, F. Jon Kull, W. Jahn, and R. R. Schröder. Electron cryomicroscopy shows how strong binding of myosin to actin releases nucleotide. *Nature*, 425(6956):423–427, Sept. 2003. URL http://www.nature.com/articles/nature02005.

E. Homsher, M. Nili, I. Chen, and L. Tobacman. Regulatory Proteins Alter Nucleotide Binding to Acto-Myosin of Sliding Filaments in Motility Assays. *Biophysical Journal*, 85(2):1046–1052, Aug. 2003. URL https://linkinghub.elsevier.com/retrieve/pii/S0006349503745433.

P. Hotulainen and P. Lappalainen. Stress fibers are generated by two distinct actin assembly mechanisms in motile cells. *Journal of Cell Biology*, 173(3): 383–394, May 2006. URL https://rupress.org/jcb/article/173/3/383/34265/Stress-fibers-are-generated-by-two-distinct-actin.

A. Houdusse, A. G. Szent-Györgyi, and C. Cohen. Three conformational states of scallop myosin S1. *Proceedings of the National Academy of Sciences*, 97(21):11238–11243, 2000.

J. Howard. Molecular motors: structural adaptations to cellular functions. *Nature*, 389 (6651):561–567, Oct. 1997. URL http://www.nature.com/articles/39247.

J. Howard. *Mechanics of Motor Proteins and the Cytoskeleton*. Sinauer Associates, Sunderland, MA, Jan. 2001.

A. Hu, F. Wang, and J. R. Sellers. Mutations in Human Nonmuscle Myosin IIA Found in Patients with May-Hegglin Anomaly and Fechtner Syndrome Result in Impaired Enzymatic Function. *Journal of Biological Chemistry*, 277(48):46512–46517, Nov. 2002. URL http://www.jbc.org/lookup/doi/10.1074/jbc.M208506200.

N. Hundt, W. Steffen, S. Pathan-Chhatbar, M. H. Taft, and D. J. Manstein. Load-dependent modulation of non-muscle myosin-2A function by tropomyosin 4.2. *Scientific Reports*, 6(1):20554, Feb. 2016. URL https://www.nature.com/articles/srep20554.

A. F. Huxley. Muscle structure and theories of contraction. *Prog. Biophys. Biophys. Chem*, 7:255–318, 1957a.

A. F. Huxley. Mechanics and models of the myosin motor. *Philosophical Transactions of the Royal Society of London. Series B: Biological Sciences*, 355(1396):433–440, 2000.

A. F. Huxley and R. Niedergerke. Structural changes in muscle during contraction: interference microscopy of living muscle fibres. *Nature*, 173(4412):971–973, 1954.

H. Huxley and J. Hanson. Changes in the cross-striations of muscle during contraction and stretch and their structural interpretation. *Nature*, 173(4412):973–976, 1954.

H. E. Huxley. The double array of filaments in cross-striated muscle. *The Journal of Cell Biology*, 3(5):631–648, 1957b.

H. E. Huxley. The Mechanism of Muscular Contraction. *Science*, 164(3886):1356–1366, 1969. URL https://www.jstor.org/stable/1726814.

R. Iino, K. Kinbara, and Z. Bryant. *Introduction: Molecular Motors*. ACS Publications, 2020.

A. Inoue, J. Saito, R. Ikebe, and M. Ikebe. Myosin IXb is a single-headed minus-end-directed processive motor. *Nature Cell Biology*, 4(4):302–306, Apr. 2002. URL http://www.nature.com/articles/ncb774.

M. Irving, T. S. C. Alien, C. Sabido-David, J. S. Craik, B. Brandmeier, J. Kendrick-Jones, J. E. Corrie, D. R. Trentham, and Y. E. Goldman. Tilting of the light-chain region of myosin during step length changes and active force generation in skeletal muscle. *Nature*, 375(6533):688–691, 1995.

P. B. Joel, K. M. Trybus, and H. L. Sweeney. Two conserved lysines at the 50/20-kDa junction of myosin are necessary for triggering actin activation. *Journal of Biological Chemistry*, 276(5):2998–3003, 2001.

P. B. Joel, H. L. Sweeney, and K. M. Trybus. Addition of lysines to the 50/20 kDa junction of myosin strengthens weak binding to actin without affecting the maximum ATPase activity. *Biochemistry*, 42(30):9160–9166, 2003.

T. M. Johnson, Z. Rajfur, K. Jacobson, and C. J. Beckers. Immobilization of the Type XIV Myosin Complex in Toxoplasma gondii. *Molecular Biology of the Cell*, 18 (8):3039–3046, May 2007. URL `https://www.molbiolcell.org/doi/full/10.1091/mbc.e07-01-0040`.

J. D. Jontes, E. M. Wilson-Kubalek, and R. A. Milligan. A 32° tail swing in brush border myosin I on ADP release. *Nature*, 378(6558):751–753, Dec. 1995. URL `http://www.nature.com/articles/378751a0`.

W. Kabsch, H. G. Mannherz, D. Suck, E. F. Pai, and K. C. Holmes. Atomic structure of the actin: DNase I complex. *Nature*, 347(6288):37–44, 1990.

G. Kalhammer, M. Bähler, F. Schmitz, J. Jöckel, and C. Block. Ras-binding domains: predicting function versus folding. *FEBS Letters*, 414(3):599–602, 1997. URL `https://febs.onlinelibrary.wiley.com/doi/abs/10.1016/S0014-5793%2897%2901076-4`.

T. Kambara and M. Ikebe. A Unique ATP Hydrolysis Mechanism of Single-headed Processive Myosin, Myosin IX. *Journal of Biological Chemistry*, 281(8):10, 2006.

D. Kamiyama and B. Huang. Development in the STORM. *Developmental Cell*, 23 (6):1103–1110, Dec. 2012. URL `https://linkinghub.elsevier.com/retrieve/pii/S1534580712004364`.

L. A. Kelley, S. Mezulis, C. M. Yates, M. N. Wass, and M. J. E. Sternberg. The Phyre2 web portal for protein modeling, prediction and analysis. *Nature Protocols*, 10(6):845–858, June 2015. URL `http://www.nature.com/articles/nprot.2015.053`.

J. Kepler. De cometis libelli tres I. astronomicus, theoremata continens de novam ... III. astrologicus, de significationibus cometarum annorum motu cometarum ... II. physicus, continens physiologiam cometarum 1607 et 1618. *De cometis libelli tres I. astronomicus, theoremata continens de motu cometarum ... II. physicus, continens physiologiam cometarum novam ... III. astrologicus, de significationibus cometarum annorum 1607 et 1618, by Kepler, Johannes, 1619.*, 1619. URL `http://adsabs.harvard.edu/abs/1619dclt.book.....K`.

T. Kiuchi, T. Nagai, K. Ohashi, and K. Mizuno. Measurements of spatiotemporal changes in G-actin concentration reveal its effect on stimulus-induced actin assembly and lamellipodium extension. *Journal of Cell Biology*, 193(2):365–380, Apr. 2011. URL https://doi.org/10.1083/jcb.201101035.

M. L. Knetsch, T. Q. Uyeda, and D. J. Manstein. Disturbed communication between actin-and nucleotide-binding sites in a myosin II with truncated 50/20-kDa junction. *Journal of Biological Chemistry*, 274(29):20133–20138, 1999.

N. Kodera and T. Ando. The path to visualization of walking myosin V by high-speed atomic force microscopy. *Biophysical Reviews*, 6(3):237–260, Dec. 2014. URL https://doi.org/10.1007/s12551-014-0141-7.

N. Kodera, D. Yamamoto, R. Ishikawa, and T. Ando. Video imaging of walking myosin V by high-speed atomic force microscopy. *Nature*, 468(7320):72–76, 2010.

M. Kovacs, K. Thirumurugan, P. J. Knight, and J. R. Sellers. Load-dependent mechanism of nonmuscle myosin 2. *Proceedings of the National Academy of Sciences*, 104(24):9994–9999, June 2007. URL http://www.pnas.org/cgi/doi/10.1073/pnas.0701181104.

M. Kovács, F. Wang, A. Hu, Y. Zhang, and J. R. Sellers. Functional Divergence of Human Cytoplasmic Myosin II: KINETIC CHARACTERIZATION OF THE NON-MUSCLE IIA ISOFORM. *Journal of Biological Chemistry*, 278(40):38132–38140, Oct. 2003. URL http://www.jbc.org/lookup/doi/10.1074/jbc.M305453200.

S. J. Kron and J. A. Spudich. Fluorescent actin filaments move on myosin fixed to a glass surface. *Proceedings of the National Academy of Sciences*, 83(17):6272–6276, Sept. 1986. URL http://www.pnas.org/cgi/doi/10.1073/pnas.83.17.6272.

A. Kryshtafovych, T. Schwede, M. Topf, K. Fidelis, and J. Moult. Critical assessment of methods of protein structure prediction (CASP)—Round XIII. *Proteins: Structure, Function, and Bioinformatics*, 87(12):1011–1020, 2019. URL https://onlinelibrary.wiley.com/doi/abs/10.1002/prot.25823.

H. Kuboniwa, N. Tjandra, S. Grzesiek, H. Ren, C. B. Klee, and A. Bax. Solution structure of calcium-free calmodulin. *Nature structural biology*, 2(9):768–776, 1995.

S. Kumar and V. M. Weaver. Mechanics, malignancy, and metastasis: the force journey of a tumor cell. *Cancer and Metastasis Reviews*, 28(1-2):113–127, 2009.

D. Köhler, C. Ruff, E. Meyhöfer, and M. Bähler. Different degrees of lever arm rotation control myosin step size. *The Journal of cell biology*, 161(2):237–241, 2003.

W. Kühne. *Untersuchungen über das Protoplasma und die Contractilität*. W. Engelmann, 1864.

U. K. Laemmli. Cleavage of Structural Proteins during the Assembly of the Head of Bacteriophage T4. *Nature*, 227(5259):680–685, Aug. 1970. URL https://www.nature.com/articles/227680a0.

B. Larijani, C. A. Rosser, and R. Woscholski. *Chemical Biology: Techniques and Applications*. John Wiley & Sons, Aug. 2006. ISBN 978-0-470-09066-4.

Q. Li, A. Gulati, M. Lemaire, T. Nottoli, A. Bale, and A. Tufro. Rho-GTPase Activating Protein myosin MYO9A identified as a novel candidate gene for monogenic focal segmental glomerulosclerosis. *Kidney International*, Jan. 2021. URL https://www.sciencedirect.com/science/article/pii/S0085253820315477.

Y.-R. Li and W.-X. Yang. Myosins as fundamental components during tumorigenesis: diverse and indispensable. *Oncotarget*, 7(29):46785–46812, Apr. 2016. URL https://www.oncotarget.com/article/8800/text/.

W. Liao, K. Elfrink, and M. Bähler. Head of Myosin IX Binds Calmodulin and Moves Processively toward the Plus-end of Actin Filaments. *Journal of Biological Chemistry*, 285(32):24933–24942, Aug. 2010. URL http://www.jbc.org/lookup/doi/10.1074/jbc.M110.101105.

I. Lister, S. Schmitz, M. Walker, J. Trinick, F. Buss, C. Veigel, and J. Kendrick-Jones. A monomeric myosin VI with a large working stroke. *The EMBO Journal*, 23(8):1729–1738, Apr. 2004. URL http://emboj.embopress.org/cgi/doi/10.1038/sj.emboj.7600180.

C.-M. Lo, D. B. Buxton, G. C. H. Chua, M. Dembo, R. S. Adelstein, and Y.-L. Wang. Nonmuscle Myosin IIB Is Involved in the Guidance of Fibroblast Migration. *Molecular Biology of the Cell*, 15:8, 2004.

H. Lodish, A. Berk, S. L. Zipursky, P. Matsudaira, D. Baltimore, and J. Darnell. *Molecular Cell Biology*. W. H. Freeman, 4th edition, 2000. ISBN 978-0-7167-3136-8.

H. Lodish, A. Berk, C. A. Kaiser, M. Krieger, M. P. Scott, A. Bretscher, H. Ploegh, and P. Matsudaira. *Molecular Cell Biology*. Macmillan, 6th edition, 2008. ISBN 978-1-4292-0314-2.

M. Lorenz and K. C. Holmes. The actin-myosin interface. *Proceedings of the National Academy of Sciences*, 107(28):12529–12534, 2010.

R. W. Lymn and E. W. Taylor. Mechanism of adenosine triphosphate hydrolysis by actomyosin. *Biochemistry*, 10(25):4617–4624, Dec. 1971. URL https://pubs.acs.org/doi/abs/10.1021/bi00801a004.

T. J. Lynch, J. P. Albanesi, E. D. Korn, E. A. Robinson, B. Bowers, and H. Fujisaki. ATPase activities and actin-binding properties of subfragments of Acanthamoeba myosin IA. *Journal of Biological Chemistry*, 261(36):17156–17162, Dec. 1986. URL http://www.jbc.org/content/261/36/17156.

F. Lynen and U. Wieland. Über die Giftstoffe des Knollenblätterpilzes. IV. *Justus Liebigs Annalen der Chemie*, 533(1):93–117, 1938. URL https://chemistry-europe.onlinelibrary.wiley.com/doi/abs/10.1002/jlac.19385330105.

M. Lyubimova and V. Engelhardt. Adenosinetriphosphatase and myosin. *Biokhimiya*, 4: 716–736, 1939.

X. Ma, J. Bao, and R. S. Adelstein. Loss of Cell Adhesion Causes Hydrocephalus in Nonmuscle Myosin II-B–ablated and Mutated Mice. *Molecular Biology of the Cell*, 18 (6):2305–2312, Apr. 2007. URL https://www.molbiolcell.org/doi/full/10.1091/mbc.E07-01-0073.

M. Machacek, L. Hodgson, C. Welch, H. Elliott, O. Pertz, P. Nalbant, A. Abell, G. L. Johnson, K. M. Hahn, and G. Danuser. Coordination of Rho GTPase activities during cell protrusion. *Nature*, 461(7260):99–103, 2009.

S. Maddirevula, F. Alzahrani, M. Al-Owain, M. A. Al Muhaizea, H. R. Kayyali, A. Al-Hashem, Z. Rahbeeni, M. Al-Otaibi, H. I. Alzaidan, and A. Balobaid. Autozygome and high throughput confirmation of disease genes candidacy. *Genetics in Medicine*, 21(3): 736–742, 2019.

E. Magistrati and S. Polo. Myomics: myosin VI structural and functional plasticity. *Current Opinion in Structural Biology*, 67:33–40, 2021.

R. Mallik and S. P. Gross. Molecular motors: strategies to get along. *Current Biology*, 14(22):R971–R982, 2004.

D. J. Manstein and M. Preller. Small Molecule Effectors of Myosin Function. In L. M. Coluccio, editor, *Myosins: A Superfamily of Molecular Motors*, Advances in Experimental Medicine and Biology, pages 61–84. Springer International Publishing, Cham, 2020. ISBN 978-3-030-38062-5. URL https://doi.org/10.1007/978-3-030-38062-5_5.

S. S. Margossian and S. Lowey. [7] Preparation of myosin and its subfragments from rabbit skeletal muscle. In *Methods in Enzymology*, volume 85, pages 55–71. Elsevier, 1982. ISBN 978-0-12-181985-9. URL https://linkinghub.elsevier.com/retrieve/pii/007668798285009X.

T. A. Masters and F. Buss. Filopodia formation and endosome clustering induced by mutant plus-end–directed myosin VI. *Proceedings of the National Academy of Sciences*, 114(7):1595–1600, 2017.

P. Maupin, C. L. Phillips, R. S. Adelstein, and T. D. Pollard. Differential localization of myosin-II isozymes in human cultured cells and blood cells. *Journal of Cell Science*, 107 (11):3077–3090, Nov. 1994. URL https://jcs.biologists.org/content/107/11/3077.

J. C. Maxwell. III. *On physical lines of force. The London, Edinburgh, and Dublin Philosophical Magazine and Journal of Science*, 23(151):12–24, Jan. 1862. URL https://www.tandfonline.com/doi/full/10.1080/14786446208643207.

R. L. Meeusen and W. Z. Cande. N-ethylmaleimide-modified heavy meromyosin. A probe for actomyosin interactions. *The Journal of Cell Biology*, 82(1): 57–65, July 1979. URL https://rupress.org/jcb/article/82/1/57/59162/Nethylmaleimidemodified-heavy-meromyosin-A-probe.

A. D. Mehta, R. S. Rock, M. Rief, J. A. Spudich, M. S. Mooseker, and R. E. Cheney. Myosin-V is a processive actin-based motor. *Nature*, 400(6744):590–593, Aug. 1999. URL http://www.nature.com/articles/23072.

E. Meijering, O. Dzyubachyk, and I. Smal. Methods for Cell and Particle Tracking. In *Methods in Enzymology*, volume 504, pages 183–200. Elsevier, 2012. ISBN 978-0-12-391857-4. URL https://linkinghub.elsevier.com/retrieve/pii/B9780123918574000094.

L. Melli, N. Billington, S. A. Sun, J. E. Bird, A. Nagy, T. B. Friedman, Y. Takagi, and J. R. Sellers. Bipolar filaments of human nonmuscle myosin 2-A and 2-B have distinct motile and mechanical properties. *eLife*, 7:e32871, Feb. 2018. URL https://elifesciences.org/articles/32871.

C. T. Mierke. Physical break-down of the classical view on cancer cell invasion and metastasis. *European journal of cell biology*, 92(3):89–104, 2013.

R. Milo and R. Phillips. *Cell Biology by the Numbers*. Taylor & Francis Ltd., New York, NY, illustrated edition edition, Jan. 2016. ISBN 978-0-8153-4537-4.

J. E. Molloy, J. E. Burns, J. C. Sparrow, R. T. Tregear, J. Kendrick-Jones, and D. C. S. White. Single-Molecule Mechanics of Heavy Meromyosin and Si Interacting with Rabbit or Drosophila Actins Using Optical Tweezers. *Biophysical Journal*, 68:6, 1995.

C. Montell and G. M. Rubin. The Drosophila ninaC locus encodes two photoreceptor cell specific proteins with domains homologous to protein kinases and the myosin heavy chain head. *Cell*, 52(5):757–772, Mar. 1988. URL http://www.sciencedirect.com/science/article/pii/0092867488904138.

P. B. Moore, H. E. Huxley, and D. J. DeRosier. Three-dimensional reconstruction of F-actin, thin filaments and decorated thin filaments. *Journal of Molecular Biology*, 50(2):279–292, June 1970. URL http://www.sciencedirect.com/science/article/pii/0022283670901920.

I. Morano, G.-X. Chai, L. G. Baltas, V. Lamounier-Zepter, G. Lutsch, M. Kott, H. Haase, and M. Bader. Smooth-muscle contraction without smooth-muscle myosin. *Nature cell biology*, 2(6):371–375, 2000.

C. A. Morris, A. L. Wells, Z. Yang, L.-Q. Chen, C. V. Baldacchino, and H. L. Sweeney. Calcium functionally uncouples the heads of myosin VI. *Journal of Biological Chemistry*, 278(26):23324–23330, 2003.

S. M. Morris and J. A. Cooper. Disabled-2 colocalizes with the LDLR in clathrin-coated pits and interacts with AP-2. *Traffic*, 2(2):111–123, 2001.

S. M. Morris, S. D. Arden, R. C. Roberts, J. Kendrick-Jones, J. A. Cooper, J. P. Luzio, and F. Buss. Myosin VI binds to and localises with Dab2, potentially linking receptor-mediated endocytosis and the actin cytoskeleton. *Traffic*, 3(5):331–341, 2002.

C. T. Murphy and J. A. Spudich. The Sequence of the Myosin 50- 20K Loop Affects Myosin's Affinity for Actin throughout the Actin- Myosin ATPase Cycle and Its Maximum ATPase Activity. *Biochemistry*, 38(12):3785–3792, 1999.

J. Ménétrey, A. Bahloul, A. L. Wells, C. M. Yengo, C. A. Morris, H. L. Sweeney, and A. Houdusse. The structure of the myosin VI motor reveals the mechanism of directionality reversal. *Nature*, 435(7043):779–785, 2005.

P. M. Müller, J. Rademacher, R. D. Bagshaw, C. Wortmann, C. Barth, J. van Unen, K. M. Alp, G. Giudice, R. L. Eccles, and L. E. Heinrich. Systems analysis of RhoGEF and RhoGAP regulatory proteins reveals spatially organized RAC1 signalling from integrin adhesions. *Nature Cell Biology*, 22(4):498–511, 2020.

A. Nagy, Y. Takagi, N. Billington, S. A. Sun, D. K. T. Hong, E. Homsher, A. Wang, and J. R. Sellers. Kinetic Characterization of Nonmuscle Myosin IIB at the Single Molecule Level. *Journal of Biological Chemistry*, 288(1):709–722, Jan. 2013. URL `http://www.jbc.org/lookup/doi/10.1074/jbc.M112.424671`.

V. Nalavadi, M. Nyitrai, C. Bertolini, N. Adamek, M. A. Geeves, and M. Bähler. Kinetic Mechanism of Myosin IXB and the Contributions of Two Class IX-specific Regions. *Journal of Biological Chemistry*, 280(47):38957–38968, Nov. 2005. URL `http://www.jbc.org/lookup/doi/10.1074/jbc.M507161200`.

K. C. Neuman and S. M. Block. Optical trapping. *Review of Scientific Instruments*, 75 (9):2787–2809, Sept. 2004. URL `https://aip.scitation.org/doi/abs/10.1063/1.1785844`.

M. Nishikawa, S. Nishikawa, A. Inoue, A. H. Iwane, T. Yanagida, and M. Ikebe. A unique mechanism for the processive movement of single-headed myosin-IX. *Biochemical and Biophysical Research Communications*, 343(4):1159–1164, May 2006. URL `https://linkinghub.elsevier.com/retrieve/pii/S0006291X06005390`.

S. Nishikawa, K. Homma, Y. Komori, M. Iwaki, T. Wazawa, A. H. Iwone, J. Saito, R. Ikebe, E. Katayama, and T. Yanagida. Class VI myosin moves processively along actin filaments backward with large steps. *Biochemical and biophysical research communications*, 290(1):311–317, 2002.

M. F. Norstrom, P. A. Smithback, and R. S. Rock. Unconventional Processive Mechanics of Non-muscle Myosin IIB. *Journal of Biological Chemistry*, 285(34):26326–26334, Aug. 2010. URL `http://www.jbc.org/lookup/doi/10.1074/jbc.M110.123851`.

C. B. O'Connell and M. S. Mooseker. Native Myosin-IXb is a plus-, not a minus-end-directed motor. *Nature Cell Biology*, 5(2):171–172, Feb. 2003. URL `http://www.nature.com/articles/ncb924`.

F. Odronitz and M. Kollmar. Drawing the tree of eukaryotic life based on the analysis of 2,269 manually annotated myosins from 328 species. *Genome Biology*, 8(9): R196, 2007. URL `http://genomebiology.biomedcentral.com/articles/10.1186/gb-2007-8-9-r196`.

T. Omelchenko. Regulation of collective cell migration by RhoGAP myosin IXA. *Small GTPases*, 3(4):213–218, Oct. 2012. URL http://www.tandfonline.com/doi/abs/10.4161/sgtp.20495.

T. Omelchenko and A. Hall. Myosin-IXA Regulates Collective Epithelial Cell Migration by Targeting RhoGAP Activity to Cell-Cell Junctions. *Current Biology*, 22 (4):278–288, Feb. 2012. URL https://linkinghub.elsevier.com/retrieve/pii/S0960982212000152.

E. O'Connor, A. Töpf, J. S. Müller, D. Cox, T. Evangelista, J. Colomer, A. Abicht, J. Senderek, O. Hasselmann, A. Yaramis, S. H. Laval, and H. Lochmüller. Identification of mutations in the *MYO9A* gene in patients with congenital myasthenic syndrome. *Brain*, 139(8):2143–2153, Aug. 2016. URL https://academic.oup.com/brain/article-lookup/doi/10.1093/brain/aww130.

E. O'Connor, V. Phan, I. Cordts, G. Cairns, S. Hettwer, D. Cox, H. Lochmüller, and A. Roos. MYO9A deficiency in motor neurons is associated with reduced neuromuscular agrin secretion. *Human Molecular Genetics*, 27(8):1434–1446, Apr. 2018. URL https://academic.oup.com/hmg/article/27/8/1434/4866401.

E. O'Connor, G. Cairns, S. Spendiff, D. Burns, S. Hettwer, A. Mäder, J. Müller, R. Horvath, C. Slater, A. Roos, and H. Lochmüller. Modulation of Agrin and RhoA Pathways Ameliorates Movement Defects and Synapse Morphology in MYO9A-Depleted Zebrafish. *Cells*, 8(8):848, Aug. 2019. URL https://www.mdpi.com/2073-4409/8/8/848.

D. Pantaloni, C. L. Clainche, and M.-F. Carlier. Mechanism of Actin-Based Motility. *Science*, 292(5521):1502–1506, May 2001. URL https://science.sciencemag.org/content/292/5521/1502.

J. D. Pardee and J. A. Spudich. Chapter 18 Purification of Muscle Actin. In L. Wilson, editor, *Methods in Cell Biology*, volume 24 of *The Cytoskeleton Part A. Cytoskeletal Proteins, Isolation and Characterization*, pages 271–289. Academic Press, Jan. 1982. URL http://www.sciencedirect.com/science/article/pii/S0091679X08606615.

H. Y. Park, S. A. Kim, J. Korlach, E. Rhoades, L. W. Kwok, W. R. Zipfel, M. N. Waxham, W. W. Webb, and L. Pollack. Conformational changes of calmodulin upon Ca2+ binding studied with a microfluidic mixer. *Proceedings of the National Academy of Sciences*, 105(2):542–547, 2008.

A. Pecci, E. Panza, N. Pujol-Moix, C. Klersy, F. D. Bari, V. Bozzi, P. Gresele, S. Lethagen, F. Fabris, C. Dufour, A. Granata, M. Doubek, C. Pecoraro, P. A. Koivisto, P. G. Heller, A. Iolascon, P. Alvisi, D. Schwabe, E. D. Candia, B. Rocca, U. Russo, U. Ramenghi, P. Noris, M. Seri, C. L. Balduini, and A. Savoia. Position of nonmuscle myosin heavy chain IIA (NMMHC-IIA) mutations predicts the natural history of MYH9-related disease. *Human Mutation*, 29(3):409–417, 2008. URL https://onlinelibrary.wiley.com/doi/abs/10.1002/humu.20661.

M. Peckham. *Coiled coils and SAH domains in cytoskeletal molecular motors*. Portland Press Ltd., 2011.

M. Peckham. How myosin organization of the actin cytoskeleton contributes to the cancer phenotype. *Biochemical Society Transactions*, 44(4):1026–1034, 2016.

O. Pertz. Spatio-temporal Rho GTPase signaling–where are we now? *Journal of cell science*, 123(11):1841–1850, 2010.

D. Phichith, M. Travaglia, Z. Yang, X. Liu, A. B. Zong, D. Safer, and H. L. Sweeney. Cargo binding induces dimerization of myosin VI. *Proceedings of the National Academy of Sciences*, 106(41):17320–17324, 2009.

T. D. Pollard and E. D. Korn. Acanthamoeba myosin I. Isolation from Acanthamoeba castellanii of an enzyme similar to muscle myosin. *Journal of Biological Chemistry*, 248 (13):4682–4690, 1973a.

T. D. Pollard and E. D. Korn. Acanthamoeba myosin ii. Interaction with actin and with a new cofactor protein required for actin activation of mg2+ adenosine triphosphatase activity. *Journal of Biological Chemistry*, 248(13):4691–4697, 1973b.

T. D. Pollard, W. F. Stafford, and M. E. Porter. Characterization of a second myosin from Acanthamoeba castellanii. *Journal of Biological Chemistry*, 253(13):4798–4808, Oct. 1978. URL `http://www.jbc.org/content/253/13/4798`.

P. L. Post, G. M. Bokoch, and M. S. Mooseker. Human myosin-IXb is a mechanochemically active motor and a GAP for rho. *Journal of Cell Science*, 111(7):941–950, 1998.

P. L. Post, M. J. Tyska, C. B. O'Connell, K. Johung, A. Hayward, and M. S. Mooseker. Myosin-IXb Is a Single-headed and Processive Motor. *Journal of Biological Chemistry*, 277(14):11679–11683, Apr. 2002. URL `http://www.jbc.org/lookup/doi/10.1074/jbc.M111173200`.

O. Pylypenko, L. Song, G. Squires, X. Liu, A. B. Zong, A. Houdusse, and H. L. Sweeney. Role of insert-1 of myosin VI in modulating nucleotide affinity. *Journal of Biological Chemistry*, 286(13):11716–11723, 2011.

I. Rayment, H. M. Holden, M. Whittaker, C. B. Yohn, M. Lorenz, K. C. Holmes, and R. A. Milligan. Structure of the actin-myosin complex and its implications for muscle contraction. *Science*, 261(5117):58–65, July 1993a. URL `https://science.sciencemag.org/content/261/5117/58`.

I. Rayment, W. R. Rypniewski, K. Schmidt-Base, R. Smith, D. R. Tomchick, M. M. Benning, D. A. Winkelmann, G. Wesenberg, and H. M. Holden. Three-dimensional structure of myosin subfragment-1: a molecular motor. *Science*, 261(5117):50–58, 1993b.

G. D. Reddy and P. Saggau. Fast three-dimensional laser scanning scheme using acousto-optic deflectors. *Journal of Biomedical Optics*, 10 (6):064038, Nov. 2005. URL `https://www.spiedigitallibrary.org/journals/Journal-of-Biomedical-Optics/volume-10/issue-6/064038/Fast-three-dimensional-laser-scanning-scheme-using-acousto-optic-deflectors/10.1117/1.2141504.short`.

M. J. Redowicz. Myosins and pathology: genetics and biology. *Acta Biochimica Polonica*, 49(4):789–804, Dec. 2002. URL https://ojs.ptbioch.edu.pl/index.php/abp/article/view/3739.

J. Reinhard, A. A. Scheel, D. Diekmann, A. Hall, C. Ruppert, and M. Bähler. A novel type of myosin implicated in signalling by rho family GTPases. *The EMBO Journal*, 14(4):697–704, Feb. 1995. URL https://www.embopress.org/doi/abs/10.1002/j.1460-2075.1995.tb07048.x.

S. E. Rice, T. J. Purcell, and J. A. Spudich. Building and Using Optical Traps to Study. *Methods in enzymology*, Volume 361:112–133, 2003.

A. J. Ridley. Rho: theme and variations. *Current Biology*, 6(10):1256–1264, 1996.

R. C. Robinson. Crystal Structure of Arp2/3 Complex. *Science*, 294(5547):1679–1684, Nov. 2001. URL https://www.sciencemag.org/lookup/doi/10.1126/science.1066333.

M. W. Rochlin, K. Itoh, R. S. Adelstein, and P. C. Bridgman. Localization of myosin II A and B isoforms in cultured neurons. *Journal of Cell Science*, 108(12):3661–3670, Dec. 1995. URL https://jcs.biologists.org/content/108/12/3661.

R. S. Rock, S. E. Rice, A. L. Wells, T. J. Purcell, J. A. Spudich, and H. L. Sweeney. Myosin VI is a processive motor with a large step size. *Proceedings of the National Academy of Sciences*, 98(24):13655–13659, 2001.

S. T. Ross, S. Schwartz, T. J. Fellers, and M. W. Davidson. Total Internal Reflection Fluorescence (TIRF) Microscopy, Apr. 2021. URL https://www.microscopyu.com/techniques/fluorescence/total-internal-reflection-fluorescence-tirf-microscopy.

A. S. Rovner. A long, weakly charged actin-binding loop is required for phosphorylation-dependent regulation of smooth muscle myosin. *Journal of Biological Chemistry*, 273 (43):27939–27944, 1998.

A. S. Rovner, Y. Freyzon, and K. M. Trybus. Chimeric Substitutions of the Actin-binding Loop Activate Dephosphorylated but Not Phosphorylated Smooth Muscle Heavy Meromyosin. *Journal of Biological Chemistry*, 270(51):30260–30263, Dec. 1995. URL http://www.jbc.org/lookup/doi/10.1074/jbc.270.51.30260.

C. Ruff, M. Furch, B. Brenner, D. J. Manstein, and E. Meyhöfer. Single-molecule tracking of myosins with genetically engineered amplifier domains. *nature structural biology*, 8 (3):4, 2001.

D. Saczko-Brack, E. Warchol, B. Rogez, M. Kröss, S. M. Heissler, J. R. Sellers, C. Batters, and C. Veigel. Self-organization of actin networks by a monomeric myosin. *Proceedings of the National Academy of Sciences*, 113(52):E8387–E8395, Dec. 2016. URL http://www.pnas.org/lookup/doi/10.1073/pnas.1612719113.

S. J. Sahl, S. W. Hell, and S. Jakobs. Fluorescence nanoscopy in cell biology. *Nature Reviews Molecular Cell Biology*, 18(11):685–701, Nov. 2017. URL http://www.nature.com/articles/nrm.2017.71.

Y. Sako, S. Minoghchi, and T. Yanagida. Single-molecule imaging of EGFR signalling on the surface of living cells. *Nature Cell Biology*, 2(3):168–172, Mar. 2000. URL https://www.nature.com/articles/ncb0300_168.

J. R. Sellers. Myosins: a diverse superfamily. *Biochimica et Biophysica Acta (BBA)-Molecular Cell Research*, 1496(1):3–22, 2000.

J. R. Sellers and C. Veigel. Direct observation of the myosin-Va power stroke and its reversal. *Nature structural & molecular biology*, 17(5):590, 2010.

M. P. Sheetz and J. A. Spudich. Movement of myosin-coated fluorescent beads on actin cables in vitro. *Nature*, 303(5912):31–35, May 1983. URL https://www.nature.com/articles/303031a0.

M. P. Sheetz, R. Chasan, and J. A. Spudich. ATP-dependent movement of myosin in vitro: characterization of a quantitative assay. *Journal of Cell Biology*, 99(5):1867–1871, Nov. 1984. URL https://rupress.org/jcb/article/99/5/1867/58607/ATPdependent-movement-of-myosin-in-vitro.

W. M. Shih, Z. Gryczynski, J. R. Lakowicz, and J. A. Spudich. A FRET-based sensor reveals large ATP hydrolysis–induced conformational changes and three distinct states of the molecular motor myosin. *Cell*, 102(5):683–694, 2000.

R. M. Simmons, J. T. Finer, H. M. Warrick, B. Kralik, S. Chu, and J. A. Spudich. *The Mechanism of Myofilament Sliding in Muscle Contraction ed H Sugi and GH Pollack*. New York: Plenum, 1993.

C. Smith and I. Rayment. Active site comparisons highlight structural similarities between myosin and other P-loop proteins. *Biophysical Journal*, 70(4):1590–1602, Apr. 1996a. URL https://linkinghub.elsevier.com/retrieve/pii/S000634959679745X.

C. A. Smith and I. Rayment. X-ray structure of the magnesium (II) ADP vanadate complex of the Dictyostelium discoideum myosin motor domain to 1.9 A resolution. *Biochemistry*, 35(17):5404–5417, 1996b.

J. A. Spudich, S. E. Rice, R. S. Rock, T. J. Purcell, and H. M. Warrick. Optical Traps to Study Properties of Molecular Motors. *Cold Spring Harbor Protocols*, 2011(11):pdb.top066662, Jan. 2011. URL http://cshprotocols.cshlp.org/content/2011/11/pdb.top066662.

W. F. Stafford, M. L. Walker, J. A. Trinick, and L. M. Coluccio. Mammalian class I myosin, Myo1b, is monomeric and cross-links actin filaments as determined by hydrodynamic studies and electron microscopy. *Biophysical journal*, 88(1):384–391, 2005.

L. A. Stein, R. P. Schwarz Jr, P. B. Chock, and E. Eisenberg. Mechanism of the actomyosin adenosine triphosphatase. Evidence that adenosine 5'-triphosphate hydrolysis can occur without dissociation of the actomyosin complex. *Biochemistry*, 18(18):3895–3909, 1979.

C. M. Stoscheck. [6] Quantitation of protein. In M. P. Deutscher, editor, *Methods in Enzymology*, volume 182 of *Guide to Protein Purification*, pages 50–68. Academic Press, Jan. 1990. URL `http://www.sciencedirect.com/science/article/pii/007668799082008P`.

F. Straub. Actin. *Studies from the Institute of Medical Chemistry University Szeged*, Vol. II (Szent-Györgyi, A. ed.):3–15, 1942.

S. Struchholz, K. Elfrink, U. Pieper, G. Kalhammer, U. Honnert, A. Grützner, W. A. Linke, W. Liao, and M. Bähler. Functional Role of the Extended Loop 2 in the Myosin 9b Head for Binding F-actin. *Journal of Biological Chemistry*, 284(6):3663–3671, Feb. 2009. URL `http://www.jbc.org/lookup/doi/10.1074/jbc.M808338200`.

Y. Suzuki, T. Yasunaga, R. Ohkura, T. Wakabayashi, and K. Sutoh. Swing of the lever arm of a myosin motor at the isomerization and phosphate-release steps. *Nature*, 396 (6709):380–383, 1998.

K. Svoboda and S. M. Block. BIOLOGICAL APPLICATIONS OF OPTICAL FORCES. *Annu. Rev. Biophys. Biomol. Stmct.*, 23:247–85, 1994.

K. Svoboda, C. F. Schmidt, B. J. Schnapp, and S. M. Block. Direct observation of kinesin stepping by optical trapping interferometry. *Nature*, 365(6448):721–727, Oct. 1993. URL `https://www.nature.com/articles/365721a0`.

H. L. Sweeney and A. Houdusse. What can myosin VI do in cells? *Current opinion in cell biology*, 19(1):57–66, 2007.

H. L. Sweeney and A. Houdusse. Structural and Functional Insights into the Myosin Motor Mechanism. *Annual Review of Biophysics*, 39(1):539–557, Apr. 2010. URL `http://www.annualreviews.org/doi/10.1146/annurev.biophys.050708.133751`.

A. Szent-Györgyi. Lost in the twentieth century. *Annual review of biochemistry*, 32(1): 1–15, 1963.

A. G. Szent-Györgyi. The Early History of the Biochemistry of Muscle Contraction. *Journal of General Physiology*, 123(6):631–641, June 2004. URL `https://rupress.org/jgp/article/123/6/631/44504/The-Early-History-of-the-Biochemistry-of-Muscle`.

A. G. Szent-Györgyi. Regulation by myosin: how calcium regulates some myosins, past and present. In *Regulatory Mechanisms of Striated Muscle Contraction*, pages 253–264. Springer, 2007.

H. Tajsharghi and A. Oldfors. Myosinopathies: pathology and mechanisms. *Acta neuropathologica*, 125(1):3–18, 2013.

E. W. Taylor and G. G. Borisy. Kinesin Processivity. *The Journal of Cell Biology*, 151(5):27–30, Nov. 2000. URL https://www.ncbi.nlm.nih.gov/pmc/articles/PMC2174361/.

M. Terrak, G. Rebowski, R. C. Lu, Z. Grabarek, and R. Dominguez. Structure of the light chain-binding domain of myosin V. *Proceedings of the National Academy of Sciences*, 102(36):12718–12723, 2005.

J. A. Theriot, T. J. Mitchison, L. G. Tilney, and D. A. Portnoy. The rate of actin-based motility of intracellular Listeria monocytogenes equals the rate of actin polymerization. *Nature*, 357(6375):257–260, 1992.

J. A. Theriot, J. Rosenblatt, D. A. Portnoy, P. J. Goldschmidt-Clermont, and T. J. Mitchison. Involvement of profilin in the actin-based motility of L. monocytogenes in cells and in cell-free extracts. *Cell*, 76(3):505–517, Feb. 1994. URL https://www.cell.com/cell/abstract/0092-8674(94)90114-7.

R. F. Thompson and G. M. Langford. Myosin superfamily evolutionary history. *The Anatomical Record*, 268(3):276–289, 2002. URL https://onlinelibrary.wiley.com/doi/abs/10.1002/ar.10160.

H. Tidow and P. Nissen. Structural diversity of calmodulin binding to its target sites. *The FEBS journal*, 280(21):5551–5565, 2013.

T. Tokiwa and Y. Tonomura. The pre-steady state of the myosin-adenosine triphosphate system. *The Journal of Biochemistry*, 57(5):616–626, 1965.

A. A. Tokmakov, A. Kurotani, T. Takagi, M. Toyama, M. Shirouzu, Y. Fukami, and S. Yokoyama. Multiple Post-translational Modifications Affect Heterologous Protein Synthesis. *Journal of Biological Chemistry*, 287(32):27106–27116, Aug. 2012. URL http://www.jbc.org/lookup/doi/10.1074/jbc.M112.366351.

E. Toprak, A. Yildiz, M. T. Hoffman, S. S. Rosenfeld, and P. R. Selvin. Why kinesin is so processive. *Proceedings of the National Academy of Sciences*, 106(31):12717–12722, 2009.

H. Towbin, T. Staehelin, and J. Gordon. Electrophoretic transfer of proteins from polyacrylamide gels to nitrocellulose sheets: procedure and some applications. *Proceedings of the National Academy of Sciences*, 76(9):4350–4354, Sept. 1979. URL http://www.pnas.org/cgi/doi/10.1073/pnas.76.9.4350.

D. R. Trentham, J. F. Eccleston, and C. R. Bagshaw. Kinetic analysis of ATPase mechanisms. *Quarterly reviews of biophysics*, 9(2):217–281, 1976.

D. A. Tumbarello, J. Kendrick-Jones, and F. Buss. Myosin VI and its cargo adaptors – linking endocytosis and autophagy. *Journal of Cell Science*, 126(12):2561–2570, June 2013. URL https://jcs.biologists.org/content/126/12/2561.

M. J. Tyska and D. M. Warshaw. The myosin power stroke. *Cell motility and the cytoskeleton*, 51(1):1–15, 2002.

M. J. Tyska, D. E. Dupuis, W. H. Guilford, J. B. Patlak, G. S. Waller, K. M. Trybus, D. M. Warshaw, and S. Lowey. Two heads of myosin are better than one for generating force and motion. *Proceedings of the National Academy of Sciences*, 96(8):4402–4407, Apr. 1999. URL http://www.pnas.org/cgi/doi/10.1073/pnas.96.8.4402.

T. Q. Uyeda, P. D. Abramson, and J. A. Spudich. The neck region of the myosin motor domain acts as a lever arm to generate movement. *Proceedings of the National Academy of Sciences*, 93(9):4459–4464, Apr. 1996. URL http://www.pnas.org/cgi/doi/10.1073/pnas.93.9.4459.

T. Q. P. Uyeda, S. J. Kron, and J. A. Spudich. Myosin step size: Estimation from slow sliding movement of actin over low densities of heavy meromyosin. *Journal of Molecular Biology*, 214(3):699–710, Aug. 1990. URL https://www.sciencedirect.com/science/article/pii/002228369090287V.

T. Q. P. Uyeda, K. M. Ruppel, and J. A. Spudich. Enzymatic activities correlate with chimaeric substitutions at the actin-binding face of myosin. *Nature*, 368(6471):567–569, Apr. 1994. URL http://www.nature.com/articles/368567a0.

T. van Leeuwen, A. S. Lubbe, P. Štacko, S. J. Wezenberg, and B. L. Feringa. Dynamic control of function by light-driven molecular motors. *Nature Reviews Chemistry*, 1(12):1–7, Nov. 2017. URL https://www.nature.com/articles/s41570-017-0096.

C. Veigel, M. L. Bartoo, D. C. White, J. C. Sparrow, and J. E. Molloy. The Stiffness of Rabbit Skeletal Actomyosin Cross-Bridges Determined with an Optical Tweezers Transducer. *Biophysical Journal*, 75(3):1424–1438, Sept. 1998. URL https://linkinghub.elsevier.com/retrieve/pii/S0006349598740615.

C. Veigel, L. M. Coluccio, J. D. Jontes, J. C. Sparrow, R. A. Milligan, and J. E. Molloy. The motor protein myosin-I produces its working stroke in two steps. *Nature*, 398(6727):530–533, Apr. 1999. URL http://www.nature.com/articles/19104.

C. Veigel, F. Wang, M. L. Bartoo, J. R. Sellers, and J. E. Molloy. The gated gait of the processive molecular motor, myosin V. *Nature Cell Biology*, 4(1):59–65, Jan. 2002. URL http://www.nature.com/articles/ncb732.

C. Veigel, J. E. Molloy, S. Schmitz, and J. Kendrick-Jones. Load-dependent kinetics of force production by smooth muscle myosin measured with optical tweezers. *Nature cell biology*, 5(11):980–986, 2003.

C. Veigel, S. Schmitz, F. Wang, and J. R. Sellers. Load-dependent kinetics of myosin-V can explain its high processivity. *Nature cell biology*, 7(9):861–869, 2005.

M. Vicente-Manzanares, X. Ma, R. S. Adelstein, and A. R. Horwitz. Non-muscle myosin II takes centre stage in cell adhesion and migration. *Nature Reviews Molecular Cell Biology*, 10(11):778–790, Nov. 2009. URL http://www.nature.com/articles/nrm2786.

K. Visscher, S. P. Gross, and S. M. Block. Construction of multiple-beam optical traps with nanometer-resolution position sensing. *IEEE Journal of Selected Topics in Quantum Electronics*, 2(4):1066–1076, Dec. 1996.

N. Volkmann, D. Hanein, G. Ouyang, K. M. Trybus, D. J. DeRosier, and S. Lowey. Evidence for cleft closure in actomyosin upon ADP release. *nature structural biology*, 7 (12):9, 2000.

M. L. Walker, S. A. Burgess, J. R. Sellers, F. Wang, J. A. Hammer, J. Trinick, and P. J. Knight. Two-headed binding of a processive myosin to F-actin. *Nature*, 405(6788): 804–807, 2000.

Y.-L. Wang. Exchange of actin subunits at the leading edge of living fibroblasts: possible role of treadmilling. *The Journal of cell biology*, 101(2):597–602, 1985.

Z.-Y. Wang, F. Wang, J. R. Sellers, E. D. Korn, and J. A. Hammer. Analysis of the regulatory phosphorylation site in Acanthamoeba myosin IC by using site-directed mutagenesis. *Proceedings of the National Academy of Sciences*, 95(26):15200–15205, 1998.

E. Warchol. *Expression, purification and characterization of human myosin 9a.* Text.PhDThesis, Ludwig-Maximilians-Universität München, Feb. 2016. URL `https://edoc.ub.uni-muenchen.de/19410/`.

D. M. Warshaw, W. H. Guilford, Y. Freyzon, E. Krementsova, K. A. Palmiter, M. J. Tyska, J. E. Baker, and K. M. Trybus. The Light Chain Binding Domain of Expressed Smooth Muscle Heavy Meromyosin Acts as a Mechanical Lever. *Journal of Biological Chemistry*, 275(47):37167–37172, Nov. 2000. URL `http://www.jbc.org/lookup/doi/10.1074/jbc.M006438200`.

M. R. Webb and J. E. Corrie. Fluorescent coumarin-labeled nucleotides to measure ADP release from actomyosin. *Biophysical journal*, 81(3):1562–1569, 2001.

A. L. Wells, A. W. Lin, L.-Q. Chen, D. Safer, S. M. Cain, T. Hasson, B. O. Carragher, R. A. Milligan, and H. L. Sweeney. Myosin VI is an actin-based motor that moves backwards. *Nature*, 401(6752):505–508, Sept. 1999. URL `https://www.nature.com/articles/46835`.

M. Whittaker, E. M. Wilson-Kubalek, J. E. Smith, L. Faust, R. A. Milligan, and H. L. Sweeney. A 35-Å movement of smooth muscle myosin on ADP release. *Nature*, 378 (6558):748–751, Dec. 1995. URL `http://www.nature.com/articles/378748a0`.

J. A. Wirth, K. A. Jensen, P. L. Post, W. M. Bement, and M. S. Mooseker. Human myosin-IXb, an unconventional myosin with a chimerin-like rho/rac GTPase-activating protein domain in its tail. *Journal of Cell Science*, 109(3):653–661, Mar. 1996. URL `https://jcs.biologists.org/content/109/3/653`.

J. Wood and M. Olson. Collective Migration: Spatial Tension Relief. *Current Biology*, 22(4):R125–R127, Feb. 2012. URL `https://linkinghub.elsevier.com/retrieve/pii/S0960982212000279`.

S. F. Wulf, V. Ropars, S. Fujita-Becker, M. Oster, G. Hofhaus, L. G. Trabuco, O. Pylypenko, H. L. Sweeney, A. M. Houdusse, and R. R. Schröder. Force-producing ADP state of myosin bound to actin. *Proceedings of the National Academy of Sciences*,

113(13):E1844–E1852, Mar. 2016. URL http://www.pnas.org/lookup/doi/10.1073/pnas.1516598113.

T. Yanagida, K. Kitamura, H. Tanaka, A. Hikikoshi Iwane, and S. Esaki. Single molecule analysis of the actomyosin motor. *Current Opinion in Cell Biology*, 12(1):20–25, Feb. 2000. URL https://linkinghub.elsevier.com/retrieve/pii/S0955067499000526.

J. Yang and Y. Zhang. I-TASSER server: new development for protein structure and function predictions. *Nucleic Acids Research*, 43(W1):W174–W181, July 2015. URL https://academic.oup.com/nar/article-lookup/doi/10.1093/nar/gkv342.

K. L. Yap, J. Kim, K. Truong, M. Sherman, T. Yuan, and M. Ikura. Calmodulin target database. *Journal of structural and functional genomics*, 1(1):8–14, 2000.

C. M. Yengo and H. L. Sweeney. Functional role of loop 2 in myosin V. *Biochemistry*, 43 (9):2605–2612, 2004.

A. Yildiz and P. R. Selvin. Fluorescence imaging with one nanometer accuracy: application to molecular motors. *Accounts of chemical research*, 38(7):574–582, 2005.

A. Yildiz, J. N. Forkey, S. A. McKinney, T. Ha, Y. E. Goldman, and P. R. Selvin. Myosin V walks hand-over-hand: single fluorophore imaging with 1.5-nm localization. *science*, 300(5628):2061–2065, 2003.

H. Yoshida, W. Cheng, J. Hung, D. Montell, E. Geisbrecht, D. Rosen, J. Liu, and H. Naora. Lessons from border cell migration in the Drosophila ovary: A role for myosin VI in dissemination of human ovarian cancer. *Proceedings of the National Academy of Sciences*, 101(21):8144–8149, 2004.

R. G. Yount, C. R. Cremo, J. C. Grammer, and B. A. Kerwin. Photochemical mapping of the active site of myosin. *Philosophical Transactions of the Royal Society of London. Series B: Biological Sciences*, 336(1276):55–61, 1992.

R. G. Yount, D. Lawson, and I. Rayment. Is myosin a "back door" enzyme? *Biophysical Journal*, 68(4 Suppl):44S–49S, Apr. 1995. URL https://www.ncbi.nlm.nih.gov/pmc/articles/PMC1281861/.

C. Yu, W. Feng, Z. Wei, Y. Miyanoiri, W. Wen, Y. Zhao, and M. Zhang. Myosin VI undergoes cargo-mediated dimerization. *Cell*, 138(3):537–548, 2009.

P. Zakrzewski, M. Lenartowska, and F. Buss. Diverse functions of myosin VI in spermiogenesis. *Histochemistry and Cell Biology*, 155(3):323–340, Mar. 2021. URL https://doi.org/10.1007/s00418-020-01954-x.

Appendix

Construct sequences

IXaMD: base pairs 444-3057 encoding amino acids 149-1019 of human myosin-IXa (NCBI: AAI40870.1); FLAG- and Avi tag; BamHI/SalI restriction sites; codon-optimized for Sf21

GGATCCATGGATGATTTATGTAGTTTACCTGATTTGAATGAGAAAACTCTCTTAGAAAACCTACGAAATCGCTTTAAGCATGAA
AAAATTTATACCTATGTTGGCAGTATTCTAATAGTTATTAACCCATTCAAGTTTCTTCCTATTTATAACCCCAAATATGTCAAAA
TGTATGATAACCACCAACTGGGAAAACTTGAGCCCCACATTTATGCTGTGGCTGATGTAGCTTATCATGCCATGCTTCAGCGCAA
AAAGAATCAGTGCATCGTGATTTCAGGAGAGAGTGGTTCTGGGAAGACTCAAAGCACAAACTTTCTTATTCACCACCTTACTGC
TCTCAGTCAGAAAGGATTTGCCAGTGGAGTAGAACAGATTATTCTTGGAGCTGGACCAGTACTTGAGGCCTTTGGAAATGCAAA
GACAGCTCATAATAACAATTCAAGTCGTTTTGGGAAGTTTATTCAAGTAAATTACCAGGAAACAGGCACTGTACTTGGTGCCTA
TGTTGAAAAATATCTACTGGAGAAGTCCAGACTCGTTTATCAGGAGCATAATGAACGGAACTATCATGTATTCTATTACCTCCTG
GCAGGAGCAAGTGAAGATGAGAGATCAGCATTCCATCTTAAGCAACCAGAGGAATATCATTATCTCAATCAGATAACAAAGAAA
CCCCTCAGACAGAGCTGGGATGATTATTGCTATGACTCTGAGCCGGATTGCTTCACGGTGGAAGGAGAAGATTTGAGACATGAC
TTTGAGCGCCTACAACTTGCCATGGAAATGGTAGGATTTCTTCCCAAGACACGAAGACAGATTTTCTCTCTTCTCTCAGCCATAC
TACATTTGGGTAATATCTGTTACAAAAAGAAGACATACCGGGATGACTCCATTGATATCTGTAATCCTGAAGTTCTGCCTATTGT
CTCAGAATTATTAGAGGTTAAAGAAGAGATGCTATTTGAAGCATTAGTTACAAGGAAGACGGTGACAGTGGGAGAAAAGCTTAT
TTTGCCATACAAGTTGGCAGAGGCTGTGACAGTGAGGAACTCCATGGCTAAGTCTCTGTATAGTGCCCTGTTTGACTGGATAGT
TTTTCGAATTAATCATGCACTTCTGAATAGTAAAGATTTAGAGCATAATACCAAGACATTGTCTATTGGTGTTCTTGATATTTTT
GGGTTTGAAGATTATGAAAATAACAGCTTTGAACAGTTCTGTATTAATTTTGCTAATGAACGTTTACAGCACTACTTTAATCAGC
ATATCTTTAAATTGGAACAAGAGGAATATAGAACTGAAGGTATCAGCTGGCACAACATAGATTACATTGATAATACCTGCTGCA
TAAATCTTATTAGCAAAAAACCAACAGGACTGCTTCATCTTTTGGATGAAGAAAGCAACTTTCCACAGGCTACAAATCAAACATT
GCTAGACAAGTTTAAGCATCAACATGAAGATAATTCTTACATCGAATTTCCAGCCGTGATGGAGCCTGCTTTCATTATAAAACAT
TATGCTGGAAAAGTAAAATATGGGGTAAAGGATTTCCGGGAAAAAAATACAGATCATATGCGCCCAGACATTGTAGCTCTTCTG
AGAAGCAGCAAGAATGCATTTATCTCTGGGATGATTGGAATTGATCCTGTAGCTGTTTTCCGATGGGCAATTCTCCGAGCTTTT
TTCAGAGCCATGGTTGCTTTCAGGGAAGCTGGGAAAAGAAACATTCACAGAAAAACTGGACATGATGATACAGCGCCATGTGCA
ATTTTGAAAAGTATGGATAGTTTTAGCTTTCTCCAACACCCAGTCCACCAGAGGAGCTTAGAGATTCTGCAGAGATGCAAGGAA
GAGAAGTACAGTATAACCCGGAAAAATCCCAGAACACCTCTTTCTGATCTCCAGGGCATGAATGCTCTAAATGAAAAAAACCAAC
ATGATACATTTGATATTGCCTGGAATGGCAGAACTGGGATTCGCCAGAGCAGACTATCAAGTGGCACCTCCTTGCTTGATAAAG
ATGGAATATTTGCTAATTCAACTAGCAGCAAACTCCTGGAGAGAGCCCATGGAATTCTCACGAGAAACAAAAATTTCAAATCCAA
GCCTGCCCTTCCAAAGCACTTGCTAGAAGTAAATTCTTTAAAGCACCTGACAAGACTGACACTACAAGATCGCATTACCAAGTCT
CTTCTTCATTTACACAAGAAGAAAAAACCTCCCAGCATCAGTGCCCAGTTTCAGGCATCATTAAGCAAGCTAATGGAAACACTTG
GTCAAGCAGAACCATATTTTGTAAAATGCATTCGCTCTAATGCTGAAAAGCTGCCCTTAAGGTTCAGTGATGTCTTGGTACTTA
GACAGCTTCGATACACCGGGATGCTGGAAACAGTTCGAATTCGCCAATCAGGATACAGCTCCAAATATTCTTTCCAGGATTTTG
TGAGCCACTTCCATGTACTTCTTCCCCGAAATATTATTCCATCCAAATTTAACATTCAGGATTTCTTCAGGAAAATAAATCTTAA
TCCAGATAATTATCAAGTTGGAAAAACCATGGTCTTTCTAAAGGAGCAGGAACGACAGCACTTACAAGATCTGCTTCACCAAGA
GGTGGGTGGTGGTCTGAACGACATCTTCGAGGCTCAGAAAATCGAATGGCACGAAGGCGGTGGCGACTACAAGGACGACGATG
ATAAGTAGGTCGAC

IXa MD skeletal; aa 692-887 of IXa MD are replaced; 3x FLAG- and Avi tag; BamHI/SalI restriction sites; codon-optimized for Sf21

AAATATTCCGGATTATTCATACCGTCCCACCATCGGGCGCGGATCCATGGACCTGTGCTCCCTGCCCGACCTGAACGAAAAGACC
CTGCTCGAGAACCTGCGTAACCGTTTCAAGCACGAGAAGATCTACACCTACGTGGGCTCCATCCTGATCGTGATCAACCCCTTCA
AGTTCCTGCCCATCTACAACCCTAAATACGTGAAGATGTACGACAACCACCAGCTGGGCAAGCTCGAGCCCCACATCTACGCTGT
GGCTGACGTGGCCTACCACGCTATGCTGCAGCGCAAGAAGAACCAGTGCATCGTGATCTCCGGCGAGTCCGGTTCCGGCAAGAC
CCAGTCTACCAACTTCCTGATCCACCACCTGACCGCTCTGTCCCAAAAGGGTTTCGCTTCCGGTGTCGAGCAGATCATCCTGGGT
GCTGGTCCCGTGCTCGAGGCTTTCGGCAACGCTAAGACCGCTCACAACAACAACTCCTCCCGTTTCGGCAAGTTCATCCAAGTGA
ACTACCAAGAGACTGGCACCGTGCTGGGCGCTTACGTCGAGAAGTACCTGCTGGAAAAGTCCCGTCTGGTGTACCAAGAGCACA
ACGAGCGCAACTACCACGTGTTCTACTACCTGCTCGCTGGTGCTTCCGAGGACGAGCGTTCCGCTTTCCACCTGAAGCAGCCCG
AGGAATACCACTACCTGAACCAGATCACCAAGAAGCCCCTGCGTCAGTCCTGGGACGACTACTGCTACGACTCCGAGCCCGACT
GCTTCACCGTGGAAGGCGAGGACCTGCGTCACGACTTCGAGCGTCTGCAGCTGGCTATGGAAATGGTCGGATTCCTGCCTAAGA
CCCGTCGTCAGATCTTCAGCCTGCTGTCCGCTATCCTGCACCTGGGCAACATCTGCTACAAGAAGAAGACCTACCGCGACGACTC
CATCGACATCTGCAACCCCGAGGTGCTGCCCATCGTGTCCGAGCTGCTGGAAGTGAAGGAAGAGATGCTGTTCGAGGCTCTGGT
CACCCGCAAGACCGTGACCGTGGGCGAGAAGCTGATCCTGCCCTACAAGCTGGCTGAGGCTGTGACCGTGCGCAACTCCATGGC
TAAGTCCCTGTACTCCGCTCTGTTCGACTGGATCGTGTTCCGTATCAACCACGCCCTGCTGAACTCCAAGGACCTGGAACACAAC
ACCAAGACCCTGTCCATCGGTGTCCTGGACATCTTCGGTTTCGAGGACTACGAGAACAACAGCTTCGAGCAGTTCTGCATCAAC
TTCGCTAACGAGAGGCTGCAGCACTACTTCAACCAGCACATCTTCAAGCTGGAACAAGAAGAGTACCGTACCGAGGGCATCTCC
TGGCACAACATCGACTACATCGATAACACCTGTTGCATCAACCTCATCTCGAAGAAGCCCACCGGCCTGCTGCACCTGTTGGACG
AGGAATCCAACTTCCCTCAGGCTACCAACCAGACTCTGCTGGACAAGTTCAAGCACCAACACGAGGACAACTCCTACATCGAGTT
CCCCGCTGTGATGGAACCCGCTTTCATCATCAAGCACTACGCCGGCAAAGTGAAGTACGGTGTCAAGGACTTCCGCGAGAAGAA
CACCGACCACATGCGTCCCGACATCGTGGCTCTGCTGCGCTCCTCCAAGAACGCCTTCATCTCCGGCATGATCTCTGGTGCTCAG
GCTGGCGAAGAGGGTGGTGGTGGAAAGAAGGGCGGAAAGAAGAAGGGTTCTATCTCCGCTCAGTTCCAGGCTTCCCTGTCCAAG
CTGATGGAAACCCTGGGCCAGGCTGAGCCTTACTTCGTGAAGTGCATCCGTTCCAACGCTGAGAAGCTGCCCCTGCGCTTCTCC
GACGTGCTGGTGTTGCGTCAGCTGCGTTACACCGGCATGCTGGAAACCGTGCGTATCCGTCAGTCCGGTTACTCCTCTAAGTAC
AGCTTCCAGGACTTCGTGTCCCACTTCCACGTGCTGCTGCCCCGTAACATCATCCCTTCCAAGTTCAACATCCAAGATTTCTTCC
GCAAGATCAACCTGAACCCCGACAACTACCAAGTCGGCAAGACTATGGTGTTCCTGAAGGAACAAGAGCGTCAGCACCTCCAGG
ACCTGCTCCACCAAGAAGTGGGCGGAGGCCTGAACGACATCTTCGAGGCTCAAAAGATCGAGTGGCACGAGGGTGGCGGCGACT
ACAAGGACCACGACGGCGATTACAAGGATCACGACATCGACTACAAGGACGATGACGATAAATAAGTCGACGAGCTCACTAGTC
GCGGCCGCTTTCGAATCTAGAGCCTGC

IXa S1; bp 444-3492 encoding aa 149-1164; codon-optimized for Sf21

ATGGATTTATGTAGTTTACCTGATTTGAATGAGAAAACTCTCTTAGAAAACCTACGAAATCGCTTTAAGCATGAAAAAATTTATA
CCTATGTTGGCAGTATTCTAATAGTTATTAACCCATTCAAGTTTCTTCCTATTTATAACCCCAAATATGTCAAAATGTATGATAA
CCACCAACTGGGAAAACTTGAGCCCCACATTTATGCTGTGGCTGATGTAGCTTATCATGCCATGCTTCAGCGCAAAAAGAATCA
GTGCATCGTGATTTCAGGAGAGAGTGGTTCTGGGAAGACTCAAAGCACAAACTTTCTTATTCACCACCTTACTGCTCTCAGTCA
GAAAGGATTTGCCAGTGGAGTAGAACAGATTATTCTTGGAGCTGGACCAGTACTTGAGGCCTTTGGAAATGCAAAGACAGCTCA
TAATAACAATTCAAGTCGTTTTGGGAAGTTTATTCAAGTAAATTACCAGGAAACAGGCACTGTACTTGGTGCCTATGTTGAAAA
ATATCTACTGGAGAAGTCCAGACTCGTTTATCAGGAGCATAATGAACGGAACTATCATGTATTCTATTACCTCCTGGCAGGAGC
AAGTGAAGATGAGAGATCAGCATTCCATCTTAAGCAACCAGAGGAATATCATTATCTCAATCAGATAACAAAGAAACCCCTCAG
ACAGAGCTGGGATGATTATTGCTATGACTCTGAGCCGGATTGCTTCACGGTGGAAGGAGAAGATTTGAGACATGACTTTGAGCG
CCTACAACTTGCCATGGAAATGGTAGGATTTCTTCCCAAGACACGAAGACAGATTTTCTCTCTTCTCTCAGCCATACTACATTTG
GGTAATATCTGTTACAAAAAGAAGACATACCGGGATGACTCCATTGATATCTGTAATCCTGAAGTTCTGCCTATTGTCTCAGAAT
TATTAGAGGTTAAAGAAGAGATGCTATTTGAAGCATTAGTTACAAGGAAGACGGTGACAGTGGGAGAAAAGCTTATTTTGCCAT

ACAAGTTGGCAGAGGCTGTGACAGTGAGGAACTCCATGGCTAAGTCTCTGTATAGTGCCCTGTTTGACTGGATAGTTTTTCGAA
TTAATCATGCACTTCTGAATAGTAAAGATTTAGAGCATAATACCAAGACATTGTCTATTGGTGTTCTTGATATTTTTGGGTTTGA
AGATTATGAAAATAACAGCTTTGAACAGTTCTGTATTAATTTTGCTAATGAACGTTTACAGCACTACTTTAATCAGCATATCTTT
AAATTGGAACAAGAGGAATATAGAACTGAAGGTATCAGCTGGCACAACATAGATTACATTGATAATACCTGCTGCATAAATCTT
ATTAGCAAAAAACCAACAGGACTGCTTCATCTTTTGGATGAAGAAAGCAACTTTCCACAGGCTACAAATCAAACATTGCTAGACA
AGTTTAAGCATCAACATGAAGATAATTCTTACATCGAATTTCCAGCCGTGATGGAGCCTGCTTTCATTATAAAACATTATGCTGG
AAAAGTAAAATATGGGGTAAAGGATTTCCGGGAAAAAAATACAGATCATATGCGCCCAGACATTGTAGCTCTTCTGAGAAGCAG
CAAGAATGCATTTATCTCTGGGATGATTGGAATTGATCCTGTAGCTGTTTTCCGATGGGCAATTCTCCGAGCTTTTTTCAGAGCC
ATGGTTGCTTTCAGGGAAGCTGGGAAAAGAAACATTCACAGAAAAACTGGACATGATGATACAGCGCCATGTGCAATTTTGAAA
AGTATGGATAGTTTTAGCTTTCTCCAACACCCAGTCCACCAGAGGAGCTTAGAGATTCTGCAGAGATGCAAGGAAGAGAAGTAC
AGTATAACCCGGAAAAATCCCAGAACACCTCTTTCTGATCTCCAGGGCATGAATGCTCTAAATGAAAAAAACCAACATGATACAT
TTGATATTGCCTGGAATGGCAGAACTGGGATTCGCCAGAGCAGACTATCAAGTGGCACCTCCTTGCTTGATAAAGATGGAATAT
TTGCTAATTCAACTAGCAGCAAACTCCTGGAGAGAGCCCATGGAATTCTCACGAGAAACAAAAATTTCAAATCCAAGCCTGCCCT
TCCAAAGCACTTGCTAGAAGTAAATTCTTTAAAGCACCTGACAAGACTGACACTACAAGATCGCATTACCAAGTCTCTTCTTCAT
TTACACAAGAAGAAAAAACCTCCCAGCATCAGTGCCCAGTTTCAGGCATCATTAAGCAAGCTAATGGAAACACTTGGTCAAGCA
GAACCATATTTTGTAAAATGCATTCGCTCTAATGCTGAAAAGCTGCCCTTAAGGTTCAGTGATGTCTTGGTACTTAGACAGCTTC
GATACACCGGGATGCTGGAAACAGTTCGAATTCGCCAATCAGGATACAGCTCCAAATATTCTTTCCAGGATTTTGTGAGCCACT
TCCATGTACTTCTTCCCCGAAATATTATTCCATCCAAATTTAACATTCAGGATTTCTTCAGGAAAATAAATCTTAATCCAGATAA
TTATCAAGTTGGAAAAACCATGGTCTTTCTAAAGGAGCAGGAACGACAGCACTTACAAGATCTGCTTCACCAAGAGGTGCTCCG
CAGAATCATATTGTTGCAGCGATGGTTCAGGGTCTTGCTGTGTAGGCAGCATTTCCTCCATCTGAGACAAGCATCTGTTATTAT
CCAGAGATTCTGGAGGAATTACCTAAATCAGAAGCAAGTCAGAGATGCAGCTGTGCAGAAGGATGCTTTTGTTATGGCTAGTGC
AGCTGCTCTTCTCCAAGCTTCCTGGCGTGCTCACTTAGAGAGGCAGCGGTACTTGGAGTTACGGGCTGCAGCCATCGTTATCCA
GCAGAAATGGAGAGATTACTATAGGCGCAGGCACATGGCTGCTATTTGCATACAAGCAAGATGGAAAGCCTACAGGGAAAGTAA
AAGGTACCAAGAACAAAGGAAAAAAATTATCCTTTTGCAATCAACATGTAGAGGATTCAGAGCAAGACAAAGATTTAAAGCTTT
AAAAGGTGGTGGTCTGAACGACATCTTCGAGGCTCAGAAAATCGAATGGCACGAAGGCGGTGGCGACTACAAGGACGACGATGA
TAAGTAGGTCGAC

Calmodulin from *Xenopus laevis* (CaMX); full-length; no tag; BamHI/XhoI restriction sites; codon-optimized for Sf21

GGATCCATGGCTGACCAACTGACAGAAGAGCAGATTGCAGAGTTCAAAGAAGCCTTCTCATTATTCGACAAGGATGGGGACGGC
ACCATCACCACAAAGGAACTTGGCACCGTTATGAGGTCGCTTGGACAAAACCCAACGGAAGCAGAATTGCAGGATATGATCAAT
GAAGTCGATGCTGATGGCAATGGAACGATTGACTTTCCTGAATTTCTTACTATGATGGCTAGAAAAATGAAGGACACAGACAGC
GAAGAGGAAATCCGAGAAGCATTCCGTGTTTTTGATAAGGATGGGAACGGCTACATCAGCGCTGCTGAATTACGTCACGTCATG
ACAAACCTCGGGGAGAAGTTAACAGACGAAGAAGTTGACGAAATGATAAGGGAAGCAGATATTGATGGTGACGGCCAAGTAAAC
TACGAAGAGTTTGTACAAATGATGACAGCAAAGTGACTCGAG

Myosin IXa loop 2 construct; nucleotides 2068-2703 encoding amino acids 690-901 of human myosin IXa, BamHI/XhoI restriction sites; codon-optimized for *E. coli*

GGATCCCGTAGCAGCAAAAATGCCTTTATTAGCGGTATGATTGGTATTGATCCGGTTGCAGTTTTTCGTTGGGCAATTCTGCGT
GCATTTTTTCGTGCAATGGTTGCATTTCGTGAAGCCGGTAAACGTAACATTCATCGTAAAACCGGTCATGATGATACCGCACCG
TGTGCAATTCTGAAAAGCATGGATAGCTTTAGCTTTCTGCAGCATCCGGTTCATCAGCGTAGCCTGGAAATTCTGCAGCGTTGT
AAAGAAGAGAAATATAGCATCACCCGTAAGAATCCGCGTACACCGCTGAGCGATCTGCAGGGTATGAATGCACTGAATGAAAAA
AATCAGCACGATACCTTTGATATCGCATGGAATGGTCGTACCGGTATTCGTCAGAGCCGTCTGAGCAGCGGCACCAGCCTGCTG
GATAAAGATGGTATTTTTGCAAATAGCACCAGCAGCAAACTGCTGGAACGTGCACATGGTATTCTGACCCGCAATAAAAACTTT
AAAAGCAAACCGGCACTGCCGAAACATCTGCTGGAAGTTAATAGCCTGAAACACCTGACACGTCTGACACTGCAGGATCGTATT

ACCAAAAGCCTGCTGCATCTGCACAAAAAAAAGAAACCGCCTAGCATTAGCGCACAGTTTCAGGCAAGCCTGAGTAAACTGATG
GAAACCCTGGGTCAAGCAGAACCGTATTTTGTTAAACTCGAG

HNMIIB S1: bp 1-2571 encoding amino acids 1-857 (NCBI: P35580.3); C terminally His tag, N terminally Flag- and Avi-tag; BamHI/NotI restriction sites; codon-optimized for Sf21

ATGGCTCAGCGTACTGGATTGGAGGACCCCGAGCGTTACCTGTTCGTGGACCGTGCTGTGATCTACAACCCCGCTACTCAGGCT
GACTGGACCGCTAAGAAGCTCGTCTGGATTCCCTCCGAGCGTCACGGTTTCGAGGCTGCTTCCATCAAAGAGGAACGCGGCGAC
GAAGTGATGGTCGAGCTGGCTGAGAACGGCAAGAAAGCTATGGTCAACAAGGACGACATCCAGAAGATGAACCCTCCGAAGTTC
TCCAAGGTCGAGGACATGGCTGAGCTGACCTGCCTGAACGAGGCTTCCGTGCTGCACAACCTGAAGGACCGTTACTACTCCGGC
CTGATCTACACCTACTCCGGACTGTTCTGCGTGGTCATCAACCCCTACAAGAACCTGCCTATCTACTCCGAGAACATCATCGAGA
TGTACCGCGGCAAAAAGCGTCACGAGATGCCTCCACACATCTACGCTATCTCCGAGTCCGCTTACCGTTGCATGCTGCAAGACCG
CGAGGACCAGTCTATCCTGTGCACTGGCGAATCCGGTGCTGGAAAGACCGAGAACACCAAGAAAGTGATCCAGTACCTGGCTCA
CGTGGCCTCCAGTCACAAGGGTAGAAAGGACCACAACATCCCCGAGTCTCCCAAGCCTGTGAAGCACCAGGGCGAGCTGGAACG
TCAACTGCTGCAGGCTAACCCCATCCTCGAGTCCTTCGGCAACGCTAAGACCGTGAAGAACGACAACTCCTCTCGTTTCGGCAAG
TTCATCCGCATCAACTTCGACGTGACCGGTTACATCGTGGGCGCTAACATCGAGACTTACCTGCTCGAGAAGTCCCGCGCTGTG
CGTCAGGCTAAGGACGAGAGAACCTTCCACATCTTCTACCAGCTGCTGTCCGGCGCTGGCGAGCACTTGAAGTCTGACCTGCTG
CTCGAGGGTTTCAACAACTACCGTTTCCTGTCCAACGGCTATATCCCCATTCCTGGCCAGCAGGACAAGGACAACTTCCAAGAGA
CTATGGAAGCCATGCACATCATGGGCTTCTCCCACGAAGAGATCCTGTCCATGCTGAAGGTGGTGTCCTCCGTCCTGCAGTTCG
GCAACATCTCCTTCAAGAAAGAGCGTAACACCGACCAGGCTTCCATGCCTGAGAACACCGTGGCTCAGAAGCTGTGCCACCTCCT
GGGCATGAACGTGATGGAATTCACCCGTGCTATCCTGACTCCTCGTATCAAAGTGGGCCGTGACTACGTGCAGAAGGCTCAGAC
CAAAGAGCAGGCCGACTTCGCTGTGGAAGCTCTGGCTAAGGCTACCTACGAGCGTCTGTTCCGTTGGCTGGTGCACCGTATCAA
CAAGGCTCTGGACCGTACCAAGCGTCAGGGCGCTTCCTTCATCGGTATCCTGGATATCGCTGGCTTCGAGATCTTCGAGCTGAA
CTCCTTCGAGCAGCTGTGCATCAACTACACCAACGAGAAGCTGCAGCAGCTGTTCAACCACACCATGTTCATCCTGGAACAAGAG
GAATACCAGCGCGAGGGTATCGAGTGGAACTTCATCGACTTCGGCCTGGACCTGCAGCCTTGCATCGACCTGATTGAGCGTCCT
GCTAACCCTCCTGGTGTCCTGGCTCTGCTGGACGAGGAATGCTGGTTCCCAAAGGCTACCGACAAGACCTTCGTGGAAAAGCTG
GTGCAAGAGCAGGGTTCCCACTCCAAGTTCCAGAAGCCTCGCCAGCTGAAGGACAAGGCTGACTTCTGCATCATCCACTACGCT
GGCAAGGTGGACTACAAGGCCGACGAGTGGCTGATGAAGAACATGGACCCTCTGAACGACAATGTGGCTACCCTGCTGCACCAG
TCCTCCGACAGATTCGTGGCTGAACTGTGGAAGGACGTGGACCGCATCGTCGGATTGGACCAAGTGACCGGCATGACCGAGACT
GCTTTCGGTTCCGCTTACAAGACCAAAAAGGGCATGTTCCGTACCGTGGGCCAGCTGTACAAAGAGTCCCTGACCAAGCTGATG
GCTACTCTGCGTAACACTAACCCCAACTTCGTGCGTTGTATCATCCCCAACCACGAGAAGCGTGCTGGCAAGCTTGACCCTCACC
TGGTGCTGGACCAACTGAGGTGCAACGGTGTCTTGGAGGGTATCCGTATCTGCCGTCAGGGTTTCCCCAACCGTATCGTGTTCC
AAGAGTTCCGTCAGCGCTACGAGATCTTGACCCCTAACGCTATCCCCAAGGGTTTCATGGACGGCAAGCAGGCTTGCGAGCGTA
TGATCCGTGCTCTGGAACTGGACCCCAACCTGTACCGTATCGGCCAGTCCAAGATCTTCTTCCGCGCTGGCGTGCTCGCTCACCT
GGAAGAAGAACGCGACCTGAAGATTACCGACATCATCATCTTTTTTCAGGCCGTGTGCCGTGGTTACCTGGCTAGGAAGGCTTT
CGCCAAGAAGCAGCAGCAACTGAGCGCTCTGAAGGTGCTGCAGAGGAACTGCGCTGCTTACCTGAAGCTGAGGCACTGGCAATG
GTGGCGTGTGTTCACCAAAGTGAAGCCTCTGCTGCAAGTGACT